Antimicrobial Bioceramics: Advanced Scaffolds and Coatings for Enhanced Orthopaedic Implant Integration

Ngoc Huu Nguyen

A thesis submitted in fulfilment of the requirements for the degree of Doctor of Philosophy

I acknowledge the support from the ARC Training Centre for Innovative Bioengineering for awarding me a scholarship to cover my tuition fees and providing invaluable support for my research and academic journey.

School of Biomedical Engineering

Faculty of Engineering

University of Sydney

2024

Statement of Originality

This is to certify that, to the best of my knowledge, the content of this thesis is my work. This thesis has not been submitted for any degree or other purposes.

I certify that the intellectual content of this thesis is the product of my work and that all the assistance received in preparing this thesis and sources have been acknowledged.

Ngoc Huu Nguyen

December 2024

Authorship Attribution Statement

This thesis contains published material: **Ngoc Huu Nguyen,** Zufu Lu, Aaron Elbourne, Krasimir Vasilev, Iman Roohani, Hala Zreiqat, and Vi Khanh Truong. Engineering antibacterial bioceramics: Design principles and mechanisms of action. Materials Today Bio 26 (2024): 101069. https://doi.org/10.1016/j.mtbio.2024.101069

This publication forms Chapter 2 of this thesis. I performed the literature review for this publication and wrote the drafts and the final manuscript.

This thesis contains published material: **Huu Ngoc Nguyen**, Iman Roohani, Andrew Hayles, Zufu Lu, Jitraporn Vongsvivut, Krasimir Vasilev, Vi Khanh Truong, Hala Zreiqat. Antibacterial activity and mechanisms of magnesium-doped baghdadite bioceramics for orthopaedic implants. Advanced NanoBiomed Research. (2024).

https://doi.org/10.1002/anbr.202400119

This publication forms chapter 3 of this thesis. I performed all the required data analysis. I wrote, formatted, and prepared the draft and manuscript. I designed and performed all the experiments described in the "experimental section" of this manuscript. Co-authors of the paper assisted and instructed me with the techniques, facilities, fabrication and characterisation material.

This thesis contains material currently under review for publication: **Huu Ngoc Nguyen,** Andrew Hayles, Iman Roohani, Zufu Lu, Frank Fei, Young No, Aaron Elbourne, Kim Chung Nguyen, Jitraporn Vongsvivut, Krasimir Vasilev, Vi Khanh Truong, Hala Zreiqat. Combating *Pseudomonas aeruginosa* and *Staphylococcus aureus* using bismuth-doped baghdadite for orthopaedic implant. (2024).

This manuscript forms chapter 4 of this thesis. I performed all the required data analysis. I wrote, formatted, and prepared the draft and manuscript. I designed and performed all the experiments described in the "experimental section" of this manuscript. Co-authors of the paper assisted and instructed me with the techniques, facilities, fabrication and characterisation material.

This thesis contains material ready for publication: **Ngoc Huu Nguyen,** Thanh Tran Phu, Zufu Lu, Thi Kim Anh Nguyen, Xuan Minh Chau Ta, Andrew Haleys, Jitraporn Vongsvivut, Iman Roohani, Krasimir Vasilev, Vi Khanh Truong, Antonio Tricoli, Hala Zreiqat. One-step synthesis of multifunctional nanospike-structured bismuth doped baghdadite coatings for orthopaedics. Materials Today.

This manuscript forms chapter 5 of this thesis. I performed all the required data analysis. I wrote, formatted, and prepared the draft and manuscript. I designed and performed all the experiments described in the "experimental section" of this manuscript. Co-authors of the paper assisted and instructed me with the techniques, facilities, fabrication and characterisation material.

Ngoc Huu Nguyen
December 2024

Supervisor Statement:

As a supervisor for the candidature upon which this thesis is based, I can confirm that the authorship attribution statements above are correct.

Hala Zreiqat

December 2024

Dedicated

To

My Mother and Father

Acknowledgments

I extend my heartfelt thanks to The University of Sydney, the Faculty of Engineering, and the School of Biomedical Engineering for the invaluable opportunity to conduct this PhD thesis project. The resources and inspiring individuals I have been privileged to work with have significantly contributed to the success of this project. I am also deeply grateful to the ARC Training Centre for Innovative Bioengineering for their generous support through a full scholarship, which made this journey possible. I also wish to acknowledge The Postgraduate Research Support Scheme (PRSS) and the School Research Funding Scheme (SRFS) for providing essential funding to attend conferences and access specialist services.

I owe immense gratitude to Professor Hala Zreiqat, an inspiring mentor and an extraordinary person. Hala, your steady support, encouragement, and guidance have profoundly impacted my life and career. Joining your group has been a life-changing opportunity, one that I will always cherish. Your kindness, patience, and insights have shaped my journey in ways I cannot express fully. I am honoured to have had the chance to work with you and look forward to staying connected as I go on board new chapters in my career.

I am also deeply appreciative of my co-supervisors, Associate Professor Vi Khanh Truong, Associate Professor Zufu Lu, and Associate Professor Iman Roohani, for their dedication, time, and expertise throughout my PhD journey. Your guidance and insights have been invaluable, and I am grateful for your support and the resources you have shared.

I would like to sincerely thank Professor Antonio Tricoli and his team, including Dr Phu Thanh Tran, Minh Chau Ta Xuan, and Kim Anh Nguyen Thi, who assisted with the coating surface and assisted me with SEM, TEM, and XRD characterisation.

I extend my sincere thanks to Professor Krasimir Vasilev from the Biomedical Engineering Laboratory at Flinders Medical Centre, College of Medicine and Public Health, Flinders University, Prof. Melissa Brown from Molecular Microbiology Lab, School of Biological Science and Engineering, Flinders University, and Associate Professor Aaron Elbourne from the Nanobiotechnology Engineering Lab, RMIT University. Thank you for hosting my research visits and providing access to your cutting-edge facilities and technology, which were instrumental in advancing my work.

My gratitude also extends to all the members of my group and the groups I visited during my research. Your invaluable assistance, brilliant suggestions, and camaraderie have been essential to my studies, and your friendship and moral support were a great comfort during challenging times. Thank you.

I would like to express my heartfelt gratitude to the Australian Nuclear Science and Technology Organisation (ANSTO) for granting beam time funding, which significantly advanced the experimental aspects of my research. Their support has been invaluable in enabling access to state-of-the-art synchrotron facilities and fostering cutting-edge scientific inquiry. I am deeply honoured to have been selected for the 2024 São Paulo School of Advanced Science on 4th Generation Synchrotron Techniques (SPSAS SyncLight) and to receive the AINSE ANSTO French Embassy Scholarship (SAAFE), which facilitated an enriching internship experience in France. Additionally, being chosen to attend the 4th Asia-Oceania Forum for Synchrotron Radiation (AOFSRR) School in 2023, with full funding, was a pivotal experience that broadened my knowledge and connected me with an inspiring community of researchers. These opportunities have been transformative in shaping my academic journey, and I am sincerely thankful for the support and recognition that made them possible.

To Dr Jitraporn (Pimm) Vongsvivut, thank you for teaching and training me in Synchrotron Science and for your guidance and mentorship. Your support as a teacher, mentor, and friend has enriched my research experience immensely.

I also would like to thank Professor David Stopar, Assistant Professor Iztok DogsaDr (University of Ljubljana), Dr Andrew Hayles, Dr Richard Bright, Dr Wenshao Li (Flinders University) Dr Kim Chung Nguyen (The University of Sydney), Dr Duy Quang Pham (Swinburn University), Dr Hoang Phuc Le (RMIT University), Dr Pham Ho Trong Nhan (Western Sydney University) for guidance and useful advice, review manuscripts, scientific discussions and psychological support.

To the staff at the School of Biomedical Engineering, The University of Sydney, Medical Biotechnology- Flinders University, and Australian Synchrotron, I am grateful for your technical support and assistance in operating equipment for testing and characterisation, which was integral to my research. I would also like to thank Flinders Microscopy and Microanalysis, Flinders Analytical and Adelaide Microscopy, the RMIT Microscopy and Microanalysis Facility (RMMF), Centre for Advanced Microscopy (CAM), the University of New South Wales Analytical Centre at the Australian National University and Queensland Node of Metabolomics and Proteomics Australia for their assistance with proteomics data acquisition and Q-MAP supported by Bioplatforms Australia, an NCRIS-funded initiative for their assistance operating types of equipment in this study.

I would like to express my deepest love and appreciation to my family, to whom this thesis is dedicated. To my mother, Nguyen Kim Phung, and my father, Nguyen Long Han, I am forever grateful for the unwavering love, sacrifices, and support you have given me throughout my life. Your encouragement has been my constant source of strength, and this achievement is as much

yours as it is mine. To my beloved sister and brother Nguyen Ngoc Minh Sang and Nguyen Chi Tan, thank you for standing by me with unwavering support and understanding.

Finally, my deepest gratitude goes to my dear wife, Truong Thi Trieu Tien. Your love, patience, and support throughout this journey have been invaluable. Thank you for being my foundation and sharing this journey with me through every challenge. I am endlessly grateful to you.

With all my love and gratitude, this thesis is dedicated to all of you.

List of publications, presentations and awards

Publication arising from this thesis:

Nguyen, Ngoc Huu, Zufu Lu, Aaron Elbourne, Krasimir Vasilev, Iman Roohani, Hala Zreiqat, and Vi Khanh Truong. Engineering antibacterial bioceramics: Design principles and mechanisms of action. Materials Today Bio 26 (2024): 101069. https://doi.org/10.1016/j.mtbio.2024.101069

Huu Ngoc Nguyen, Iman Roohani, Andrew Hayles, Zufu Lu, Jitraporn Vongsvivut, Krasimir Vasilev, Vi Khanh Truong, Hala Zreiqat. Antibacterial activity and mechanisms of magnesium-doped baghdadite bioceramics for orthopaedic implants. Advanced Nanomedical research. (2024). https://doi.org/10.1002/anbr.202400119

Huu Ngoc Nguyen, Andrew Hayles, Iman Roohani, Zufu Lu, Frank Fei, Young No, Aaron Elbourne, Kim Chung Nguyen, Jitraporn Vongsvivut, Krasimir Vasilev, Vi Khanh Truong, Hala Zreiqat. Combating Pseudomonas aeruginosa and Staphylococcus aureus using bismuth-doped baghdadite for orthopaedic implant. Journal of Colloid and Interface Science. (2024). (Under review).

Ngoc Huu Nguyen, Thanh Tran Phu, Zufu Lu, Thi Kim Anh Nguyen, Xuan Minh Chau Ta, Andrew Haleys, Jitraporn Vongsvivut, Iman Roohani, Krasimir Vasilev, Vi Khanh Truong, Antonio Tricoli, Hala Zreiqat. One-step synthesis of multifunctional nanospike-structured bismuth doped baghdadite coatings for orthopaedics. Materials Today. (Ready to submit).

Other publications related to this thesis:

- Alemie, Markos Negash, Richard Bright, **Ngoc Huu Nguyen**, Vi Khanh Truong, Dennis Palms, John D. Hayball, and Krasimir Vasilev. "Surface Chemistry Induced IgG

Unfolding and Modulation of Immune Responses." *ACS Applied Materials & Interfaces* 16, no. 38 (2024): 50507-50523.

- Nguyen Tien Thanh[#], **Ngoc Huu Nguyen[#],** Giang Tuyet Pham, Jitraporn Vongsvivut, Melissa H. Brown, Vi Khanh Truong, and Krasimir Vasilev. Synchrotron macro-ATR-FTIR micro-spectroscopy to unlock silver ion-induced biochemical alterations in bacteria. Materials Advances 4, no. 23 (2023): 6342-6352.
- Gangadoo, Sheeana, **Huu Nguyen**, Piumie Rajapaksha, Hala Zreiqat, Kay Latham, Daniel Cozzolino, James Chapman, and Vi Khanh Truong. Inorganic nanoparticles as food additives and their influence on the human gut microbiota. Environmental Science: Nano 8, no. 6 (2021): 1500-1518.

National and International Conferences:

- **Ngoc Huu Nguyen**, Zufu Lu, Iman Roohani, Frank Fei, Young No, Jitraporn Vongsvivut, Krasimir Vasilev, Vi Khanh Truong, Hala Zreiqat. The antibacterial activity of bismuth-doped baghdadite for infection prevention in orthopaedic implants. SydneyMSK Annual Scientific Meeting. 2024. (Awarded for top presentation)
- **Ngoc Huu Nguyen,** Iman Roohani, Andrew Hayles, Zufu Lu, Young No, Frank Fei, Krasimir Vasilev, Jitraporn Vongsvivut, Vi Khanh Truong, Hala Zreiqat. Investigating the non-antibiotic antibacterial activity of bioceramics for infection prevention and biocompatibility in orthopaedic implants. Australian Society for Microbiology Annual Scientific Meeting. 2024.
- **Ngoc Huu Nguyen,** Iman Roohani, Zufu Lu, Young No, Frank Fei, Krasimir Vasilev, Jitraporn Vongsvivut, Vi Khanh Truong, Hala Zreiqat. Next-generation bioceramics of magnesium-doped baghdadite: a breakthrough against orthopaedic implant-associated infections. ASBTE Regional Showcase. 2023. (Awarded for an Outstanding Talk)

- **Ngoc Huu Nguyen,** Iman Roohani, Zufu Lu, Krasimir Vasilev, Jitraporn Vongsvivut, Vi Khanh Truong, Hala Zreiqat. Elucidating the antimicrobial mechanism of silver ions using synchrotron macro-ATR-FTIR microspectroscopy. Australia Synchrotron User Meeting. 2022.
- **Ngoc Huu Nguyen,** Iman Roohani, Zufu Lu, Krasimir Vasilev, Jitraporn Vongsvivut, Vi Khanh Truong, Hala Zreiqat. Nanostructured surface and substituted bioceramics for antibacterial applications. Emerging Leaders Showcase- Flinders Medicine & Public Health. (2022).

Awards

- Top presentation at SydneyMSK annual scientific meeting 2024.
- AINSE ANSTO French Embassy Scholarship (SAAFE), 2024.
- I was honoured to be selected to participate in the São Paulo School of Advanced Science on 4th Generation Synchrotron Techniques at CNPEM, Brazil, in 2024.
- School Research Funding Scheme (SRFS), 2024
- I received the ASBTE Student Award for an Outstanding Talk at the ASBTE 2023.
- I was honoured to be selected to attend the 4th Asia Oceania Forum on Synchrotron Radiation Research School, Thailand, in 2023.
- University of Sydney Postgraduate Research Support Scheme Award, in 2023.
- I was honoured with the Poster Slam Award at the Synchrotron User Meeting in 2022.

Table of Contents

List of Figures

List of tables

List of Abbreviations

Ag	Silver
ATCC	American Tissue Cell Culture
ATR-FTIR	Attenuated Total Reflectance Fourier Transform Infrared
BAG	Baghdadite
BCP	Biphasic calcium phosphate
BG	bioactive glasses
Bi^{3+}	Bismuth ions
Bi-BAG	Bismuth doped baghdadite
CLSM	Confocal laser scanning microscopy
Cu	Copper
DCF	Dichlorofluorescein
DNA	Deoxyribonucleic acid
DMSO	Dimethyl sulfoxide
E. Coli	*Escherichia coli*
ESKAPE	*Enterococcus faecium, Staphylococcus aureus, Klebsiella pneumoniae, Acinetobacter baumannii, Pseudomonas aeruginosa, and Enterobacter spp.*
Fn	Fibronectin
FnBPs	Fibronectin-binding proteins
FSP	Flame spray pyrolysis
Ga-HAp	Gallium-doped HAp
GSH	Reduced glutathione
HA/HAp	Hydroxyapatite

HOBs	human osteoblast cells
HT	Hardystonite
IAIs	Implant-associated infections
Mg^{2+}	Magnesium ions
Mg-BAG	Magnesium doped baghdadite
MRSA	Methicillin-resistant *Staphylococcus aureus*
MTA	mineral trioxide aggregate
NK	Natural killer
OD	The optical density
P. aeruginosa	*Pseudomonas aeruginosa*
PBS	Phosphate-buffered saline
ROS	reactive oxygen species
S. aureus	*Staphylococcus aureus*
SD	*Standard deviation*
SEM	Scanning electron microscopy
Sr-HT	Strontium-doped hardystonite
Te	Tellurium
WHO	World Health Organization
XPS	X-ray photoelectron microscopy
XRD	X-ray diffraction
Y-TZP	Zirconia-stabilized yttria
Zn	Zinc

Abstract

Orthopaedic implants are crucial in treating bone-related conditions. However, implant-associated infections (IAIs) remain a significant challenge, often leading to implant failure and exacerbating antibiotic resistance. Baghdadite bioceramics (BAG, $Ca_3ZrSi_2O_9$) have shown great promise due to their bioactivity and bone compatibility, but they inherently lack antibacterial properties. This research addresses this limitation by enhancing the antibacterial of BAG through chemical and physical modification achieved by doping BAG with biocompatible metal ions, magnesium-doped baghdadite (Mg-BAG) and bismuth-doped baghdadite (Bi-BAG) for scaffold and coating applications. This study demonstrates the synergistic chemistry and antibacterial activity of Mg-BAG and Bi-BAG against representative Gram-negative *Pseudomonas aeruginosa* and Gram-positive *Staphylococcus aureus*. Multifaceted antibacterial mechanisms are elucidated, including biomolecule alterations, generation of intracellular reactive oxygen species (ROS), and membrane depolarisation. Furthermore, this study presents pioneers using flame spray pyrolysis (FSP) technology to develop Bi-BAG coating nanostructured spike-like coatings on titanium substrates. This is the first study to utilise FSP for creating multifunctional nanocoating with Bi-BAG spikes on orthopedic implants. This unique surface modification significantly enhances the synergy of antibacterial chemicals and topography properties while maintaining the biocompatibility of the titanium substrate. Furthermore, the bioactivity of the Bi-BAG coating promotes human osteoblast cells (HOBs) proliferation and mineralisation over seven days. The FSP technique ensures uniform coating, enhancing the overall biological activity of the implant. This research provides a promising non-antibiotic strategy to combat IAIs, offering multifunctional bioceramics that contribute to advancing next-generation biomaterials for orthopaedic applications.

CHAPTER 1:

INTRODUCTION

The global increase in ageing populations has led to a surge in bone diseases such as osteoarthritis and femoral head necrosis, driving the demand for effective bone repair and replacement solutions [1, 2]. Annually, over 200,000 bone transplants are operated worldwide to restore bone defects [3], with the global implant market predicted to grow at an annual rate exceeding 5%, reaching an estimated $145.6 billion by 2030 [4]. However, the restoration of bone defects caused by trauma, infection, osteoporosis, or resection of malignant tissue remains a big clinical problem. Allografts and autografts are examples of traditional methods that have big problems, such as limited availability of healthy tissue, morbidity at donor sites, and an increased risk of infection and disease transmission [4]. In recent years, bioceramic implants have emerged as a promising alternative due to their biocompatibility and ability to support bone regeneration through bioactivity [5]. Despite these advantages, the clinical application of bioceramics is still hindered by their lack of inherent antibacterial properties, which compromises their effectiveness in preventing implant-associated infections (IAIs).

IAIs are a leading cause of premature implant failure, presenting a significant obstacle in orthopaedic treatment. Orthopaedic implant infection rates range from 2-5% [4], increasing to a concerning 30% in the case of open fractures [4, 5], Common pathogens such as *Pseudomonas aeruginosa* (*P. aeruginosa*) and *Staphylococcus aureus* (*S. aureus*), are frequently implicated in IAIs, presenting a critical challenge for the success of orthopaedic implants [6, 7]. Tackling infections with antibiotics is increasingly problematic due to the alarming increase in antibiotic-resistant organisms. Conventional approaches such as device replacement and prolonged antibiotic treatment, unintentionally exacerbate the escalating problem of antibiotic resistance [8]. According to the World Health Organization (WHO), antibiotic resistance ranks among the top ten global threats, with fatalities related to this issue projected to grow from 700,000 to 10 million by 2050, surpassing cancer as the primary cause of death worldwide [6]. Thus, there is a critical need to design next-generation antimicrobial

synthetic bioceramics. There is, therefore, an urgent need to develop next-generation antimicrobial synthetic bioceramics that can effectively combat IAIs without relying on antibiotics.

Among the potential bioceramics, baghdadite (BAG, $Ca_3ZrSi_2O_9$), a calcium silicate-based ceramic, is gaining recognition as a promising synthetic bone substitute due to its excellent bioactivity, biodegradability and ability to promote the regeneration of complex, large bone defects [7-11]. Despite these advantages, BAG scaffolds are limited in their antibacterial activity. Current strategies to address this limitation are transition-metal ions such as copper ions (Cu^{2+}), zinc ions (Zn^{2+}), and silver ions (Ag^{+}), which have demonstrated varying levels of effectiveness in combating a wide range of bacteria [12, 13]. For instance, Ag^{+} and Cu^{2+} coatings have been developed for implants to inhibit bacterial growth, disrupt bacterial cell membranes, interfere with essential cellular processes and inhibit biofilm formation [14]. However, the use of Ag^{+} and Cu^{2+} is limited by concerns about their toxicity [15] and the risk of contributing to antibiotic resistance [16], and the antibiotic resistance [15].

Magnesium ion (Mg^{2+}) and bismuth ion (Bi^{3+}), have been recognised for their antibacterial properties [17-21], biocompatibility, and ability to stimulate bone regeneration, making them promising candidates for doping in bioceramics [22, 23]. These ions not only enhance antibacterial activity but also contribute to bone regeneration and compatibility, offering a multifaceted solution for IAIs challenges [22, 23]. In chapters 3 and 4, we aim to dope Bi^{3+} or Mg^{2+} into baghdadite bioceramic to produce the next generation of Mg^{2+} doped baghdadite (Mg-BAG) and Bi^{3+} doped baghdadite (Bi-BAG), with antibacterial activity against the commonly isolated orthopaedic pathogens. Mg-BAG and Bi-BAG offer an innovative, non-antibiotic and cost-effective strategy for developing antibacterial bone prostheses. In addition, the surface roughness was known to play a significant role in modulating osteointegration and

bacterial adhesion [24-27]. Eventually, this study will explore the antibacterial performance at various roughness levels.

Titanium (Ti), widely used in hip, knee, and dental implants, is the material of choice for orthopaedic applications due to its favourable properties, including low density, non-toxicity, and excellent biocompatibility [28]. However, titanium has poor bioactivity and lacks inherent antibacterial properties leading to potential implant loosening and postoperative infections [29]. To address these limitations, this study introduces the first application of flame spray pyrolysis (FSP) technology for the one-step sintering and coating of Bi-BAG onto titanium implants. This innovative approach offers a strategic method to combat implant-associated infections. The novelty of this work lies in the fabrication of nanostructured coatings with spike-like features on titanium surfaces. These coatings, characterised by increased surface area and unique morphology, significantly enhance antibacterial efficacy by preventing bacterial adhesion and proliferation. To address this limitation, this study presents the first application of flame technology for the one-step sintering and coating of Bi-BAG on Ti implants. This innovative approach offers a strategic method to combat implant-associated infections. The novelty of this work lies in the fabrication of nanostructured coatings with spike-like features on Ti surfaces. These coatings, characterised by increased surface area and unique morphology, significantly enhance antibacterial efficacy by preventing bacterial adhesion and proliferation.

This study aims to develop Mg-BAG and Bi-BAG with two applications each focusing on developing advanced biomaterials for orthopaedic applications (Figure 1.1):

(1) The first part focuses on Mg-BAG and Bi-BAG scaffolds with effective antibacterial activity against common orthopaedic pathogens, including Gram-negative *P. aeruginosa* and Gram-positive *S. aureus*. This section investigates the scaffolds' multifaceted antibacterial mechanisms, including alterations to biomolecules, generation of intracellular reactive oxygen

species, and induction of membrane depolarisation, ultimately disrupting bacterial membrane integrity.

(2) The second part of this research focuses on developing Bi-BAG nanocoatings with spike-like structures using flame technology, a novel and cost-effective one-step synthesis approach for bioceramics. This innovative technique ensures uniform, nanostructured coatings with enhanced surface topography, distinguishing it as a significant advancement in the field. The Bi-BAG nanocoating exhibits multifaceted antibacterial mechanisms, including the generation of intracellular reactive oxygen species (ROS) and membrane depolarisation. Using synchrotron ATR-FTIR microspectroscopy and proteomics, Bi-BAG coating disrupts bacterial metabolic processes and compromises biomolecular integrity through multiple antibacterial mechanisms. These combined actions provide robust antibacterial efficacy, addressing the critical challenge of implant-associated infections. Moreover, the Bi-BAG coating can enhance human osteoblast (HOB) proliferation and mineralisation, key markers for bone regeneration and implant integration.

Mg-BAG and Bi-BAG present next-generation bioceramics for orthopaedic scaffolds and medical coatings with infection prevention and simultaneously promoting successful integration with host tissue.

GAPS IN KNOWLEDGE

Despite advancements in orthopaedic implant technology, several critical knowledge gaps continue addressing infection-associated challenges. IAIs remain a significant concern due to the rising prevalence of antibiotic resistance. While bioceramics like baghdadite are valued for their bioactivity and compatibility with bone tissue, their potential antibacterial properties have been minimally investigated. Specifically, there is a limited understanding of how modifications to baghdadite, such as doping with biocompatible ions like Mg^{2+} and Bi^{3+}, can influence bacterial inhibition mechanisms. This gap highlights the urgent need to develop strategies for enhancing the antibacterial activity of these materials as non-antibiotics for infection prevention The exact interactions between these dopants and bacterial cells, particularly their effects on cellular membranes, biomolecular pathways, and intracellular processes, remain unclear. Additionally, there is insufficient data on balancing antibacterial efficacy with maintaining the material's biocompatibility, creating uncertainty in developing effective dosing strategies.

Another notable gap exists in coating technology for orthopaedic implants. While FSP is recognised for producing high-quality nanostructured coatings, its application to bioceramics has not been sufficiently explored. Specifically, the potential of FSP to create uniform, functional coatings that achieve a balance between strong antibacterial properties and the promotion of osteoblast activity has not been systematically studied. Moreover, the antibacterial performance of Mg^{2+} and Bi^{3+} doped bioceramics against key orthopaedic pathogens, such as Gram-negative *P. aeruginosa* and Gram-positive *S. aureus*, remains poorly understood. The mechanisms these materials disrupt bacterial processes and their comparative efficacy against different bacterial strains have not been thoroughly characterised. Similarly, the interaction of these materials with bone cells, such as osteoblasts, under realistic biological conditions has not been adequately addressed, limiting their translation into clinical use.

These gaps highlight the need for in-depth studies to elucidate the antibacterial mechanisms of doped bioceramics, optimise advanced coating techniques like FSP, and evaluate the biological and antibacterial performance of these materials under conditions relevant to orthopaedic applications.

RESEARCH QUESTIONS, AIMS AND EXPECTED OUTCOMES

Research Questions

This research aims to develop advanced antibacterial bioceramics for scaffolds and coatings optimised for orthopaedic implants. Specific questions this thesis addresses are:

- How do Mg^{2+} and Bi^{3+} dopants enhance the antibacterial properties of the BAG bioceramics scaffold?
- What are the multifaceted antibacterial mechanisms of Mg-BAG and Bi-BAG scaffolds, including their effects on bacteria?
- Can FSP effectively produce uniform coatings with spike-like features on titanium implants?
- How effective are FSP coatings on titanium in preventing infection?
- How do FSP coatings on titanium implants influence osteoblast adhesion, proliferation and mineralisation?

Expected Outcomes

- A comprehensive understanding of the antibacterial mechanisms of Mg^{2+} and Bi^{3+} dopants in baghdadite bioceramics**,** including their impact on bacterial disruption and inhibition.

- A validated FSP technique for applying durable, nanostructured bioceramic coatings on orthopaedic titanium implants.

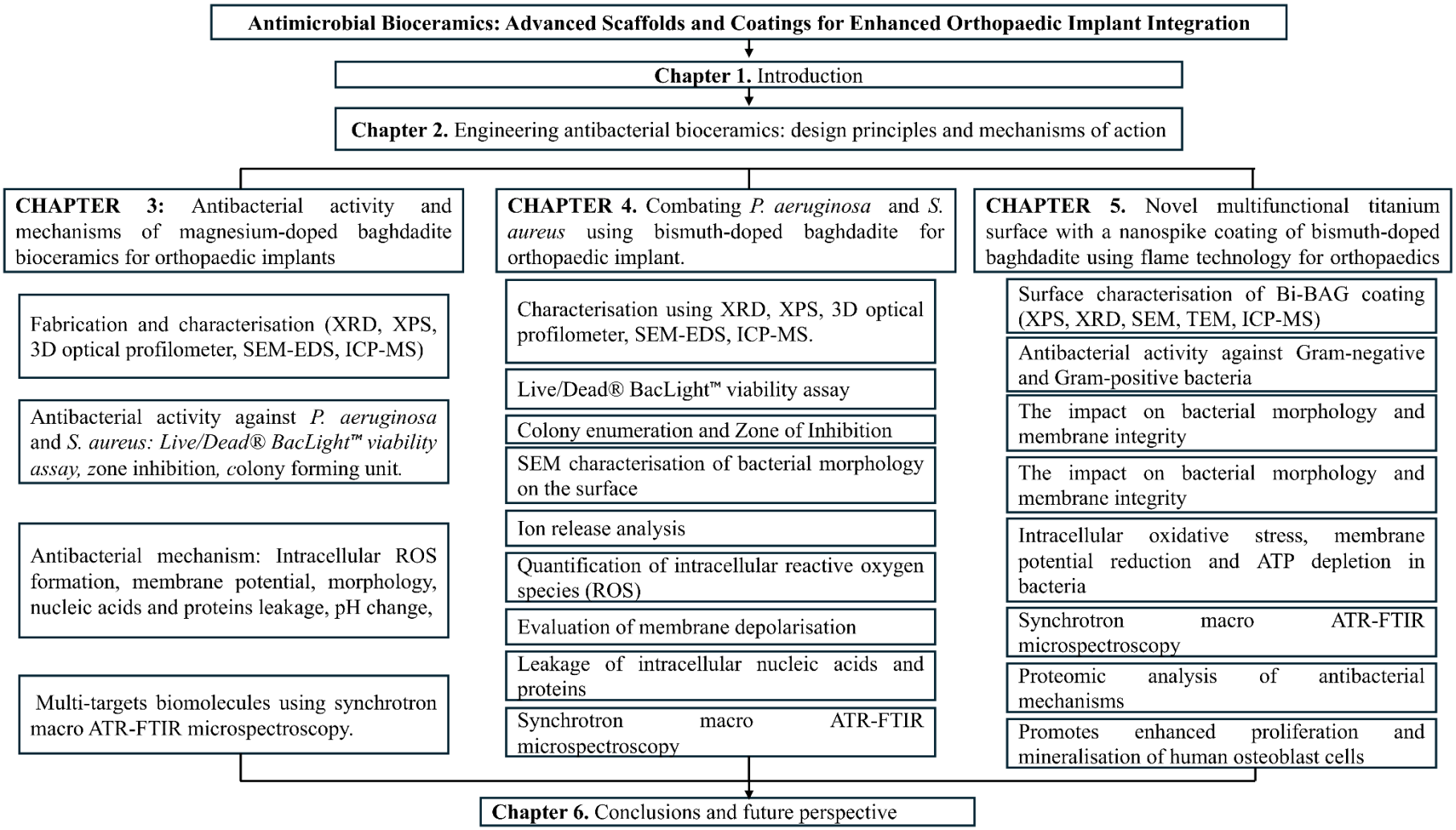

Figure 1.1. The flowchart illustrates the research framework of the thesis.

CHAPTER 2:

ENGINEERING ANTIBACTERIAL BIOCERAMICS: DESIGN PRINCIPLES AND MECHANISMS OF ACTION

Ngoc Huu Nguyen[1], Zufu Lu[1], Aaron Elbourne[2], Krasimir Vasilev[3], Iman Roohani[1], Vi Khanh Truong[3*], Hala Zreiqat[1*]

[1]School of Bioengineering, The University of Sydney, Camperdown, NSW 2006, Australia

[2]School of Science, RMIT University, Melbourne, Victoria 3001, Australia

[3]Biomedical Nanoengineering Laboratory, College of Medicine and Public Health, Flinders University, Bedford Park SA 5042, Australia

Published in Material Today Bio. 26, 01069. 2024

https://doi.org/10.1016/j.mtbio.2024.101069

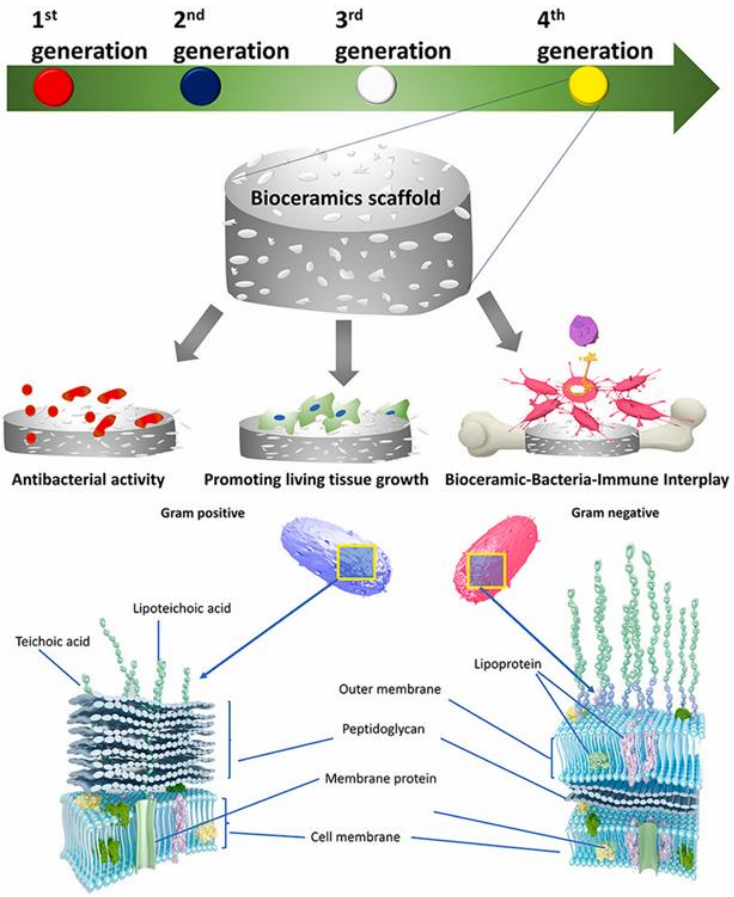

Abstract

The urgency to address skeletal abnormalities and diseases through innovative approaches has led to a significant interdisciplinary convergence of engineering, 3D printing, and design in developing individualised bioceramic bioscaffolds. This review explores the recent advancements and future trajectory of non-antibiotic antibacterial bioceramics in bone tissue engineering, an importance given the escalating challenges of orthopaedic infections, antibiotic resistance, and emergent pathogens. Initially, the review provides an in-depth exploration of the complex interactions among bacteria, immune cells, and bioceramics in clinical contexts, highlighting the multifaceted nature of infection dynamics, including protein adsorption, immunological responses, bacterial adherence, and endotoxin release. Then, focus on the next-generation bioceramics designed to offer multifunctionality, especially in delivering antibacterial properties independent of traditional antibiotics. A key highlight of this study is the exploration of smart antibacterial bioceramics, marking a revolutionary stride in medical implant technology. The review also aims to guide the ongoing development and clinical adoption of bioceramic materials, focusing on their dual capabilities in promoting bone regeneration and exhibiting antibacterial properties. These next-generation bioceramics represent a paradigm shift in medical implant technology, offering multifunctional benefits that transcend traditional approaches.

Keywords: Bioceramics, implant-associated infection, antimicrobial, orthopaedic implant.

2.1 INTRODUCTION

The reconstruction of extensive bone defects caused by trauma, infection, osteoporosis, or resection of malignant tissue remains a major challenge in clinical treatment. Allografts and autografts suffer serious drawbacks, such as limited availability of healthy tissue, morbidity at donor sites, and risks of infection and disease transmission. Metal and alloy implants possess the necessary mechanical strength but are excessively rigid, not resorbable, and perform poorly in biocompatibility and bioactivity, often leading to aseptic loosening, infection and other post-surgery complications. An excellent alternative to have emerged in recent years is bioceramic implants, which are biocompatible and highly bioactive [30-32]. But despite their advantages, bioceramics available in the clinic are still lacking in natural bone's resistance to bacterial infection, which significantly hampers their ability to prevent and combat implant-associated infections [33-37]. To fight against infection problems, bioceramics scaffolds with various antibacterial strategies are developed for bone repair and regeneration [38, 39].

IAIs are some of the primary factors related to premature implant failure. Strategies to treat implant infections primarily rely on administering antibiotics and surgical intervention. More than 200,000 bone transplants are performed annually worldwide to repair bone defects [40], with the global implant market predicting more than five per cent annual growth and is expected to reach $145.6 billion in 2030 [41]. Implant-associated infections have been growing steadily, with a marked increase in cases reported over recent years. According to the WHO, antibiotic resistance is one of the top ten global public health concerns confronting humanity, and the fatalities related to this issue might grow from 700,000 to 10 million by 2050, surpassing cancer as the primary cause of death worldwide [42-44]. Biofilms are responsible for approximately 80% of these infections, presenting a considerable challenge to healthcare systems and patient outcomes [45]. Bacterial antibiotic resistance and the formation of biofilm

seriously reduce the efficacy of antibiotics[46, 47] as antimicrobials must cross the biofilm to effectively inhibit bacterial growth infections frequently. This escalating problem underscores the urgent need for innovative strategies to develop the next generation of bioceramic biomaterials with suitable chemical and topological features, which are considered the most crucial prerequisites for biofilm formation to prevent and combat implant-associated infections. The most critical considerations for designing and manufacturing bioceramics are their resistance to microbial colonisation and biofilm formation. Developing bioceramics with integrated antibacterial properties is crucial in addressing the escalating challenges of implant-associated infections and antibiotic resistance, ultimately ensuring long-term success.

The top five bacteria causing implant infection, critical in the context of osteomyelitis, include *S. aureus, Staphylococcus epidermidis, P. aeruginosa, Enterobacter cloacae, and Escherichia coli* [48]. *S. aureus* is notable for invading, colonising, and thriving within the bone, making it a particularly formidable pathogen in the case of osteomyelitis (Figure 2.1). Gram-positive and Gram-negative bacteria have distinct cell shapes, biochemistry, and biomolecular mechanisms that enable them to survive and grow on the implant surface [49]. Furthermore, they are difficult to remove and resist the immune system and frequently become a cause of opportunistic infections [50].

This review provides a comprehensive analysis of bioceramic-associated infections and the importance of developing the next generation of antibacterial bioceramics implants for orthopaedic reconstructive surgeries. An important focus will be the investigation of the complex interplay between various factors influencing bioceramic infection, such as protein adsorption, immune cell response, bacterial adhesion, and endotoxin release. Knowledge gained will inform the strategies to develop the next generation of antimicrobial bioceramics biomaterials to prevent implant infection. By providing a comprehensive understanding of

antibacterial mechanisms and strategies, we hope to pave the way for developing innovative solutions for preventing implant-associated infections and advancing next-generation bioceramics.

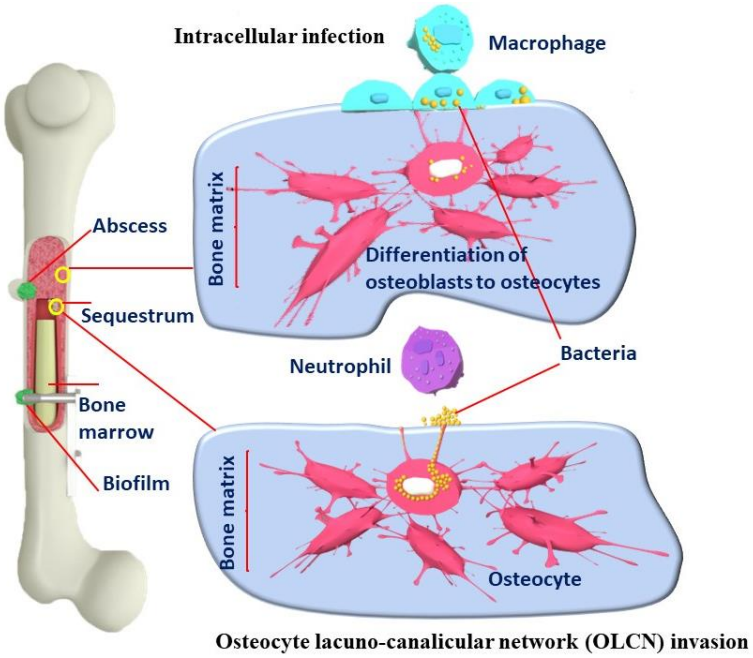

Figure 2.1. Bacterial strategies in osteomyelitis. Bacteria have a variety of pathogenic pathways. Bacteria persistence is most likely caused by intracellular infection of osteoblasts, osteoclasts, and osteocytes, and macrophages promote bacterial dispersion and multiorgan failure. Bacteria can evade hosting immune cells by invading the osteocyte-lacuna canalicular network, most found within a sequestrum. Through diffusion constraints and metabolic variety, Bacteria biofilms on implant surfaces and necrotic bone confer immune cell and antibiotic resistance. Bacteria can be found in both long bones and soft tissue. In the centre of an abscess, bacteria cells are detected, surrounded by a fibrous pseudo capsule and dead and live immune cells.

2.2 ADVANCEMENTS AND CHALLENGES OF BIOCERAMICS FOR BONE TISSUE ENGINEERING

The biocompatible, osteoconductive, and biodegradable properties of bioceramics and their composite biomaterials make them ideal biomaterials for use in bone tissue engineering [30, 31]. Table 1 summarises the properties of bioceramics in bone tissue engineering.

Table 2.1. Summary of the key aspects and significance of bioceramics

Aspect	Significance	Ref
Nature of the bioactive bond	Apatite formation on the surface of bioceramics is pivotal in indirect bonding. The hydroxycarbonate apatite crystals were bound to layers of collagen fibrils generated by osteoblasts at the interface. The chemical bonding of the hydroxycarbonate apatite layer to collagen formed a strong interface connection. Five surface reactions at the surface occur: cation exchange and Si-OH group formation, on which amorphous calcium phosphate phase deposits, crystallising to HCA, which binds to collagen.	[51, 52]
Bioceramics are biocompatible	Bioceramics closely mimic the composition of natural bone, promoting excellent compatibility with host tissue. They do not harm the natural tissues of the body and can be used for long-term implantation. Bioceramics provides a scaffold for bone cell attachment, migration, and proliferation, promoting new bone	[23, 53, 54]

	formation. Some bioceramics can induce osteogenic differentiation of stem cells, further enhancing bone regeneration.	
Bioceramics can be designed to be resorbable	Bioceramics can be designed with controlled degradation rates, enabling gradual replacement with native bone tissue as new bone forms.	[30, 55-57]
Bioceramics can be combined with other biomaterials	The incorporation of polymers (as composite) and metals (as coating), to create composite materials with enhanced properties for bone tissue engineering.	[54]
Bioceramics can be designed with different compositions and properties	They are versatile and customisable for various bone tissue engineering applications	[30, 58]
Bioceramics can be fabricated into	Bioceramics are allowing for the creation of patient-specific implants that fit better and have improved stability using additive manufacturing techniques	[22, 59] [22]

various shapes and sizes		
TAntibacterial properties	Some bioceramics exhibit antimicrobial properties, reducing the risk of infection in bone tissue engineering.	[60, 61]
Cost-effectiveness	Bioceramics can be produced at a relatively low cost, making them a more accessible option for bone tissue engineering.	[62, 63]

Bioceramics can be made from various materials, including bioactive glasses (BG), calcium phosphates, and silicate-based ceramics, each with various advantages depending on the application [10, 64]. This adaptability enables the development of bioceramics with customised characteristics to satisfy the needs of various clinical circumstances. Advances in material science and fabrication technologies, such as 3D printing have enabled the creation of bioceramic-based scaffolds with controlled porosity, mechanical strength, and degradation rates, allowing for better integration with the host tissue and improved tissue regeneration [65, 66].

Bioceramics infection represents an important drawback to their successful clinical application. One of the primary concerns is bacterial adhesion and colonisation on the surface of bioceramic implants, which can contribute to biofilm formation and difficult-to-treat persistent infections. In addition, the widespread usage of antibiotics raises concerns regarding the emergence of antibiotic-resistant bacteria creating difficulty for long-term infection control strategies [67]. Infections can also hinder the osseointegration of bioceramic implants and induce an adverse immune response, resulting in implant failure [68]. Furthermore, balancing the antimicrobial properties, mechanical properties, biocompatibility, and bioactivity of bioceramics can be

difficult because modifying one property can deleteriously affect the others. It is essential to overcome these obstacles to develop infection-resistant bioceramic implants with the desired biological and mechanical properties.

Designing bioceramic materials with inherent antimicrobial properties, such as incorporating antimicrobial ions (e.g., silver (Ag), copper (Cu), or zinc (Zn)) or developing ceramics with specific surface topographies that discourage bacterial adhesion, is one approach. In the other approach, antimicrobial peptides or agents can be incorporated into the material so that they can be released in a controlled and sustained manner, providing local antibacterial activity without causing systemic adverse effects. Additionally, combining bioceramics with other biomaterials to create composites may enhance the equilibrium between antimicrobial properties and other desirable characteristics, such as mechanical strength and biocompatibility [69, 70]. Complex structures with customised surface properties that inhibit bacterial adhesion and biofilm formation can also be fabricated using advanced fabrication techniques, such as 3D printing. Researchers can address the challenges of infection-related complications in bioceramics by investigating these novel approaches. Figure 2.2 presents the evolution of bioceramics and the innovations and achievements in bioceramics-based scaffolds with diverse antibacterial properties aimed at addressing bone implant-associated infections and bone deformities. Various strategies, such as drug-induced, ion-mediated, physically activated, and combined antibacterial methods, are employed in these advanced scaffolds to enhance their effectiveness in promoting bone healing and preventing infections. The production methods of ceramics, such as 3D printing, significantly impact their antimicrobial properties. Firstly, The 3D printing process can influence the surface characteristics of the final products, thereby impacting their antimicrobial performance [71]. Secondly, the microstructure and surface characteristics, which are influenced by the manufacturing technique, are key determinants of the ability of bioceramics to resist microbial colonisation [72].

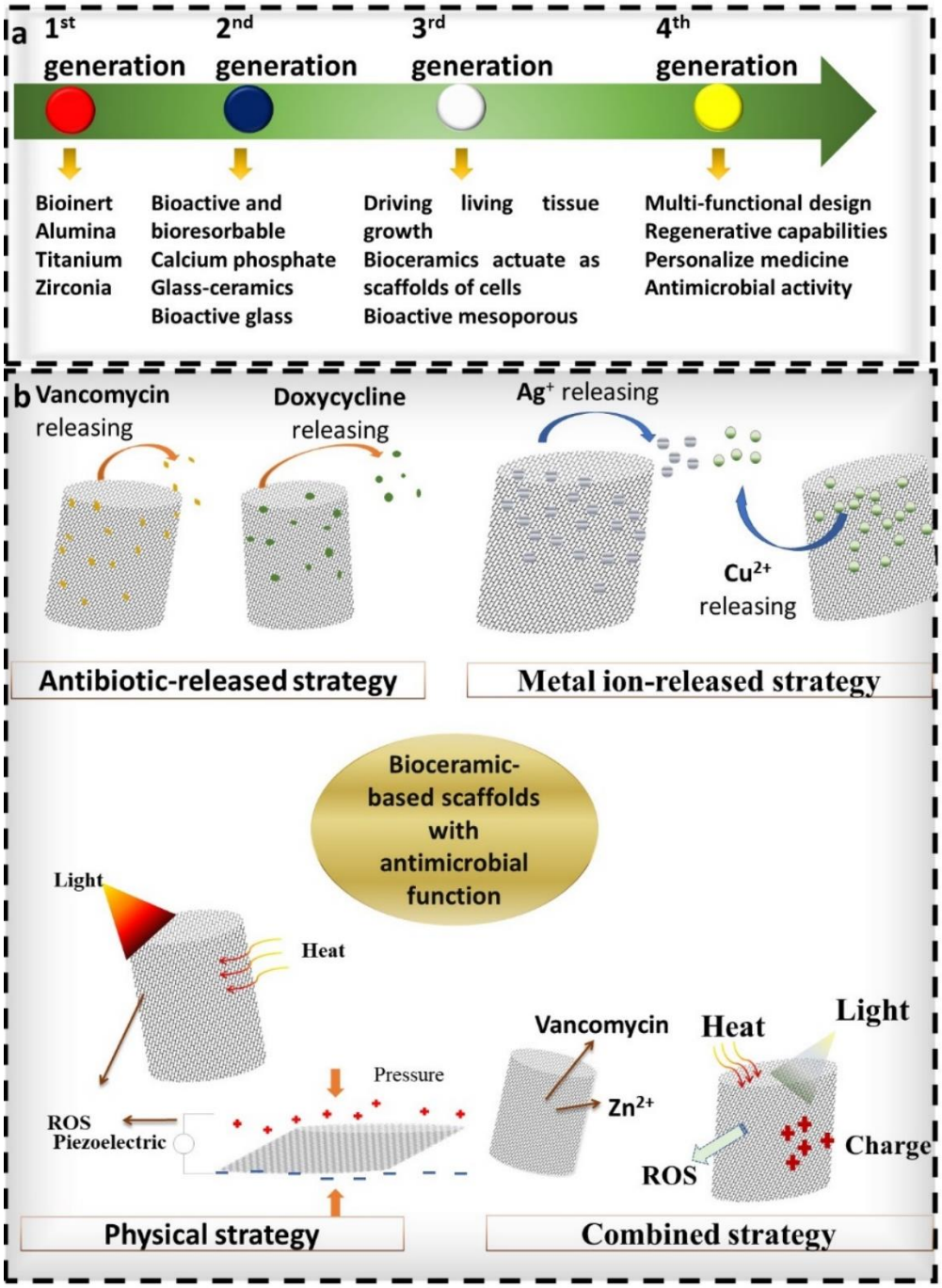

Figure 2.2. Evolution and advancements of bioceramics. a) A schematic overview of the fourth generations of bioceramics, illustrating their progressive development. b) The innovations and achievements in bioceramics-based scaffolds with diverse antibacterial properties for addressing bone implant-associated infections and bone deformities. These include scaffolds employing drug-induced, ion-mediated, physically activated, and combined antibacterial strategies to enhance their effectiveness in promoting bone healing and preventing infections.

The development of next-generation bioceramic scaffolds requires a multidisciplinary approach that combines cutting-edge techniques and methodologies (Figure 2.2 & Figure 2.3). This includes computer-assisted graded pore design for optimal scaffold architecture, advanced synthesis of ceramic powders to tailor material properties, and the utilisation of 3D printing technologies for precise and custom fabrication [73]. In addition, the incorporation of antibacterial agents and surface modifications can improve the resistance of the scaffold to infection while promoting cell formation and tissue integration [74, 75]. *In vivo* studies are essential for evaluating the performance of these novel bioceramic scaffolds ensuring that they meet the desired biocompatibility (Figure 2.3). Calcium silicate-based bioceramics including mineral trioxide aggregate (MTA), have been evaluated in dental applications through subcutaneous implantation models, demonstrating encouraging outcomes against oral pathogens [76]. Similarly, Hydroxyapatite (HAp) bioceramics doped with antimicrobial ions like Ag^{+} and Zn^{2+} were tested in rat tibia osteomyelitis and rabbit femoral defect to determine whether they are effective at preventing infections and promoting bone regeneration [77]. By integrating these strategies, researchers can successfully design and develop bioceramic scaffolds for orthopaedic and dental implant applications, effectively addressing the ongoing challenges in these fields.

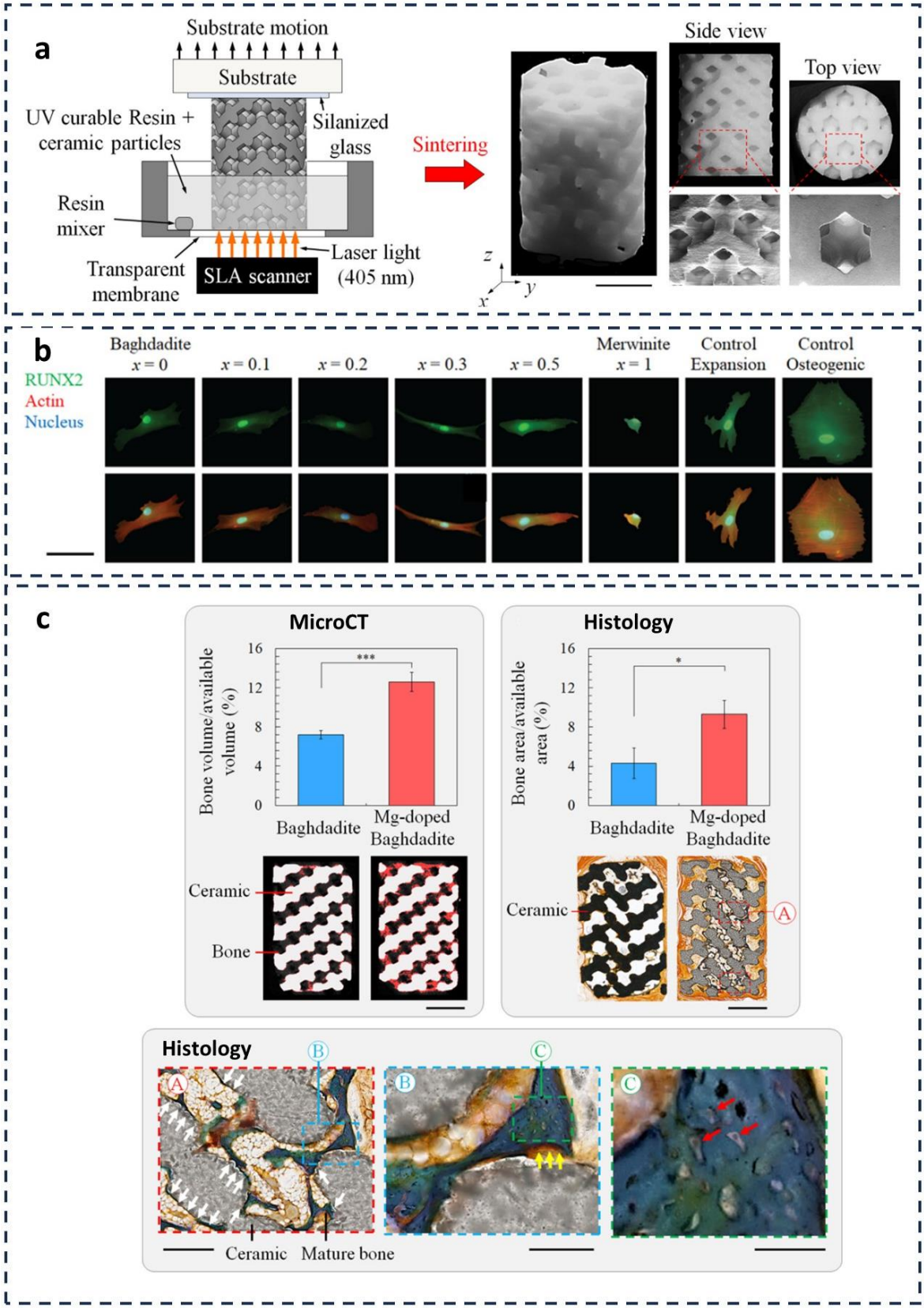

Figure 2.3. Advancements in bioceramic scaffold magnesium doped baghdadite fabrication and cellular response evaluation. a) A multi-panel figure showcasing the SLA-based

fabrication process of bioceramic scaffolds. b) the expression of osteogenic marker RUNX2 in cells cultured on different scaffold compositions. c) the comparative analysis of bone volume and histological integration between standard and magnesium-doped baghdadite scaffolds. (Adapted with permission from ref [22]).

2.3 THE COMPLEX INTERACTIONS IN BIOCERAMIC-ASSOCIATED INFECTIONS: BACTERIA, BIOCERAMICS, AND IMMUNE CELLS

Bacterial attachment to the surface of biomaterials is the initial step in the formation of biofilms [78]. When bacteria colonise a surface, they create colonies, eventually expanding into huge heterogeneous structures called biofilms. The stages of biofilm growth are bacterial adhesion, microcolony establishment, biofilm maturation, and biofilm dissipation (Figure 2.4). Biofilms protect microorganisms from environmental changes, antibiotic dosages, host immunity and assist horizontal gene transfer [79].

The bacteria initiate intercellular communication within the biofilm and rapidly regulate gene expression, allowing for temporal adaptations like phenotypic diversity and low-nutrient survival [80]. Bacterial biofilms are difficult to remove, causing repeated infections that affect bioceramics performance, healing, and disease progression [81]. At the molecular level, biofilm formation begins with the binding of adhesins and cell wall proteins like fibronectin-binding proteins (FnBPs) to substrates, resulting in the congregation of bacteria and the subsequent production of extracellular polymeric compounds [82]. *Staphylococci* possess a variety of surface-associated adhesins involved in both initial biofilm cell attachment and intercellular adhesion throughout biofilm maturation [83]. Covalently bound cell wall proteins, non-covalently binding proteins and non-protein components contribute to *Staphylococcal* adhesion and biofilm development [84]. *S. aureus* produces two fibronectin-binding proteins, FnBPA and FnBPB, encoded by the genes *fnbA* and *fnbB* [85]. The FnBPs feature an N-terminal region, and these domains are involved in the binding of fibrinogen and elastin. The binding of

FnBPs to fibronectin promotes bacterial invasion into epithelial, endothelial, and keratinocyte cells [86]. For instance, the *S. aureus* genome encodes more than twenty adhesins [87]. The pathophysiology of *S. aureus* infections is characterised by biofilm formation, which binds to a substrate and anchors it. Then, adhesins and cell wall proteins like FnBPs that bind fibronectin molecules cause *S. aureus* to congregate and form a biofilm. The maturation stage involves increased extracellular polymeric compounds produced by the biofilm matrix and increased *S. aureus* aggregation. For final dispersal, *S. aureus* cells return to the planktonic stage [88]. A previous study reported that a double knockout of *fnbA* and *fnbB* in *S. aureus* resulted in a loss of fibronectin binding and the ability to produce biofilms on microtiter plates and shear flow conditions. The complementation of *fnbA* or *fnbB* alone on a plasmid restored these characteristics and the capacity to agglutinate *S. aureus* [89].

Biofilms can be single or mixed species and exhibit distinct multicellular behaviours, making them difficult to eradicate and contributing to the problem of antibiotic resistance. These bacteria reproduce, mature, and thrive on the surface of bioceramics, where resources are plentiful resulting in an increase in antibiotic resistance in large microbial populations [90]. For instance, fluconazole and vancomycin sensitivity decreased in a polymicrobial biofilm, including *Candida albicans* and *Staphylococcus epidermidis*, respectively [91]. The extracellular polymeric matrix provides the biofilm with increased antibacterial resistance. This gel-like matrix inhibits phagocytosis, opsonisation, physical stress, and antibacterial diffusion [92]. As a result, microbes deep within the surface of gadgets continue to thrive. An ionically charged extracellular matrix can interact electrostatically and inhibit the action of various cationic antimicrobials, such as aminoglycosides [93]. Additionally, biofilms provide an isolated habitat for infections to share genetic information via plasmids. The spread of these plasmids between species exacerbates the problem of antibiotic resistance [94].

Therefore, to avoid the formation of biofilms, it is necessary to adhere closely to all aseptic surgery standards. Another method of reducing the chances of bacterial adherence is to develop novel materials or improve the surface of implanted medical devices to prevent them from attracting hazardous biofilm infections [94]. Multifunctional coatings on a zirconia surface, a nanostructured surface, and controlled antibiotic release can potentially make significant contributions towards this objective [95].

2.3.1 Host immune response to bioceramic-associated infections and bone regenerations

The host immune system reacts to both germs and the biomaterial surface of an implant, identifying it as a foreign body [96]. This reaction activates the coagulation cascade, complement system, platelets, and immune cells, mainly neutrophils [97]. The constant release of ROS from bioceramics causes metabolic stress and depletion of oxidative resources, reducing neutrophils' ability to fight germs [98]. Several studies indicate innate immune cells as important anti-infective biomaterial targets. Innate immune cells adhere to biomaterials within hours, while lymphocytes do not [99]. The innate immune effectors against planktonic *Staphylococci* species are neutrophils and macrophages [100]. Their ability to directly kill microbes is necessary for infection clearance to be successful. The failure of the host to eliminate the bacterial burden is commonly related to mortality. Macrophages and neutrophils control the balance of inflammation and tissue repair required for biomaterial integration [101].

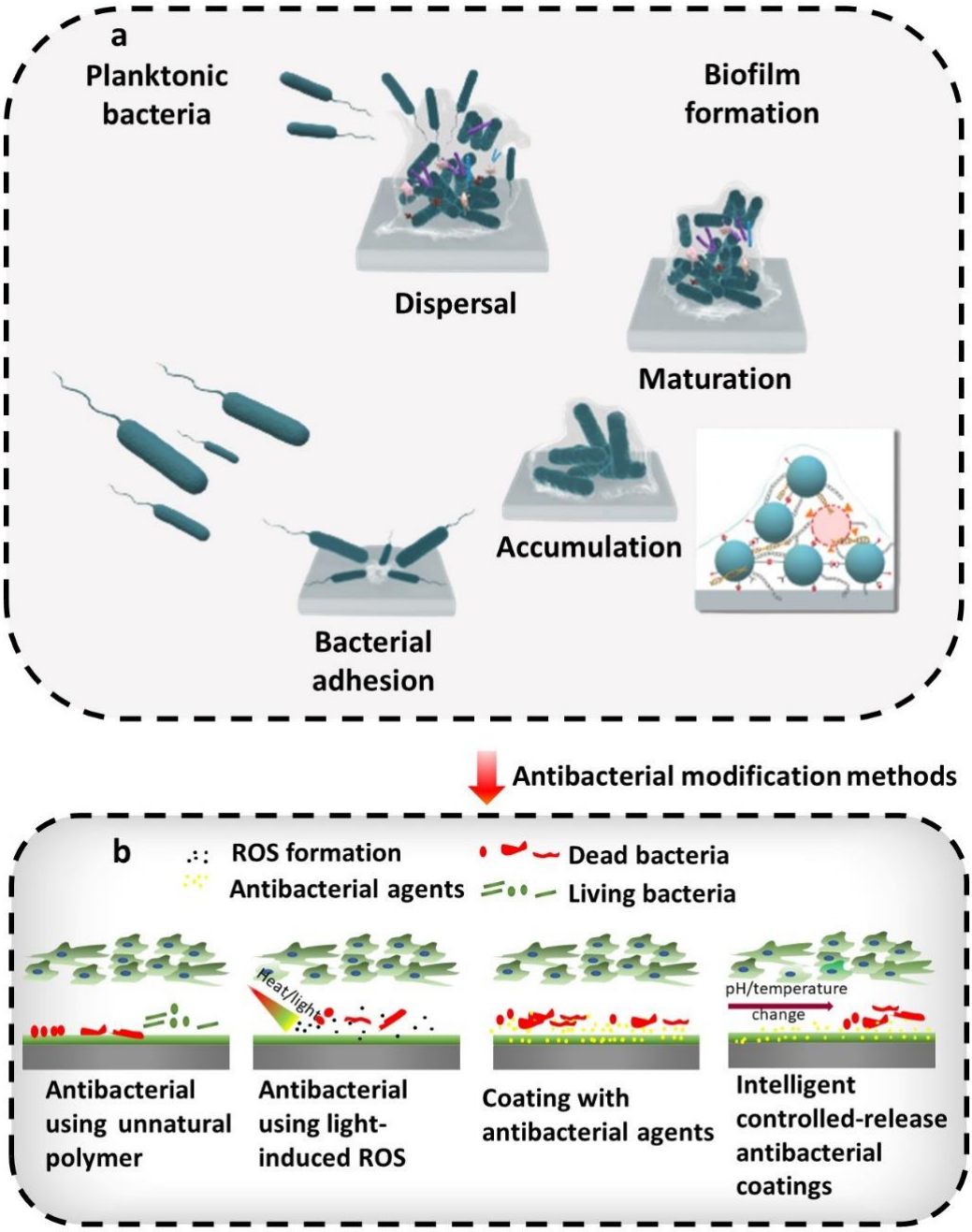

Figure 2.4. The schematic illustration of stages of biofilm formation and main antibacterial modification methods. a) A model of biofilm formation with common characteristics, including bacterial adhesion, accumulation, maturation, and dispersal. Planktonic cells interact and adhere to the surface of the biomaterial. Bacteria cluster together and form microcolonies due to intercellular contacts mediated by adhesins and cell wall proteins. FnBPs build a bridge between fibronectin (Fn) molecules, promoting bacterium aggregation. Extracellular polymeric compounds are produced as part of the biofilm maturation process, during which the biofilm matrix gradually thickens, and larger bacterium aggregations called towers form. Biofilm

production is facilitated by the expression of the polysaccharide intercellular adhesin and the release of extracellular deoxyribonucleic acid (DNA) obtained from bacteria and dead host cells. b) Schematic representation of various antibacterial modification strategies for bioceramics. These strategies include: incorporating antibacterial activity through the use of unnatural polymers, which can be designed and engineered to target and disrupt bacterial cell walls or membranes; utilising light-induced reactive oxygen species (ROS) generation to damage bacterial cells and inhibit their growth; coating bioceramic surfaces with antibacterial agents, such as metal ions, to enhance their antimicrobial properties; and implementing intelligent controlled-release antibacterial coatings that can respond to specific stimuli, allowing for a targeted and sustained release of antimicrobial agents. These approaches aim to improve the antibacterial performance of bioceramics in various medical applications.

2.3.1.1 Innate immunity in bioceramic infection defense and bone regeneration

Neutrophils are activated immediately and are the first cell type to gather around a biomaterial in the innate immune system. These cells are responsible for eliminating cellular debris and pathogens by phagocytosis, reactive oxygen species production, degranulation, and the generation of pathogen-encapsulating neutrophil extracellular traps (NETs) [102]. The inflammatory response is maintained by neutrophils releasing IL-1 and chemokines (MCP-1 and CXCL1) that attract monocytes. Neutrophils are vital in the fight against *Staphylococci* infection around the implant [103]. Many potent antimicrobial proteins and components are found in neutrophil intracellular granules, making them extremely effective in killing bacteria intracellularly. The fact that decreased neutrophil activity around the implant increases the risk of biomaterial infection highlights the importance of maintaining normal neutrophil function near the biomaterial [104]. Furthermore, the activation of neutrophils is enhanced by biomaterial-specific processes. First, extracellular matrix/blood proteins and complement factors coat the biomaterial, providing additional sites for neutrophil adherence and activation [105]. Second, accumulating evidence shows that surface properties of biomaterials affect neutrophil activity [106]. For example, in this process, the adsorption of blood/extracellular

matrix proteins and complement components activates neutrophils. They produce ROS, degradation enzymes, and NETosis in response to local trauma or pathogen-induced proinflammatory stimuli. This is due to metabolic fatigue, increased ROS generation and NETosis, and/or inflammasome activation linked to decreased bacterial uptake and death [107]. Neutrophils, on the other hand, produce NETs to extracellularly trap and kill germs, which is the final stage of an active neutrophil death process called NETosis [104, 108]. It is impacted in the presence of a biomaterial and is thought to be a major contributor to the destructive inflammation associated with non-immunocompatible biomaterials, resulting in impaired neutrophil phagocytosis and tissue healing. Therefore, anti-infective strategies should attempt to reduce neutrophil-mediated inflammation caused by unregulated ROS and NETs generation while restoring or increasing their anti-infective effects [104].

Macrophages, as professional phagocytes, provide a second line of defence against any bacterial problems in the region of the biomaterial [104, 109]. Macrophages release various cytokines and growth factors that tightly regulate the osteogenic function of mesenchymal stem cells [110]. Monocytes develop from myeloid progenitor cells, which differentiate into monoblasts, pro-monocytes, and ultimately monocytes. The presence of colony-stimulating factors released by stromal cells in the blood and tissues induces this cell development [111]. After biomaterial implantation, monocyte-derived inflammation macrophages are recruited and undergo phenotypic alterations to adapt to the local microenvironment. The major macrophage subtypes are M1 or M2 macrophage subtypes [112]. The M1 macrophage activated by strong inflammatory stimuli like toll-like receptor ligands or interferon-γ (IFN-γ) is responsible for proinflammatory cytokine production, phagocytosis, and antigen presentation [113]. M2 macrophages develop in response to interleukin (IL) such as IL-4, IL-13, or IL-10 stimulation and are principally important for moderating the inflammatory response and coordinating tissue regeneration [114]. However, the proinflammatory M1

signature of macrophages in response to bacterial infection [115]. Numerous effectors contribute to M1 macrophages' enhanced microbicidal activity and mostly involve the uptake of bacteria within the degradative phagolysosome. This process requires the formation of ROS and nitric oxide NO. Additionally, several genes involved in M1 polarisation are increased in response to bacterial infections, including those encoding the cytokines tumour necrosis factor (TNF)-, IL-6, IL-12, and IL-1, as well as chemokines CCL2, CCL5, and CXCL8 [115]. Finally, an M1 macrophage characteristic is its enhanced ability to educate adaptive immunity via antigen presentation [116]. Notably, bioceramics are critical regulators of macrophage immunomodulation via ion products such as SiO_4^{4-}, Ca^{2+}, and Mg^{2+} [117]. Macrophages activated with bioceramics secreted much more cytokines, chemokines, and proteases that govern inflammation and subsequent osteogenesis/angiogenesis. The paracrine route mediated by bioceramic-induced macrophage exosomes has not been fully understood in bioceramic-mediated bone repair.

Dendritic cells are significant because they play an essential role in initiating and regulating immune responses [118]. Dendritic cells are the primary antigen-presenting cells, linking the innate and adaptive immune systems. They capture process, and present antigens to T cells, triggering specific immune responses against pathogens. For instance, bioactive glass has been observed to influence the maturation and activation of dendritic cells positively [118, 119]. Strontium (Sr)-containing BG can promote dendritic cell maturation, leading to an increase in the expression of co-stimulatory molecules and pro-inflammatory mediators [120]. This enhanced response can improve the capacity of the host to manage infection and facilitate healing.

Natural killer (NK) cells play an important role in bioceramics infection and immune response due to their ability to recognise and prevent infected cells without prior sensitisation. They are

part of the innate immune system and contribute to the initiation of the defence against infections. In the case of bioceramics-associated infections, NK cells can aid in limiting the dissemination of the infection and promoting a quicker resolution of the inflammatory response. Certain bioceramics, such as silicon-substituted calcium phosphate, have been demonstrated to stimulate NK cell activity, thereby increasing their cytotoxic potential against infected cells. This increased NK cell activity may contribute to a more effective immune response against pathogens, preventing further infection and promoting tissue integration and healing around implanted bioceramic materials

2.3.1.2 Bioceramics and adaptive immunity: Modulating T and B lymphocyte responses for improved infection defence and bone regeneration

T lymphocytes are a heterogeneous group of immune cells that include T helper cells, cytotoxic T cells, and regulatory T cells, each of which performs a distinct function in the immune response [121]. When implanted, bioceramics interact with the host immune system, including T lymphocytes [122]. T lymphocytes play an essential role in adaptive immunity, which is essential for protecting the body from pathogens and promoting tissue repair [123]. Understanding the interaction between bioceramics and T lymphocytes can shed light on how these biomaterials influence the immune response and contribute to the prevention and control of implant-associated infections.

Bioceramics can modulate T lymphocyte activation and proliferation, which influences the overall immune response against pathogens and plays a role in tissue regeneration. For instance, HAp promotes CD^{4+} T cell proliferation and Th1 cytokine secretion, such as interferon-gamma, thereby aiding in infection control [122, 124]. Moreover, bioceramics can affect the ratio of regulatory T cells to effector T cells, thereby preserving immune homoeostasis and preventing excessive inflammation [125, 126]. Understanding the

relationship between bioceramics and T lymphocytes can guide the development of bioceramics with enhanced antimicrobial and osteoinductive properties, thereby promoting a balanced and effective immune response against bioceramics-associated infections.

B lymphocytes are critical because they are vital in the adaptive immune response to infections [123]. Antigens on pathogens can be recognised and bound by B cells, resulting in the production and secretion of antibodies. These antibodies can neutralise pathogens, stimulate immune cell phagocytosis, and activate the complement system, all contributing to pathogen clearance. Bioceramics, such as BG, can influence B cell function by augmenting antibody production and humoral immunity [97, 123]. This may result in enhanced pathogen clearance and contribute to the overall immune response of the host against bioceramics-associated infections. By producing specific antibodies that recognise and neutralise pathogens, B cells play a crucial role in the adaptive immune response. Some bioceramics can enhance the production of pathogen-specific antibodies by stimulating B cell activation and differentiation into antibody-secreting plasma cells [127]. This increased antibody production can aid in opsonising and neutralising bacteria, thereby facilitating their removal by phagocytic cells and preventing colonisation on bioceramic surfaces. In addition, the humoral immune response can contribute to the formation of immunological memory, which can offer long-term protection against recurrent infections.

2.3.1.3 Bioceramic-mediated modulation of host immune response for enhanced bone regeneration

Bioceramics can modulate the expression of numerous inflammatory cytokines and chemokines, influencing the immune response to infection and tissue repair of the host. For example, BG has been shown to stimulate the production of pro-inflammatory cytokines,

including IL-1 beta and TNF-α [128]. These cytokines enhance the capacity of the host to control infection by promoting inflammation and recruiting immune cells to the infection site.

On the other hand, HAp has been shown to inhibit the release of pro-inflammatory cytokines while fostering the production of anti-inflammatory cytokines such as interleukin-10 (IL-10) [129]. This modulation aids in resolving inflammation and promoting tissue healing by fostering an environment more conducive to tissue repair and regeneration. The balanced expression of inflammatory and anti-inflammatory cytokines assures an efficient immune response to bioceramics-associated infections while minimising the risk of tissue damage caused by excessive inflammation.

Bone infection disrupts the balance between bone-forming osteoblasts and bone-resorbing osteoclasts, resulting in pathological bone loss and impaired healing [130]. Under their osteoimmunomodulatory properties, bioceramics can assist in restoring this equilibrium and fostering bone regeneration. The regulation of cytokines and chemokines is a mechanism by which bioceramics modulate the osteoimmune environment. HAp can stimulate the production of anti-inflammatory cytokines, such as interleukin (IL)-10 and transforming growth factor-beta (TGF-β) [131, 132], while inhibiting the production of pro-inflammatory cytokines, such as tumour necrosis factor-alpha (TNF-α) and interleukin-6 (IL-6) [133, 134]. This modification to the cytokine profile can reduce inflammation and promote bone healing.

Moreover, bioceramics can affect immune cell differentiation and function. HAp, for instance, have been shown to promote the differentiation of anti-inflammatory M2 macrophages while inhibiting the differentiation of pro-inflammatory M1 macrophages [135, 136]. This modification of macrophage polarisation can contribute to an osteoimmune environment that is more conducive to bone regeneration. Such effects underscore the potential of bioceramics

to interact beneficially with the host immune system, enhancing both the biological integration and functional outcomes of bone implants.

2.4 Antibacterial bioceramics strategies in bone tissue engineering

Key points

- Bioceramics doped with metal ions can prevent bacterial infections in medical implants.
- Understanding the mechanisms by which metal ions disrupt bacterial growth is crucial for developing effective antibacterial materials.
- Surface modification techniques, such as nanopatterning and coatings, can prevent bacterial adhesion and biofilm formation on implant materials.
- Smart antibacterial bioceramics with stimulus-responsive mechanisms show promise for preventing implant-related infections.

Antibacterial bioceramics are crucial in bone tissue engineering, ensuring successful implant integration and infection prevention. Various strategies have been developed to achieve this, including antibacterial adhesion, incorporation of metal ions, nanotechnology applications, and smart responses to bacterial presence. By employing these innovative approaches, researchers can create bioceramic materials with enhanced antimicrobial properties, promoting tissue regeneration and reducing the risk of infection. Ultimately, these advancements contribute to regenerative medicine and improve the clinical success of bioceramic-based implants.

2.4.1 The antibacterial activity of ions released from doped bioceramics

In comparison to other strategies for enhancing the antibacterial properties of bioceramics, metal-doped bioceramics have gained popularity for several reasons. First, metals ions such as Ag^{+}, Cu^{2+} and Zn^{2+} display a broad spectrum of antimicrobial activities against various bacterial strains, including Gram-positive and Gram-negative species [137-140]. This broad-

spectrum activity renders metal ions doped bioceramics highly effective against various infections. In addition, the combination of metal ions and bioceramics can produce synergistic antibacterial effects, thereby enhancing the antimicrobial performance of bioceramics [141]. This synergy produces an antibacterial action that is effective and long-lasting, preventing bacterial adhesion, colonisation, and biofilm formation on the surface of medical devices. For example, Zn^{2+} and Ag^{+} doped HAp coatings exhibited synergistic antibacterial activity against methicillin-resistant *S. aureus* (MRSA). Zn^{2+} and Ag^{+} combined effect was greater than their individual effects when administered separately. A further benefit is the regulated release of metal ions. Metal ions may be incorporated into bioceramics in various ways, allowing for the release of ions over time. This controlled release ensures a sustained antibacterial effect, thereby minimising the risk of bacterial resistance development and potential side effects. Figure 2.5 indicates that incorporating these elements into bioceramics may increase their biological activities.

In certain instances, incorporating metal ions into bioceramics can enhance their mechanical properties, such as hardness, fracture toughness, and wear resistance. In orthopaedic applications, where the mechanical performance of the implant is crucial to its long-term stability and success, this can be advantageous. In addition, numerous metal ions, such as Ag^{+}, Cu^{2+}, and Zn^{2+} have demonstrated biocompatibility and pose minimal risk to human tissue. By doping bioceramics with these metal ions, the resultant material retains its biocompatibility ensuring its suitability for medical applications. Therefore, metal ions doped bioceramics offer many benefits over other antibacterial modification strategies. These advantages make them an appealing option for enhancing the antibacterial performance of bioceramic materials in a variety of medical applications.

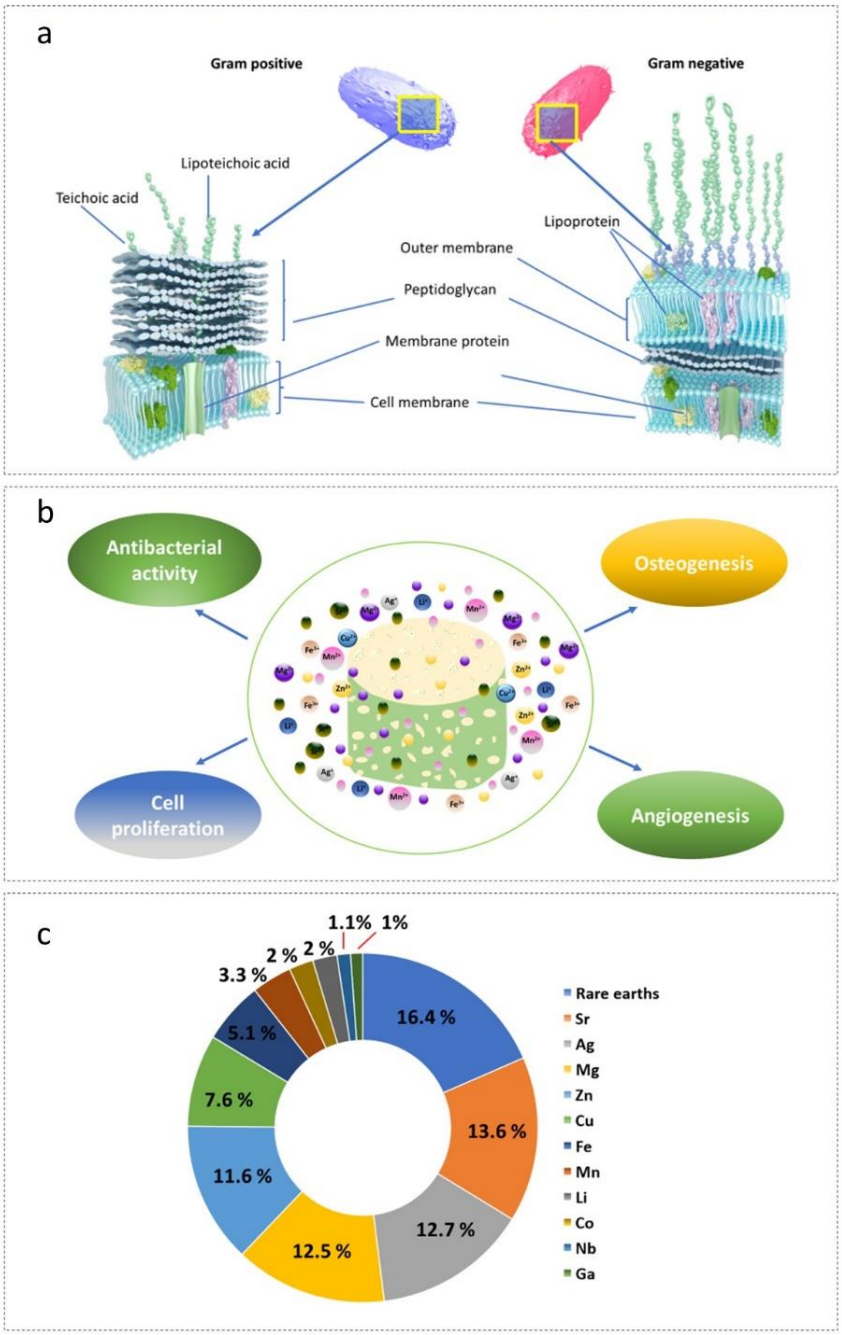

Figure 2.5. Recent developments and mechanisms of antimicrobial toxicity of metal and metal ions in the field of metal-doped bioceramics for bone tissue engineering. a) Structure of Gram negative and Gram positive where different strategies target different components for antibacterial activity. b) Biological responses to metal ions on bioceramics matrices. c) different metal ions doped in bioactive glasses and bioceramics.

Table 2.2. Metals doped bioceramics for antibacterial activity

Metal	Bioceramics	Antibacterial activity	Mechanisms	Application	Ref
Silver	HA/chitosan nanocomposite coatings, coating	Broad-spectrum against bacteria, fungi, and viruses	Release of Ag^+ ions that damage bacterial cell membranes and intracellular biomolecules induce oxidative stress and ROS production.	Orthopedic and dental materials, bone-related implants, wound dressings	[142, 143]
Copper	Calcium Phosphate and tricalcium phospahte	Effective against *E. coli, S. aureus*	Membrane permeability alteration, protein function disruption	Bone graft substitutes, dental Implant coatings, bone regenerationmplants,	[144, 145]
Zinc	Bioactive Glass, Zinc oxide nanocrystals, Zn-modified HA	Gram-positive and Gram-negative bacteria	Inhibition of microbial adhesion interferes with bacterial cell membrane and intracellular processes and induces oxidative stress and ROS production.	Bone repair, multifunctional bone implants, Coating for metal implants	[146, 147]

			Bone repair, multifunctional bone implant		
Magnesium	MgO nano-layer, magnesium-substituted HA	Antibacterial and biofilm prevention	Alkaline environment creation, competitive inhibition of calcium binding	Orthopedic applications, implant coatings	[18, 148]
Gallium	HA	*P. aeruginosa*, MRSA	Iron metabolism interference, membrane damage	Osteoconductive scaffolds, infection-resistant surfaces	[149, 150]
Cerium	Zirconium Oxide	Wide range of bacteria including multi drug resistant strains	Oxidative stress induction, membrane disruption	Prosthetic devices, antimicrobial films	[151, 152]
Cobalt	HA	Various bacterial strains	Co ion release leading to antibacterial activity, angiogenesis promotion	Vascular stents, bone tissue scaffolds	[153]
Bismuth	Calcium Phosphate	Effective against a broad range of pathogens, including *H.*	Bi ions disrupt enzyme activities and bind to bacterial proteins, inhibiting their functions	Used in gastrointestinal devices, dental	[20, 154]

		pylori and *E. coli*		fillings, and as a radiopaque material	
Strontium	Calcium Phosphate	*S. aureus*,	Osteoinduction, ionic substitution affecting bacteria metabolism	Dental applications, bone defect fillers	[155, 156]
Manganese	Bioactive glass, nano HA	*E. coli, Shigella dysenteriae, S. aureus*	Increase pH in medium, ROS production	Bone implant	[157, 158]
Irion	Nano HA	*Shigella dysenteriae*	ROS production		[158]

2.4.1.1 Antibacterial activity of copper ions

Copper ions (Cu^{2+}) is a very important element that plays a role in a lot of different enzymatic systems and helps make cytochrome oxidase and superoxide dismutase, two enzymes that are important for cellular respiration (antioxidant defence) depending on their oxidation state [159]. Firstly, Cu^{2+} is attracted to cysteine and has a strong affinity for thiols, which is the only thiol-containing amino acid in the body. However, when Cu^{2+} is bound to cysteine, it goes through a process of homeostasis. When Cu^{2+} binds to cysteine, it is reduced to Cu^{+}, which makes cystine the oxidised dimer of cysteine [160, 161]. Second, Cu-catalysed reactions can oxidise biomolecules, such as reduced glutathione (GSH). GSH has a strong affinity for covalently linking Cu^{2+} and other bacterial proteins, such as cysteine-rich metallothioneins. These proteins have an unusually high number of cysteine residues in their sequence and most likely have a function in metal toxicity defence [162]. In addition, bacterial cells have copper

efflux pumps, such as the CopA, a P-type copper efflux ATPase that keeps the intracellular content of copper low. Other Cu-binding proteins include the CueO multi-Cu oxidase and the CusCFBA multicomponent efflux transport system, contributing to intracellular Cu homeostasis and bacterial cell defence [163, 164]. In summary, Cu is an important element, and bacteria can keep it balanced by avoiding its toxicity inside the body. Therefore, high concentrations of copper ions can damage important enzymes, like those that help bacteria get their energy from the main energy source in the respiratory electron transport chains, which are made up of cysteines.

The precise mechanism of antimicrobial activity of Cu^{2+} remains unclear, but several lines of likely interconnected pathways have been proposed, and it is expected that a sequence of different pathways leads to bacterial cell death, including disruption of the cell membrane, intracellular alteration of biochemical processes, and induction of DNA damage. The first mechanism, the antibacterial properties of copper ions, have been shown to attach to bacterial cell walls, impairing the integrity and function of the cell membrane and related proteins. For example, copper and ion binding to phospholipids may modify the physicochemical properties of the membrane, reducing membrane fluidity and flexibility. Additionally, this may enhance oxidative stress at the membrane surface due to increased hydroxyl radicals and may disrupt the electron transfer chain by direct or indirect contact with the quinone pool [165]. A previous study showed that the release of copper ions from metallic surfaces results in severe membrane damage, as evidenced by the complete breakdown of the membrane into lipids in *E. coli* following treatment with a soluble copper salt. These findings show that oxidation of membrane lipids is the fundamental mechanism by which copper ions kill bacteria, either by disrupting and degrading the membrane or impeding cell growth and division upon uptake [166].

2.4.1.2 Antibacterial activity of silver ions

Ag^+ is well known to be toxic to bacteria, viruses, fungi, and various other organisms while posing little or no toxicity to humans [167-169]. The most common mechanism of action for Ag compounds is widespread disruption of cellular functions as a result of direct damage to the cell membrane or intracellular biomolecules and induction of oxidative stress as a result of metal-mediated ROS production, culminating in the formation of free radicals and widespread cellular damage [170].

The electrostatic attraction between the negatively charged bacterial surface and the positively charged Ag^+ to adhere to the cell wall and membrane is the primary mode of action of this metal ion. The charge interaction between the bacterial cell and the Ag^+ can affect the cell surface zeta potential, increasing membrane permeability, depolarisation, and decreasing respiratory potential [170]. Finally, a complete loss of membrane integrity causes irreversible cell damage and death. Ag^+ rapidly reacts with the sulfhydryl groups on the bacterial cell membrane, exchanging the terminal hydrogen atom to form a stable S–Ag bond and thus completely inhibiting the respiratory chain, electron transfer, protein secretion, and lipid biosynthesis. A recent study established that Ag^+ primarily targets the bacterial membranes of *E. coli* and *P. aeruginosa* [171].

For example, The previous study showed Ag^+ substituted HAp (Ag-HAp) bioceramics have superior osteoconductivity and high antibacterial activity and proposed a method for the antibacterial activity of such bioactive ceramics to be induced by the stern interface [172]. Due to the trace dopant Ag^+ enrichment in the stern layer of the electric double layer at the negatively charged surface of Ag-HAp bioceramics, the concentration of Ag^+ at the stern interface of Ag-HAp bioceramics is almost 5 times that in the bulk solution during this

antibacterial process. HAp with trace Ag^{+} generates a positive shift in the zeta potential and an increase in hydrophilicity, which may aid in inhibiting bacterial development.

2.4.1.3 Antibacterial activity of strontium

Strontium ion (Sr^{2+}) is essential for the development of bioceramic applications involving bone regeneration and implant integration and is renowned for its osteoinductive and antibacterial properties. Substantial antibacterial activity has been observed in Sr^{2+} doped hardystonite (Sr-HT), an exceptional coating, against formidable pathogens including *Pseudomonas aeruginosa* and MRSA, strains notorious for their resistance to antibiotics (Figure 2.6) [173]. By enhancing its antibacterial properties and stimulating bone repair and regeneration, HT becomes a valuable material for dental and orthopedic implants when Sr^{2+} is infused into it. Technological advancements encompass Sr^{2+} doped chromium oxide, which is renowned for its effectiveness against multidrug-resistant *Escherichia coli* [174]. The application of Sr and selenium co-substituted HAp in bone tissue engineering is enhanced by the combination of the antimicrobial and bone regenerative properties of both elements [175]. Moreover, due to their increased surface area and irregularity, Sr^{2+} doped titanium dioxide nanorods show enhanced cellular responses and heightened antibacterial activity [176, 177]. Finally, amorphous Sr^{2+} calcium phosphate is identified as a substance capable of remineralising dental structures and enhancing resistance to cariogenic bacteria [178]. A multifaceted strategy is exemplified by the incorporation of Sr^{2+} into diverse bioceramics, which provides improved mechanical, chemical, and biological characteristics that are essential for medicinal applications.

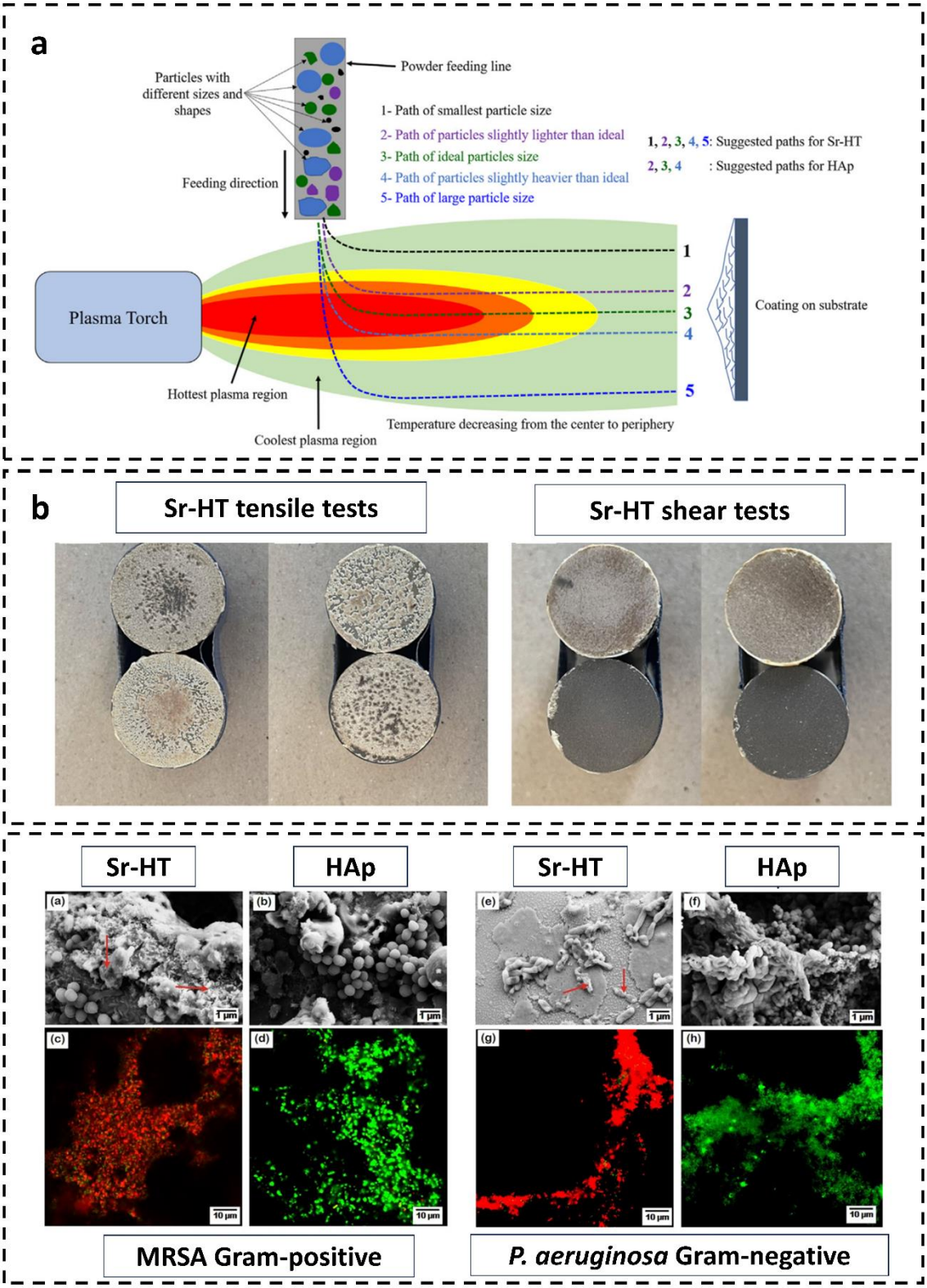

Figure 2.6. Antibacterial efficacy Sr-HT. a) illustrates the trajectory of bioceramic particles of various sizes and shapes within a plasma spray coating process, identifying optimal paths for Sr-HT and HAp particles. b) displays the results of tensile and shear tests for Sr-HT coatings, demonstrating the mechanical adhesion and integrity of the coatings. c) provides a

comparative analysis of the surface morphology and antibacterial activity of Sr-HT and HAp coatings against MRSA (Gram-positive) and *P. aeruginosa* (Gram-negative) bacteria, with fluorescent images indicating bacterial adhesion and viability. (Adapted with permission from ref [173].

2.4.1.4 Antibacterial activity of zinc ions

Zn^{2+} interact with the negative charge of the bacterial membrane. A strong ionic connection between Zn^{2+} and the bacterial surface is created by reverse charges, causing electrostatic forces. Furthermore, binding Zn^{2+} to the bacterial membrane may increase membrane permeability, causing pores in the bacterial surface, triggering membrane rupture and cytoplasmic leaking, resulting in cell death [179]. Zn^{2+} has a role in regulating bacterial cell proliferation, differentiation, and membrane structure conservation. Additionally, they participate as cofactors in many critical metabolic pathways, including the synthesis and breakdown of carbohydrates, lipids, and proteins [180, 181]. The positive effects of Zn^{2+} are dominant at low concentrations, whereas high amounts impede bacterial development. For example, an excess of Zn^{2+} may compete with other metals and induce a metal mismatch in various metal-binding proteins, resulting in protein dysfunction, enzymatic inactivation, or protein denaturation [182].

2.4.1.5 Antibacterial activity of iron ions

Iron ions are a critical microelement for bacterial life and involve various biological processes, including DNA synthesis and energy metabolism. On the other hand, iron ions can be toxic to bacterial cells in high concentrations. In the biology process, iron is found in two oxidation states: oxidised Fe^{3+} and reduced Fe^{2+}. Although bacteria can acquire Fe^{3+} from their environment, they rapidly convert it to Fe^{2+}. In addition, Fe^{2+} produces a significant amount of •OH by speeding the Fenton and Haber-Weiss reactions [183]. These radicals contribute to oxidising the lipids of the membrane and damaging the proteins and DNA. In addition, free

radicals produced in this way, such as O_2^{-}• and •OH, can rupture the cell envelope via an electrostatic, dipole-dipole, hydrogen bond, hydrophobic, and van der Waals forces. This results in the disarray and destruction of the cell membrane, resulting in the death of the bacterium [184].

2.4.1.6 Antibacterial activity of gallium ions

Gallium ions (Ga^{3+}) is a semimetal element that stimulates osteoblasts and promotes bone growth [185]. Ga^{3+} may substitute for Fe^{3+} ions in many metabolic reactions due to their high resemblance (i.e., same ionic radius, electronegativity, coordination number, etc.). With this capacity, gallium serves as a diagnostic and therapeutic agent for metabolic problems of both soft and hard tissues. Recent research has also shown that gallium ions have an antibacterial effect, which is based on the exchange of iron ions in the process of protein metabolism. Ga^{3+} can interfere with bacterial metabolism, DNA replication, and other critical cellular processes, ultimately leading to bacteria cell death. Ga also exhibits synergistic effects with other antibiotics, enhancing their antibacterial activity and reducing the development of antibiotic resistance. Moreover, Ga-based materials, such as Ga nanoparticles, can be synthesised and modified for various biomedical applications, including wound healing, implant coatings, and drug delivery systems. Despite the promising results, further studies are needed to investigate the antibacterial mechanisms of Ga and optimise its efficacy for clinical use.

Gallium-doped HAp (Ga-HAp) is a biomaterial that is increasingly being used in antibacterial orthopaedic applications (Figure 2.7) [149]. By introducing gallium ions into HAp matrices, the biocompatibility and osteoconductivity of HAp are maintained while simultaneously providing strong antibacterial effects. Ga-HAp has exhibited a notable capacity to impede the growth and reproduction of several harmful bacteria, such as MRSA and Pseudomonas aeruginosa, which are frequently responsible for implant-associated illnesses. The antibacterial

effect of Ga^{3+} is due to its capacity to break the integrity of bacterial cell walls and hinder essential metabolic pathways. Furthermore, the ability of Ga to imitate calcium interferes with the iron metabolism in bacteria, enhancing its antibacterial effectiveness. The dual activity of Ga-HAp renders it highly suitable for bone tissue engineering applications that require infection prevention and bone regeneration. This composite material utilises a synergistic approach by combining the proven ability of HAp to regenerate bone with the effective antibacterial properties of gallium. This creates new opportunities for the advancement of biomedical implants.

2.4.2 Metal and ion doping in bioceramics: a strategic approach to antibacterial efficacy

Understanding the antibacterial mechanisms of metals and metal ions is crucial for optimising their performance in clinical applications. In this section, we discuss four primary mechanisms of antibacterial properties associated with metals and metal ions: (1) generation of reactive oxide species, (2) protein dysfunction and loss of enzyme activity, (3) disruption of membrane function, and (4) genotoxicity. Figure 2.8 illustrates these mechanisms, providing a comprehensive overview of how metals and metal ions exert their antibacterial effects on bacteria.

2.4.2.1 Generation of reactive oxide species

Some metal ions have been demonstrated to induce intracellular ROS in various studies. For example, exogenous hydrogen peroxide or substances that catalyse the generation of superoxide (O2•-), such as paraquat, cause DNA damage and block some enzyme activity required for cell development in *E. coli* [186, 187]. Mutants lacking in ROS-scavenging enzymes and other cellular antioxidants commonly show altered sensitivity to ions of Cr, As, Tellurium (Te), Fe, and Cu [187]. Cu (II) or Te (IV) exposure reduces enzyme activity, causing DNA damage. Thus, metal toxicity may be owing to ROS-mediated cellular damage, and

different metal-catalysed oxidation processes may cause specific protein, membrane, or DNA damage [187]. The mechanisms that have been proposed to account for the increased ROS production include:

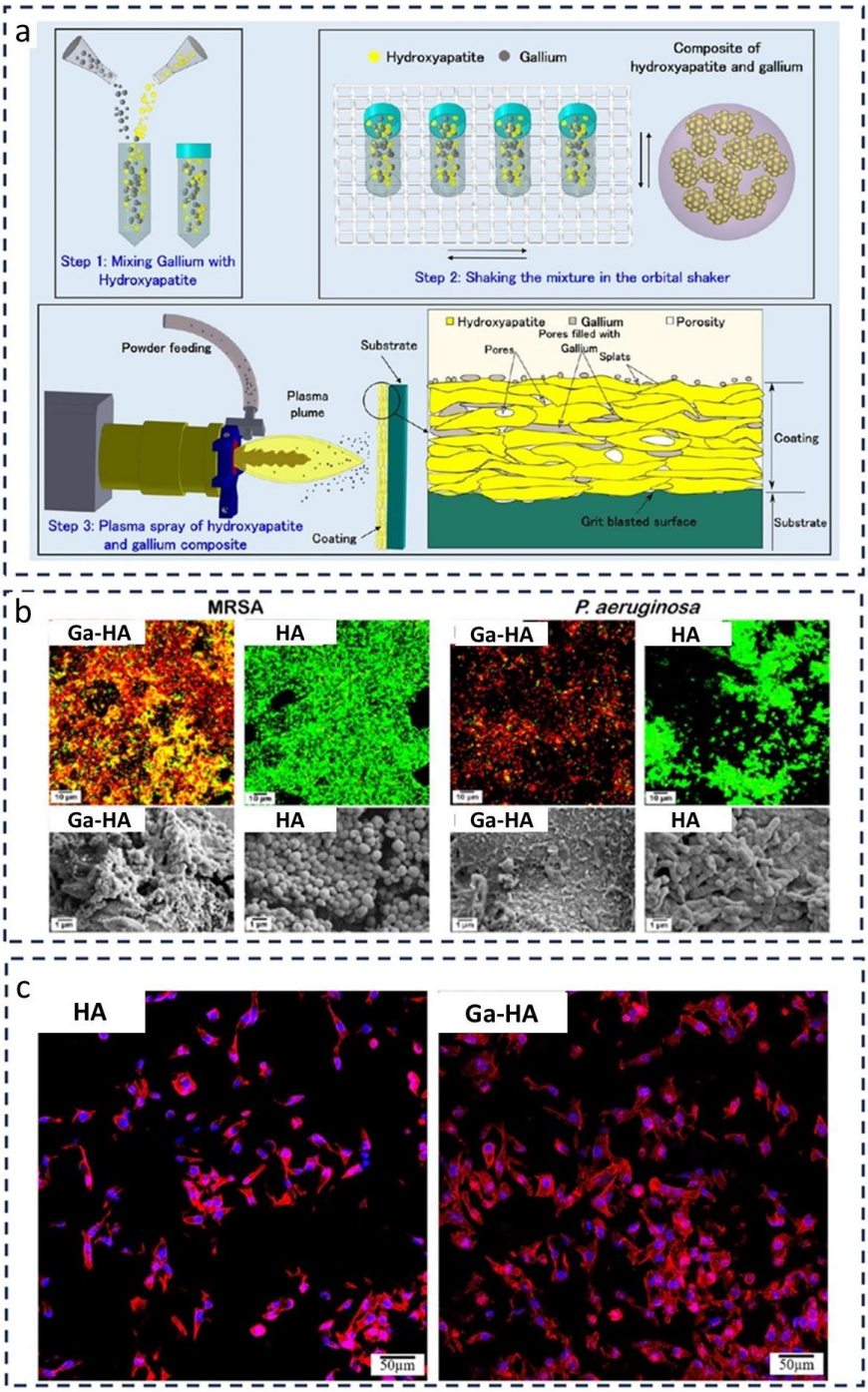

Figure 2.7. Synthesis and antibacterial evaluation of Ga-HAp.a) depicts the sequential procedure for fabricating a composite material of HAp and gallium. This involves the initial

stage of blending the components, followed by agitation in an orbital shaker, and ultimately applying the mixture onto a substrate using plasma spraying. (b) illustrates the antimicrobial properties of Ga-HAp against MRSA and *P. aeruginosa*. It includes confocal microscopy pictures that display live/dead staining, as well as scanning electron microscopy images that disclose the surface morphology of the coatings. (c) demonstrates the interaction between HAp and Ga-HAp with cellular structures, emphasising the ability of the doped material to support bone growth. This is shown using fluorescent labelling to visualise the cell nuclei and actin filaments. (Adapted with permission from ref [149]).

First, redox-active transition metals other than Fe, such as Cu, Cr, Co, V, and Ni, can catalyse Fenton chemistry [188]. Cu has been demonstrated to catalyse the formation of hydroxyl radicals, and other metals may do the same [189]. Because numerous variables influence the ability of these transition metals to engage in Fenton chemistry, determining whether these reactions occur *in vivo* and their rates is difficult [189]. On the other hand, in phosphate buffer at pH 7, Cu (I), Cr (I), and Co (I) catalyse Fenton chemistry faster than Fe(I), whereas Ni(I) catalyses this reaction at a slower rate [187, 190].

Second, transition metals may interfere with the coordination of Fe ions. The solvent-exposed [4Fe–4S] clusters of proteins appear to be the principal metal targets. However, most of these atoms are sheltered by coordination bonds, and only 20% are projected to be Fenton active. Metals can directly or indirectly destroy [4Fe–4S] clusters, releasing Fenton-active Fe ions into the cytoplasm and increasing ROS production [191]. Some Fenton-inactive metals (including Ag^{+}, Hg^{2+}, and Ga^{3+}) create ROS, which may explain why bacteria require or upregulate ROS-detoxification enzymes to tolerate hazardous concentrations of these elements [187, 192].

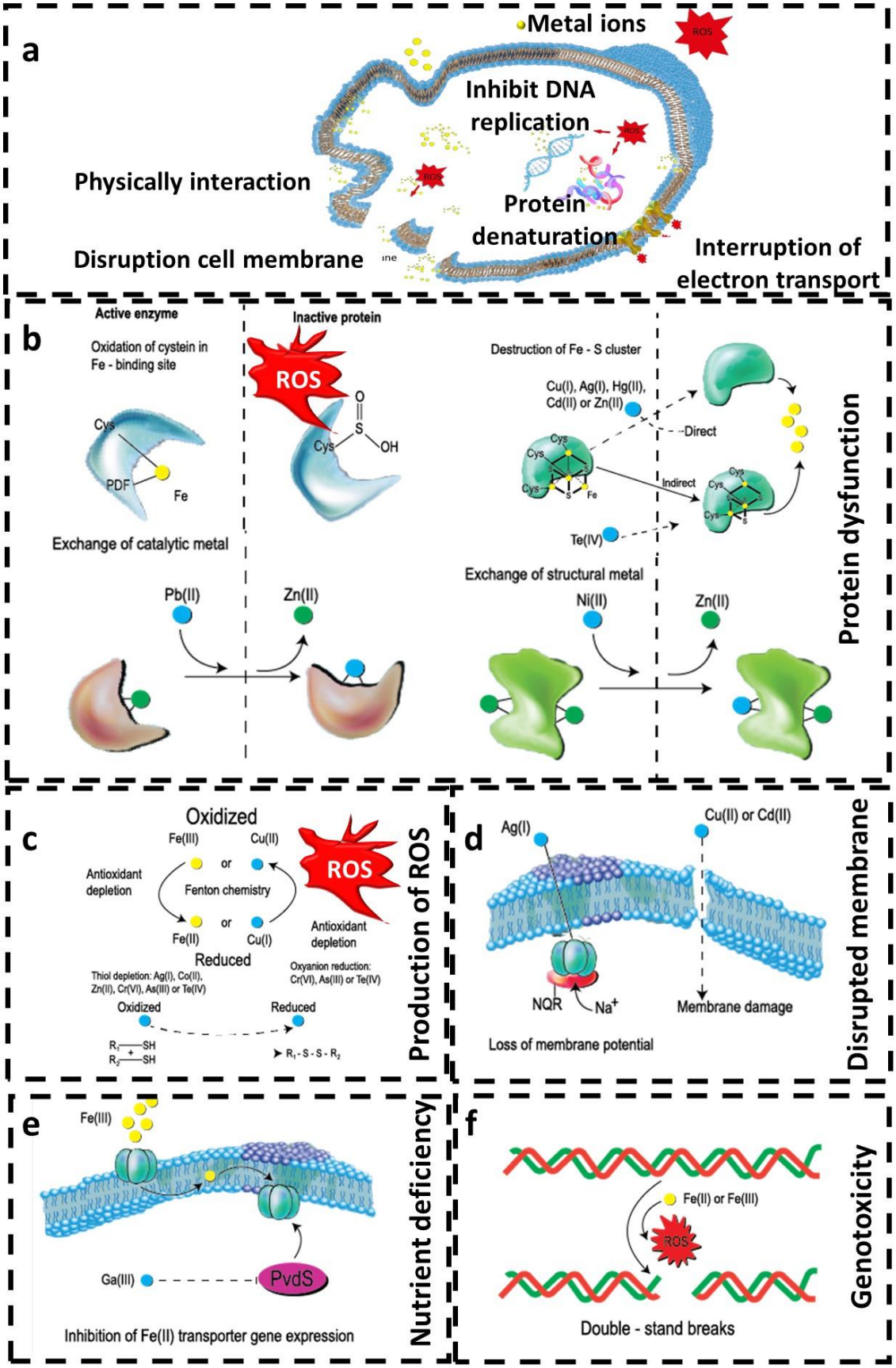
a
Metal ions
ROS
Inhibit DNA replication
Physically interaction
Protein denaturation
Disruption cell membrane
Interruption of electron transport
b
Active enzyme
Oxidation of cystein in Fe - binding site
Cys
PDF
Fe
Exchange of catalytic metal
Inactive protein
ROS
Cys
S
O
OH
Destruction of Fe - S cluster
Cu(I), Ag(I), Hg(II), Cd(II) or Zn(II)
Direct
Indirect
Te(IV)
Exchange of structural metal
Pb(II)
Zn(II)
Ni(II)
Zn(II)
Protein dysfunction
c
Oxidized
Fe(III)
Cu(II)
or
Antioxidant depletion
Fenton chemistry
ROS
Fe(II)
Cu(I)
Antioxidant depletion
Reduced
Thiol depletion: Ag(I), Co(II), Zn(II), Cr(VI), As(III) or Te(IV)
Oxyanion reduction: Cr(VI), As(III) or Te(IV)
Oxidized
Reduced
R1—SH
R2—SH
R1 - S - S - R2
Production of ROS
d
Ag(I)
Cu(II) or Cd(II)
NQR
Na+
Membrane damage
Loss of membrane potential
Disrupted membrane
e
Fe(III)
Ga(III)
PvdS
Inhibition of Fe(II) transporter gene expression
Nutrient deficiency
f
Fe(II) or Fe(III)
ROS
Double - stand breaks
Genotoxicity

Figure 2.8. Antibacterial mechanisms involve interconnected processes such as protein dysfunction, oxidative stress, membrane impairment, nutrient interference, and genotoxic effects. a) Antibacterial activity is multiple and often interconnected mechanisms. b) Metals and ions toxicity can cause protein dysfunction by inhibiting enzyme activity. c) The formation of extracellular and intracellular ROS and the depletion of antioxidants result in oxidative stress and the damage of lipids, proteins, and DNA. d) Metals and ions interact with the cell membrane via electrostatic interactions, impairing membrane function. e) The toxicity of some metals and ions can interfere with nutrient assimilation. f) Metals and metal ions can be genotoxic, interfering directly with proteins and DNA, impairing their function and disrupting cellular metabolism.

Third, thiol-mediated reduction of various metal species, such as Fe (III) and Cu (III), produces ROS via intermediate radical chemistry [193]. Moreover, thiol-mediated reduction can create Fenton active metal species such as Cr (III), Cr (IV), and Cr(V) [194]. Fe (III), Cu (II), and Cr (VI) result in the generation of ROS via a sulphur radical intermediary. Reduced thiols, such as glutathione (GSH), are a critical antioxidant in the bacterial cell. GSH, on the other hand, can be depleted by oxidising thiophilic metals such as Ag, cadmium (Cd) (II), or (As) (III). Thus, the anti-oxidative defences of bacteria are weakened, and its vulnerability to subsequent metal-mediated ROS increases [195]. However, whether radicals are involved in ROS generation or microbial metal poisoning *in vivo* is unclear.

2.4.2.2 Metals and ions causing protein dysfunction and loss of enzyme activity

Recent research revealed that intracellular proteins are also targets of metal toxicity due to the abundance of amino acid-mediated binding sites, which primarily consist of reduced thiols from cysteine side chains, carboxy groups from aspartates and glutamates, and highly reactive primary amines from lysine side chains [195]. When metal ions bind to susceptible amino acids, they catalyse their oxidation, impair protein function, decrease protein stability, and mark the protein for degradation [196]. Another study showed that Ga^{3+} inhibit or kills bacteria by taking up another metal ion instead of the essential one due to their chemical similarities. Once inside

the cell, these ions disrupt metabolic pathways due to the inability of bacterial cells to reduce them, irreversibly impairing cell metabolism [197].

Some metals and ions can potentially cause site-specific damage to biological proteins. For example, hazardous concentrations of Cr(vi) rapidly increase protein carbonyl levels in *S. cerevisiae* within minutes [198]. In *E. coli*, just a few amino acid residues per protein are vulnerable to metal-catalysed oxidation [199]. Metal-catalysed oxidation of amino acid side chains produces carbonyl compounds employed as a marker of oxidative protein damage. *In vivo*, oxidation of amino acid side chains can reduce catalytic activity and cause protein degradation. Thus, metals could potentially cause site-specific damage to biological proteins, leading to metal poisoning. The most heavily oxidised proteins are cytosolic enzymes involved in glycolysis or subsequent catabolic reactions. A bacterial Fe–S dehydratase family is susceptible to metal-specific inactivation [187]. These elements harm Fe–S–containing dehydratases *in vitro* and inhibit them *in vivo* at doses that cause bacteriostasis [191]. This suggests the metals inflict little or no further damage to the proteins compared to proteins not repaired by proteins like cysteine desulphurase or SufA. However, in this case, the destruction of the [4Fe–4S] clusters in dehydratases occurs exclusively in aerobic conditions. Unlike soft metal cations, the metalloid oxyanion Te(iv) promotes indirect oxidation of Fe–S clusters, most likely via ROS intermediates [187].

2.4.2.3 Metals and metal ions induce the function of membranes

Metal cations adsorb on polymers with strongly electronegative chemical groups in bacterial membranes and exert bactericidal toxicity [200]. Exposure to toxic metals such as Ag and Al dramatically alters the cytoplasmic membrane integrity of *E. coli and S. aureus.* Cell death can be attributed to membrane disruption or apparent cell wall separation. Other research suggests that certain metals, particularly Ag, harm the bacterial electron transport chain. Lipid

peroxidation has also been connected to the toxicity of Cu (II) and Cd (II) in bacteria and yeast, and it has been hypothesised that this is a deadly mode of action for antimicrobial metallic surfaces constructed of Cu and its alloys. This is consistent with the discovery that metal exposure increases the concentration of thiobarbituric acid reactive compounds in cell extracts. Consistent with this concept, introducing genetic alterations that enhance the unsaturated fatty acid content of cell membranes or feeding the growth medium with polyunsaturated fats leads to an increase in the level of TBARS after metal exposure.

2.4.2.4 Genotoxicity

Genotoxicity is a term that relates to the use of mutagens such as Cr (IV) and other cations that damage DNA [201]. For example, many studies have indicated that when *E. coli* is exposed to high quantities of iron, the bacteria DNA damage can be catalysed by Fe-mediated Fenton chemistry, resulting in lethal DNA damage [202]. Increased Fe concentrations in bacterial cells are caused by mutations that cause Fenton-active Fe to accumulate in the cell, which accelerates DNA damage and results in cell death [203].

Metals and metal ions in high concentrations are toxic to prokaryotic cells due to their redox properties. For example, numerous studies have linked the antibacterial activity of Cu to its ability to transition between Cu^{+} and Cu^{2+}, which can generate reactive oxygen species under aerobic conditions. Copper Fenton explains how H_2O_2 decomposes into •OH, leaving the catalytic metal oxidised. Additionally, Cu has been associated with extracellular DNA damage during cell lysis, which may limit post-mortem horizontal gene transfer of resistance via transformation [201]. However, Cu^{2+} prefers an oxidation state in solution. As a result, a reducing agent (•O2, NADPH oxidase from the respiratory chain, or intracellular thiols) is required to convert Cu^{2+} to Cu^{+} and continue the production of •OH. Warnes et al. showed that Cu toxicity for *Enterococcus faecalis* and *Enterococcus faecium* involves direct and indirect

copper ion action, ROS production, and respiratory chain and DNA repair failure. The authors contend that Fenton production of •OH is not the fundamental cause of DNA damage, but rather Cu (II)-induced denaturation of bacterial DNA. The same authors later validated the function of ROS in methicillin-resistant *S. aureus* DNA damage [204].

2.4.3 Engineering surface topography for anti-biofouling: lessons for designing bioceramics

Surface topography is typically altered through the use of anti-biofouling techniques that result in passive structuration [205]. As bacteria meet the surface structure, these strategies employ structural units such as polymer brushes or nanotubes placed over the surface, preventing them from adhering and breaking apart the membrane as they meet it. These approaches increase antifouling activity over longer periods, although they may not effectively eradicate an infection [95]. Additionally, surface alterations can have a broader biological impact. In addition to influencing bacterial adherence, the final topography of glass surfaces with various nanostructures affects bacteria metabolism [206, 207].

Natural antibacterial activity based on mechanical interactions was first reported. For example, the wings of insects such as cicadas or dragonflies are nanopatterned with high-aspect-ratio cone-like nanopillars that are toxic to bacteria such as *P. aeruginosa* [208]. This may result from an evolutionary response to the environment, which prevents the production of biofilms that impair the aerodynamics of such insects.

Studying bacterial adhesion to bioceramics is crucial for understanding and improving antibacterial activity because it provides insights into the initial stages of bacterial colonisation on implant surfaces. Bacterial adhesion is the first step in developing biofilms, which are complex communities of microorganisms embedded in a self-produced extracellular matrix.

Biofilms are highly resistant to antibiotics and the host immune system, making them challenging to treat and remove. By studying bacterial adhesion to bioceramics, we can identify factors that influence this process and develop strategies to minimise bacterial colonisation. This could include modifying the surface properties of bioceramics or incorporating antibacterial agents into their composition. Understanding bacterial adhesion to bioceramics is essential for designing next-generation implant materials with enhanced antibacterial properties, ultimately reducing the risk of implant-associated infections and improving patient outcomes.

2.4.3.1 Surface properties influencing bacterial adhesion

The chemical composition of the surface influences the microorganisms attached to it [209]. Because surface chemistry determines the ability of bacteria to adhere, maintaining a smooth substrate is crucial [210]. Additionally, bacterial adhesion was shown to be greatest on hydrophilic surfaces with positive surface charge characteristics, followed by hydrophobic substrates with negative surface charge characteristics, and lowest on hydrophilic substrates with negative surface charge characteristics [211]. The extremely hydrophobic or hydrophilic surfaces inhibited *E. coli* adherence [212]. This finding contradicts normal surface chemistry adhesion trends for hydrophilic bacteria, which show that bacterial adherence increases with increasing hydrophobicity and decreases with decreasing surface energy. The conflict could be caused by surface roughness and topography, which affect bacterial adhesion behaviour when surfaces interact with bacteria.

A rough surface has more surface area, which makes it more favourable for bacteria to adhere [213]. However, the influence of surface roughness on adhesion appears to be related to the degree of roughness, surface topography, and material compositions [214]. Some previous research has been conducted on bioceramic materials; however, the findings remain

contentious. Wassmann et al. studied the adherence of *S. epidermidis* to the surface of a zirconia ceramic implant [215]. The findings demonstrate that altering the roughness of the surface does not influence the quantity of bacterial adherence. Dutra et al. investigated the influence of surface roughness on bacterial adherence to zirconia-stabilized yttria (Y-TZP) ceramics [216]. The authors discovered that the quantity of adhering bacteria remains constant when the surface roughness is reduced. Thus, surface roughness does not play a significant role in bacterial adherence, and a Y-TZP material exhibits a low susceptibility to bacterial adhesion. Kang et al. investigated the effect of several polishing procedures on the roughness and adherence of *Streptococcus mitis* on zirconia ceramic surfaces [217]. The results indicate that the quantity of adhering bacteria increases proportionately when the surface roughness rises. The previous studies on the sample surfaces have employed roughness values in the micron to the submicron range. A bioceramic surface with a roughness of nanoscale or submicron is unknown regarding bacterial adherence. The surface topography influences bacterial adherence, as shown in Figure 2.9. Because *S. aureus* has low mobility and prefers low-lying topographies like valleys, grooves, and pits, a rough, rugged, high-amplitude groove-like surface topography significantly promotes initial *S. aureus* adhesion and biofilm growth [218, 219]. Defined micro-scale features such as scratches, pits, and grooves will boost the bacterial-surface attachment strength [220]. In Figure 2.9, for example, samples A, B, and C have more bacterial adhesions than samples D, E, and F because they contain more micro-scale characteristics. Sample E (R_a 1.51 nm), with a shallow unidirectional surface texture, has more sites for initial bacterial attachment than sample F (Ra 1.11 nm), with a homogeneous and damage-free surface, resulting in higher bacterial adherence.

There have been inconsistent findings addressing the bacterial adhesion patterns about surface chemistry due to various factors. Firstly, the hydrophobicity of the substrate, the roughness and texture of the substrate, as well as the porosity and fibrousness of the material, can all affect

bacterial adhesion behaviour [211, 221-223]. Limiting the substrate roughness effect is necessary to deduce precise correlations between substrate chemistry and bacterial adherence. Second, variations in experimental assays used to determine bacterial adhesion, such as drop-casting inoculation and the rinse phase, have been observed due to velocity gradient, gravity, and drying effects [211, 224, 225].

Achieving the balance between surface characteristics that inhibit bacterial adhesion while simultaneously promoting osteogenic cell functions represents a pivotal challenge in designing advanced bioceramics for orthopaedic applications. This balance is essential to prevent infection and ensure the successful integration of the implants with bone tissue. Current research efforts focus on engineering bioceramic surfaces with dual functionality. One effective strategy involves crafting a moderately rough surface topography incorporating precisely defined micro- and nano-scale features. These features are strategically designed to reduce bacterial attachment by minimising areas where bacteria can easily adhere while providing the necessary cues to enhance osteoblast adhesion, proliferation, and differentiation. This is achieved through careful modulation of the surface's mechanical strength and its chemical and physical properties.

Furthermore, the quality of implant surfaces is defined by an intricate interplay of mechanical, topographical, and physicochemical properties. Alterations in one property can significantly impact the others, influencing the overall biological response to the implant [226]. For example, increasing the micro-scale roughness might enhance bone cell functions. Still, it could provide more niches for bacterial growth unless nano-scale modifications are simultaneously applied to counteract this effect. As a result, the physical and chemical properties of bioceramics can be tailored with high precision to achieve these multifaceted requirements. Advanced manufacturing techniques such as laser micromachining and chemical vapour

deposition are employed to fine-tune these properties, allowing for developing surfaces optimally designed to combat bacterial colonisation while supporting osteogenesis.

2.4.3.2 Environmental factors influencing bacterial adhesion

Environmental factors that influence bacterial adherence include temperature, bacterial density, chemical modification, antimicrobials existence, and associated flow characteristics [227]. Flow parameters are considered dominating elements because they have a major impact on the number of bacteria adhered to as well as the structure and function of the biofilm. Katsikogianni et al. demonstrated that flow conditions affected bacterial adherence to various substrates. The quantity of adhering bacteria reduced dramatically as the shear rate was increased from 150 sec^{-1} to 1,500 sec^{-1} [228]. Mohamed et al. demonstrated that when the number of receptors per cell is increased, *S. aureus* adherence to collagen-coated coverslips increases between 50–300 sec^{-1} and decreases above 500 sec^{-1} [229]. Therefore, bacterial attachment does not have an optimal flow rate because the delivery rate must be matched with the force acting on the enclosed bacteria.

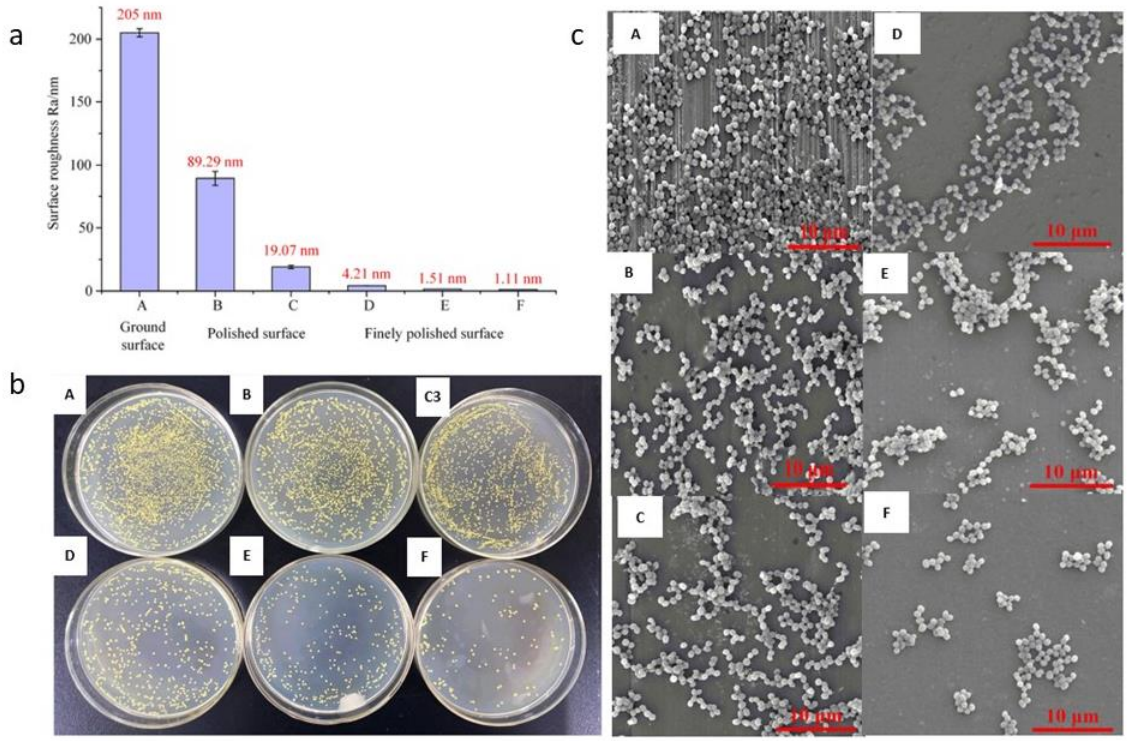

Figure 2.9. The morphology and distribution of the attached *S. aureus* bacteria on the state variation from rough to smooth of Y-TZP bio-ceramic surfaces. a) the average surface roughness with A (205nm), B (89.29nm, C (19.07nm), D (4.21nm), E (1.51nm), F (1.11nm). b) the CFU results of the number of bacteria adhered to the sample surfaces. Sample A has the largest number of adhering bacteria, in samples B–E, the number of adhering bacteria gradually decreases, and sample F has the least number of adhering bacteria on the surface. c) The morphology and density of the bacteria adhering to the surface under SEM. Microorganisms almost totally cover the surface (Ra 205 nm). The protruded topographical characteristics of the surface layer (Ra 89.29 nm) are removed, and the places where the bacteria can be attached and fixed are fewer. The smooth region of the surface (Ra 19.07 nm) gradually grows as the original ground textures and flaws are removed. The surfaces (Ra 4.21 nm and 1.51 nm) the number and density of the bacteria adhering to the surface are reduced. The quantity and density of the adhering bacteria are the lowest because no texture remains on the surface, and the entire surface becomes exceedingly smooth (Adapted with permission from ref [195]).

Adhesion can be affected by changes in pH and electrolyte concentrations of KCl and NaCl [230]. Bacteria adjust their activity and synthesis of proteins involved in various cellular activities in response to changes in internal and external pH. Studies have demonstrated that a

gradual increase in acidity is preferable to a quick increase caused by adding HCl [231]. This indicates that bacteria have systems in place that enable them to adjust to tiny changes in the pH of their surroundings. However, other biological functions do not adapt as readily to pH variations. The pH of the bone tissue environment is frequently below 7, whereas the pH of healthy tissues is typically in the range of 7.35 to 7.45, depending on the tissue [232]. HAp and biphasic calcium phosphate (BCP) are ceramic materials commonly used as bone substitutes. The porosity of these materials, as well as the decrease in pH in the surrounding area because of surgical trauma, may, however, predispose them to bacterial infections. Recent studies demonstrated that when the pH of the solution was reduced from 7.4 to 6.8, the adhesion of S*taphylococci* to both HAp and BCP surfaces was dramatically reduced [231, 232]. Furthermore, they discovered in this investigation that the pores in HAp and BCP ceramics were not large enough to allow the internalisation of *Staphylococci*. As a result, their anti-adherent capabilities appeared to improve when the pH value was dropped, indicating that the bioceramics HAp and BCP are not impaired when used in orthopaedic applications. In addition, using tricalcium silicate-based cement such as MTA, a previous study demonstrated that the pH of MTA is 10.5 at the time of mixing and can increase to 12.9 after 3 hours of setting [231]. High pH affects the structure of endodontic bacterial cells by producing DNA breakdown and cellular protein damage, which results in a reduction in the survival of the bacterial cells. MTA has antibiofilm action; the pH increase during the setting process is primarily responsible for this. The generation of calcium hydroxide during the hydration reaction of MTA has the potential to cause the pH to rise. Therefore, MTA demonstrated antimicrobial action against a variety of different bacterial biofilms, including those formed by *S. aureus*, *E. coli*, *P. aeruginosa*, *Porphyromonas gingivalis*, and *Candia albicans* [233, 234].

2.4.3.3 Proteins corona influencing bacterial adhesion

Biomolecules such as extracellular matrix proteins adsorb onto the material surface when an implant is inserted into host tissue, generating a conditioned protein coating that promotes adherence of free-floating planktonic bacteria to the implant surface. Then, the adhering bacteria divide the number rapidly and release adhesive secretions, creating dense colonies of connected cells called biofilms [235, 236]. Notably, serum or tissue proteins such as albumin, fibrinogen, laminin, and denatured collagen enhance or inhibit bacterial adherence. These proteins attach to the surface of the substratum, adhering to the bacterial surface or remaining present in the liquid medium during the adhesion period. Most interactions between bacteria and proteins occur through specialised ligand-receptor interactions rather than broad bindings. Proteins can alter the adhesion behaviour of bacteria by modifying the physicochemical properties of the surface membrane of bacteria [237, 238].

Fibronectin is a protein that increases adhesion-promoting bacterial adherence to biomaterial surfaces [239] especially S*taphylococci [240]*. There are two known S*taphylococci* binding sites in Fn: one in the N-terminal domain and the other towards the C-terminus. *S. epidermidis* has a greater affinity for the C-terminal segment and many bacteria have fibronectin-binding proteins that can bind to an increasing number of fibronectin sites [241, 242]. *S. aureus* generates surface proteins that may be important in initial host tissue attachment. The microbial surface components recognising adhesive matrix molecules bind specifically to extracellular matrix components. *S. aureus* has two FnBPs, FnBPA and FnBPB, encoded by the closely related genes *fnbA* and *fnbB*. Almost all clinical isolates of *S. aureus* have one of two genes. FnBPs are implicated in infection pathogenesis. Almost all clinical isolates of *S. aureus* have the surface proteins FnBPA and FnBPB. FnBPs are involved in the pathophysiology of infection [242].

Bacterial adherence to biomaterials and host tissues is also mediated by fibrinogen. Fibrinogen increases bacterial adherence by connecting biomaterial surfaces with fibrinogen membrane receptors [243]. *In vivo*, bacteria that can specifically bind surface-adsorbed fibrinogen are reported to be more clinical orthopaedic device-associated infections [244]. Charville et al. found that *S. aureus, S. epidermidis*, and *Escherichia coli* adhered better to pre-adsorbed fibrinogen than to protein-free PVC substrates [245]. The greatest increase was seen in *S. aureus*, whose adherence to fibrinogen-coated substrates was five times that of uncoated controls. *S. aureus* adhesion to polyurethane surfaces with pre-adsorbed fibrinogen was reported by Baumgartner et al. Pei et al. showed that *S. epidermidis* adhesion to non-functional fibrinogen-coated control catheters was roughly half that of fibrinogen-coated catheters [246]. The observations suggest that certain fibrinogen-mediated interactions between bacterial cells and substrates improve bacterial adherence in the presence of fibrinogen.

2.4.3.4 Hydrogels with surface-modified bioceramics for infectious bone repair

Hydrogels and surface-modified bioceramics combined constitute a potentially effective strategy for tackling the difficulty associated with infectious bone repair [247]. Combining two complementary components can create multifunctional bioceramics with enhanced antimicrobial properties and improved bone regenerative capabilities. The ability of hydrogels to mimic the extracellular matrix can serve as effective carriers for the delivery of antimicrobial agents, such as antibiotics [248], antimicrobial peptides [249], or metal ions [250]. The hydrogel matrix can facilitate the controlled and localised release of these agents, helping to combat bacterial colonisation and biofilm formation at the site of infection. Furthermore, the hydrogel component can improve the handling properties and drug-loading capacity of the bioceramic scaffolds [251], overcoming some of the limitations associated with direct bioceramic implantation.

2.4.4 Smart antibacterial bioceramics with stimulus-responsive mechanisms: emerging innovations for medical implant applications

Smart antibacterial bioceramics with stimulus-responsive mechanisms offer a promising and innovative way to address IAIs. Despite being in early development stages, these biomaterials have piqued the interest of the research community due to their potential to transform medical implant technology. However, there is a limited number of studies on smart antibacterial bioceramics, making this research a valuable addition to the field.

Antibacterial stimuli-responsive bioceramics are designed to release antimicrobial agents in response to environmental cues such as temperature, pH, or the presence of bacteria [252]. This targeted release allows for more efficient and effective bacterial eradication while minimising the risk of antimicrobial resistance and adverse effects on surrounding healthy tissues. To optimise the performance of these smart materials, a comprehensive understanding of the interactions between the bioceramic matrix, antimicrobial agents, and environmental stimuli is necessary.

Future research will focus on optimising the response time and sensitivity of smart antibacterial bioceramics to specific environmental cues, as well as ensuring their long-term stability and biocompatibility. These include incorporating smart polymers that respond to environmental changes, designing bioceramics with switchable surface properties to control bacterial adhesion and release, and creating coatings or surface treatments to detect and respond to particular bacterial species or infection biomarkers.

To fully realise the potential of stimulus-responsive antibacterial bioceramics, many obstacles must be addressed despite the growing interest in this field. These obstacles include optimising the response time and sensitivity of the materials to specific stimuli, ensuring long-term stability and biocompatibility, and scaling up manufacturing processes for clinical use. In

addition, additional *in vitro* and *in vivo* studies are required to evaluate the safety, efficacy, and overall performance of these materials in various medical applications.

In conclusion, smart antibacterial bioceramics with stimulus-responsive mechanisms represent an exciting and emerging research field with the potential to impact implantable biomaterials substantially. By addressing current challenges and advancing our understanding of these materials, researchers can create innovative solutions for infection prevention and treatment in medical implant applications, thereby improving patient outcomes and reducing healthcare costs.

5. CHALLENGES AND FUTURE DIRECTIONS

Developing biomaterials with enhanced antibacterial properties is critical to addressing the growing problem of implant-associated infections. However, the complexity of these biomaterials frequently creates significant challenges to their successful clinical translation [253]. Complex biomaterials, while often demonstrating superior antibacterial properties, can be challenging to manufacture on a large scale [254]. Incorporating multiple functions, such as customised surface topographies, controlled release of antimicrobial agents, and intrinsic antibacterial mechanisms, can greatly complicate the manufacturing process. This complexity can result in greater production costs, lower scalability, and challenges in promising consistent quality and accuracy, critical for successful clinical adoption. Moreover, incorporating these complex biomaterials into current clinical processes can be a challenging endeavour, demanding significant changes to established methods and practices [255]. Regulatory organisations frequently need significant testing and documentation to assure the safety, efficacy, and reliability of these complex biomaterials, which might cause delays in their clinical implementation [255].

In contrast, simpler biomaterials are more likely to be adopted successfully in clinical applications [255]. Due to the simplicity of their production, they are more readily available and cost-effective. Regulatory agencies are more inclined to approve less complex biomaterials due to the ease with which their safety and effectiveness can be evaluated. Furthermore, integrating less complex bioceramics into established clinical workflows frequently results in insignificant disruption. Despite these challenges, developing improved antibacterial bioceramics is critical. The complexity of these materials must be carefully balanced with practical clinical translation considerations. Strategies that prioritise the balance of antibacterial efficacy and manufacturing simplicity, regulatory compliance, and clinical integration may be critical to successfully bringing these next-generation biomaterials to the centre of patient care.

The traditional focus on antibacterial bioceramics in bone tissue engineering is now being expanded in various tissue interfaces, demonstrating the broad applicability and versatility. Notably, recent advancements in research introduce antibacterial bioceramics into ophthalmology, a significant shift from their conventional use. The development of antibacterial glass-based sputtered coatings for ocular prostheses offers a novel approach to reducing infection risks associated with ocular implants [256]. This innovation highlights the adaptability of bioceramics to diverse biological environments and their potential to transform ocular prosthetic applications by enhancing safety and efficacy. Additionally, exploring bioactive glass and glass-ceramic for orbital implants further emphasises the expanding scope of bioceramic applications beyond skeletal repair towards improving outcomes in ocular rehabilitation [257]. These emerging applications highlight a pivotal evolution in the use of antibacterial bioceramics, from their foundational role in bone regeneration to their promising potential in addressing complex challenges in ophthalmic medicine. The versatility and

adaptability of bioceramics to various tissue interfaces offer great potential for enhancing patient care and clinical outcomes in numerous medical disciplines.

6. CONCLUSIONS

To tackle the increasing worldwide risks posed by drug-resistant pathogenic microbes, researchers have made significant efforts to create antimicrobial bioceramics that not only kill pathogenic microbes but also promote the adhesion and growth of healthy cells. This means the next-generation bioceramics for biomedical applications should simultaneously prevent microbial infection and promote tissue regeneration. Perfect bioceramics should have superior biocompatibility and antibacterial properties to suppress bacterial growth and secondary infections, as well as sufficient mechanical resistance for surgical insertion. Bioceramics have been promising biomaterials for various biomedical applications, such as orthopedic implants and tissue regeneration, for a long time. Bioceramics with metal ions have been successfully doped in recent research as prospective therapeutic agents for improved bone regeneration. The combinatory features of ion-doped bioceramics led to an increased interest in these materials for various biomedical applications including bone regeneration. Due to the continuous emergence of bacterial resistance, more research is devoted to developing novel antimicrobial agents. Antibiotic-resistant bacterial strains pose an increasing threat, necessitating the development of effective and long-lasting antibacterial materials. Metals have been used, and their antimicrobial properties have been extensively studied. Like antibiotics, metals have a distinct effect on bacterial and mammalian targets due to their divergent metal transport systems and metalloproteins. This enables the long-term use of metal-based bioceramics as antimicrobial agents with minimal adverse effects on the host. Identify the qualities of surfaces that bacteria feel, decipher the molecular mechanisms by which bacteria sense surfaces, and identify how to adjust surfaces. Microbes interacting with surfaces remain a mystery in

physics, biochemistry, genetics, biomedical, and biotechnology. The chemical composition of the substance, the surface charge, the hydrophobicity, and simply the surface roughness or physical configuration all influence the adhesion of bacteria to a biomaterial surface. Additionally, their surface energy, the number of unoccupied binding sites, and hydrophobic/hydrophilic properties can be rapidly altered by serum protein adsorption or binding and the production of biofilms. Antibacterial properties of bioceramics prevent bacteria from adhering to implant surfaces, minimising infection risk. Multifunctional bioceramics offer many advantages and the capacity to fine-tune them, making them an indispensable component in biomedical applications. As discussed in this review, new approaches have the potential to understand bacteria surface interactions and guide applications for orthopaedic implants.

CHAPTER 3:

ANTIBACTERIAL ACTIVITY AND MECHANISMS OF MAGNESIUM-DOPED BAGHDADITE BIOCERAMICS FOR ORTHOPAEDIC IMPLANTS

Huu Ngoc Nguyen[1], Iman Roohani[1,2], Andrew Hayles[3], Zufu Lu[1], Jitraporn Vongsvivut[4], Krasimir Vasilev[3], Vi Khanh Truong[3,5*], Hala Zreiqat[1*]

[1]Tissue Engineering and Biomaterials Research Unit, School of Biomedical Engineering, The University of Sydney, Camperdown, NSW 2006, Australia

[2]School of Biomedical Engineering, Faculty of Engineering and Information Technology, University of Technology Sydney, Sydney NSW, Australia

[3]College of Medicine and Public Health, Flinders University, Bedford Park SA 5042, Australia

[4]Infrared Microspectroscopy Beamline, ANSTO Australian Synchrotron, Clayton, Victoria 3168, Australia

[5]Healthcare Engineering Innovation Group (HEIG), Department of Biomedical Engineering and Biotechnology, Khalifa University of Science and Technology, Abu Dhabi, UAE

Published in Advanced NanoBiomed Research:

https://doi.org/10.1002/anbr.202400119

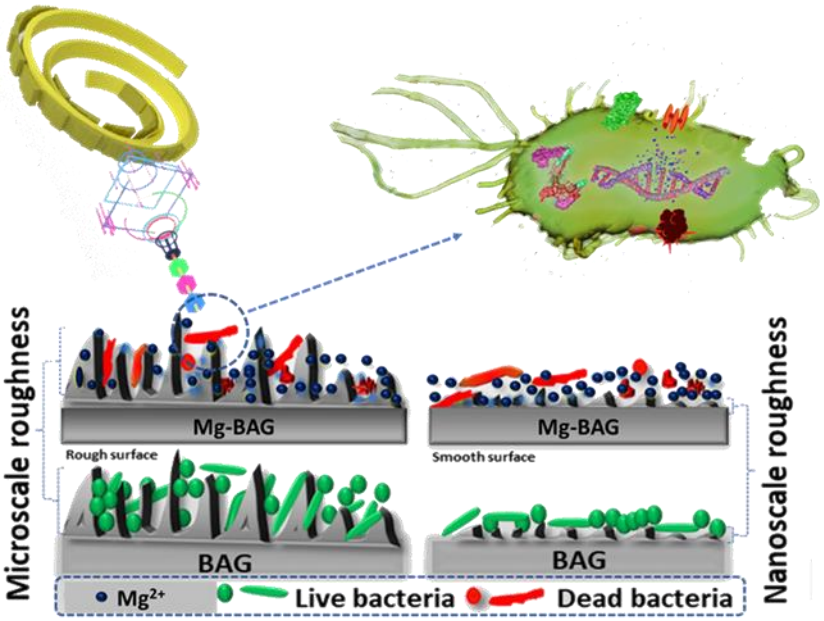

Abstract

Baghdadite (BAG, $Ca_3ZrSi_2O_9$), a calcium silicate compound with zirconium incorporation shows significant potential in medical implants. However, its susceptibility to infections poses a considerable challenge. To tackle this problem, doping biocompatible magnesium ions (Mg^{2+}) into BAG to create Mg-BAG enhances antibacterial activity and prevents infection in orthopaedic implants. Mg-BAG demonstrates effectiveness against Gram-positive *S. aureus* and Gram-negative *P. aeruginosa*. This study found that the antibacterial activity of Mg-BAG is multifaced including causing the generation of ROS within cells and disrupting membrane potential, resulting in leakage of intracellular contents. The synchrotron macro attenuated total reflectance Fourier transform infrared (ATR-FTIR) microspectroscopy shows the impact of Mg-BAG on bacteria, resulting in modifications to biomolecules such as lipids, protein structures and the stability of nucleic acids. The combined effect of Mg^{2+} and intracellular ROS formation contributes to the disruption of biomolecules and bacterial cell death. Mg-BAG is a promising next-generation bioceramic offering innovative non-antibiotic solutions for preventing infection.

3.1. INTRODUCTION

Various synthetic materials (e.g. scaffolds) have been created to address the drawbacks of autografts and allografts. However, a significant obstacle hindering the success of these scaffolds is the risk of microbial infection, contributing to implant failure. Bacterial colonisation on implant surfaces often undermines their functionality. Infection rates are reported to be between 2% and 5% in the case of orthopaedic implants [258], increasing to a concerning 30% in the case of open fractures [258, 259]. IAIs are commonly linked to *P. aeruginosa* and *S. aureus* and pose a challenge to the success of orthopaedic implants [82, 260, 261]. After revision surgery, there is a recurrence rate of around 33% for infections resulting in an increase in treatment cost range from $17,000 to $150,000 per patient [247]. Unfortunately, diagnosing an implant infection poses a challenge to success due to the difficulty in eliminating bacteria. Addressing infections with antibiotics proves to be problematic given the concerning rise of antibiotic-resistant organisms. Traditional approaches such as replacing devices and administering antibiotics for periods unintentionally worsen the growing issue of AMR [262]. The WHO predicts that by 2050, AMR could lead to 10 million deaths annually, surpassing the current cancer mortality rate and potentially costing the global economy $100 trillion if preventive measures are not implemented [263]. Thus, there is an urgent need to develop and design next-generation antimicrobial synthetic bioceramics for effective prevention and minimising the risk of IAIs.

The increasing interest in BAG as a synthetic bone substitute can be attributed to its properties, such, as bioactivity, biodegradability and ability to support the healing of large bone defects [7-11]. However, its effectiveness in preventing bacterial growth is limited. Current strategies involve the use of transition-metal ions such as copper (Cu^{2+}), zinc (Zn^{2+}), and silver (Ag^{+}), which show varying degrees of success, against bacteria [12, 13]. Some studies developed on

creating Ag^{+} and Cu^{2+} coatings for implants to inhibit bacterial growth, disrupt bacterial cell membranes, interfere with essential cellular processes and prevent biofilm formation [14]. However, the use of Ag^{+} and Cu^{2+} is limited by concerns about their toxicity [15]. and the potential for developing antibiotic resistance [16].

Previous research has reported that incorporating Mg^{2+} into BAG can improve its mechanical strength and biological properties, benefiting bone tissue engineering [22]. Additionally, magnesium ions play a role in biological processes such as promoting bone formation (osteogenesis) and the development of blood vessels (angiogenesis), both vital for effective bone healing. By incorporating Mg^{2+} into BAG (Mg-BAG), the ability of the material to support *in vitro* and *in vivo* bone repair is significantly enhanced by promoting cell adhesion and growth and stimulating the mineralisation of the matrix for better integration with natural bone tissue [11, 22, 23, 264]. Furthermore, Mg^{2+} has reported bactericidal and bacteriostatic potential [17-21, 265]. Mg^{2+} work by disrupting membranes and interfering with their functions making them effective against bacteria. In addition, they offer cost-effective antibacterial properties and biocompatibility [17-21]. This study investigates the effectiveness of Mg-BAG in preventing infections.

The surface topography of biomaterials is recognised to influence bone integration and the adhesion of bacteria [231, 260]. While implant surface micro-roughness has been shown to promote bone cell proliferation and osteogenic differentiation [24-27, 266, 267], it can also increase the risk of infections [268, 269]. In contrast, nano-roughness topographies may have the ability to eliminate microbes by disrupting their cell walls [270]. However, the relationship between surface roughness and cellular adhesion remains a topic of debate with studies have shown varying results.

This study aims to investigate the antimicrobial properties of Mg-BAG against commonly orthopaedic implant-related pathogens *P. aeruginosa* and *S. aureus*. We further explored the antimicrobial effect in response to the micron and sub-micron roughness Mg-BAG and the multifaceted antibacterial mechanisms involved in this response, including alterations to biomolecules, the generation of intracellular reactive oxygen species and membrane depolarisation, ultimately leading to disrupting bacterial membrane integrity.

3.2. RESULTS AND DISCUSSION

3.2.1. Fabrication and characterisation of magnesium-doped baghdadite

We synthesised bioceramic BAG discs with the dimensions of 14mm diameter and × 2 mm height using a solid-state synthesis method, Mg^{2+} is a dopant, as described in Figure 3.1 and Figure 3.S1 [22, 23]. The approach enables precise control over the doping of Mg^{2+} into BAG via substituting Zr^{2+} or Ca^{2+} with divalent Mg^{2+}. The successful doping of Mg^{2+} into BAG was demonstrated through spectroscopic techniques including Energy Dispersive X-ray Spectroscopy (EDS), X-ray photoelectron spectroscopy (XPS) and X-ray diffraction (XRD) analysis shown in Figure 3.2a, 2b & 2c. Elemental mapping of the Mg-BAG surface discovered a distribution of Ca, Zr, Si, O, and Mg. The uniform distribution of these elements across Mg-BAG surfaces, confirmed through EDS analysis, provides evidence of the successful synthesis process that achieved homogenous doping of Mg throughout the surfaces. Additionally, detecting the Mg 1s peak in Mg-BAG indicates the successful integration of Mg^{2+}.

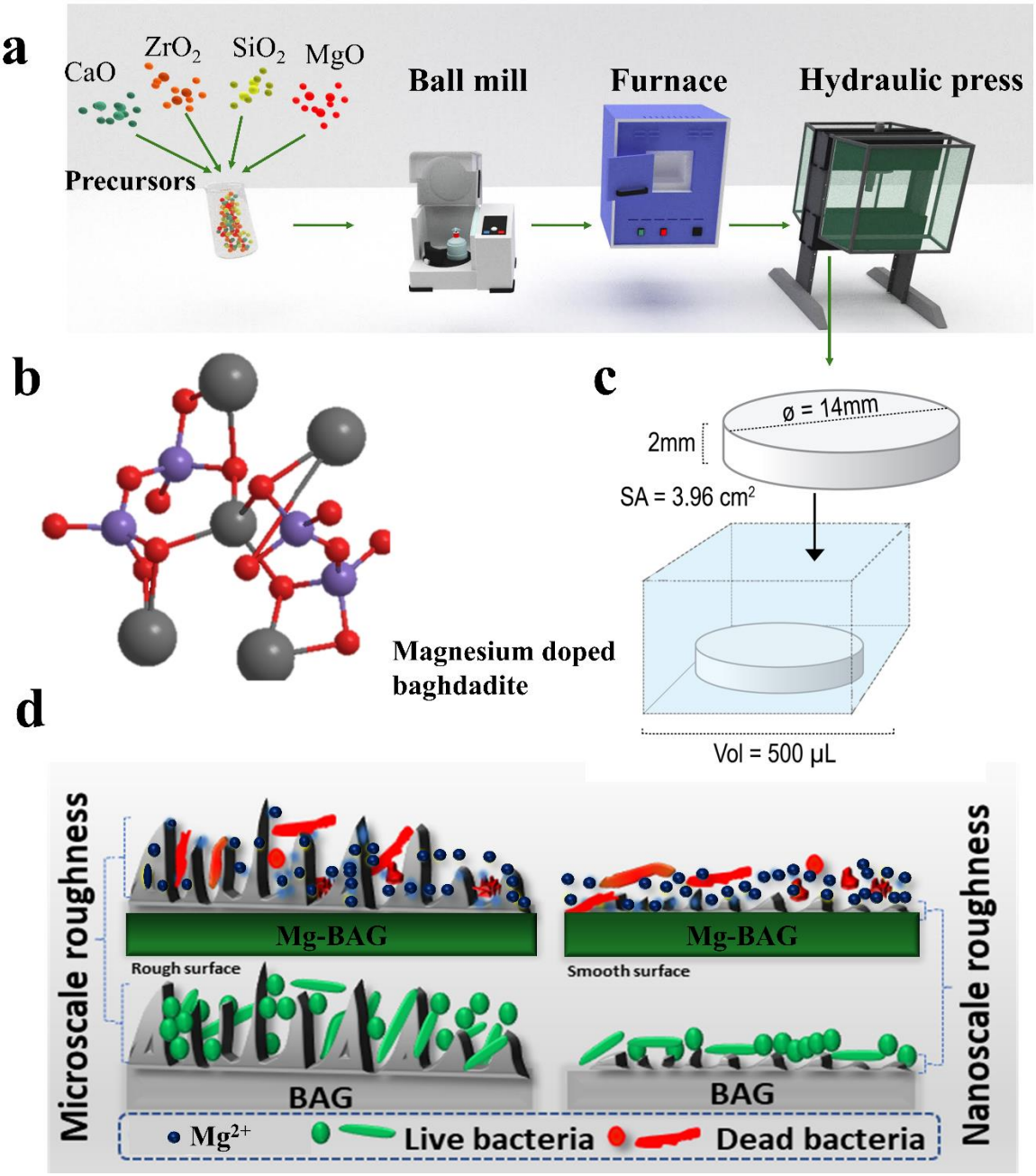

Figure 3. Schematic of Mg-BAG fabrication. a) The synthesis process of Mg-BAG starts from mixing precursors in a ball mill, then sintering in a furnace and forming into discs using a hydraulic press. b) Molecular structure of Mg-BAG with the arrangement of Ca, Zr, Si, Mg. c) Representation of a disc-shaped Mg-BAG sample, detailing dimensions (diameter = 14mm, thickness = 2mm) and surface area (SA = 3.96 cm²). d) Comparison of microscale and nanoscale surface roughness on Mg-BAG and BAG, demonstrating the interaction with live and dead bacteria.

The microscale and sub-microscale topographies of the implant surface play a role in the initial bacterial attachment and the biofilm formation [271-273]. In this study, the sample surfaces were polished to a smooth finish. We used 3D profilometry to assess the surface texture of HAp, BAG and Mg-BAG, as illustrated in Figure 2d and detailed in Table 3.5.S1. The unpolished surfaces referred to as "rough," for HAp BAG and Mg-BAG showed areas at a scale with average roughness (R_a) values of 1.264 ± 0.051 μm 1.932 ± 0.268 μm and 1.640 ± 0.180 μm respectively. On the other hand, the polished surface known as "smooth," had features at a scale with significantly lower R_a values of 0.115 ± 0.002 μm for HAp, 0.347 ± 0.017 μm for BAG and 0.223 ± 0.010 μm for Mg-BAG.

3.2.2 Assessing the antibacterial activity of Mg-BAG.

We evaluated the antibacterial performance of HAp, BAG and Mg-BAG, specifically targeting their impact on Gram-negative *P. aeruginosa* and Gram-positive *S. aureus*. These two pathogens are strongly associated with IAIs [260]. The BacLight™ Live/Dead fluorescent dye assay was used to evaluate the viability of cells based on the integrity of their membranes on surfaces [274]. Our results indicated that BAG displayed activity leading to roughly 12% of cells being dead while HAp showed no bactericidal effect against *P. aeruginosa* or *S. aureus* (Figure 3.3). In contrast, after a three-hour incubation, both Mg BAG showed a notable increase in dead cells compared to BAG and HAp, with approximately 75% of the population being affected for both bacterial strains ($p < 0.001$). Extending the incubation time to six hours did not increase the percentage of cells indicating that Mg-BAG can effectively inhibit most bacteria within the first three hours of exposure. Additionally, the roughness of the surface did not significantly impact the bactericidal properties of Mg-BAG.

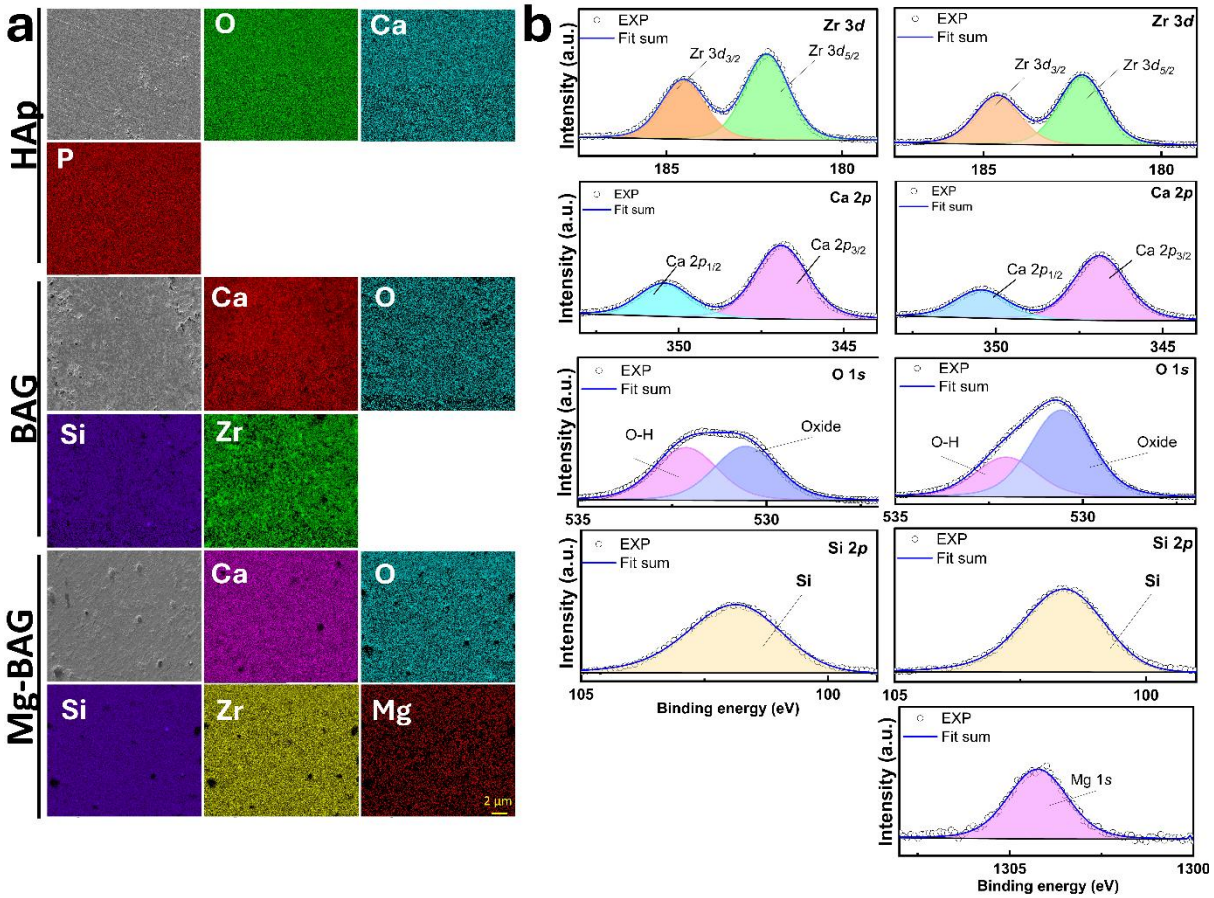
a
HAp
BAG
Mg-BAG
O
Ca
P
Si
Zr
Mg
2 μm
b
EXP
Fit sum
Zr 3d
Zr 3d3/2
Zr 3d5/2
Ca 2p
Ca 2p1/2
Ca 2p3/2
O 1s
O-H
Oxide
Si 2p
Si
Mg 1s
Intensity (a.u.)
Binding energy (eV)

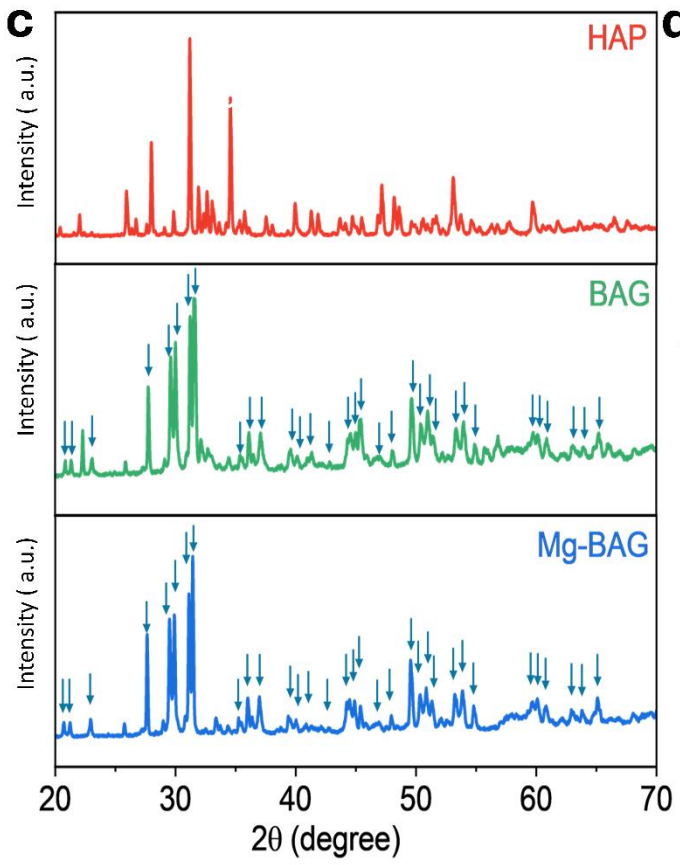
c
HAP
BAG
Mg-BAG
Intensity (a.u.)
2θ (degree)

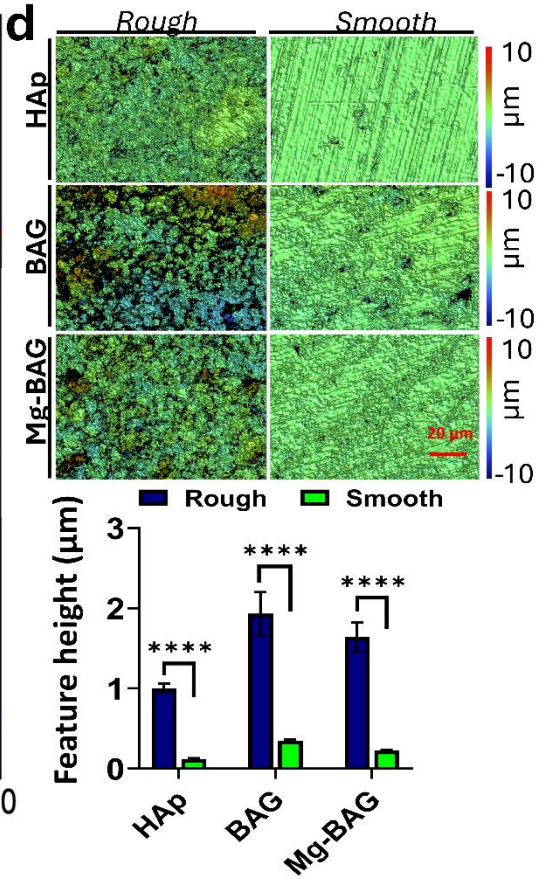
d
Rough
Smooth
HAp
BAG
Mg-BAG
10
μm
-10
20 μm
Feature height (μm)
****

Figure 3.2. Compositional and surface roughness analysis of HAp, BAG, and Mg-BAG. a) EDS mapping reveals the distribution of elements on the sample surfaces. b) XPS spectra provide insights into the elemental makeup and chemical states of Zr, Ca, Si and Mg. c) XRD patterns illustrate the diffraction angles and intensities associated with the crystalline phases, found in the samples. d) Detailed surface topography analysis conducted using 3D profilometry. n= 3 ± SD, **** $p < 0.0001$.

To investigate if the antibacterial effects we observed were dependent on contact we conducted the disk diffusion assay (Figure 3.3c, Figure 3.5.S3, Table 3.5.S2) [275, 276]. The BAG bioceramic, regardless of being smooth or rough showed minimal inhibition zones (~0.7 ± 0.55 mm) against *P. aeruginosa* and exhibited no inhibition zone against *S. aureus*. On the other hand, our engineered Mg-BAG demonstrated significant inhibition zones ranging from 3.33 ± 1.52 to 4.00 ± 1.00 mm against both *P. aeruginosa* and *S. aureus* as detailed in Table 3.5.S2. These findings align with our previous observation that the antibacterial effectiveness of Mg BAG is not influenced by surface roughness.

Although bacterial resistance to heavy metals such as Cd [277], Zn [278], Ag [279-281] and Cu [282] through efflux systems has been well-documented, and no resistance specifically to Mg^{2+} has been reported. This investigation revealed that the antibacterial activity of Mg-BAG could effectively kill both *S. aureus* and *P. aeruginosa.* Importantly, this effect was observed regardless of the surface roughness of the doped BAG samples. This outcome is promising because surface roughness is a property that facilitates bone integration [283], but also promotes bacterial attachment [284].

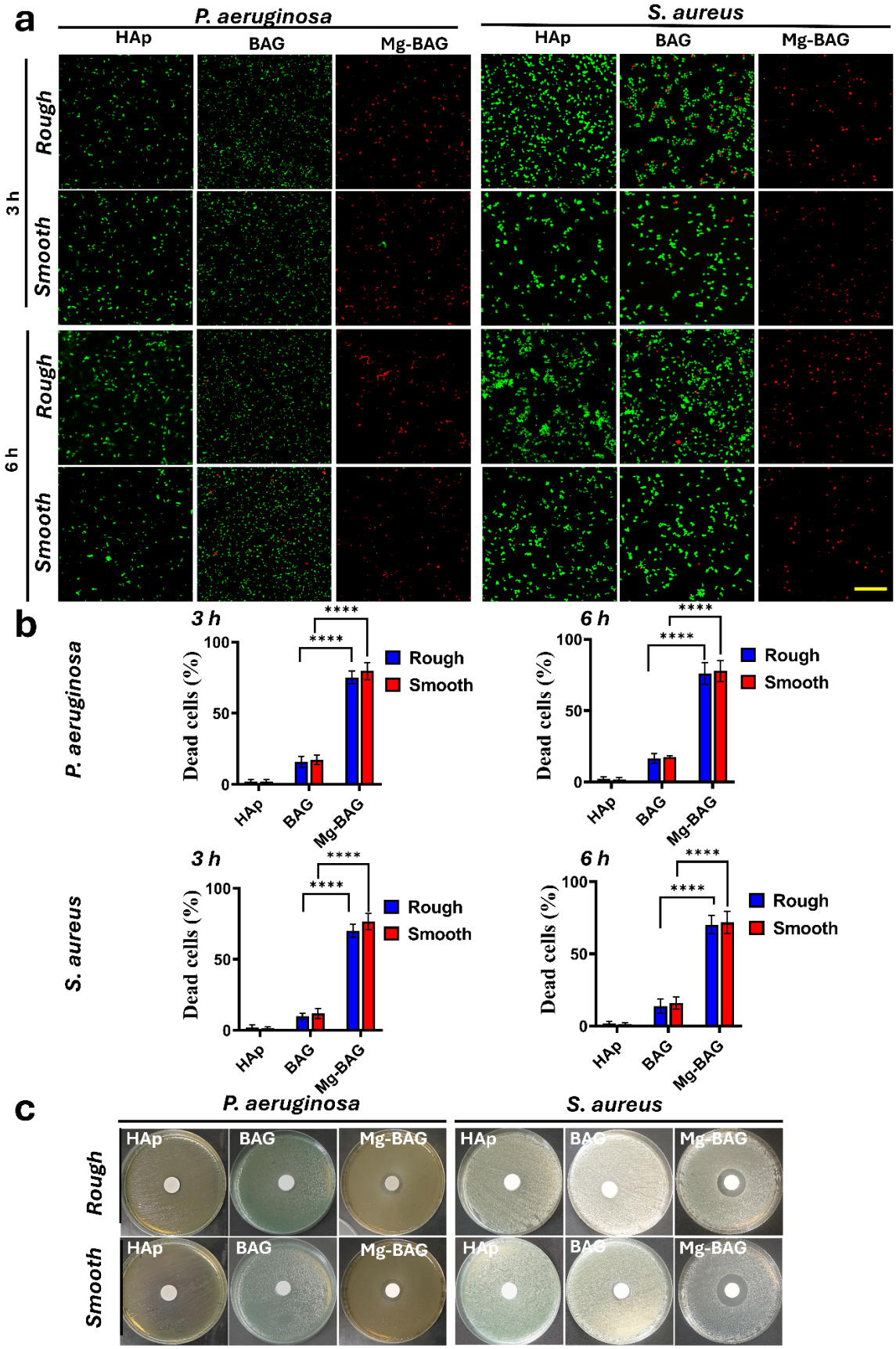
a
P. aeruginosa
S. aureus
HAp
BAG
Mg-BAG
3 h
6 h
Rough
Smooth
b
P. aeruginosa
S. aureus
3 h
6 h
Dead cells (%)
Rough
Smooth
****
c
P. aeruginosa
S. aureus
Rough
Smooth
HAp
BAG
Mg-BAG

Figure 4. Evaluating the antibacterial efficacy of HAp, BAG and Mg-BAG, *against P. aeruginosa* and *S. aureus*. a) Live/Dead fluorescence micrographs depicting *P. aeruginosa* and *S. aureus* incubated on HAp, BAG, and Mg-BAG surfaces for 3 or 6 hours, providing visual evidence of antibacterial activity. Green and red fluorescent spots represent live and dead bacteria, respectively. The scale bar represents 20 μm. b) Quantitative analysis of bacterial cell viability derived from fluorescence micrographs, illustrating the comparative effectiveness of the samples. c) Zone of inhibition assay underscoring the antibacterial properties of Mg-BAG. n = 3 ± SD, **** $p < 0.0001$.

The period right after bacteria attach is crucial, in determining if an infection will occur [285]. This early-stage action is critical in clinical scenarios where rapid infection prevention is required for successful implant integration [286]. The ions released from Mg-BAG interact with and disrupt processes within bacteria leading to damage and ultimately bacterial death. Bacteria cell surfaces are negatively charged due to components like the peptidoglycan layer, lipopolysaccharides and phosphate groups in the cell envelope. This charge facilitates the binding of metal ions [287, 288]. Research on how ions are released from Mg-BAG samples shows that Mg^{2+} are released from the surfaces of the doped glass, contributing to their combined antibacterial effect.

Our previous research has shown that Mg-BAG is highly biocompatible and bioactive [22]. This combination of properties, along with antibacterial effectiveness, makes Mg-BAG bioceramics promising for use in applications. Additionally, their antibacterial properties could be especially beneficial for patients or situations with a risk of infection.

3.2.3. Study antibacterial mechanisms of Mg-BAG

Previous studies have demonstrated that Mg^{2+} can be used for antibacterial properties because it enhances the production of ROS, disrupts bacterial metabolic processes by engaging with the negatively charged components of the bacterial cell wall and membrane and creates an alkaline environment that hinders bacterial growth [17-19]. To investigate the ion release rate from Mg-

BAG, we employed inductively coupled plasma mass spectrometry (ICP-MS) to quantify the ion concentrations for 3, 6 and 24 hours, as shown in Figure 3.4b. Interestingly, no significant differences were observed in ion release rate across surfaces. We observed Mg^{2+} concentration of 7.8 ppb/mm^3 after 3 h, increasing to 10 ppb/mm^3 at 6 h and then 11 ppb/mm^3 at 24 h for Mg-BAG samples.

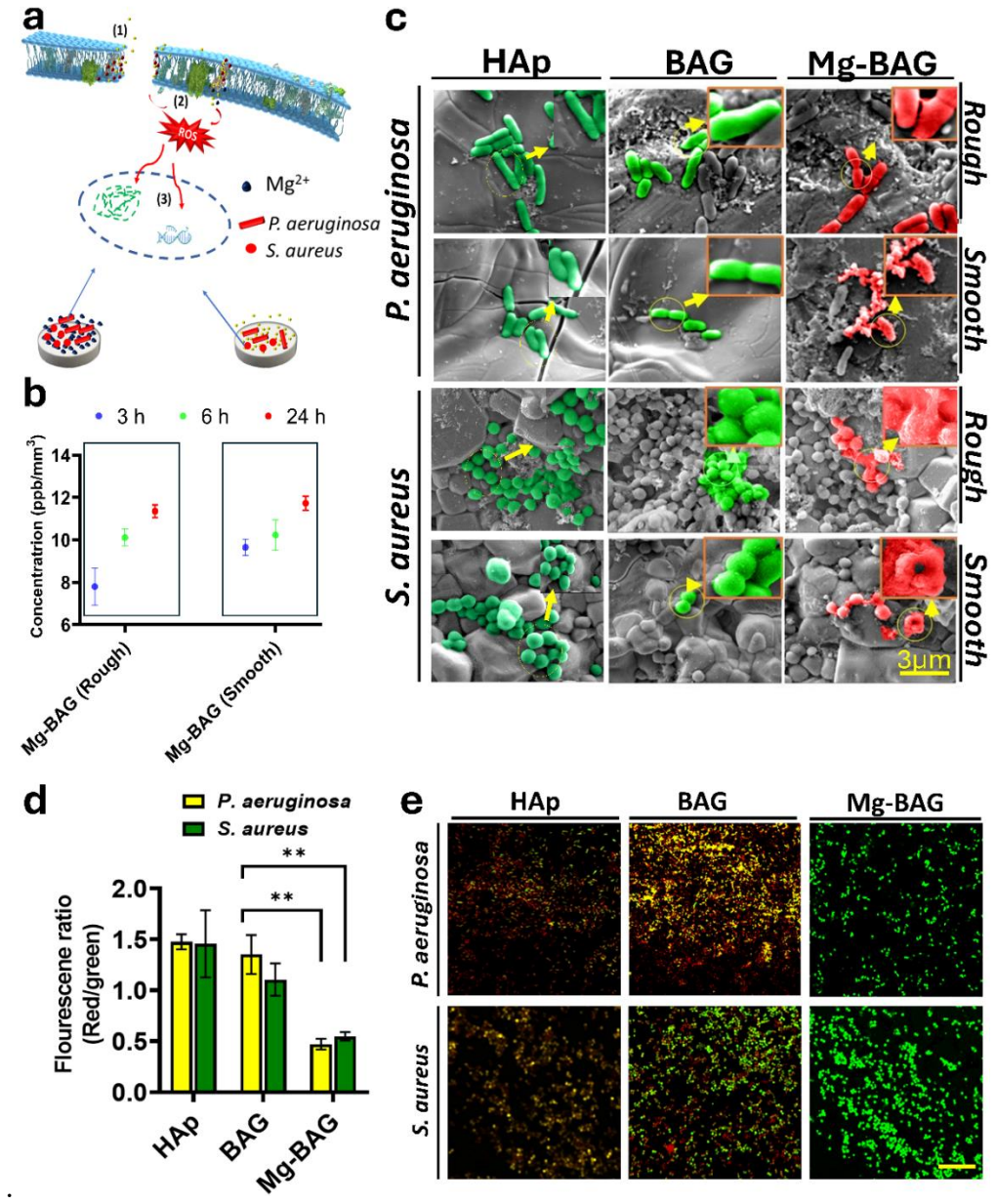

Figure 3.4. The multifaceted antibacterial mechanisms of Mg-BAG bioceramics. a) Schematic representation of multi-target mechanisms of antibacterial action of Mg-BAG. b)

Quantification of Mg^{2+} release from rough and smooth surfaces of Mg-BAG over time. c) SEM images illustrate these altered morphologies of bacteria exposed to Mg-BAG, including wrinkled, uneven, and irregular shapes and swollen cells exhibiting signs of damage. d) Membrane potential of *P. aeruginosa* and *S. aureus*. E) CLSM micrographs of *P. aeruginosa* and *S. aureus* on doped bioceramics. Green fluorescence indicates a high degree of membrane polarisation. The scale bar represents 20 µm. n = 3 ± SD, ** $p< 0.01$.

The study of the shapes of *S. aureus* and *P. aeruginosa* on modified bioceramics was conducted using microscopy (SEM) as shown in Figure 3.4c. Both bacterial strains showed changes in appearance on the smooth and rough surfaces of Mg-BAG. Specifically, the bacteria exhibited wrinkled, uneven, and irregular shapes when interacting with Mg-BAG. These alterations seemed to result in Mg^{2+} ions interacting with the negatively charged bacterial cell wall and membrane components, compromising their integrity and function. In contrast, bacteria exposed to HAp and BAG retained their original shapes, maintained their surface and preserved their membrane structure.

To assess the mechanism behind the antibacterial effectiveness of Mg-BAG we examined the membrane potential of both bacteria after exposure to HAp, BAG and Mg BAG surfaces. This was done using the *Bac*Light™ bacterial membrane potential kit. Ion pumps like the Na/K ATPase pump and the proton pumps (H^+-ATPase) in bacteria are essential for maintaining the gradient across the cell membrane [289]. This gradient is crucial for functions such, as ATP production and nutrient absorption and contributes to a high membrane potential. Mg^{2+} can interfere, with the function of ion pumps by disrupting their normal operation. Mg^{2+} competes with ions like calcium ions (Ca^{2+}) and potassium ions (K^+) at binding sites in ATP-dependent pumps such as Na^+/K^+ ATPase. When Mg^{2+} binds to channels or pumps, it can change the shapes of these transport proteins reducing their effectiveness in maintaining ion gradients. Specifically, Mg^{2+} inhibits pumps that create proton gradients necessary for ATP production and energy generation.

Bacterial cells with functioning ion pumps preserve a membrane potential, indicated by a red fluorescence signal from the accumulation of the $DiOC_2(3)$ dye in polarised cells. Conversely, when ion pumps are compromised by Mg^{2+} there is a membrane depolarisation, leading to a shift towards green fluorescence observed in cells exposed to Mg-BAG surfaces (Figures 3.4d and 3.4e). This shift signifies disrupted ion homeostasis further illustrating how Mg^{2+} impairs the integrity and function of bacterial membranes [290]. Thus, green fluorescence signifies bacteria with membranes, while red fluorescence indicates a membrane potential commonly observed in healthy, energised cells. Our results demonstrate depolarisation in bacteria exposed to Mg-BAG bioceramic, suggesting a disruption in membrane integrity. An analysis of bacterial samples adhering to BAG showed a red-to-green fluorescence ratio of approximately 1.4. In contrast, on the Mg-BAG, the ratio decreased to around 0.5, indicating a compromised membrane potential due to disrupted ion pumps.

In the presence of ROS, the compound 2′− 7′- dichlorodihydrofluorescein diacetate (DCFH-DA) undergoes oxidation into a highly fluorescent form known as 2′,7′-dichlorofluorescein (DCFH). This transformation enables the measurement of levels of ROS as illustrated in Figure 3.5a. ROS are normally generated when Mg^{2+} interact with cellular components to initiate redox reactions, leading to the formation of ROS-like superoxide anions (O_2^-), hydroxyl radicals (OH•) and hydrogen peroxide (H_2O_2) [291]. Our research findings indicated very low level ROS detected within *P. aeruginosa* and *S. aureus* cells growing on BAG surfaces (See Figures 3.5b and 3.5c). Remarkably, exposure to Mg-BAG surfaces resulted in a marked 3-4-fold elevation of ROS production in both bacterial species, regardless of the roughness of the surface. This indicates that releasing Mg^{2+} ions from Mg-BAG surfaces induces ROS and Mg^{2+} can indirectly generate ROS through a redox reaction [292-294]. In the context of Mg^{2+}, cellular enzymes, including NADPH oxidase, are activated and capable of accepting electrons to molecular oxygen (O_2), leading to superoxide anion (O_2^-) generation. The Fenton reaction

can also occur with the involvement of Mg^{2+}, in which hydrogen peroxide converts into highly reactive hydroxyl radicals [295]. These ROS can deliver oxidative stress to the bacterial cell, damaging lipids, proteins, and DNA, causing homeostasis dysregulation. It may cause leakage of cellular content and disequilibrium in ion gradients, inducing cell death. Therefore, the interaction between Mg^{2+} release, membrane disruption and ROS generation remarkably increases the antibacterial activity of these Mg-BAG surfaces, which strongly supports their applications as potent infective bacteria-controlling biomaterials.

The localised alteration in pH occurs due to the release of Mg^{2+} ions from the material. When magnesium interacts with the environment, magnesium hydroxide is produced ($Mg(OH)_2$) [296]. This process enhances the levels of alkalinity, leading to antibacterial properties [297]. Our research into properties uncovered a notable increase in pH levels in a solution containing Mg-BAG as shown in Figure 3.5.S4. This alkaline environment, created by releasing ions during the degradation of Mg-BAG, boosts the activity by disrupting their cellular functions that thrive in acidic conditions. The combined impact of the pH, Mg^{2+} release and ROS formation significantly improves the antibacterial potency of Mg-BAG.

As membrane depolarisation can lead to loss of cell contents, we investigated the leakage of nucleic acids and proteins into the supernatant following incubation on Mg-BAg (Figure 3.6). The results show a significant increase in nucleic acids and proteins in the culture medium from bacteria exposed to Mg-BAG, compared to those on HAp and BAG. These findings highlight the significant impact of Mg-BAG surfaces on releasing nucleic acids and proteins from bacterial cells, indicating a disruption of cell envelope integrity. Interestingly, the actions of Mg-BAG are very similar to those of quaternary ammonium compounds (QACs), also cationic compounds that kill bacteria by interfering with the cell envelope and causing leakage of cell contents [298].

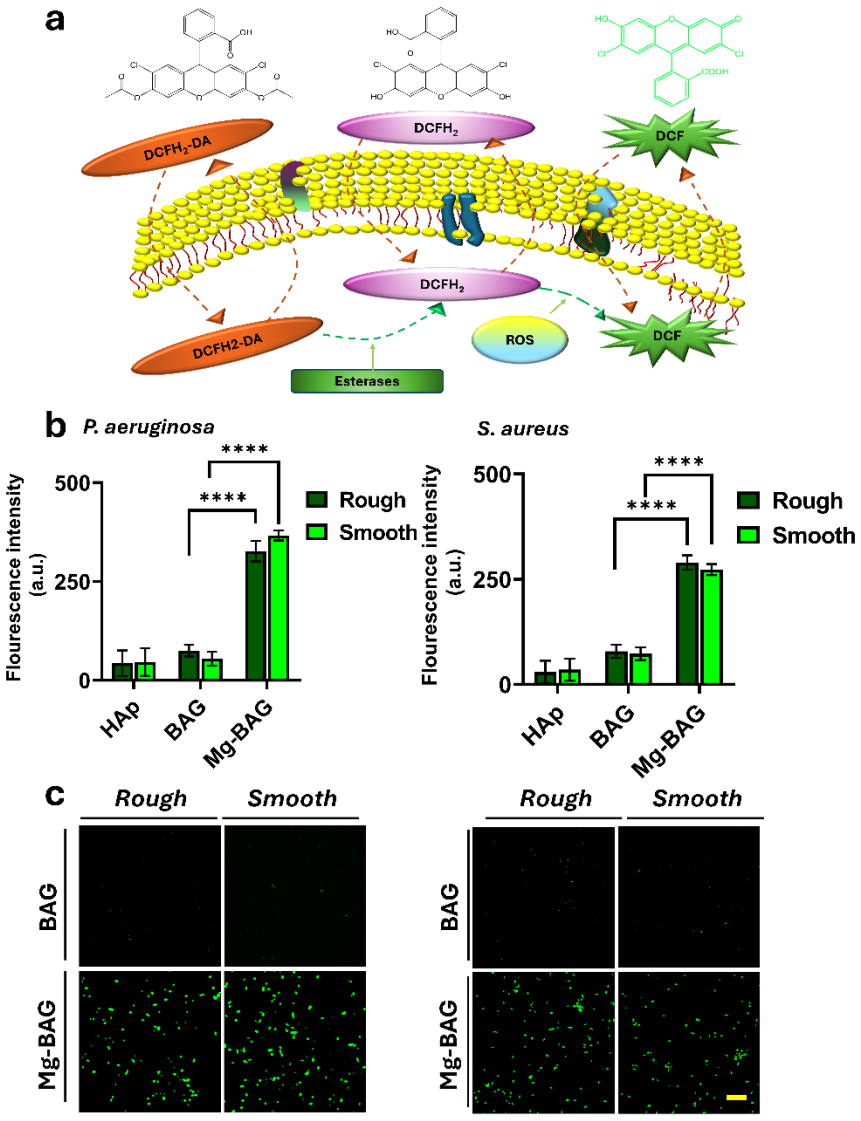

Figure 3.5. Intracellular ROS formation in *P. aeruginosa* and *S. aureus*. a) A schematic illustrating how the ROS detection assay works. The probe DCFH-DA enters the cells where intracellular esterases convert it into $DCFH_2$ which stays inside the cell. When it interacts with ROS, $DCFH_2$ is transformed into the fluorescent DCF allowing for the detection of ROS. b) Fluorescence measurements from CLSM images show the ROS produced in *P. aeruginosa* and *S. aureus*. Mg-BAG surfaces induce higher levels of ROS compared to HAp and BAG surfaces. The increase in ROS is likely due to the release of Mg^{2+} ions from the Mg-BAG stimulating reactions in the cells and causing stress. This ROS formation indicates oxidative damage in the bacterial cells. c) CLSM images of *P. aeruginosa* and *S. aureus* on the surface. Green fluorescence indicates the presence of ROS. The scale bar represents 30 µm. N = 3 ± SD, **** $p < 0.0001$.

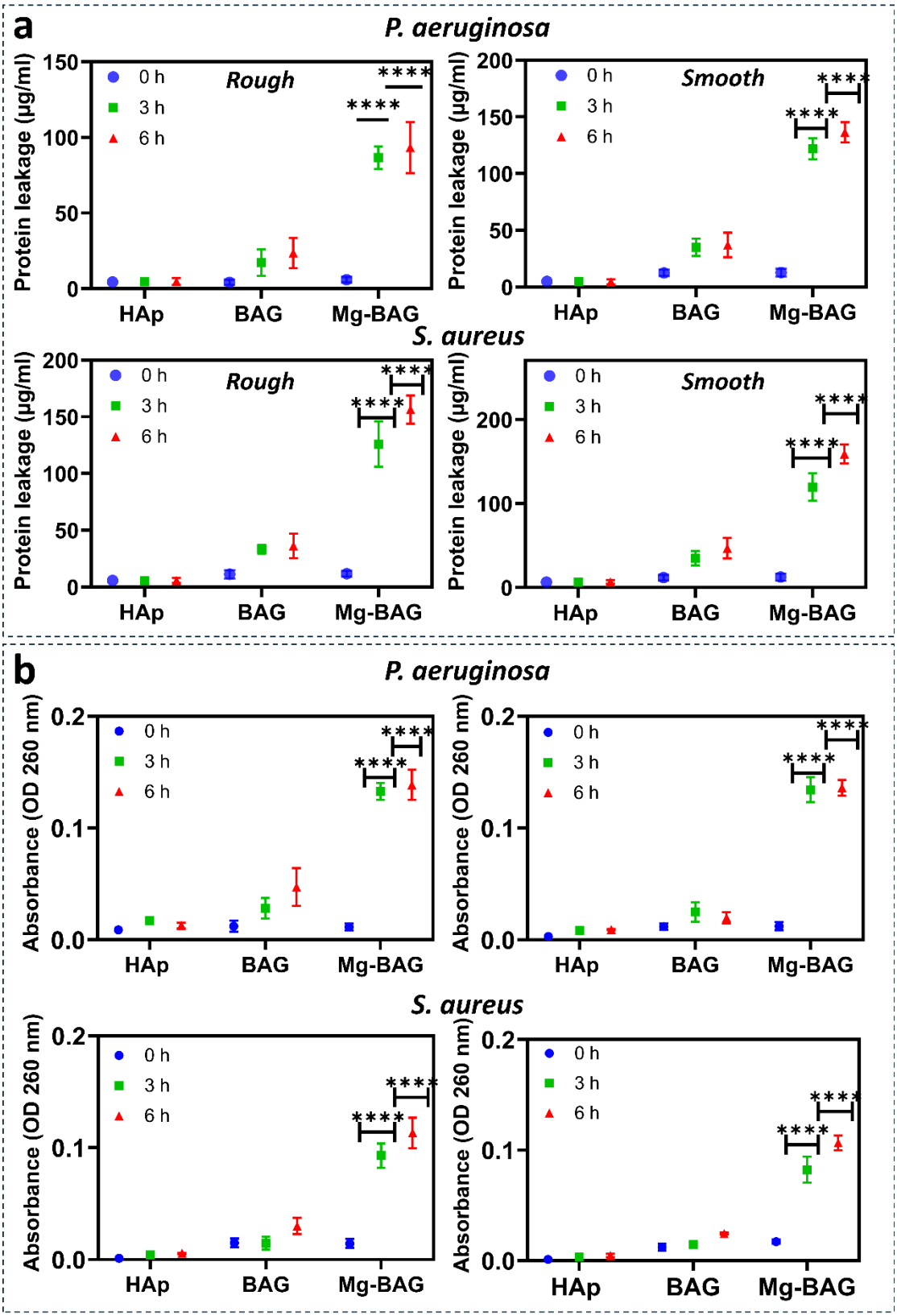

Figure 3.6. Quantitative assessment of the leakage of intracellular components from bacterial cells following incubation on Mg-BAG. a) Measurement of protein leakage from *P. aeruginosa*

and *S. aureus* cells, reflecting the impact of these Mg-BAG on cellular membrane permeability and potential disruption of vital cellular processes. b) Evaluation of nucleic acid release from *P. aeruginosa* and *S. aureus* cells, indicating the extent of cellular membrane damage and the potential for compromised cellular integrity.

3.2.4 Variation in lipids, proteins, and nucleic acids profiles observed using synchrotron ATR-FTIR microspectroscopy

The potential enhancement of antibacterial activity by Mg-BAG may be due to a cooperative or synergistic effect arising from releasing metal ions during their contact with the microorganisms. Previous studies show that metal ions play a crucial role in the creation and breakdown of key macromolecules, including carbohydrates, lipids, proteins, and nucleic acids [299, 300]. Herein, we use Synchrotron-sourced macro attenuated total reflectance Fourier-transform infrared (ATR-FTIR) microspectroscopy to elucidate the mechanisms behind the biomolecule changes induced by our Mg-BAG within bacterial cells (Figures 3.7a and 3.8a) [301-303]. By analysing three spectral regions containing crucial biomolecular information, including the ν(C-H) stretching modes representing lipid composition (3000-2850 cm^{-1}), the amide I and II bands representing proteins (1700-1450 cm^{-1}), and the vibrational modes related to nucleic acids and polysaccharides (1150-1000 cm^{-1}). This approach provided valuable insights into the structural modifications induced by the Mg-BAG on bacterial cells.

The resulting heat maps displayed variations in intensity within these spectral regions (Figures 3.7b and 3.8b). Despite the normalisation of the maps, a noticeable decrease in intensity was observed in the C-H, amide II, and nucleic acid regions after exposure to Mg-BAG. Additionally, the score plots (Figures 3.7c and 3.8c) demonstrated distinct differences between the *P. aeruginosa* and *S. aureus* groups on BAG and Mg-BAG surfaces. We performed principal component analysis (PCA) to compare bacteria on undoped BAG and Mg-BAG surfaces (Figures 3.7d and 3.8d). The PCA score for the principal components, namely PC1, PC2, and

PC3, would represent the linear combination of variables that best distinguishes between the two groups. PC1 explains that most of the difference between the groups accounted for 95% of the difference between BAG and Mg-BAG. Similarly, for *S. aureus*, PC-1 accounted for 97% between BAG and Mg-BAG. This plot enabled the identification of absorption peaks representing noteworthy biomolecular differences, and the corresponding biomolecular compounds are summarised in Table 3.1. Within the lipid region, changes to the methyl/methylene groups of the phospholipids within the cell membrane were observed, as evidenced by the peaks at 2925 and 2852 cm^{-1}. Most of the peaks in the PC-1 loadings were located in the amide bands, as indicated by the bands at 1954, 1637, 1514, 1452 and 1400 cm^{-1}. Changes in the 1236 and 1082 cm^{-1} bands demonstrated variations within the nucleic acid regions. These spectral changes suggest that biological damage has occurred at the molecular level. This damage can be attributed to various factors, including oxidative stress and exposure to surface interactions with antibacterial agents. The observed biomolecular changes align with the effects of ion release, ROS formation and membrane depolarisation.

The lipid content, particularly phospholipids which are a dominant component of the bacterial membrane, is crucial for the structural integrity and function of the cell [304, 305]. These phospholipids can interact with metal cations with their reactive phosphoryl groups adjacent to carboxyl groups of unaltered lipids [306]. In addition, metal ions trigger the oxidation of susceptible amino acids, thereby reducing protein stability, impairing function, and marking them for degradation [184]. Changes in the spectra associated with protein peaks also make sense, considering the actions of oxidative stress upon cellular proteins. Proteins affected by oxidative stress can be unfolded, leaving them functionally inactive. This effect has repercussions for virtually all cellular metabolic processes, evidenced by the high rate of bacterial cell death. For example, the loss of membrane potential can be regarded as a direct repercussion of oxidative stress generated by the metal ions leached from Mg-BAG.

Furthermore, various metal ions have been known to enhance ROS levels, which leads to nucleic acid damage [184, 307]. Our study represents the first account of how Mg-BAG can cause changes in the lipids of *P. aeruginosa* and *S. aureus*, disrupt protein synthesis or stability, and interfere with the genetic material of the bacteria.

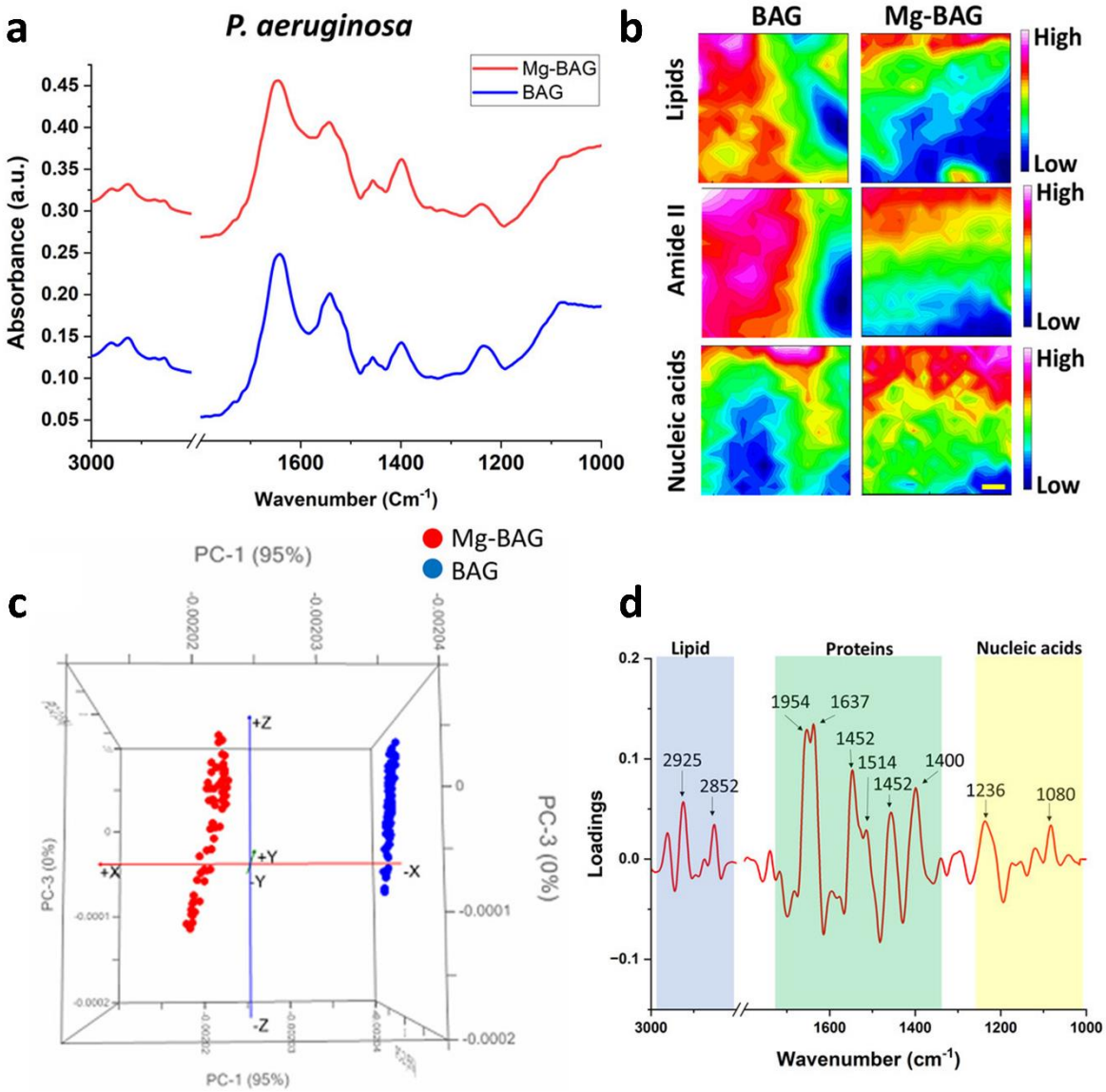

Figure 3.7. Synchrotron-sourced macro-ATR-FTIR microscopy data identified biomolecular changes in *P. aeruginosa* after exposure to Mg-BAG. a) The average spectra from HCA. b) Synchrotron macro-ATR-FTIR maps. Scale bar present 5µm. c) The comparative principal component analysis (PCA) 3D score plots. d) PCA loading spectra for PC1.

Table 3.1. Summary of key wavenumbers for functional groups identified in the loading plots of *P. aeruginosa* and *S. aureus.*

Bacterial cell	Wavenumber (cm^{-1})	Assignment	Ref.
P. aeruginosa and s. aureus	~2925	ν_{as}(C–H) from methylene (–CH_2) groups of lipids	[308, 309]
	~2852	ν_{s}(C–H) from methylene (–CH_2) groups of lipids	[308-310]
	~1654	Amide I: α-helix	[308, 309]
	~1637	Amide I: antiparallel β-sheet	[311, 312]
	~1452 ~1514	C–H stretching of CH_2 and CH_3 groups in cellular proteins, nucleic acids and lipids	[308, 309]
	~1452	δ_{as}(CH3) of proteins (possibly in DNA and RNA)	[308, 309]

~1400	$\nu_s(COO^-)$ associated with $\delta s(CH_3)$ of proteins	[308, 309]
~1236	$\nu_{as}(PO^{2-})$ of DNA	[313, 314]
~1080	$\nu_s(PO^{2-})$ of the phosphodiester backbone of nucleic acids (DNA and RNA) and phospholipids	[308, 309]

Our Mg-BAG bioceramics exhibit antibacterial activity due to the release of Mg^{2+}, which disrupts bacterial cell membranes, impairing ion homeostasis and leading to increased intracellular ROS production, ultimately causing bacterial cell death. Unlike other metal-doped biomaterials, Mg-BAG avoids cytotoxicity ensuring excellent biocompatibility [22]. Therefore, Mg-Bag balances human osteoblast cells (HOBs) and antibacterial activity. They can also enhance the viability of MG63 cells (Figure 3.5.S5). That indicates no adverse effects on cell viability. This dual functionality makes Mg-BAG particularly advantageous in bone tissue engineering, where it can act as both a preventing infection agent and a regenerative scaffold.

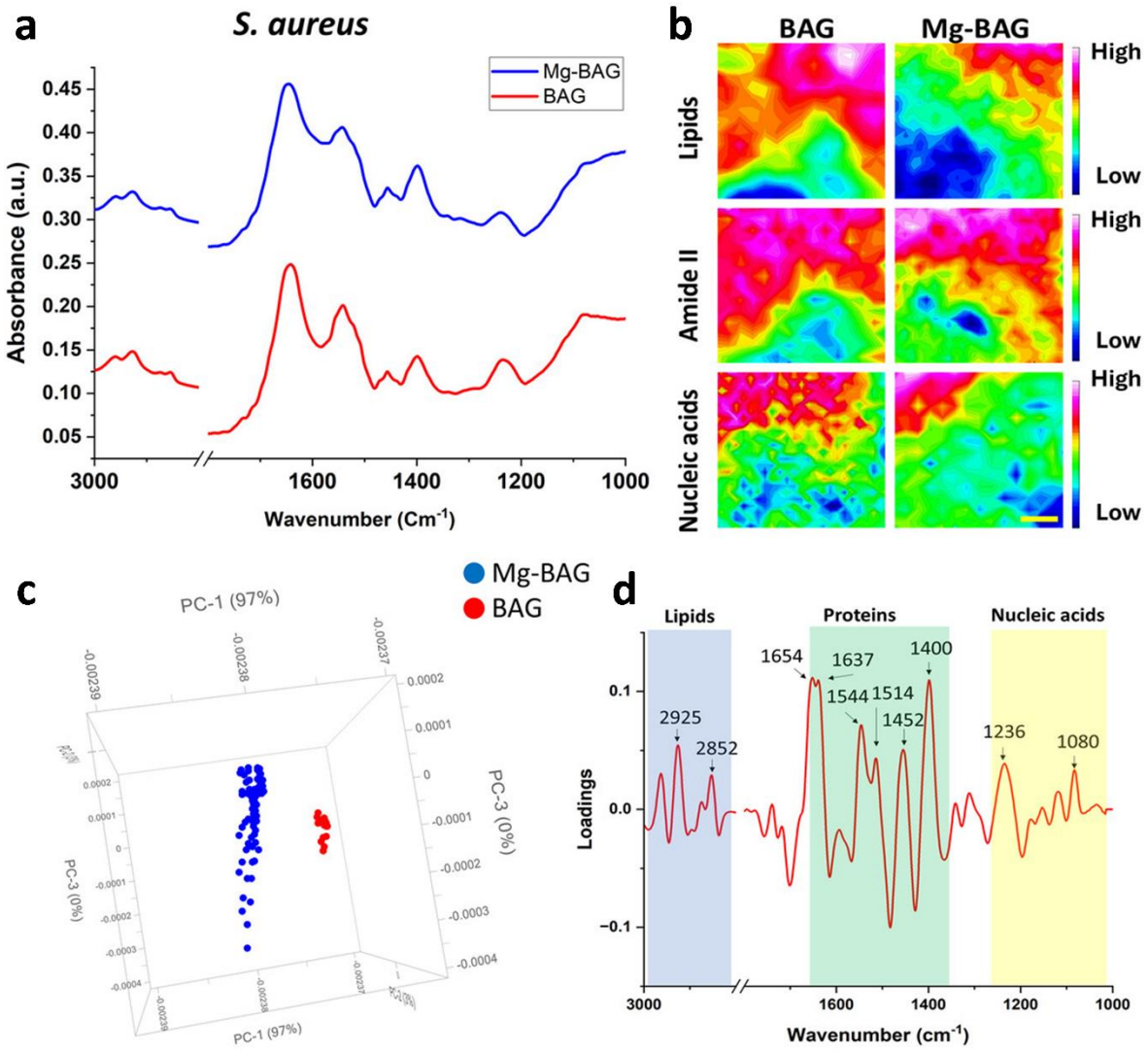

Figure 3.8. Synchrotron-sourced macro-ATR-FTIR microscopy data identified biomolecular changes in *S. aureus* after exposure to Mg-BAG. a) The average spectra from HCA. b) Synchrotron macro-ATR-FTIR. Scale bar present 5µm. c) The comparative principal component analysis (PCA) 3D score plots. d) PCA loading spectra for PC1.

These findings suggest that Mg-BAG is a promising multifunctional implant technology that can enhance the success rate of bone regeneration therapies by simultaneously promoting tissue integration and preventing infections. Balancing antibacterial activity with bone regenerative properties opens new avenues for designing Mg-BAG-coated implants or scaffolds that could significantly reduce infection risks and improve patient outcomes.

3.3 CONCLUSION

In this study, we have successfully engineered the baghdadite by doping it with Mg^{2+} to impart antibacterial properties to the material. Our finding demonstrates the synergistic and broad-spectrum antibacterial activity of Mg-BAG against both clinically relevant pathogens Gram-negative *P. aeruginosa* and Gram-positive *S. aureus*. We have elucidated the multifaceted antibacterial mechanisms by analysing cell morphology, ROS formation, membrane potential, leakage of cell contents and biomolecular changes. This study represents a breakthrough in our understanding of Mg-BAG, highlighting their potential as next-generation multifunctional bioceramics for bone regeneration applications. However, the lack of pre-conditioning to simulate protein adsorption at the implant surface is a limitation; future studies will include *in vivo* models and a broader panel of clinically relevant bacteria to fully assess Bi-BAG's translational potential

3.4 EXPERIMENTAL SECTION

Fabrication and Characterizations of Mg-BAG: HAp*,* BAG, and Mg-BAG discs were prepared following steps presented in a previous study using a solid-state synthesis route [22, 23]. The powders were mixed for 1 h at 100 rpm for BAG and 5h at 200 rpm for Mg-BAG using a planetary ball mill (PM400 Retsch, Germany). After homogenisation, the obtained mixture was calcined in an electric furnace (RHF, Carbolite UK) at 1300ºC of Mg-BAG for 1350 °C of BAG. For the preparation of the discs, the calcined powders were ground in the planetary ball mill for 3 h at 150 rpm, then uniaxially pressed at 30 MPa to obtain disc-shaped green bodies. These were then sintered in an electric furnace (RHF, Carbolite UK) at 1300ºC of Mg-BAG and 1350 °C of BAG to obtain disc samples. Surface topography evaluation was conducted using optical 3D profilometry. The average roughness (R_a) was used in this study. The

elemental distribution diagrams were obtained through energy dispersive XPS (A Thermo Scientific K-alpha and analysed with CasaXPS software).

Cultures and conditions: HAp, BAG, and Mg-BAG were tested for antibacterial activity against two bacterial strains: *P. aeruginosa* (ATCC 15692) and *S. aureus* (ATCC 25923). Bacterial strains were recovered from glycerol stocks stored at -80°C and streaked for purity on tryptone soy agar (TSA). One isolated colony of each species was transferred aseptically from TSA to 5 mL of tryptone soy broth (TSB) and cultured at 37 °C until the late log phase (approximately 6-8 h). Baghdadite and doped baghdadite samples were aseptically placed in sterile 24-well plates and immersed in 0.5mL of the 10^5 CFU/mL bacterial suspensions, then incubated for 3 or 6 h.

Live/Dead® BacLight™ viability assay: CLSM was used to visualise and quantify the proportions of live and dead cells using the LIVE/DEAD® BacLight Bacterial Viability Kit (Molecular Probes, Invitrogen, USA), which contains SYTO9 and propidium iodide fluorescent dyes. SYTO9 enters all cells, binding to nucleic acids and fluorescing green. Propidium iodide (PI) only enters cells with disrupted membranes and has a stronger affinity for nucleic acids than SYTO9. PI fluoresces red and indicates dead or viable cells [315]. SYTO9 and PI were prepared in equal proportions at 1.5 µL/mL in phosphate-buffered saline (PBS), and 1 mL of the solution was used to immerse each sample for 15 minutes in the dark at room temperature. After staining, samples were imaged with a Zeiss_LSM880 (Zeiss, Oberkochen, Germany) CLSM. Using a dual emission filter, the CLSM was set up to image both live cells in green (Syto9, Ex/Em 480/500 nm) and dead cells in red (PI, Ex/Em 490/635 nm).

Colony enumeration: The colony forming unit (CFU) determination and log reduction data were performed. Following incubation, sample discs were vortexed in PBS for 15 seconds,

then sonicated for 5 minutes before being vortexed for another 15 seconds and serially (1:10) diluted. In triplicate, serially diluted samples (10 µL) were dropped onto TSA plates and incubated for 18 hours at 37 °C. Viability assays were performed by standard plate counts, and the quantity of CFU per sample was calculated using the number of colonies counted, the aliquot size and the dilution factor. A log reduction value was calculated for the 2 sample types (BAG, Mg-BAG) compared to a HAp control.

Zone of Inhibition: Bacterial lawn plates were prepared by transferring 100 µL aliquots of bacterial cell suspension (at $1x10^5$ CFU/mL) onto a TSA plate and then evenly spreading it across the surface. Untreated and doped baghdadite discs were aseptically placed in defined quadrants of the plate and left to incubate overnight at 37 °C. The following day, the inhibition zones were measured by recording the radius from the centre of the disc to the perimeter of the clear zone of inhibition.

SEM characterisation of bacterial morphology on the surface: SEM was used to observe the morphological changes according to previous studies [316]. Disc samples were cultured with bacteria (approx. 1 x 10^5 cfu/ml) and incubated in TSB medium at 37ºC for 3 h and 6 h. After incubation, all discs were washed twice with PBS (pH 7.4) to remove unattached cells. The bacterial cells were fixed in 4% glutaraldehyde for 1 h at room temperature. The samples were dehydrated in sequential graded ethanol (30%, 50%, 70%, 90%, 100%). Finally, all samples were coated with 2nm platinum. Samples were then observed in a FEI Inspect F50 (FEI Company, Oregon, USA) at 5kV with a working distance of 5 mm.

Ions release analysis: To assess the release of Mg ions from the Mg-BAG samples, we immersed the samples in 0.5 mL of TSB media at 37°C for 3 and 6 hours. After incubation, the supernatants were collected and centrifuged to remove debris or particles. The supernatants were then treated with HNO_3 to dissolve any remaining solids and diluted to a concentration

of less than 5% to avoid matrix effects during ICP-MS analysis. The concentration of Mg^{2+} in the supernatants was measured using ICP-MS with a Varian 720-ES system from the United States. Standard solutions of known concentrations were prepared to calibrate the instrument before the analysis. The concentration of Mg ions in the samples was determined using the standard curve generated from the standards.

The ROS level determination: To investigate the ROS levels in target bacteria, we used an intercellular ROS formation assessed using a DCFDA/H2DCFDA- Cellular ROS Assay Kit (ab113851, Abcam, USA). Following incubation with HAp, BAG and Mg-BAG samples, bacteria were incubated with DCFH-DA (50 µM) in the dark for 30 minutes according to the manufacturer's instructions. The samples were then immediately imaged with a Zeiss_LSM880 CLSM using Ex/Em of 485/535 nm. Images were taken at three random locations per sample. The fluorescence intensity of each image was then determined using ImageJ v1.53a (NIH, Maryland, USA). The ROS level was calculated based on the fluorescence intensity of the DCF, which is converted to a highly fluorescent compound by ROS. Higher fluorescence intensity indicates higher ROS levels in the bacterial cells.

Determination of cell membrane potentials: Following incubation, the membrane potential of bacterial cells was measured using the BacLight Bacterial Membrane Potential Kit (Invitrogen, ThermoFisher, Massachusetts, USA). The staining procedure was carried out according to the instructions of the manufacturer. The samples were immediately imaged using a Zeiss_LSM880 CLSM, Ex/Em 482/497 nm. 3 micrographs were taken randomly, and the images were imported into ImageJ v1.53a. Fluorescence intensity was measured in the green and red channels, and a red-to-green ratio was calculated using the acquired intensities.

Leakage of intracellular nucleic acids and proteins: Following incubation on the baghdadite and doped baghdadite samples for 3h and 6h, we measured the optical density of the

supernatant at 260nm to quantify the nucleic acid content. The BCA (bicinchoninic acid) assay is commonly used for measuring protein concentration. To use this assay, a standard curve is first generated using known concentrations of a protein standard, such as bovine serum albumin (BSA). Protein samples and the BCA working reagent are added to a 96-well microplate. After incubating the plate for a specific amount of time at $37^{O}C$, the absorbance of each well is measured at a specific wavelength using a microplate reader. The protein concentration in the sample is determined by comparing the absorbance of the sample to the standard curve. Using a microplate reader to measure the absorbance of the samples allows for quick and accurate determination of the protein concentration in each well of the plate.

Synchrotron macro-ATR-FTIR: To study the biochemical changes in bacterial cells exposed to BAG and Mg-BAG samples, we used synchrotron ATR-FTIR microspectroscopy at Australian Synchrotron. Bacterial cells were grown and treated according to the previous experimental design for 6 hours with the smooth group of BAG, Mg-BAG samples, after which they were collected and deposited onto the ATR crystal of the synchrotron microscope. ATR-FTIR spectra were then collected across the 3400-1000 cm^{-1} spectral range, allowing for the identification and quantification of various molecular vibrations and functional groups. The resulting spectra were then analysed using various chemometric methods, such as hierarchical clustering analysis (HCA), second derivative spectroscopy, and principal component analysis (PCA), to identify changes in the biochemical composition of the bacteria. HCA was used for quality control and to identify outlier spectra, while second-derivative spectroscopy enhanced the resolution of overlapping peaks. PCA was used to explore the treatment groups' clustering patterns and chemical composition differences.

Statistical analyses: Statistical significance was evaluated using one-way analysis of variance (ANOVA) with Tukey's multiple comparisons test. p-value < 0.05 was considered statistically

significant. All experiments were performed in triplicate and data are presented as mean and standard deviation (SD).

3.5 Supporting information

3.5.1 Experimental section

pH Measurement: Sterilized discs of HAp, BAG, and Mg-BAG were prepared and placed individually in 24-well plates. Each disc was immersed in 1 mL of TSB medium. The pH of the TSB medium was measured at three-time points: 0 hours (immediately after immersion), 3 hours, and 6 hours. At each time point, the TSB medium from each well was thoroughly mixed to ensure uniformity, and the pH was recorded using a Thermo Fisher Scientific pH meter calibrated with standard pH buffers (pH 4.0, 7.0, and 10.0) before each measurement. All measurements were performed in triplicate for each group. The average pH values and standard deviations were calculated for each time point and plotted to compare the pH changes over time.

MTT Assay for Cell Viability: Cell viability was evaluated at 1 and 3 days using the MTT assay. The culture medium was replaced with 200 µL of MTT reagent (0.5 mg/mL in serum-free medium), followed by incubation at 37°C for 4 hours. After the incubation period, the MTT solution was carefully removed, and the formazan crystals produced by metabolically active cells were dissolved in 200 µL of dimethyl sulfoxide (DMSO). The optical density (OD) of the dissolved formazan was measured at 570 nm using a microplate reader to quantify cell viability. Media without cells served as a negative control. Each experiment was performed in triplicate, and the results were reported as mean ± standard deviation (SD).

Confocal microscopy for cell morphology: Cell morphology and cytoskeletal organisation were visualised using CLSM. At the selected time points (1 and 3 days), cells were fixed with 4% paraformaldehyde for 20 minutes at room temperature. The discs were then permeabilised

with 0.1% Triton X-100 for 10 minutes. The actin cytoskeleton was stained using Alexa Fluor 488-phalloidin (Thermo Scientific) for 90 minutes, and nuclei were counterstained with DAPI (Thermo Scientific) for 10 minutes. After staining, the samples were washed thoroughly with phosphate-buffered saline (PBS) to remove excess dyes. Confocal microscopy imaging was performed using a laser scanning microscope equipped with the appropriate filters. Alexa Fluor 488-phalloidin was excited with a 488 nm laser, and emission was captured in the green fluorescence channel (approximately 500–550 nm). DAPI was excited with a 405 nm laser, and emission was captured in the blue fluorescence channel (approximately 450–490 nm). Images were acquired at a resolution sufficient to visualise the cytoskeletal and nuclear structures, and representative images were collected for each group.

3.5.2 Result

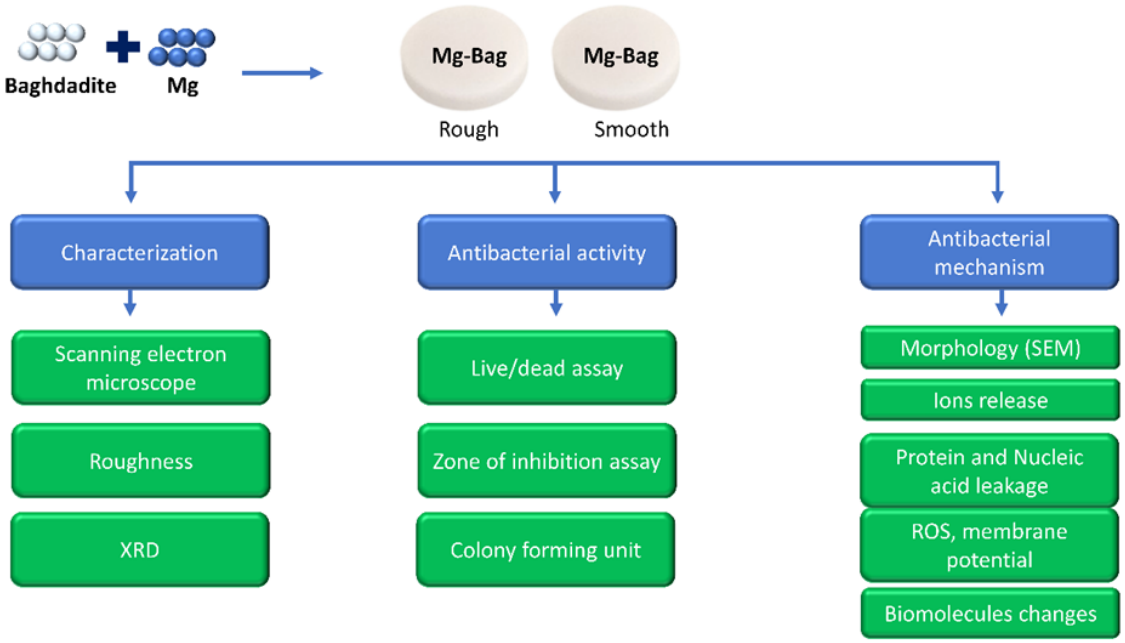

Figure 3.5.S1. Schematic diagram of the preparation and evaluation of the antibacterial activity of HAp, BAG and Mg-BAG.

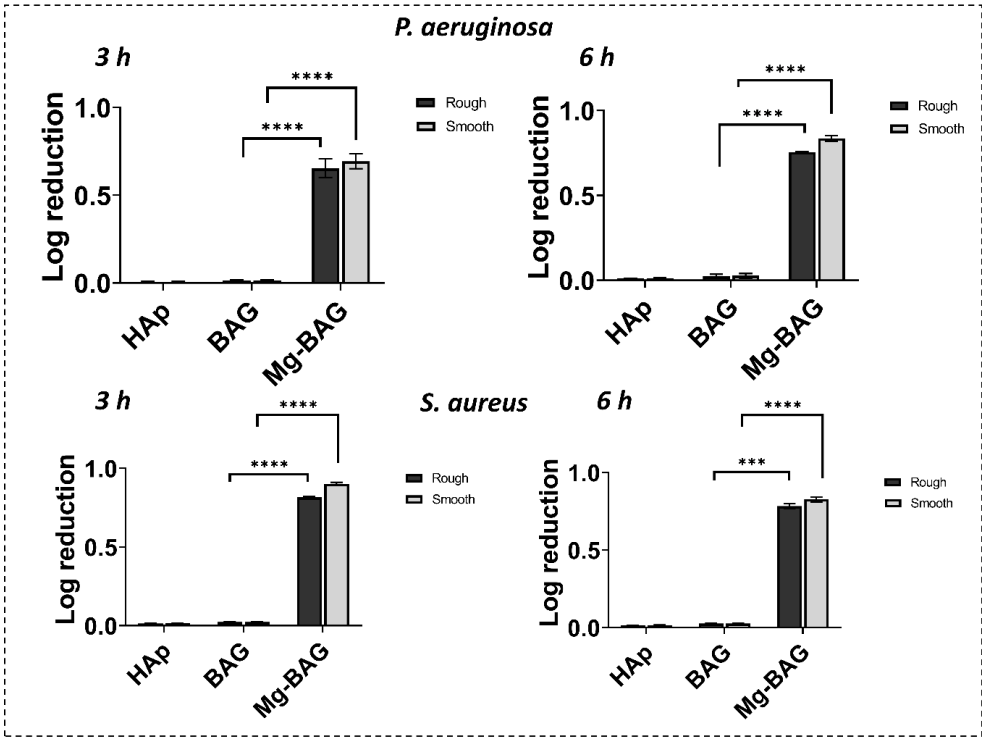

Figure 3.5.S2. Antibacterial efficacy of HAp, BAG, Mg-BAG against *P. aeruginosa* and *S. aureus*. Quantitative analysis of zone of inhibition assay. n = 3 ± SD, **** $p < 0.0001$.

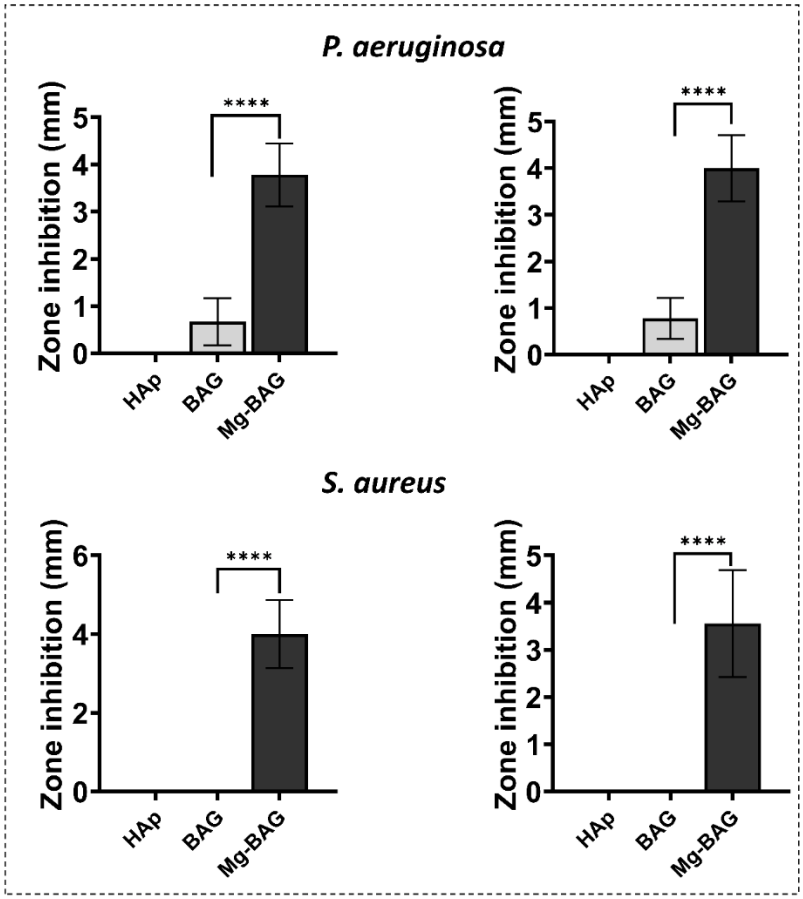

Figure 3.5.S3. Zone inhibition of HAp, BAG, Mg-BAG against *P. aeruginosa* and *S. aureus*. Quantitative analysis of zone of inhibition assay. n = 3 ± SD, **** $p < 0.0001$.

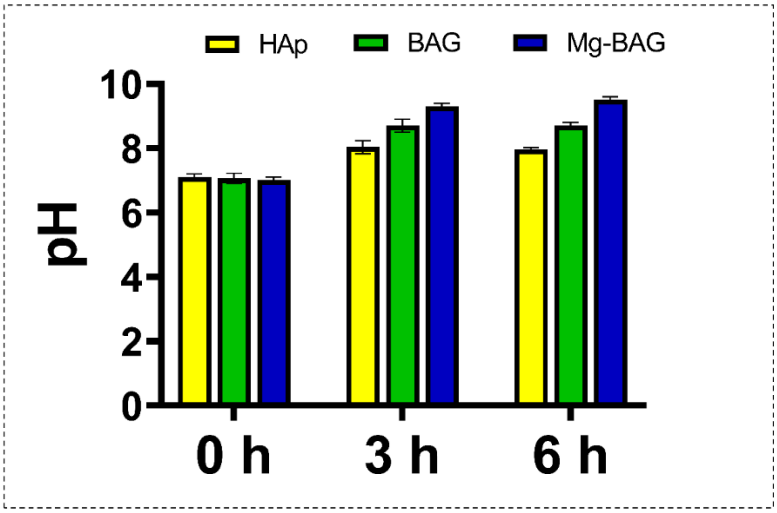

Figure 3.5.S4. pH variability over time for different bioceramics. The pH changes at 0, 3, and 6 hours for HAp, BAG and Mg-BAG.

Table 3.5.S1. Summary of the rough measurement (µm) of HAp, BAG, Mg-BAG

Rough surface	HA	1.264± 0.051
	BAG	1.932± 0.268
	Mg-BAG	1.640± 0.180
Smooth surface	HA	0.115± 0.002
	BAG	0.347± 0.017
	Mg-BAG	0.223± 0.010

Table 3.5.S2. Summary of zone inhibition (mm) of *P. aeruginosa* and *S. aureus* exposed to HA, BAG, Mg-BAG

Bacteria	Surface	HA	BAG	Mg-BAG
P. aeruginosa	*Rough*	ND	1.33 ± 0.57	4.00 ± 1.00
	Smooth	ND	1.66 ± 0.57	4.33 ± 1.15
S. aureus	*Rough*	ND	ND	3.33 ± 1.52
	Smooth	ND	ND	4.00 ± 1.73

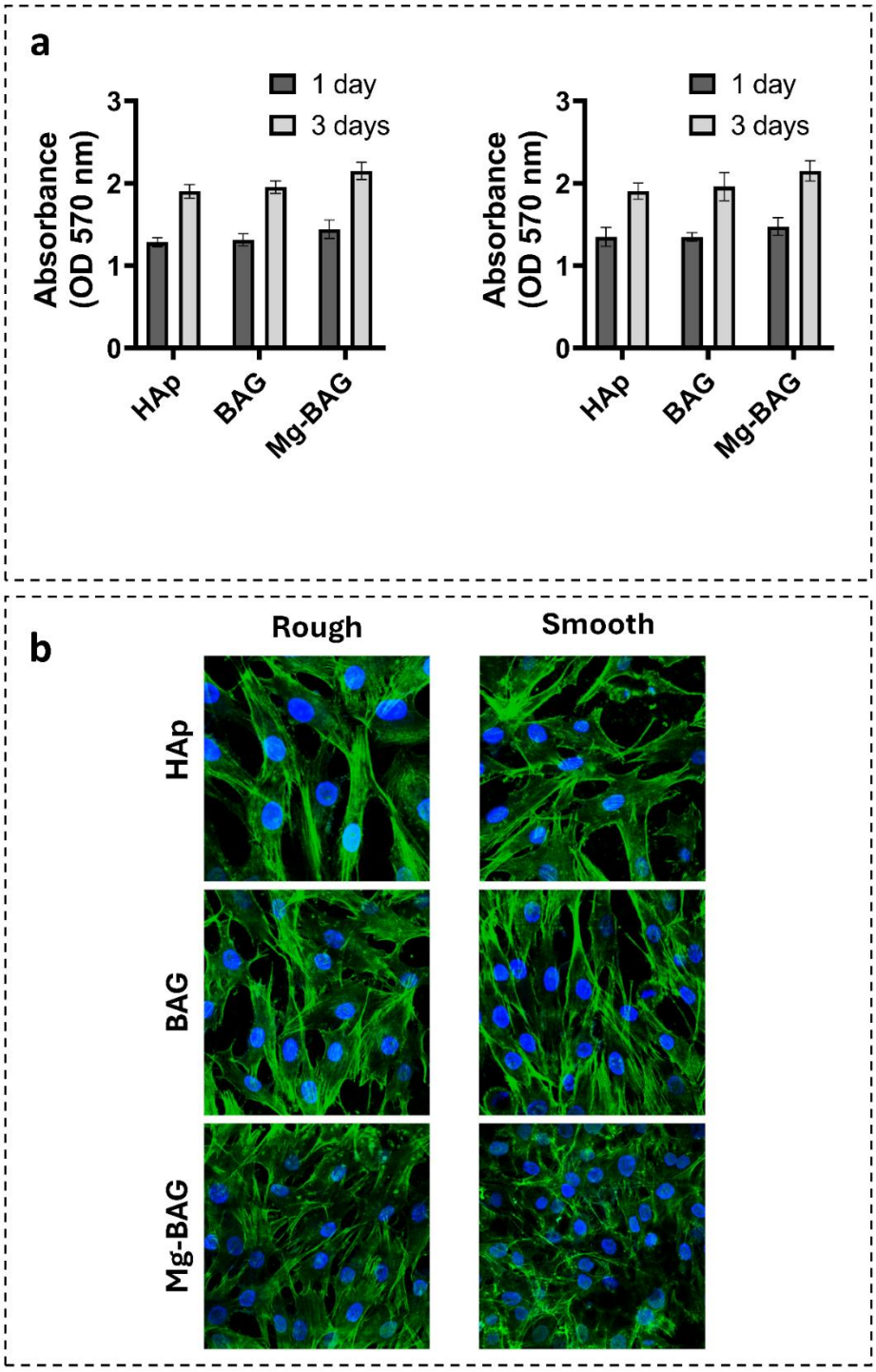

Figure 3.5.S5. Mg-BAG enhances MG63 cells viability. a) Absorbance values were observed after culturing cells onto HAp, BAG, and Mg-BAG for 1 day and 3 days. b) Cells on the surface of HAp, BAG, and Mg-BAG discs after 3 days of incubation, stained with phalloidin for the F-actin (Alexa Fluor 568, green) and DAPI for the nucleus (blue).

CHAPTER 4:

COMBATING *Pseudomonas aeruginosa* and *Staphylococcus aureus* USING BISMUTH-DOPED BAGHDADITE FOR ORTHOPAEDIC IMPLANT

Huu Ngoc Nguyen[a], Andrew Hayles[b], Iman Roohani[a,c], Zufu Lu[a], Frank Fei[a], Young No[a], Aaron Elbourne[d], Kim Chung Nguyen[e], Jitraporn Vongsvivut[f], Krasimir Vasilev[b], Vi Khanh Truong[b,g]*, Hala Zreiqat[a]*

[a]Tissue Engineering and Biomaterials Research Unit, School of Biomedical Engineering, The University of Sydney, Camperdown, NSW 2006, Australia

[b]Biomedical Nanoengineering Laboratory, College of Medicine and Public Health, Flinders University, Bedford Park SA 5042, Australia

[c]School of Biomedical Engineering, Faculty of Engineering and Information Technology, University of Technology Sydney, Sydney NSW, Australia

[d]School of Science, STEM College, RMIT University, Melbourne, VIC 3001, Australia

[g]Healthcare Engineering Innovation Group (HEIG), Department of Biomedical Engineering and Biotechnology, Khalifa University of Science and Technology, Abu Dhabi, UAE

[e]School of Engineering, RMIT University, Melbourne, VIC, 3001 Australia

[f]Infrared Microspectroscopy Beamline, ANSTO Australian Synchrotron, Clayton, Victoria 3168, Australia

Submitted to Journal Colloid and Interface Science. (Under review)

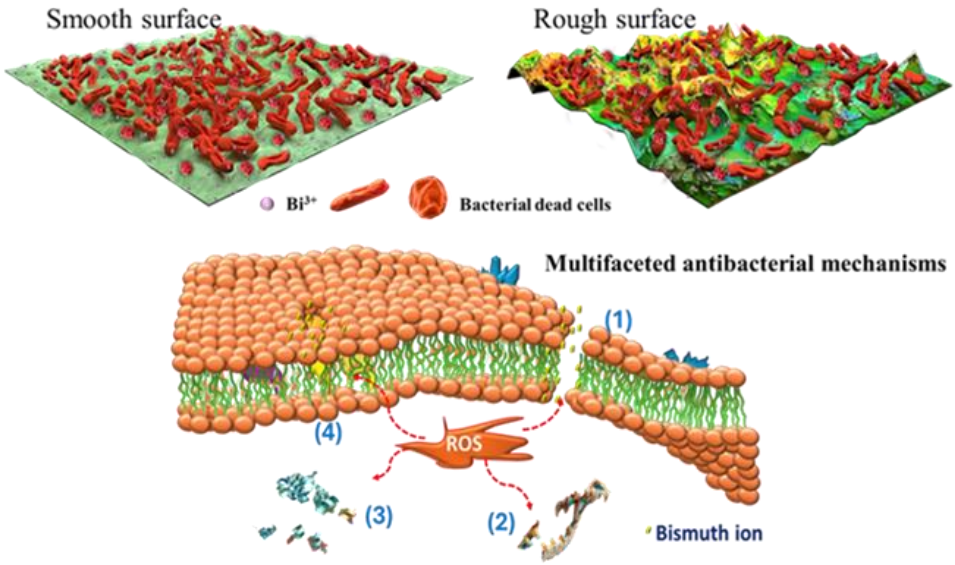

Abstract

Chapter 4 focuses on studying the antibacterial activity and mechanisms of bismuth-doped baghdadite (Bi-BAG). Bismuth (Bi^{3+}) was selected due to its well-documented broad-spectrum antibacterial activity and biocompatibility. Additionally, previous studies have shown that bismuth-doped baghdadite can enhance the radiopacity and human osteoblast cells, which is advantageous for postoperative imaging and implant monitoring. Therefore, this chapter investigates the antibacterial activity and mechanisms and biological responses of Bi-BAG, aiming to establish a multifunctional bioceramic with improved antimicrobial performance in infection prevention orthopaedic applications. This study investigates the multifunctional properties of bismuth-doped baghdadite (Bi-BAG) for its potent antibacterial activity against Gram-negative *P. aeruginosa* and Gram-positive *S. aureus* for preventing orthopaedic implant infection. Our pioneering biomaterial boasts antimicrobial activity without the incorporation of antibiotics, thus demonstrating significant promise in addressing the rising issue of antibiotic resistance. This work elucidates the multifaceted mechanisms of action of Bi-BAG, including its ability to disrupt bacterial membranes, generate intracellular ROS, and induce significant biochemical alterations in bacterial cells. Using advanced Synchrotron techniques such as macro-ATR-FTIR microspectroscopy, we analysed the biomolecular changes in bacteria exposed to Bi-BAG, while electron microscopy provided insights into morphological damage. Bi-BAG consistently showed higher bactericidal activity than BAG and HAp. Bi-BAG shows great promise as a biomaterial for infection prevention in biomedical implant applications.

4.1 INTRODUCTION

The development of synthetic materials, such as scaffolds, aims to overcome the limitations of autografts and allografts [317]. BAG, a calcium silicate-based ceramic, retains biocompatibility and offers multifunctional properties, making it suitable for various applications in tissue engineering and regenerative medicine [318]. Recent studies have demonstrated that Bi-BAG structure enhances its radiopacity mechanical properties and bioactivity compared to unmodified BAG [23]. However, the antibacterial activity of this material has yet to be investigated. Tackling infection using antibiotics is problematic given the rise in AMR [319]. The alarming rise in AMR often referred to as "superbugs," has drastically reduced the efficacy of these treatments. To combat this problem, developing next-generation antimicrobial bioceramics holds immense promise for effectively preventing and mitigating the risk of implant-associated infections. Therefore, further research must explore the antibacterial properties of Bi-BAG to overcome existing limitations while addressing the pressing infection control issue.

Infection rates fluctuate between 2-5% for routine implants [258]. However, they escalate to an alarming 30% in instances of open fractures [258, 259]. Treatment of implant-associated infections frequently necessitates revision surgery, which, although essential, bears a high recurrence rate (approximately 33%) and imposes a considerable financial burden ranging from $17,000 to $150,000 per patient [247]. Traditional treatment modalities, including implant replacement and extended antibiotic administration, further exacerbate the troubling uptick in AMR [262]. The WHO has issued an unequivocal warning: AMR could potentially claim 10 million lives annually by 2050, thereby exceeding current cancer mortality rates and inflicting a catastrophic $100 trillion hit on the global economy [263]. Recent statistics suggest that AMR

is already on track to be accountable for nearly 10 million deaths by 2030, underscoring the pressing need to confront this crisis [320].

These infections, commonly instigated by Gram-negative *P. aeruginosa* and Gram-positive *S. aureus*, constitute a significant threat to the success of implants and the well-being of patients [82, 260, 261]. Both pose significant challenges due to their ability to form biofilms on implant surfaces. Biofilms offer a protective environment for bacteria, enhancing their resistance to antibiotics and the host immune response, which complicates treatment and increases the risk of chronic infection. *P. aeruginosa* is resistant to multiple antibiotics and can thrive in various environments, making it a formidable pathogen in implant-related infections. Similarly, *S. aureus* is a leading cause of implant-associated infections due to its virulence and resistance to conventional antibiotic therapies.

Bi^{3+} recognised antimicrobial properties, when combined into a composite with BAG, can enhance its functionality by imparting strong antibacterial activity against pathogens commonly associated with implant-related infections. Bismuth compounds have garnered significant attention for their antibacterial properties in treating infections caused by *Helicobacter pylori* and other pathogenic bacteria [321]. The mechanisms through which bismuth exerts its antibacterial effects are multifaceted, involving interference with bacterial enzyme function, and modulation of biofilm formation. The sustained efficacy of bismuth drugs is notable, as there have been no reported resistant strains, which is attributed to their ability to target multiple pathways within the bacteria [322]. In this work, we aim to enhance baghdadite bioceramics by doping BAG with Bi^{3+} to produce Bi-BAG with antibacterial activity.

Minimising bacterial attachment to the surface using control roughness could reduce the spreading of pathogens. Bacterial attachment occurs on a rougher surface compared to its

adhesion on a smooth surface [25]. On the other hand, bacteria have been found to colonise smooth surfaces, such as electropolished stainless steel [25]. Hence, surface roughness alone does not appear to predict bacterial attachment and surface topography needs to be considered next. This study investigates the antibacterial activity of bacteria on surfaces with micron and submicron scales.

In this study, we explore the antibacterial activity of Bi-BAG against *P. aeruginosa* and *S. aureus* for orthopaedic implant applications (Figure 4.1). The investigation researches the multifaceted antibacterial mechanisms of Bi-BAG, including reactive oxygen species generation within bacterial cells, membrane potential, and leakage of intracellular components. Furthermore, synchrotron-sourced macro-attenuated ATR-FTIR microspectroscopy is employed to analyse biomolecular changes in bacteria exposed to Bi-BAG, providing insights into its multi-target actions on bacterial components.

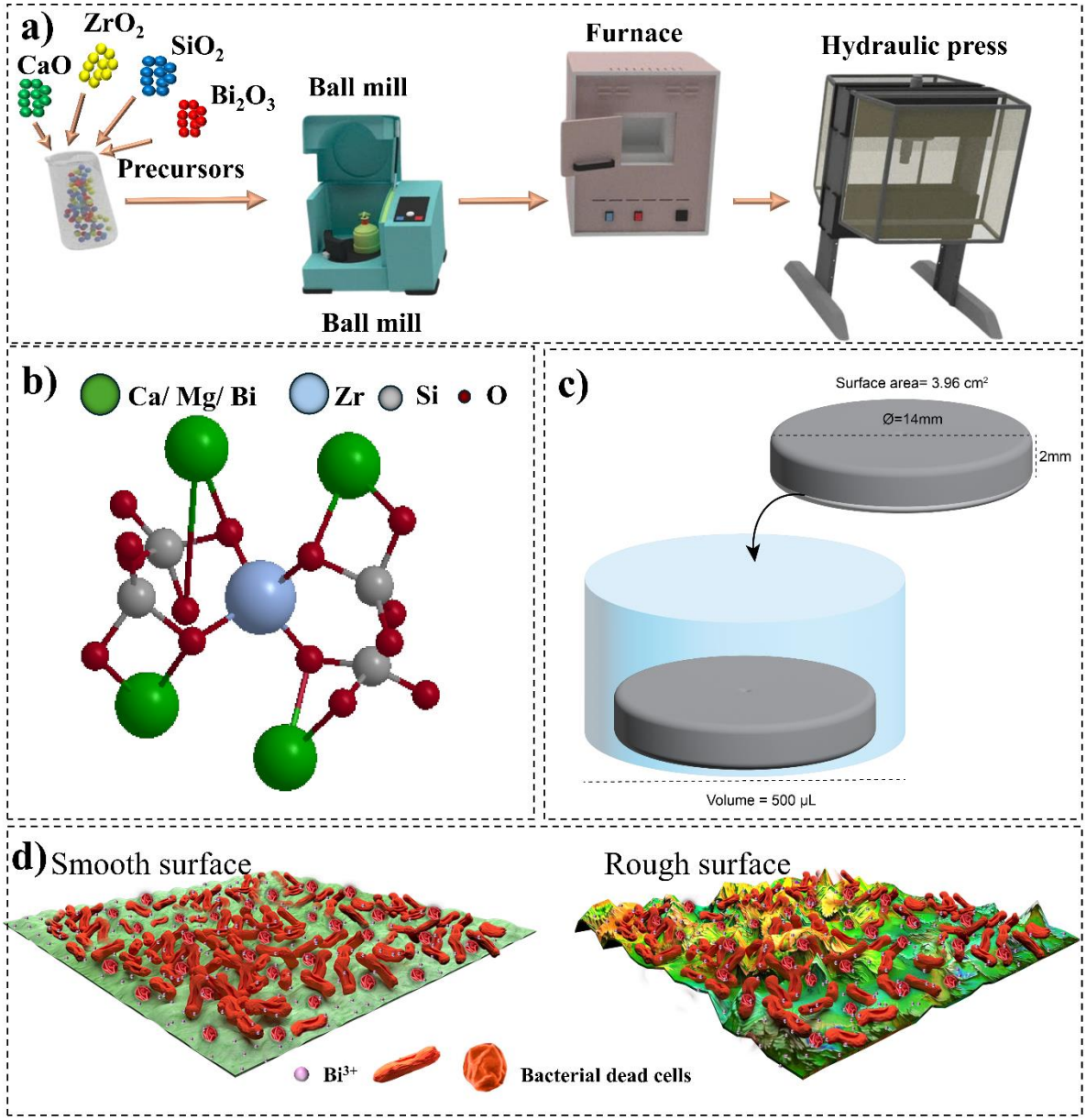

Figure 4.1. The schematic representation of Bi-BAG fabrication. a) The synthesis of Bi-BAG commences with the precursors within a ball mill, sintering in a furnace and ultimately being transformed into discs via a hydraulic press. b) The molecular architecture of Bi-BAG is depicted, showcasing the spatial arrangement of Ca, Zr, Si, Bi and O atoms. c) A disc-shaped Bi-BAG sample, with dimensions being specified (diameter = 14mm, thickness = 2mm) and an accompanying surface area (SA = 3.96 cm^2) is calculated. d) A comparative analysis of micro- and nano-roughness surface between Bi-BAG interactions with bacteria on the surface.

4.2. RESULTS AND DISCUSSION

4.2.1 Bi-BAG compositions and surface roughness

In this study, Bi-BAG were synthesised using a solid-state method, and their structural and surface properties were thoroughly analysed using various spectroscopic techniques, including energy dispersive XRD, EDS and XPS. XRD confirms the crystalline phases of Bi-BAG compared to its baghdadite (Figure 4.2a). Elemental mapping of the Bi-BAG surface exhibited an even distribution of Ca, Zr, Si, O, and Bi (Figure 4.2b). The successful doping of Bi^{3+} into the BAG structure was further confirmed by the detection of characteristic Bi peaks in the EDS spectra, the clear elemental mapping of Bi, Ca, Zr, Si, and O, which showed a uniform distribution of these elements across the Bi-BAG surfaces (Figure 4.2c), provides evidence of the successful synthesis process achieving homogenous doping of Bi^{3+} throughout the surfaces. In addition, XPS illustrates successful Bi incorporation, with distinct Bi 4f peaks observed in the Bi-BAG samples (Figure 4.2d). This was in addition to the characteristic peaks for Ca, Zr, and Si, which were present in both BAG and Bi-BAG.

A detailed analysis of surface topography using 3D profilometry revealed notable differences in surface roughness between rough and smooth Bi-BAG and BAG samples (Figures 4.2e and 4.2f). Rough surfaces exhibited a micron scale, while smooth surfaces were a sub-micron scale. Quantitative surface roughness measurements confirmed that the rough surfaces had significantly higher irregularity than smooth ones ($p<0.0001$), in both Bi-BAG and BAG. This increased surface roughness is expected to play a key role in improving the biological performance of the material, as rougher surfaces have been shown to enhance cell adhesion and proliferation [323], critical factors for successful tissue integration in bone regeneration applications.

The combined results suggest that Bi-BAG, with its enhanced surface chemistry due to Bi^{3+} doping and the modifiable surface roughness, could offer superior performance compared to undoped BAG. Incorporating Bi potentially improves the antibacterial properties and provides the opportunity to tailor surface characteristics to optimise tissue interactions. These findings have important implications for designing next-generation biomaterials, particularly in antibacterial surfaces and tissue engineering, where surface composition and topography are crucial for ensuring biocompatibility, preventing infection, and promoting tissue regeneration.

In summary, the successful doping of Bi^{3+} into BAG, along with the observed surface topography variations, suggests that Bi-BAG may have enhanced antibacterial activity and improved biological performance compared to conventional BAG. The ability to modulate surface roughness further allows for the customisation of the material for specific biomedical applications, such as implants, where antibacterial properties and tissue integration are critical for long-term success.

4.2.2 Antibacterial activity of Bi-doped BAG

The time shortly after the initial bacterial attachment represents a decisive period determining whether an infection will occur [29]. We evaluated the antibacterial activity of Bi-BAG against both *P. aeruginosa* and *S. aureus*, which are two pathogens that are strongly associated with IAIs for 3 hours and 6 hours [260]. The *Bac*Light™ Live/Dead fluorescent dye assay assessed bacterial cell viability. Our findings revealed that after 3 h of bacterial incubation, unmodified BAG exhibited a moderate degree of antibacterial activity, resulting in approximately 12% dead cells. We compared this with HAp, a commonly used rough implant coating that promotes osteointegration [324], which did not possess any bactericidal effect against *P. aeruginosa* and *S. aureus* (Figure 4.3a & 4.3b). Conversely, Bi-BAG demonstrated a significant increase ($p < 0.001$) in dead cells compared to BAG and HAp, accounting for approximately 70-80% of the

bacterial population for both bacterial species. Increasing the incubation duration to 6 h did not increase the proportion of dead cells, indicating Bi-BAG can eradicate most viable bacteria during the first 3 h of exposure. Furthermore, surface roughness did not have a significant influence on the bactericidal activity of Bi-BAG.

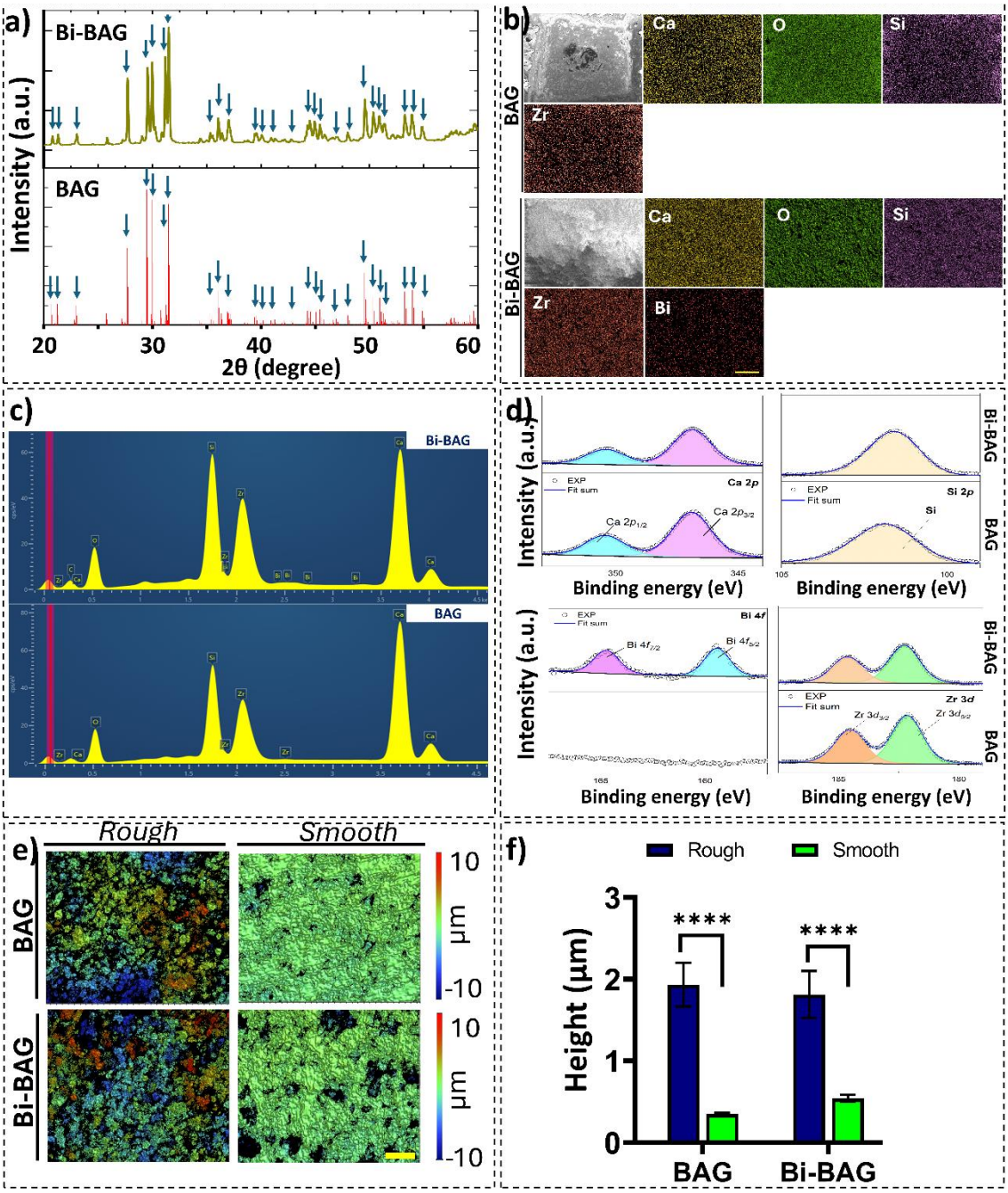

Figure 4.2. Chemical and structural characterisation of Bi-BAG. a) XRD measurements of the crystalline phases of Bi-BAG compared to its baghdadite (BAG). b & c) Scanning electron

microscopy energy-dispersive X-ray spectroscopy. The scale bar is 20 µm. d) XPS measurements of the elemental composition and the chemical states of bismuth, calcium, zirconium and silicon embedded in the Bi-BAG. e & f) A surface topography analysis was conducted using 3D profilometry, which quantified the surface roughness features. n = 3 ± SD, **** $P < 0.0001$. The scale bar represents 20 µm.

To determine whether the observed antibacterial effects were contact-dependent, we employed a disk diffusion assay [275, 276] to evaluate the influence of leached compounds (Figure 4.3c & 4.3d). The BAG bioceramic, whether smooth or rough, exhibited negligible inhibition zones (~0.7 ± 0.55 mm) against *P. aeruginosa*, and demonstrated no inhibition zone against *S. aureus*. However, our engineered Bi-BAG displayed considerable inhibition zones (ranging from 3.33± 1.52 to 5± 1.00 mm) against *P. aeruginosa* and *S. aureus*. Comparison of the inhibition zones between rough and smooth surfaces yielded no significant difference, aligning with our fluorescence-based measurements.

Although bacterial resistance to heavy metals such as Cd [277], Zn [278], Ag [279-281], and Cu [282] through efflux systems has been well-documented, to date, we are not aware of any reports that document resistance specifically to Bi^{3+}. This study revealed that the antibacterial activity of Bi-BAG is broad-spectrum, killing both Gram-negative *P. aeruginosa* and Gram-positive *S. aureus* pathogens. Importantly, this effect was observed regardless of the surface roughness of the doped BAG samples. This outcome is promising because surface roughness is a property that facilitates bone integration [283], but also promotes bacterial attachment [284]. Hence, any increase in bacterial attachment elicited by rough-doped bioceramics can be counterbalanced by the synergy of the antibacterial action of the leached ions.

Our previous studies showed that Bi-BAG possesses excellent biocompatibility with human osteoblast cells [22, 23]. Therefore, the combination of biocompatibility and antibacterial activity makes Bi-BAG bioceramics promising materials for orthopaedic applications. They

could be used to fabricate implants or scaffolds for bone tissue engineering. Furthermore, the antibacterial properties could make these materials particularly useful in high-risk patients or in situations where there is a high risk of infection.

4.2.3 The influence of Bi-BAG on morphology and intracellular ROS

The understanding of antibacterial mechanisms is a critical element in the development of antimicrobial materials, allowing for precise tailoring of performance based on physical and chemical characteristics. Toward this understanding, we used SEM analysis (Figure 4.4a) to evaluate morphological changes in both bacterial species after 6 h incubation with Bi-BAG. We noted distinct morphological changes on *S. aureus* and *P. aeruginosa* on both smooth and rough surfaces of Bi-BAG. Specifically, we identified the wrinkled and rough appearance of the cells, indicating a broad envelope-wide disturbance, thus explaining one contributor to cell death. This observation was independent of surface roughness, further supporting our previous results demonstrating an equivalent antibacterial effect for both surface topographies.

The proposed antibacterial mechanism of Bi-BAG is illustrated in Figure 4.4b. Bi^{3+} ions disrupt bacterial membranes and generate ROS within the bacterial cells. The interaction of Bi^{3+} ions with the bacterial membrane initiates oxidative stress, damaging essential cellular components such as proteins, lipids, and DNA, ultimately resulting in cell death. Quantitative analysis (Figure 4.4c) confirmed the time-dependent release of Bi^{3+} from Bi-BAG and its penetration into both bacterial strains. The concentration of Bi^{3+} within the bacteria increased significantly over time, with the highest concentration observed after 24 h of incubation. In addition, in Gram-positive and Gram-negative bacteria, the anionic nature of the cell surface determined by peptidoglycan, lipopolysaccharides and phosphate heads of the lipid bilayer promotes the binding of metal cations [30, 31]. This result indicates that while a statistically significant increase in Bi^{3+} release was observed between 3 and 6 hours (Figure 4.4c),

measurable levels of Bi^{3+} were maintained in the medium up to 24 hours.

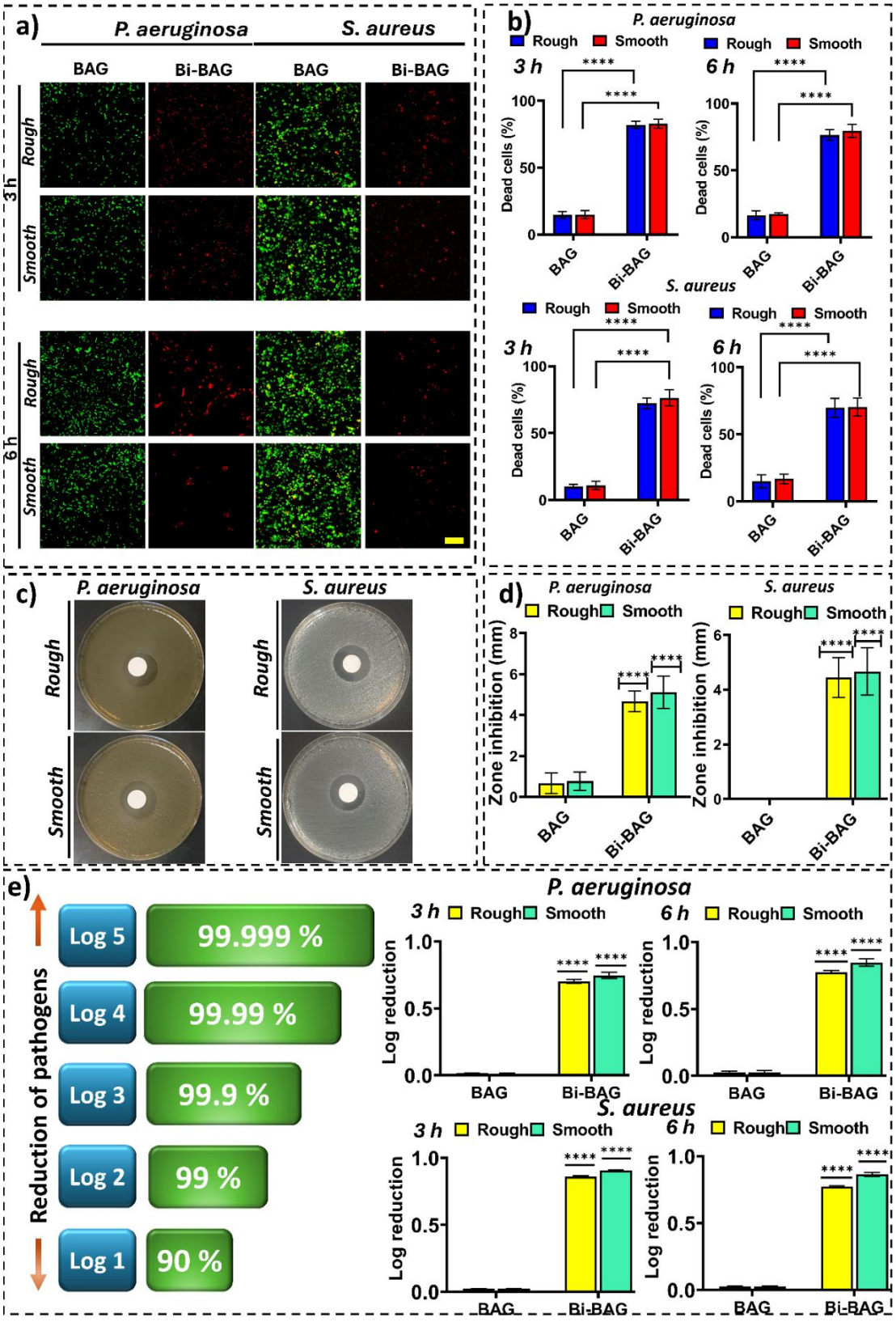

Figure 5. Bi-BAG enhances the antibacterial activity against *P. aeruginosa* and *S. aureus*. a) Confocal micrographs showing Live/Dead assay results for *P. aeruginosa* and *S. aureus* on rough and smooth surfaces of BAG and Bi-BAG materials after 3 and 6 hours of incubation. Green fluorescence (Syto9) represents live cells, and red fluorescence (PI) represents dead cells. b) Quantification of dead cells (%) obtained from confocal micrographs. c) Zone of inhibition assay. d) Quantitative measurements of the inhibition zone (mm) for *P. aeruginosa* and *S. aureus*. e) Log reduction in colony forming units (CFUs) of *P. aeruginosa* and *S. aureus* after 3 and 6 hours of surface exposure. $n = 3 \pm SD$, **** $P < 0.0001$.

We employed the DCFH-DA staining assay to measure the intracellular oxidative stress induced by Bi-BAG (Figure 4.4d). Initially, DCFH-DA is a non-fluorescent compound that enters cells and is converted into DCFH by intracellular esterase. In the presence of ROS, DCFH oxidises to the highly fluorescent compound DCF, allowing ROS levels to be quantified. Our findings revealed no substantial intracellular ROS in *P. aeruginosa* and *S. aureus* cells cultured on BAG surfaces (Figures 4.4e and 4.4f). However, when exposed to Bi-BAG, regardless of the surface roughness, we observed a remarkable 3 to 4-fold increase in ROS generation in both *P. aeruginosa* and *S. aureus* cells. This suggests that metal ion release from Bi-BAG surfaces stimulates intracellular ROS production, resulting in oxidative stress and subsequent bacterial damage. It is well documented that metal ions increase intracellular ROS generation [28], which can subsequently damage various cell components. One example is oxidative damage to lipids, which creates lipid peroxides that can influence membrane permeability and disrupt ion channels and homeostasis [29]. The downstream effect of this can be loss of cell contents and disruption of electrochemical gradients.

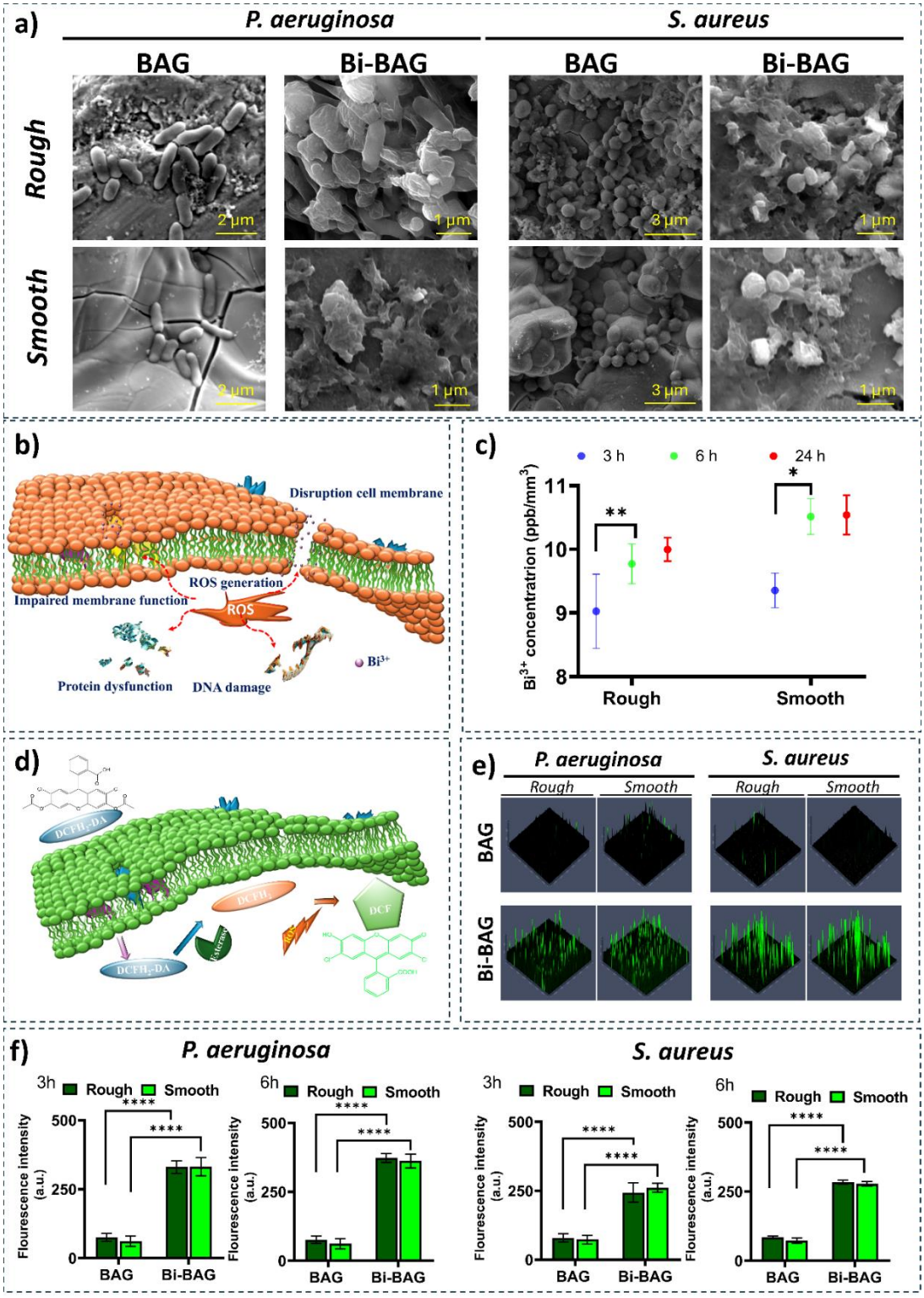

Figure 4.4. Antibacterial mechanisms of Bi-BAG against *P. aeruginosa* and *S. aureus* involving Bi^{3+} release and intracellular ROS generation. a) SEM images showing the morphology changes of *P. aeruginosa* and *S. aureus* after 24 h of incubation with Bi-BAG. b) A schematic depicting Bi^{3+} ions causing intracellular ROS production, damaging bacterial

components, and multiple events contributing to cell death. c) Quantification of Bi^{3+} release from Bi-BAG after 3 h, 6 h, and 24 h. d) The ROS detection mechanism using DCFH-DA kits is schematically illustrated. ROS generated inside bacterial cells oxidises the reagent to fluorescent DCF, enabling the visualisation of oxidative stress. e) Confocal microscopy images showing ROS generation (green fluorescence) in *P. aeruginosa* and *S. aureus* after 3 h and 6 h incubation with Bi-BAG. f) Quantification of ROS fluorescence intensity. n = 3 ± SD, * $P < 0.05$, ** $P < 0.01$, **** $p < 0.0001$.

The results of this study provide strong evidence that doping baghdadite with Bi^{3+} ions significantly enhances its antibacterial properties against both *P. aeruginosa* and *S. aureus*. The SEM analysis indicates that Bi-BAG disrupts bacterial cell membranes more effectively than BAG. The ROS data corroborates these findings, as the increased ROS production in Bi-BAG leads to oxidative stress and bacterial death. These findings have significant implications for the development of bioceramic materials in biomedical applications, particularly in the prevention of implant-associated infections. By enhancing the antibacterial properties of baghdadite through Bi^{3+} doping, Bi-BAG emerges as a promising material for use in orthopaedic implants for infection prevention. The ability to tailor surface roughness to optimise antibacterial efficacy without relying on external antibiotic use presents a valuable strategy for mitigating the growing threat of AMR.

4.2.4 The influence of Bi-BAG on membrane polarisation and leakage of intracellular contents

The mechanism of antibacterial activity of Bi-BAG was further evaluated by examining its effects on bacterial membrane polarisation, protein leakage, and nucleic acid leakage. We measured the membrane potential of both pathogens following incubation on the BAG and Bi-BAG, using the *Bac*Light™ bacterial membrane potential kit. Healthy cells with functional ion pumps have a high membrane potential due to the continuous maintenance of an electrochemical gradient between the cytoplasm and the extracellular environment. This

enables the visualisation of membrane polarisation through a red-shifted signal in healthy cells. In contrast, cells with compromised membranes exhibit a fluorescent shift towards the green spectrum (Figure 4.5a) [30]. The ratio of red to green signal intensities is a quantitative measure of net membrane depolarisation. Our results reveal significant membrane depolarisation in bacteria exposed to Bi-BAG bioceramic, indicating a disruption in membrane integrity. Analysis of the bacterial samples adhered to BAG determined that the ratio of red to green fluorescence was approximately 1.3. In contrast, the red-to-green ratio was lowered to approximately 0.5 in samples incubated on Bi-BAG. This is indicative of a compromised membrane potential resulting from disrupted ion pumps.

As membrane depolarisation can lead to loss of cell contents, we investigated the leakage of nucleic acids and proteins into the supernatant following incubation on Bi-BAG (Figure 4.5b & 4.5c). We noted a significant increase ($P < 0.0001$) in both nucleic acids and proteins in the culture medium from bacteria exposed to Bi-BAG, in comparison to those on undoped baghdadite, independent of the surface roughness. These findings highlight the significant impact of Bi-BAG surfaces on releasing nucleic acids and proteins from bacterial cells, further supporting the disruption of cell envelope integrity. Interestingly, the actions of Bi-BAG are very similar to those of quaternary ammonium compounds (QACs), which are also cationic compounds that kill bacteria by interfering with the cell envelope and causing leakage of cell contents [31].

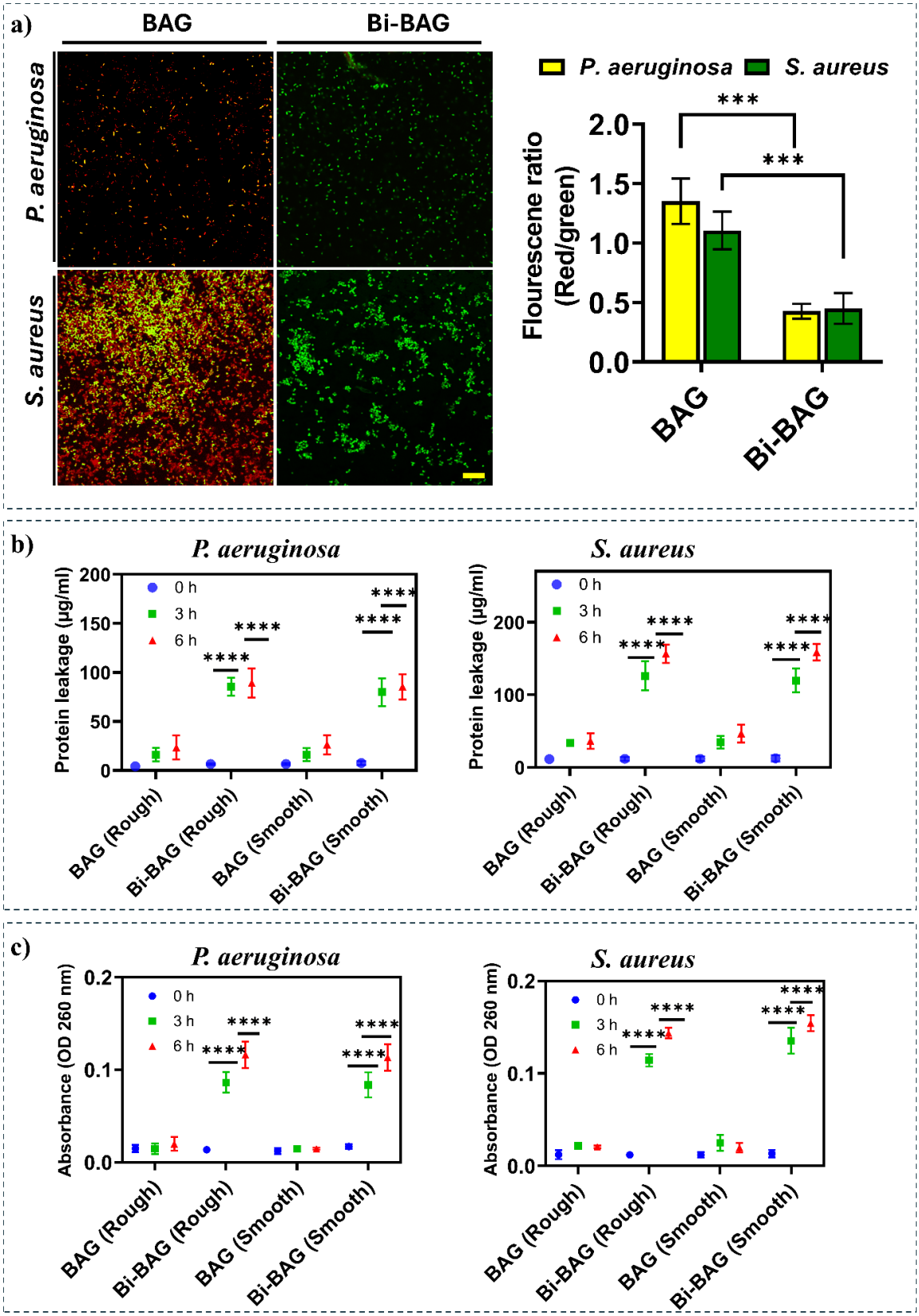

Figure 6. Effect of Bi-BAG on bacterial membrane potential and leakage of cell contents. a) Fluorescence micrographs and quantification of *P. aeruginosa* and *S. aureus* incubated on

BAG and Bi-BAG, showing membrane damage using a LIVE/DEAD BacLight^{TM} Bacterial membrane potential. Scale bar = 10 μm. The fluorescence ratio (red/green) indicates the extent of membrane damage. *** indicate significant differences $p < 0.001$. b) Quantifying protein leakage from *P. aeruginosa* and *S. aureus* after 0 h, 3 h, and 6 h incubation with BAG and Bi-BAG. c) Quantification of nucleic acid leakage from *P. aeruginosa* and *S. aureus* after 0 h, 3 h, and 6 h of incubation with BAG and Bi-BAG. Data are presented as mean ± SD (n = 3). **** indicate significant differences $p < 0.0001$.

4.2.5 Bi-BAG multi-targets biomolecules including lipids, proteins and nucleic acids

This study used Synchrotron Macro ATR-FTIR microspectroscopy to analyse the biochemical changes in *P. aeruginosa* and *S. aureus* upon exposure to BAG and Bi-BAG surfaces. The aim was to evaluate the impact of Bi-BAG on the bacterial biomolecule alternation and to understand the mechanisms of Bi-BAG enhanced antibacterial activity.

In *P. aeruginosa*, the heatmaps (Figure 4.6a) revealed significant differences between bacteria exposed to BAG and Bi-BAG. In the C-H (3000–2800 cm^{-1}), amide II (1705–1600 cm^{-1}), and polysaccharide (1200–1000 cm^{-1}) regions, Bi-BAG-treated bacteria showed notably lower absorbance compared to those on BAG, indicating a disruption of lipid, protein, and carbohydrate components of the bacterial cell membrane. The reduction in the Polysaccharide region suggests degradation or damage to the bacterial cell wall, primarily composed of peptidoglycans and polysaccharides. The PCA (Figure 4.6b) further highlighted the differences between BAG and Bi-BAG-treated bacteria. The PCA 3D plot shows distinct clustering of the spectra for *P. aeruginosa* exposed to the two materials, with 94% of the variation captured in the first principal component. This separation indicates significant biochemical alterations induced by Bi-BAG. The PCA loadings plot (Figure 4.6c) identified key wavenumbers that contributed to this differentiation, notably in the C-H stretching (~2913 cm^{-1}), Amide II (~1643 cm^{-1}), and polysaccharide (~1082 cm^{-1}) regions. These findings confirm that Bi-BAG causes substantial disruption of the bacterial membrane and intracellular components.

Similarly, in *S. aureus*, the heatmaps (Figure 4.6d) showed significant reductions in the same biochemical regions when exposed to Bi-BAG. The lower absorbance in the C-H, Amide II, and Polysaccharide regions indicates that Bi-BAG disrupts the lipid membrane, protein structures, and polysaccharide components of *S. aureus* more effectively than BAG. The polysaccharide region, associated with bacterial cell wall integrity, exhibited particularly low absorbance on Bi-BAG surfaces, suggesting that Bi-BAG severely compromises the cell wall structure of *S. aureus*.

The PCA 3D plot for *S. aureus* (Figure 4.6e) confirmed these observations, showing a clear distinction between the biochemical profiles of bacteria exposed to BAG and Bi-BAG, with 97% of the variation captured by the first principal component. The PCA loadings plot (Figure 6F) identified significant differences in the C-H (~2963 cm^{-1}), Amide II (~1550 cm^{-1}), and polysaccharide (~1082 cm^{-1}) regions, corroborating the biochemical damage caused by Bi-BAG (Figure 4.6F).

The results from Synchrotron macro-ATR-FTIR microspectroscopy demonstrate that Bi-BAG significantly alters the biomolecule composition of both *P. aeruginosa* and *S. aureus*. The decreased absorbance in the lipid (C-H), protein (Amide II), and carbohydrate (Polysaccharide) regions for both bacterial strains suggest that Bi^{3+} doping disrupts multiple components of bacterial cell structure, leading to cell membrane damage, protein denaturation, and degradation of polysaccharides. These changes align with the antibacterial mechanisms above, including intracellular ROS formation, membrane disruption and interference with bacterial cell wall synthesis.

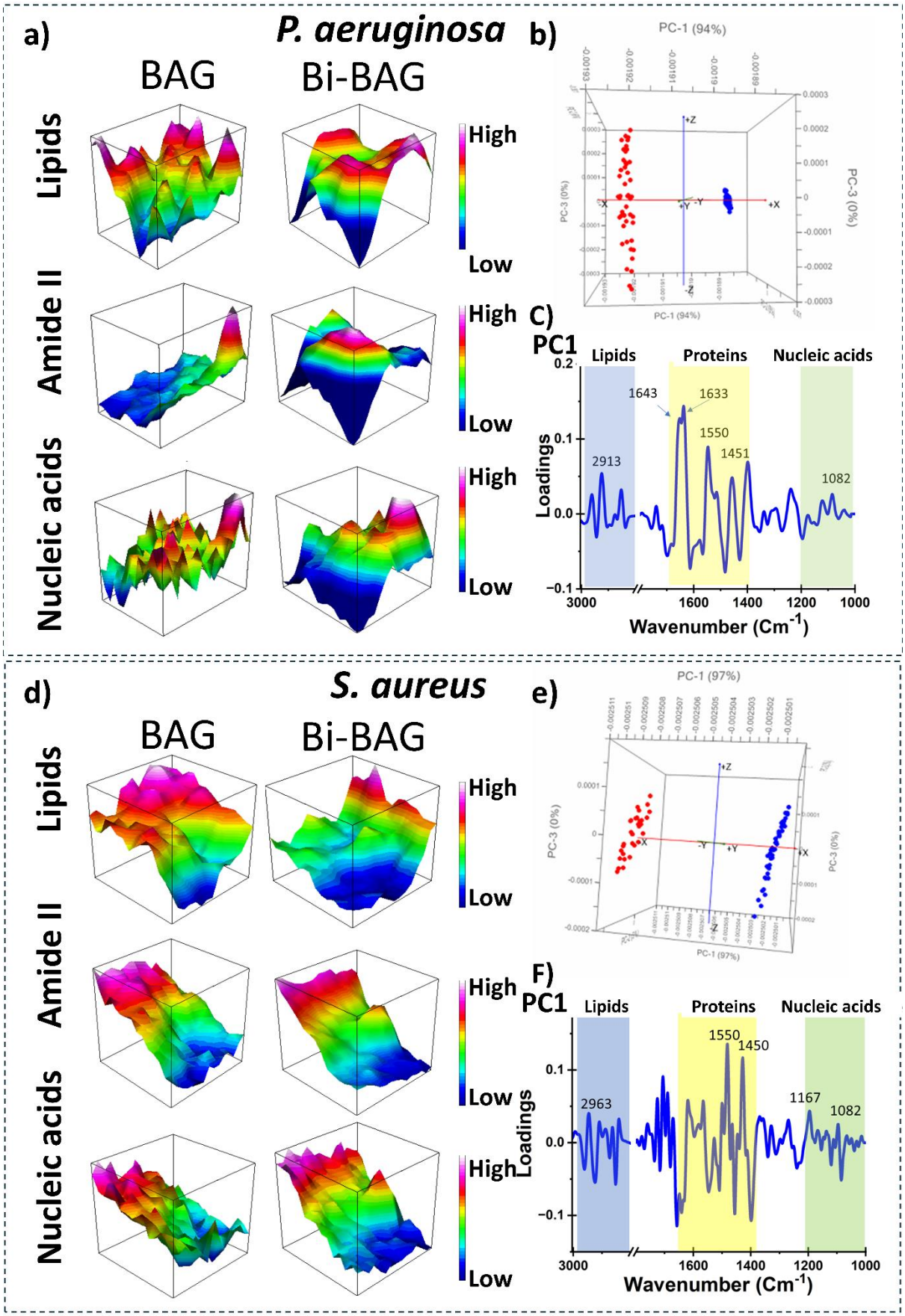
a)
P. aeruginosa
BAG
Bi-BAG
Lipids
Amide II
Nucleic acids
High
Low
b)
PC-1 (94%)
PC-3 (0%)
C)
PC1
Lipids
Proteins
Nucleic acids
2913
1643
1633
1550
1451
1082
Loadings
Wavenumber (Cm-1)
d)
S. aureus
e)
PC-1 (97%)
F)
2963
1550
1450
1167
1082

Figure 4.6. Synchrotron cacro ATR-FTIR microspectroscopy analysis of biochemical changes in *P. aeruginosa* and *S. aureus* exposed to BAG and Bi-BAG surfaces. a & d) Heatmaps of absorbance in the C-H (3000–2800 cm^{-1}), Amide II (1705–1600 cm^{-1}), and Polysaccharide (1200–1000 cm^{-1}) regions for *P. aeruginosa*, and *S. aureus*, respectively. The scale bar represents 20 µm. b & e) Principal Component Analysis (PCA) 3D plots comparing the spectral differences. c & f) Loading plots of PCA components, showing key wavenumbers that contributed to separating bacterial spectral data on BAG and Bi-BAG.

The PCA results support these findings by showing a distinct separation between the spectra of bacteria exposed to BAG and Bi-BAG. This clear distinction confirms that Bi-BAG induces significantly more biochemical changes in bacterial cells than BAG which likely accounts for its enhanced antibacterial efficacy.

Overall, these findings highlight the potential of Bi-BAG as an antibacterial material for biomedical applications, particularly in preventing infections on implant surfaces. The ability to disrupt essential biochemical pathways in Gram-negative and Gram-positive bacteria underscores its broad-spectrum antibacterial activity, making it a promising alternative to conventional antibiotic-loaded materials.

4.2.6 Bi-BAG enhanced HOBs and anti-inflammatory

To evaluate the biocompatibility of Bi-BAG, this study was conducted to understand cellular interactions, viability, and immunomodulation. Confocal imaging was used to analyse the morphology and cytoskeletal organisation of HOBs cells on rough and smooth surfaces of the materials, providing insights into cell attachment and proliferation. Confocal microscopy (Figure 4.7a) showed HOBs cell morphology on HAp, BAG, and Bi-BAG surfaces. HOBs cells cultured on Bi-BAG demonstrated enhanced attachment and well-organized actin cytoskeletal structures compared to those on BAG and HAp. On both rough and smooth surfaces, Bi-BAG facilitated denser cell coverage, with elongated cell morphology indicative of favourable cell-material interactions. This can be attributed to Bi-BAG improves surface chemistry, facilitating better cell-material interactions.

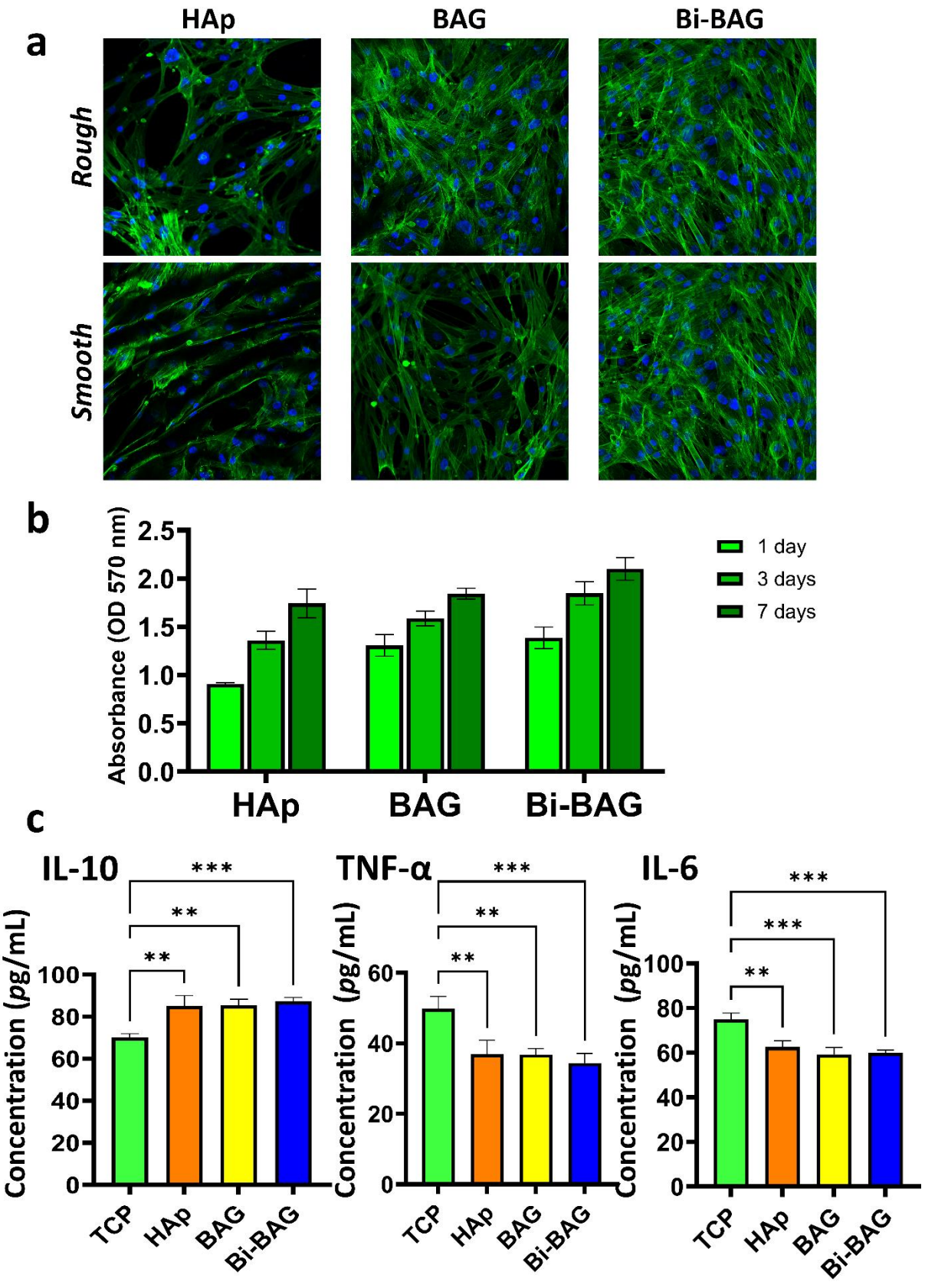

Figure 7. Confocal microscopy and biological assay analysis of HOBs cells and macrophages. a) Confocal micrograph of HOBs cells stained with DAPI (blue) to visualise nuclei and

Phalloidin to label the F-actin cytoskeleton demonstrating cell morphology and organisation. b) MTT assay results indicating the viability of HOBs cells under different conditions. c) Anti-inflammatory response of macrophages quantified by ELISA Kit with specific inflammatory markers.

The MTT assay was employed to quantify metabolic activity as an indicator of cell viability, assessing the materials' bioactivity over time. The MTT assay (Figure 4.7b) quantified the metabolic activity of HOBs cells on surfaces over 1, 3, and 7 days. Bi-BAG consistently demonstrated the highest cell viability, with significantly higher optical density (OD 570 nm) values compared to BAG and HAp ($p < 0.001$). This trend was observed across all time points, with the most pronounced difference on day 7. These results indicate that Bi-BAG promotes cellular metabolic activity and proliferation more effectively than HAp and BAG. BAG also showed moderate improvement in cell viability over HAp, further supporting the role of material composition in enhancing bioactivity. Therefore, Bi-BAG is more bioactive material than undoped BAG and HAp.

Furthermore, macrophage cytokine profiling was performed to investigate the immunomodulatory potential of Bi-BAG for minimising inflammation and promoting tissue integration. The cytokine assay (Figure 4.7c) measured the secretion of IL-10 (anti-inflammatory cytokine), TNF-α, and IL-6 (pro-inflammatory cytokines) by macrophages cultured on HAp, BAG and Bi-BAG compared to tissue culture plate as a control (TCP). Bi-BAG significantly increased IL-10 levels compared to BAG and HAp ($p < 0.001$), highlighting its anti-inflammatory potential. Conversely, Bi-BAG significantly reduced the secretion of TNF-α and IL-6 ($p < 0.001$), indicating its ability to suppress inflammation. Cytokine profiling provided critical insights into the immunomodulatory potential of the materials. Bi-BAG's ability to enhance IL-10 secretion while suppressing TNF-α and IL-6 suggests that it can create an anti-inflammatory environment conducive to healing and integration. These cytokine shifts are consistent with Bi^{3+} mediated blockade of the NF-κB axis coupled with STAT3-dominated

IL-10 induction [325, 326]. This property is particularly advantageous for implant applications, where excessive inflammation can hinder tissue integration and long-term success.

4.3 CONCLUSION

The relatively similar antibacterial profiles of Mg-BAG and Bi-BAG suggest that the baghdadite ceramic itself may contribute to antimicrobial activity, potentially through ionic dissolution products such as Ca^{2+}, Si^{4+}, and Zr^{4+}. These may act synergistically with the doped ions (Mg^{2+} or Bi^{3+}), creating a hostile microenvironment for bacteria. This study demonstrates that Bi-BAG is a potent antibacterial material, effectively inhibiting *P. aeruginosa* and *S. aureus*, two major pathogens responsible for implant-associated infections. Combining Bi^{3+} ion release, ROS generation, and bacterial membrane disruption positions Bi-BAG as a promising alternative to BAG. Synchrotron-based ATR-FTIR microspectroscopy provided valuable insights into the biochemical alterations in bacterial cells, while electron microscopy confirmed the extensive morphological damage induced by Bi-BAG. Importantly, the antibacterial activity of Bi-BAG is independent of surface roughness, further enhancing its potential for clinical applications. Additionally, this study demonstrates that Bi-BAG supports the attachment, proliferation, and viability of HOB cells and promotes an anti-inflammatory effect. These findings indicate that Bi-BAG prevents bacterial infections, enhances HOBs, and reduces inflammation. Bi-BAG emerges as promising for improving implant success.

4.4 MATERIAL AND METHODS

4.4.1 Fabrication and Characterisations of Bi-BAG

BAG and Bi-BAG discs were prepared following the steps presented in previous studies [23]. In brief, BAG and Bi-BAG were prepared using a solid-state synthesis route. The powders were mixed for 1 h at 100 rpm for BAG using a planetary ball mill (PM400 Retsch, Germany). After homogenisation, the obtained mixture was calcined in an electric furnace (RHF, Carbolite

UK) at 1350 °C of BAG and Bi-BAG for 3 h. For the preparation of the discs, the calcined powders were ground in the planetary ball mill for 3 h at 150 rpm, then uniaxially pressed at 300 MPa to obtain disc-shaped green bodies. These were then sintered in an electric furnace (RHF, Carbolite UK) at 1350°C of BAG and Bi-BAG for 3 h to obtain disc samples. Surface topography evaluation was conducted using optical 3D profilometry. The average roughness (Ra) was used in this study. The elemental analysis was carried out by using scanning electron microscope energy dispersive X-ray (SEM-EDS) and X-ray photoelectron spectroscopy (XPS) (A Thermo Scientific K-alpha and analysed with CasaXPS software).

4.4.2 Cultures and conditions

BAG and Bi-BAG were tested for antibacterial activity against two bacterial strains: *Pseudomonas aeruginosa* (ATCC 15692) and *Staphylococcus aureus* (ATCC 25923). Bacterial strains were recovered from glycerol stocks stored at -80°C and streaked for purity on tryptone soy agar (TSA). One isolated colony of each species was transferred aseptically from TSA to 5 mL of tryptone soy broth (TSB) and cultured at 37 °C until the late log phase (approximately 6-8 h). Baghdadite and doped baghdadite samples were aseptically placed in sterile 24-well plates and immersed in 0.5mL of the 10^5 CFU/mL bacterial suspensions, then incubated for 3 or 6 h.

4.4.3 Live/Dead® BacLight™ viability assay

Confocal laser scanning microscopy (CLSM) was used to visualise and quantify the proportions of live and dead cells using the LIVE/DEAD® BacLight Bacterial Viability Kit (Molecular Probes, Invitrogen, USA), which contains SYTO9 and propidium iodide fluorescent dyes. SYTO9 enters all cells, binding to nucleic acids and fluorescing green. Propidium iodide (PI) only enters cells with disrupted membranes and has a stronger affinity for nucleic acids than SYTO9. PI fluoresces red and indicates dead or viable cells [42]. SYTO9

and PI were prepared in equal proportions at 1.5 μL/mL in phosphate-buffered saline (PBS), and 1 mL of the solution was used to immerse each sample for 15 minutes in the dark at room temperature. Samples were immediately imaged with a Zeiss LSM880 (Zeiss, Oberkochen, Germany) CLSM. Using a dual emission filter, the CLSM was set up to image both live cells in green (Syto9, Ex/Em 480/500 nm) and dead cells in red (PI, Ex/Em 490/635 nm).

4.4.4 Colony enumeration

The colony forming unit (CFU) determination and log reduction data (Figure S4, Supporting Information) were performed. Following incubation, sample discs were vortexed in PBS for 15 seconds, then sonicated for 5 minutes before being vortexed for another 15 seconds and serially (1:10) diluted. In triplicate, serially diluted samples (10 μL) were dropped onto TSA plates and incubated for 18 hours at 37 °C. Viability assays were performed by standard plate counts, and the quantity of CFU per sample was calculated using the number of colonies counted, the aliquot size and the dilution factor. A log reduction value was calculated for the 3 sample types (BAG and Bi-BAG), in comparison to a HAp control.

4.4.5 Zone of Inhibition

Bacterial lawn plates were prepared by transferring 100 μL aliquots of bacterial cell suspension (at $1x10^6$ CFU/mL) onto a TSA plate and then evenly spreading it across the surface. Untreated and doped baghdadite discs were aseptically placed in defined quadrants of the plate and left to incubate overnight at 37 °C. The following day, the inhibition zones were measured by recording the radius from the centre of the disc to the perimeter of the clear zone of inhibition.

4.4.6 SEM characterisation of bacterial morphology on the surface

SEM was used to observe the morphological changes according to previous studies [43]. Disc samples were cultured with bacteria (approx. 1×10^6 CFU/ml) and incubated in TSB medium

at 37°C for 3 h and 6 h. After incubation, all discs were washed twice with PBS (pH 7.4) to remove unattached cells. The bacterial cells were fixed in 4% glutaraldehyde for 1 h at room temperature. The samples were dehydrated in sequential graded ethanol (30%, 50%, 70%, 90%, 100%). Finally, all samples were coated with 2nm platinum. Samples were then observed in a FEI Inspect F50 (FEI Company, Oregon, USA) at 5kV with a working distance of 5 mm.

4.4.7 Ion release analysis

To assess the release of Bi^{3+} ions from the BAG and Bi-BAG samples, we immersed the samples in 0.5 mL of TSB media at 37°C for 3 and 6 hours. After incubation, the supernatants were collected and centrifuged to remove debris or particles. The supernatants were then treated with HNO_3 to dissolve any remaining solids and diluted to a concentration of less than 5% to avoid matrix effects during ICP-MS analysis. The concentration of Bi^{3+} in the supernatants was measured using inductively coupled plasma-mass spectrometry (ICP-MS) with a Varian 720-ES system from the United States. Standard solutions of known concentrations were prepared to calibrate the instrument before the analysis. The concentration of Bi^{3+} ions in the samples was determined using the standard curve generated from the standards.

4.4.8 Quantification of intracellular reactive oxygen species (ROS)

To investigate the presence of ROS in target bacteria, we used an intercellular ROS formation assay utilising DCFDA/H_2DCFDA- Cellular ROS Assay Kit (ab113851, Abcam, USA). Following incubation with BAG and Bi-BAG samples, bacteria were incubated with DCFH-DA (50 µM) in the dark for 30 minutes according to the manufacturer's instructions. The samples were immediately imaged with a Zeiss LSM880 CLSM using Ex/Em of 485/535 nm. Images were taken at three random locations per sample. The fluorescence intensity of each image was then determined using ImageJ v1.53a (NIH, Maryland, USA). The ROS level was calculated based on the fluorescence intensity of the DCF, which is converted to a highly

fluorescent compound by ROS. Higher fluorescence intensity indicates higher ROS levels in the bacterial cells.

4.4.9 Evaluation of membrane depolarisation

Following incubation, the membrane potential of bacterial cells was measured using the *BacLight* Bacterial Membrane Potential Kit (Invitrogen, ThermoFisher, Massachusetts, USA). The staining procedure was carried out according to the manufacturer's instructions. The samples were immediately imaged using a Zeiss LSM880 CLSM, Ex/Em 482/497 nm. 3 micrographs were taken randomly, and the images were imported into ImageJ v1.53a. Fluorescence intensity was measured in the green and red channels, and a red-to-green ratio was calculated using the acquired intensities.

4.4.10 Leakage of intracellular nucleic acids and proteins

Following incubation on the BAG and Bi-BAG samples for 3h and 6h, we collect supernatant and centrifuge 13000 rpm for 5 minutes to remove the bacterial cells. Then, we measured the optical density of the supernatant at 260nm to quantify the nucleic acid content. The BCA (bicinchoninic acid) assay is commonly used for measuring protein concentration. To use this assay, a standard curve is first generated using known concentrations of a protein standard, such as bovine serum albumin (BSA). Protein samples are then added to a 96-well microplate, along with the BCA working reagent. After incubating the plate for 30 minutes at 37°C, the absorbance of each well is measured at 562 nm using a microplate reader. The protein concentration in the sample is determined by comparing the absorbance of the sample to the standard curve. Using a microplate reader to measure the absorbance of the samples allows for quick and accurate determination of the protein concentration in each well of the plate.

4.4.11 Synchrotron-sourced macro-ATR-FTIR

To investigate the biomolecular changes in bacterial cells exposed to BAG and Bi-BAG, synchrotron ATR-FTIR microspectroscopy was performed at the Australian Synchrotron, Victoria. Bacterial cells were cultured and treated according to the previously established experimental design, using the smooth group of BAG and Bi-BAG samples for a 6-hour exposure. Post-treatment, the bacterial cells were collected and carefully deposited onto the ATR crystal of the synchrotron microscope. ATR-FTIR spectra were acquired across the spectral range of 3400–1000 cm^{-1}, enabling the detection and quantification of molecular vibrations and functional groups. The collected spectra were subjected to detailed chemometric analysis, including HCA, second-derivative spectroscopy, and PCA. HCA was applied for quality control and the identification of outlier spectra. Second-derivative spectroscopy improved the resolution of overlapping spectral peaks, facilitating more precise interpretation. PCA was employed to explore clustering patterns and differences in the chemical composition between the treatment groups, providing insights into the biomolecular effects of BAG and Bi-BAG on bacterial cells.

4.4.12. HOBs viability on HAp, BAG and Bi-BAG

HAp, BAG, and Bi-BAG discs were sterilised using ultraviolet (UV) light for 20 minutes. The sterilised discs were placed individually into 24-well plates, with each group containing three replicates. HOBs were seeded onto the surface of each disc at a density of $3x10^4$ cells per disc in 90 μL of cell suspension. The plates were incubated at 37°C for 90 minutes for initial cell attachment. After the attachment period, each disc was carefully transferred to a new well to avoid interference from unattached cells. Subsequently, 1 mL of culture medium was added to each well, and the samples were incubated under standard conditions (37°C, 5% CO_2) for 1, 3, or 7 days. Then, MTT and CLSM assays were carried out.

HOBs cells were fixed with 4% paraformaldehyde for 20 minutes. The coatings were then incubated with 0.1% Triton-X (Sigma) for 10 min. Next, it was incubated with Alexa 488-phalloidin (Thermo Scientific) for 90 min. Subsequently, DAPI (Thermo Scientific) was applied and incubated for 10 min. The coatings were then washed with 2 mL of PBS afterwards. CLSM was used to image phalloidin and DAPI stained samples using ZEISS LM800 and analysed with ZEN (blue) and Imaris software.

4.4.13 MTT assay for cell viability

At each time point (1, 3, and 7 days), cell viability was assessed using the MTT assay. The culture medium was replaced with 200 µL of MTT reagent (0.5 mg/mL in serum-free medium), and the discs were incubated at 37°C for 4 hours. After incubation, the MTT solution was carefully aspirated, and the formazan crystals formed by metabolically active cells were dissolved by adding 200 µL of dimethyl sulfoxide (DMSO). The optical density (OD) of the resulting solution was measured at 570 nm using a microplate reader to quantify cell viability. Media without cells served as the negative control. All experiments were conducted in triplicate, and the data were reported as mean ± standard deviation (SD).

4.4.14 Anti-inflammatory assay

Macrophage experiments were conducted using THP-1 cells differentiated into macrophages. THP-1 cells were cultured in RPMI-1640 medium supplemented with 10% FBS and 1% PS. Differentiation was induced by treating the cells with 100 ng/mL of phorbol 12-myristate 13-acetate (PMA) for 24 hours. After differentiation, macrophages were washed with PBS and seeded onto sterilised discs in 24-well plates at a density of 5x 10^4 cells per well.

The macrophages were incubated on the discs for 24 hours, after which the culture supernatants were collected and analysed for cytokine levels. The concentrations of IL-10, TNF-α, and IL-6 were measured using enzyme-linked immunosorbent assay (ELISA) kits (Invitrogen, Thermo

Fisher Scientific) according to the manufacturer's instructions. Absorbance was measured at 450 nm using a microplate reader, and cytokine concentrations were calculated using standard curves. All experiments were performed in triplicate, and results were expressed as mean ± SD.

4.2.15 Statistical analyses

Statistical significance was evaluated using one-way analysis of variance (ANOVA) with Tukey's multiple comparisons test. P-value < 0.05 was considered statistically significant. All experiments were performed in triplicate and data are presented as mean and standard deviation (SD).

4.5 Supporting information

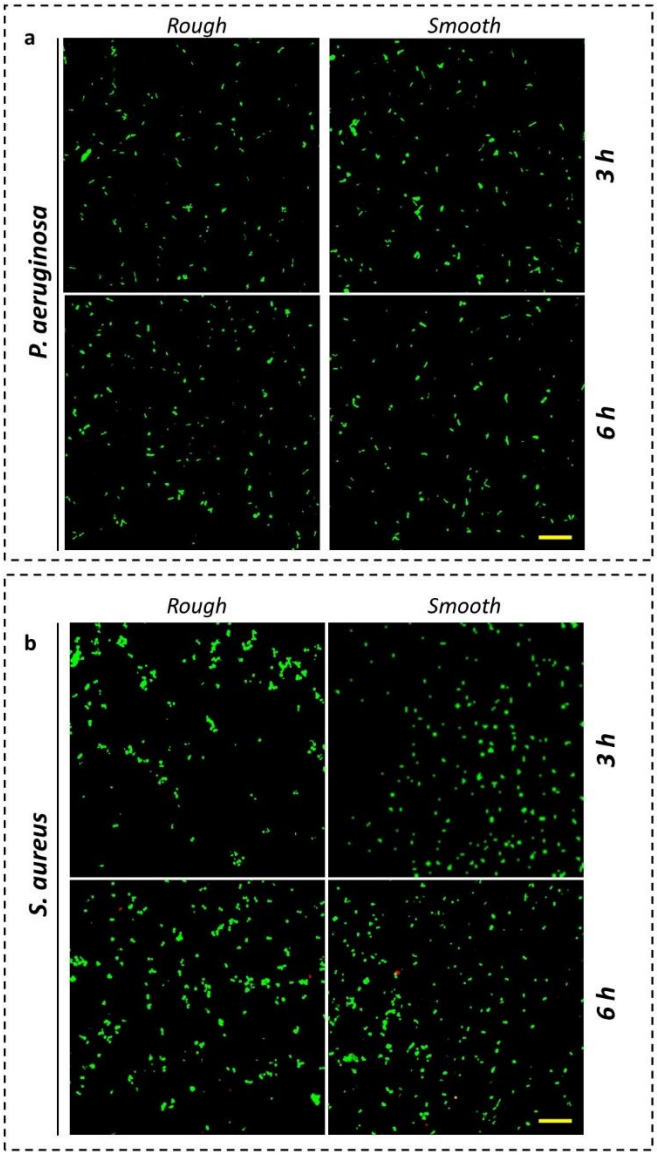

Figure 4.5.S1. Live/Dead fluorescence micrographs depicting *P. aeruginosa* (a) and *S. aureus* (b) incubated on HAp surfaces for 3 or 6 hours, providing visual evidence of no antibacterial activity. The scale bar represents 20 μm.

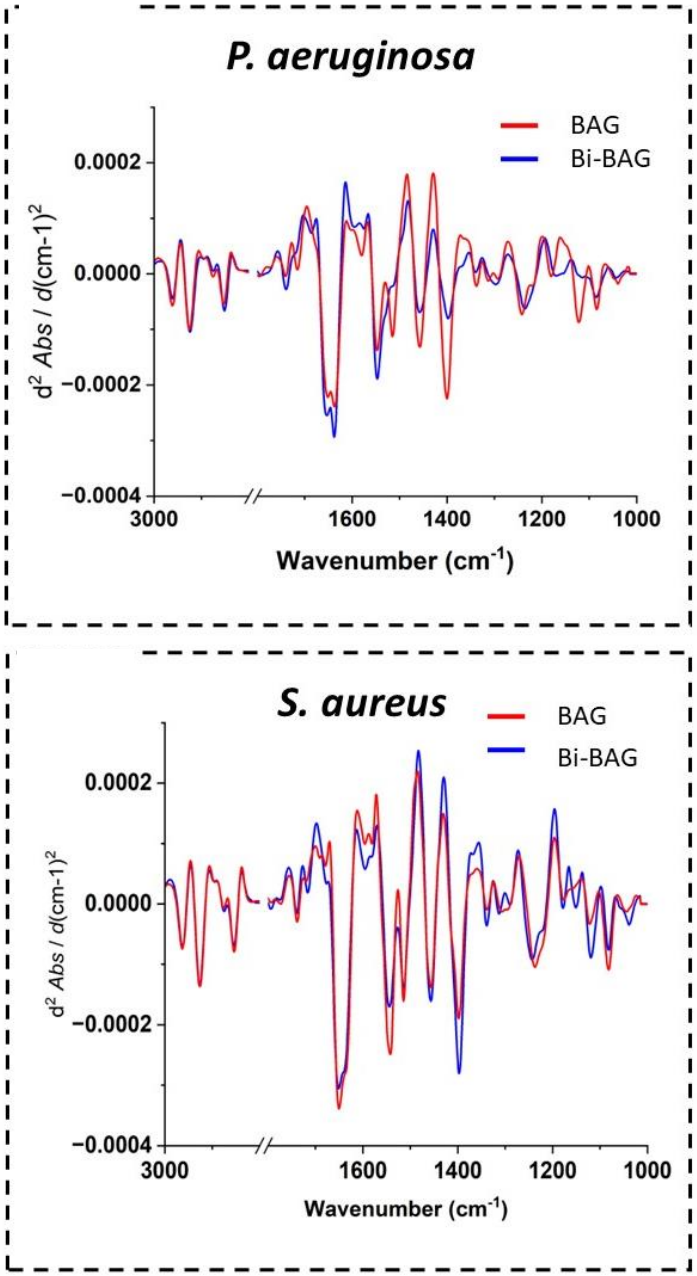

Figure 4.5.S2. Comparisons of the average EMSC-corrected 2nd derivative spectra of *P. aeruginosa* and *S. aureus* on BAG and Bi-BAG.

Table 4.5.S1. Summary of zone inhibition (mm) of *P. aeruginosa* and *S. aureus* exposed to HA, BAG and Bi-BAG

Surface	HAp	BAG	Bi-BAG

Bacteria				
P. aeruginosa	*Rough*	ND	1.33 ± 0.57	4.66 ± 0.57
	Smooth	ND	1.66 ± 0.57	5.00 ± 1.00
S. aureus	*Rough*	ND	ND	4.00 ± 1.00
	Smooth	ND	ND	4.33 ± 1.15

CHAPTER 5:

NOVEL MULTIFUNCTIONAL TITANIUM SURFACE WITH A NANOSPIKE COATING OF BISMUTH-DOPED BAGHDADITE USING FLAME TECHNOLOGY FOR ORTHOPAEDICS

Ngoc Huu Nguyen[1] , Thanh Tran Phu[2], Zufu Lu[1], Thi Kim Anh Nguyen[2], Xuan Minh Chau Ta[2], Wenshao Li[3], Jitraporn Vongsvivut[4], Andrew Haleys[3], Qi Quang[2], Kim Chung Nguyen[6],Iman Roohani[1,5], Krasimir Vasilev[3], Antonio Tricoli[2], Vi Khanh Truong[3,7]*, Hala Zreiqat[1]*

[1]Tissue Engineering and Biomaterials Research Unit, School of Biomedical Engineering, University of Sydney, NSW 2006, Australia

[2] Nanotechnology Research Laboratory, Faculty of Engineering, University of Sydney, NSW 2006, Australia

[3]Biomedical Nanoengineering Laboratory, College of Medicine and Public Health, Flinders University, Adelaide SA 5042, Australia

[4]Infrared Microspectroscopy Beamline, ANSTO Australian Synchrotron, Clayton, Victoria 3168, Australia

[5]School of Biomedical Engineering, Faculty of Engineering and Information Technology, University of Technology Sydney, Sydney NSW, Australia

[6]School of Science, STEM College, RMIT University, Melbourne, VIC 3001, Australia

[7]Healthcare Engineering Innovation Group (HEIG), Department of Biomedical Engineering and Biotechnology, Khalifa University of Science and Technology, Abu Dhabi, UAE

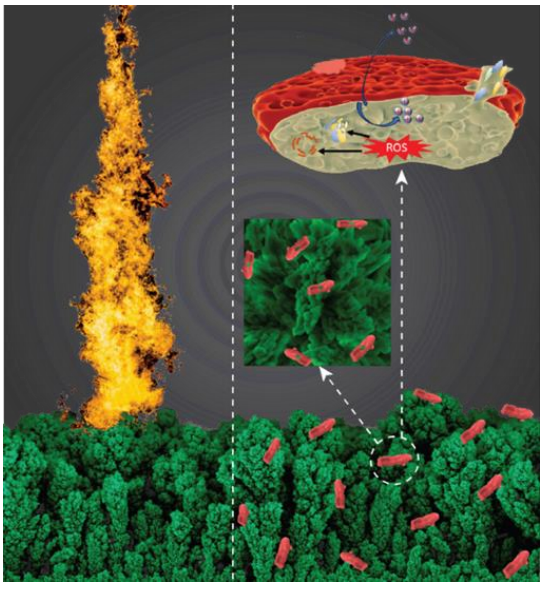

Abstract

Orthopaedic devices and implants frequently fail due to bacterial infections. In this study, we present a novel approach to enhance the antibacterial properties of orthopaedic implants by leveraging Bi-BAG bioceramics and flame spray pyrolysis technology (FSP). This research is the first to employ FSP technology for creating nanocoating and surface modification with Bi-BAG spikes-like, significantly increasing the surface area and enhancing the antibacterial efficacy. The Bi-BAG coating effectively inhibits the growth of common orthopaedic pathogens; Gram-negative *P. aeruginosa* and Gram-positive *S. aureus*, while maintaining the biocompatibility of the titanium substrate. Moreover, the innovative FSP technology ensures a uniform coating. This research may inform the development of a new generation of orthopaedic implants that could help reduce the incidence of post-operative infections and improve patient outcomes.

5.1 INTRODUCTION

Orthopaedic implants are crucial in restoring mobility and improving the quality of life for patients with bone-related diseases and injuries [327]. As the global population ages, the prevalence of bone diseases such as osteoarthritis and femoral head necrosis is surging, increasing the demand for effective bone repair and replacement solutions [328]. However, the risk of IAIs remains a significant concern, often leading to severe complications, prolonged antibiotic treatments and implant failure, resulting in elevated medical expenses and perhaps higher mortality rates [329-331]. The likelihood of infection after internal fixation is between 0.4% and 16.1% depending on the type of fracture [332]. Bacteria have diversified strategies to adhere to natural and synthetic surfaces with higher survival rates [333]. Among these, *P. aeruginosa* and *S. aureus* are members of the six nosocomial pathogens including *Enterococcus faecium*, *S. aureus*, *Klebsiella pneumoniae*, *Acinetobacter baumannii*, *P. aeruginosa*, and *Enterobacter* (ESCAPE) group, six nosocomial pathogens characterised by multidrug resistance and virulence, posing a significant threat to orthopaedic implants [334].

Traditional approaches, such as replacing the implant and using antibiotics over extended periods, can exacerbate AMR. According to the WHO, AMR could surpass cancer by causing up to 10 million deaths annually by 2050, with a potential economic impact of $100 trillion [318]. Alarmingly, recent data suggests that AMR-related deaths could reach 10 million deaths by 2030 [320]. Therefore, there is an urgent need to explore new strategies for next-generation biomaterials that balance biocompatibility with antibacterial properties without relying on antibiotics.

Titanium (Ti) stands out as a preferred material for implants owing to its low density, non-toxicity, and excellent biocompatibility, widely used in hip, knee, and dental implants [28]. However, its use is hindered by poor bioactivity and antibacterial properties, leading to

potential implant loosening and postoperative infections [29]. To address these challenges, we developed a multifunctional bioceramics coating using Bi-BAG with enhanced antibacterial properties. This coating integrates nanotechnology with physical and chemical antibacterial mechanisms to effectively prevent bacterial colonisation and reduce the risk of IAIs. BAG, $Ca_3ZrSi_2O_9$, a calcium zirconium silicate, has shown excellent biocompatibility and osteoconductive properties in pre-clinical studies in sheep over a duration of up to six months, making it a promising bioceramic for orthopaedic applications [264]. In a previous study, we demonstrated that Bi-BAG significantly enhanced the function of primary human bone-derived cells and improved radiopacity, indicating its potential for treating bone defects [23]. Unlike silver or copper, which can exhibit cytotoxicity at higher concentrations [335, 336], Bi^{3+} demonstrates a broader antibacterial spectrum, making it a safer choice for orthopaedic implants [337, 338]. Bi^{3+} provide a broader antibacterial spectrum and may thus be a safer choice for orthopaedic implants [334, 335]. Bi^{3+} disrupts bacterial membranes, interferes with bacterial metabolism, and generates ROS making them a strong additive for combating IAIs [336][339]. To apply this innovative material to titanium surfaces, we employed FSP technology. We selected it for its ability to produce uniform, high-quality coatings in a single step, making it both scalable and efficient for biomedical applications [340, 341]. Furthermore, FSP enables precise control over particle size and morphology, ensuring consistent nanostructured coatings. Inspired by the mechano-biocidal properties observed in nature, we designed the Bi-BAG coating to feature a nanospike reminiscent of antibacterial structures observed in nature found on insect wings, such as those of cicadas and dragonflies [271, 342]. These natural surfaces exhibit remarkable antibacterial activity through physical mechanisms, where nanoscale spikes mechanically disrupt bacterial membranes.

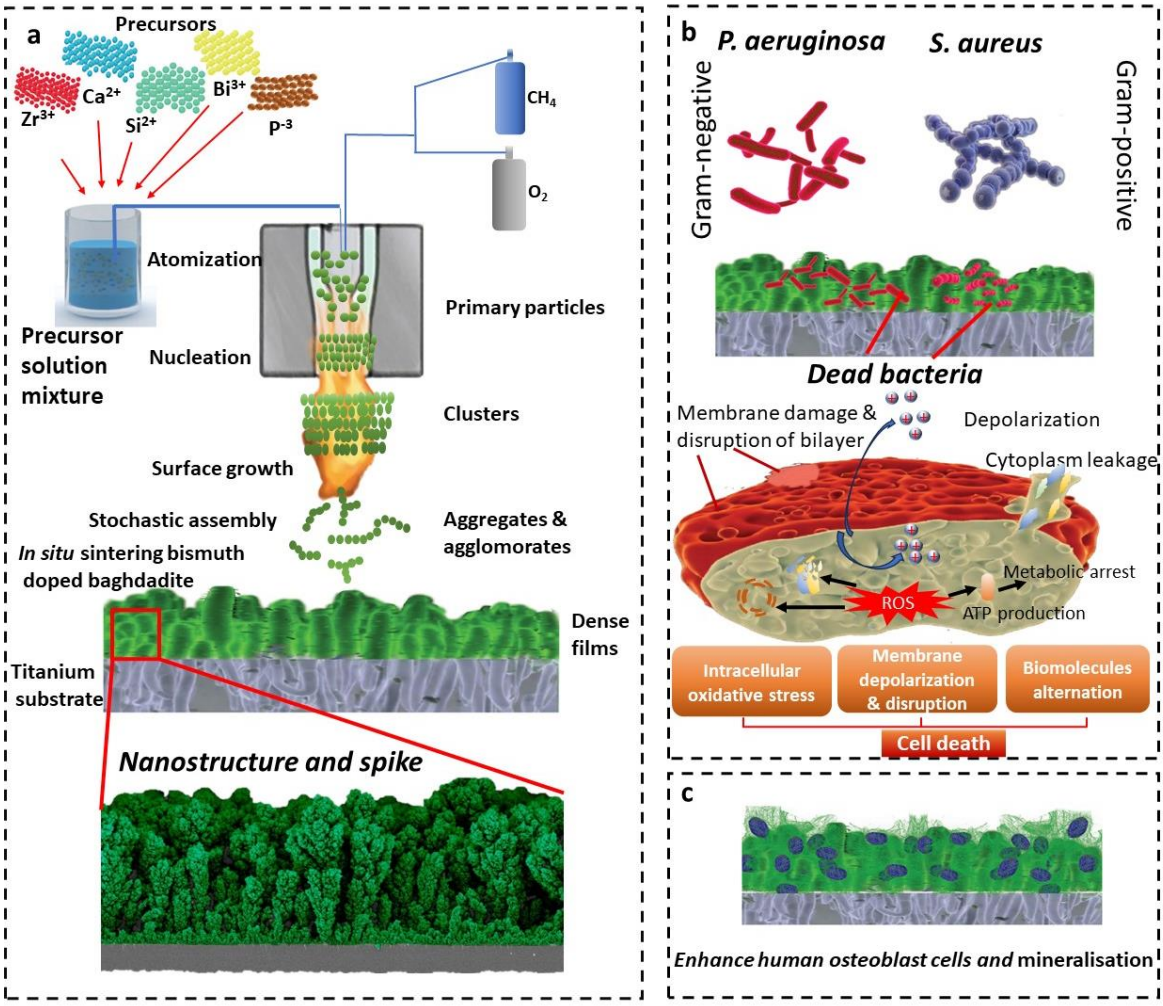

Figure 5.1. Illustration of the flame spray pyrolysis technology coating method to create bismuth-doped baghdadite (Bi-BAG) nanospike-coated on titanium. a) Details the step-by-step process of forming nanostructured spikes on the titanium surface, from the precursor solution mixture to nucleation, leading to forming primary particles, which then grow, aggregate, and sinter to form dense, spike-like films. **b)** Demonstrates the enhanced antibacterial activity of the nanospike coating against Gram-negative *P. aeruginosa* and Gram-positive *S. aureus*, highlighting the mechanisms of bacterial membrane damage, depolarisation, cytoplasmic leakage, and cell death induced by reactive oxygen species (ROS) and disruption of metabolic processes. c) Shows the promotion of human osteoblast cell growth and mineralisation by the Bi-BAG coated surface.

A key novelty of our study is the development of a nanocoating with spike-like features on titanium surfaces, a technique shown to significantly enhance antibacterial efficacy (Figure 5.1). The use of FSP to apply this Bi-BAG coating represents a first in the field, enabling the

formation of nanocoating with surface modifications, including spikes that increase surface area and bolster antibacterial performance. Our research also provides a comprehensive understanding of the multifaceted antibacterial mechanisms of the Bi-BAG coating. These mechanisms include the generation of intracellular ROS, induction of membrane depolarisation, and disruption of metabolic pathways and various biomolecules within bacterial cells. By applying FSP for Bi-BAG application and elucidating these multiple modes of antibacterial action, this work lays the foundation for next-generation orthopaedic implant materials that support infection prevention and better integration with host tissue, ultimately aiming to improve patient outcomes.

5.2. RESULTS

5.2.1 Surface characterisation of Bi-BAG coating titanium surface using flame technology

In this study, we prepared a nanocoating with spike-like using a custom-built FSP system described in our previous studies [341, 343, 344]. The materials were deposited directly on Ti discs in one minute at a height above a burner of 8 cm (see details in the experimental section). The structural and compositional analysis of the Bi-BAG spike-like nanocoated titanium surface revealed a unique architecture and chemical composition. SEM imaging (Figure 5.2a & 5.2b) demonstrated that the spike-like exhibit a uniform and dense distribution across the titanium surface, with an average height of approximately 200 nm. The results also highlighted the sharp and pointed morphology of the nanospikes (~50nm). TEM (Fig. 5.2c & 5.2d) provided detailed insights into the internal structure of the spike-like. The lattice fringes observed in the HRTEM image (Fig. 5.2e & 5.2f)) indicated a well-ordered crystalline phase with a measured lattice d-spacing of 0.2 nm. The high-resolution image also confirmed the continuity and integrity of the Bi-BAG coating, ensuring uniform functionalisation across the titanium substrate. Elemental mapping using EDS (Fig. 5.2f) demonstrated the homogeneous distribution of key bioactive elements, including Ca, Si, Zr, O, and Bi.

The surface chemistry was investigated using XPS. Survey XPS spectra (Figure S5.1) confirmed the presence of anticipated elements, including calcium (Ca), phosphorus (P), silicon (Si), zirconium (Zr), and bismuth (Bi), as well as oxygen (O), carbon (C), and titanium (Ti) from the substrate, on the surface of the materials. The XPS analysis provided atomic ratios of these elements at the surface.

5.2.2 Flame technology coating Bi-BAG shows antibacterial activity against Gram-negative and Gram-positive bacteria.

To comprehensively evaluate the antibacterial activity of the Bi-BAG spike-like coating, we conducted live/dead assays and plate counting against Gram-negative *P. aeruginosa* and Gram-positive *S. aureus*, two prominent pathogens strongly implicated in IAIs [260, 345]. The initial period following bacterial attachment is critical in determining the possibility of infection, emphasising the importance of rapid infection prevention for successful implant integration in clinical settings [286, 346]. CLSM images in Figure. 5.3a revealed substantial differences in bacterial viability with live bacteria appearing green (SYTO9) and dead bacteria fluorescing red (PI). The Bi-BAG coating significantly enhnaced antibacterial activity, evidenced by the predominance of red fluorescence compared to HAp and BAG at both 6 h and 24 h.

Quantitative analysis of the antibacterial rate (Figure. 5.3b) confirmed Bi-BAG the superiority of the Bi-BAG coating. The results showed that Bi-BAG coating achieved an antibacterial activity of approximately 80% against both pathogens within the first 6 hours, and this efficacy remained substantial by 24 hours. In contrast, the BAG coating exhibited markedly lower efficacy, registering 18% and 10% antibacterial activities against *P. aeruginosa* and *S. aureus,* respectively, at 6 hours, declining further to 10% for *P. aeruginosa* and 2% for *S. aureus* by 24 hours. Meanwhile, the HAp coating displayed no significant antibacterial effect against either bacterial strain throughout our study.

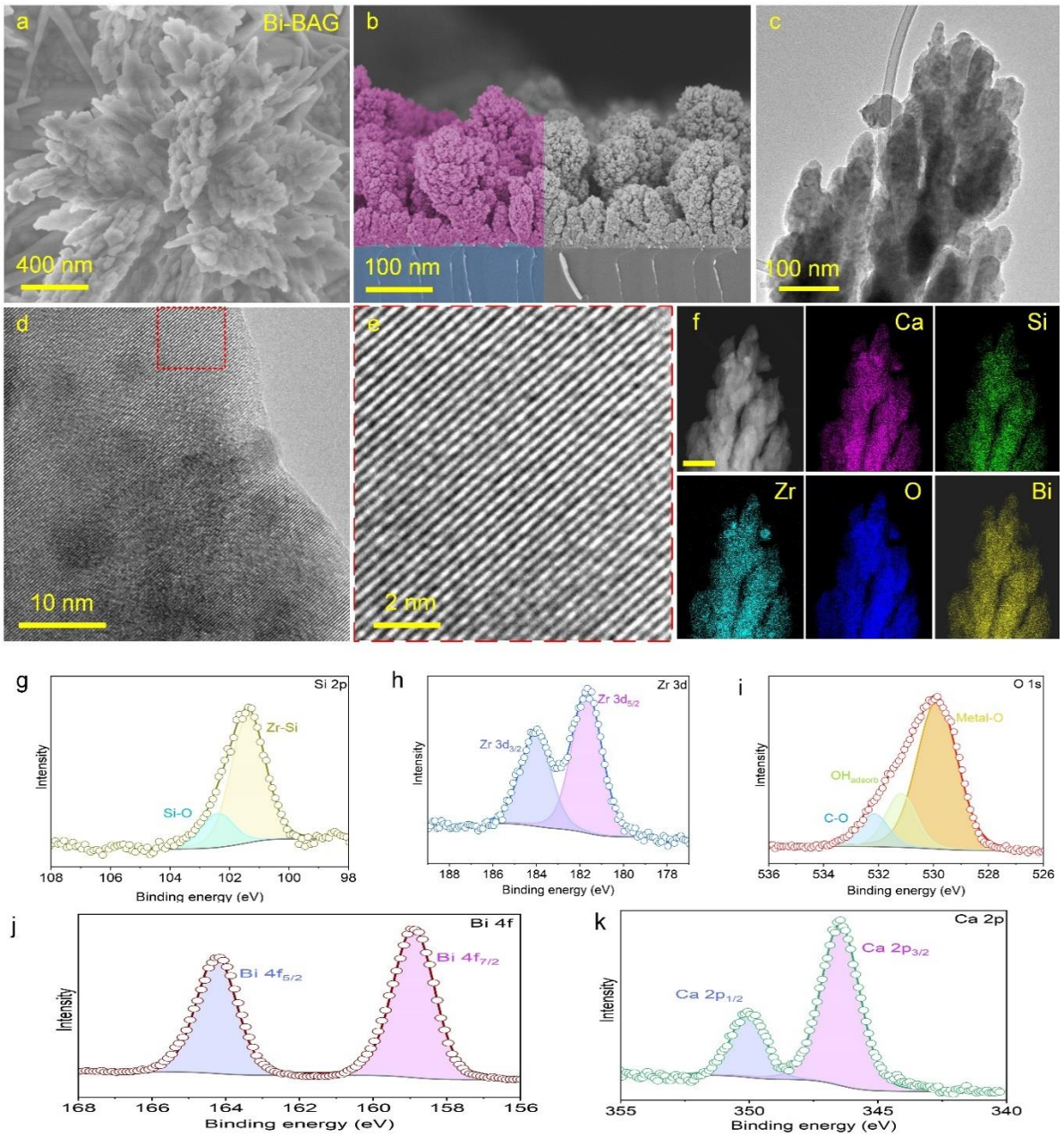

Figure 5.2. Nanoscale characterisation of Bi-BAG coatings. a) SEM image of Bi-BAG nanorods. b) Cross-sectional SEM view showing the dense coating structure. c) TEM image of a single Bi-BAG nanorod. d) High-resolution TEM image of the nanorod with lattice fringes. e) Magnified view from d) highlighting the crystalline structure. f) Elemental mapping for Ca, Si, Zr, O, and Bi, confirming the presence and distribution of these elements in the nanorods. g-k) XPS spectra for Si 2p, Zr 3d, O 1s, Bi 4f, and Ca 2p, demonstrating the chemical states of the elements within the Bi-BAG structure.

The log reduction in bacterial viability (Figure. 5.3c) further confirmed these findings. For *P. aeruginosa*, Bi-BAG coatings achieved a log reduction of approximately 1 at both 6 and 24 hours, while BAG demonstrated a reduction below 0.5, and HAp exhibited negligible antibacterial activity ($p < 0.0001$). Similarly, Bi-BAG coatings significantly reduced the viability of *S. aureus* compared to HAP and BAG.

5.2.3 Bi-BAG coating impact on bacterial morphology and membrane integrity

The SEM images in Figure. 5.4a reveals distinct morphological changes of *P. aeruginosa* and *S. aureus* on different surfaces at 6h and 24h intervals. On the HAp and BAG coatings, the bacteria largely maintained their normal morphology, displaying plump, clearly defined rod and cocci shapes, respectively. In contrast, on the Bi-BAG coating, the bacteria exhibited a wrinkled and shrunken appearance, indicating membrane damage and cell death

To assess bacterial membrane integrity, we used a fluorescent dye FM4-64 that binds specifically to lipid bilayers [354]. In Figure 5.4b, confocal laser scanning microscopy (CLSM) images show reduced fluorescence intensity and irregular cell outlines on the Bi-BAG coating surface, suggesting compromised membranes. In contrast, bacteria on the HAp and BAG surfaces exhibited higher fluorescence intensity and more regular shapes, indicating intact membranes. These findings were further corroborated by confocal microscopy findings, where the Bi-BAG samples displayed reduced fluorescence intensity, suggestive of impaired membrane function.

Focused ion beam-scanning electron microscopy (FIB-SEM) cross-sectional images (Figure 5.4c) revealed bacterial interactions with Bi-BAG coatings. While BAG coatings exhibited spike-like nanostructures, the bacteria showed limited membrane deformation and penetration into these surfaces. In contrast, Bi-BAG demonstrated strong interactions with bacterial cells, evident from significant membrane disruption, deep bacterial penetration into the spike-like

nanocoating, and noticeable structural deformation of the bacteria. Arrows in the FIB-SEM images highlight Bi-BAG spikes to effectively penetrate bacterial membranes.

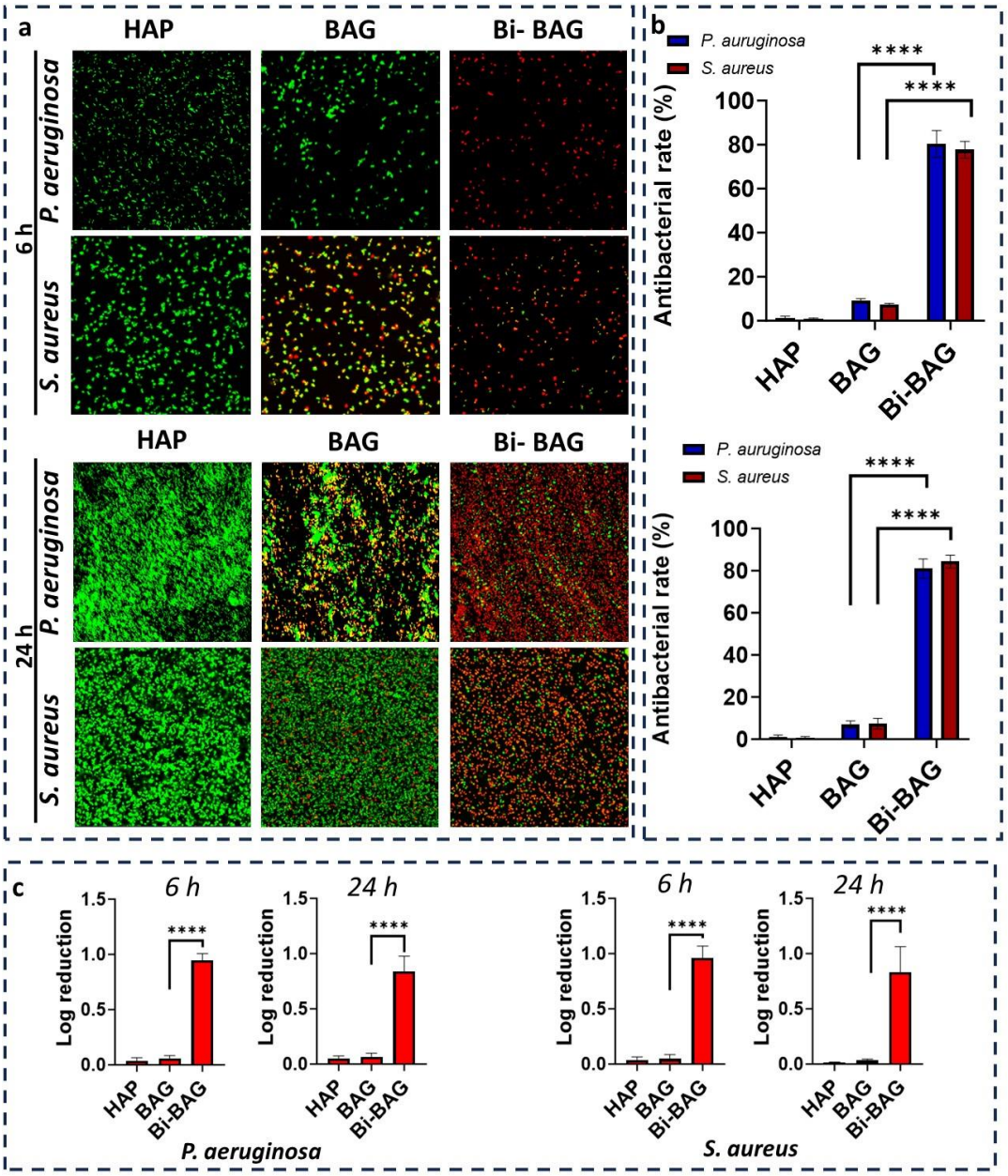

Figure 5.3. Antibacterial activity of Bi-BAG coating using flame technology against gram-negative and positive bacteria for 6h and 24 h. a) Confocal images showing the antibacterial activity of Bi-BAG coating against *P. aeruginosa* and *S. aureus*. b) Quantitative antibacterial activity of Bi-BAG coating. c) Log reduction showing the reduction of bacteria after exposure to Bi-BAG coating.

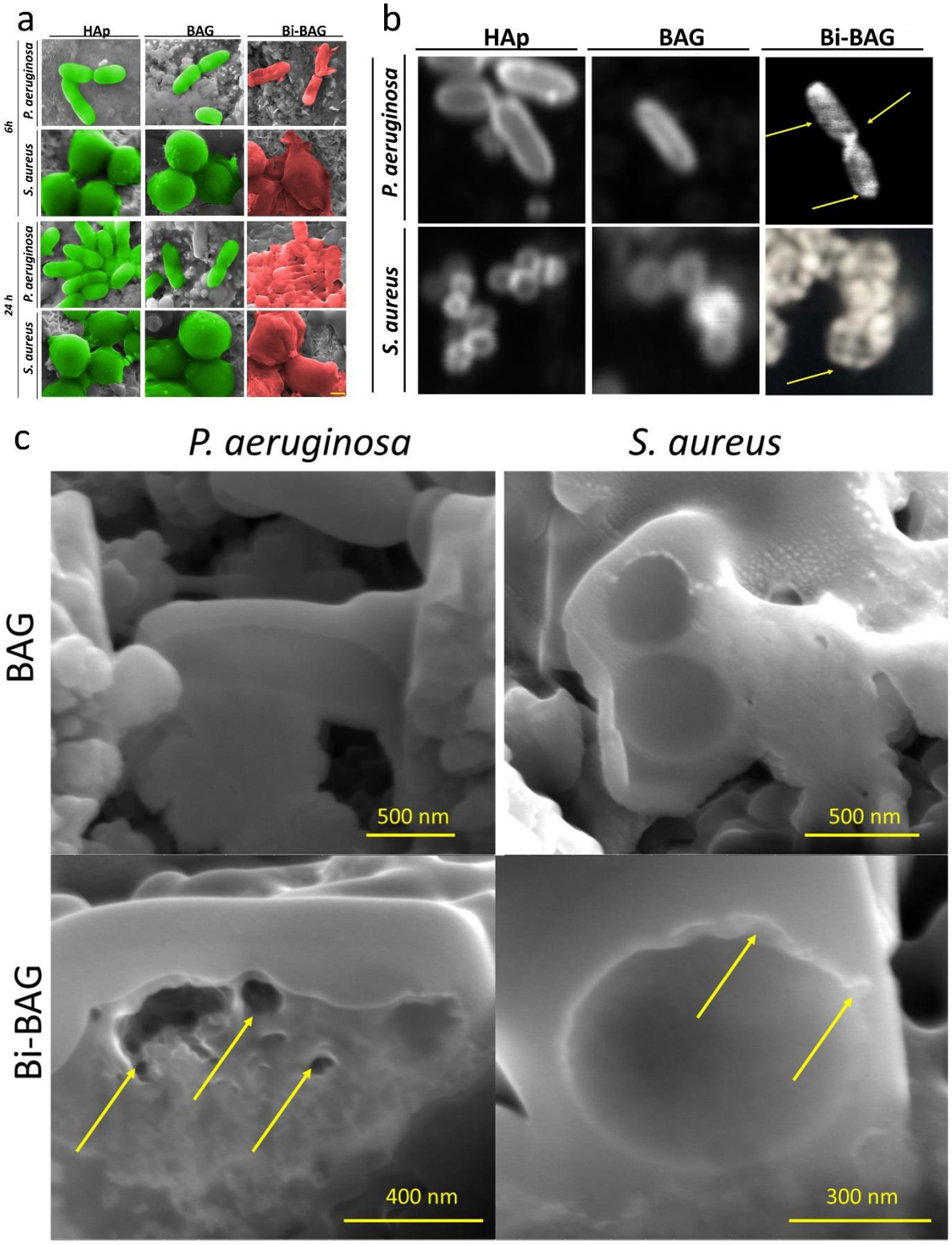

Figure 8. Morphology and membrane integrity of bacteria on different surfaces at 24h intervals. a) SEM images show the wrinkled and shrunken appearance of bacteria on Bi-BAG surface, compared to the smooth and intact bacteria on HAp and BAG surfaces. b) Confocal microscope Eryscan high-resolution images with FM4-64 fluorescence staining show the

compromised bacterial membranes in the Bi-BAG samples, indicated by the reduced fluorescence intensity and irregular shape. c) FIB-SEM analysis cross-section of bacteria interact with Bi-BAG spike-like nanocoating.

5.2.4 Intracellular oxidative stress, membrane potential reduction and ATP depletion in bacteria by Bi-BAG

To elucidate the antibacterial mechanisms of Bi-BAG, we assessed ROS formation in bacterial cells after exposure to Bi-BAG coating [347]. Confocal images (Figure 5.5a) indicate that Bi-BAG treated cells exhibit higher fluorescence intensity compared with cells treated with HAP and BAG, suggesting elevated ROS levels in the Bi-BAG group. To further assess the antibacterial mechanisms of the Bi-BAG coating, we examined its effects on bacterial membrane potential. Disruptions in membrane potential can lead to cellular dysfunction and ultimately cell death [348]. Moreover, membrane potential and ROS production are closely interconnected, as ROS can damage cell membranes and alter membrane potential [349]. The Bi-BAG treated cells showed lower fluorescence intensity for polarised membranes (and higher intensity for depolarised membranes), compared with those treated with depolarisation in the Bi-BAG group (Figure 5.5b). HAp or BAG, indicating membrane depolarisation in the Bi-BAG group (Figure 5.5b). The findings suggest that Bi-BAG disrupts the membrane potential, which is essential for maintaining cellular homeostasis and ATP synthesis.

Next, we assessed the Bi-BAG coating on bacterial ATP levels to further elucidate its antibacterial effects. ATP is a ket molecule in cellular energy metabolism, playing an essential role in growth, replication, and stress response [350]. Additionally, a complex relationship exists between ROS production and ATP levels, given that ROS can damage the cellular machinery required for ATP synthesis [351]. The Bi-BAG coating showed lower bioluminescence intensity than HAp and BAG treated -bacteria cells, indicating reduced ATP levels in the Bi-BAG group (Figure 5.5c). Furthermore, the intensity decreased with time in

Bi-BAG treated suggesting that the coating impairs metabolic activity necessary for bacterial survival and proliferation.

In summary, the data in Figure 5.5 strongly support the hypothesis that the Bi-BAG coating exerts a potent antibacterial effect through multiple mechanisms, including the induction of oxidative stress, disruption of membrane potential, and impairment of bacterial metabolism. These findings provide a comprehensive understanding of the antibacterial action of the Bi--BAG coating and highlight its potential as an effective coating for orthopaedic implants.

5.2.5 Synchrotron macro ATR-FTIR microspectroscopy analysis reveals the effect of Bi-BAG coating on bacterial biomolecules

We utilised synchrotron macro ATR-FTIR microspectroscopy to investigate the molecular mechanisms underlying the antibacterial activity of the Bi-BAG coating. This technique offers high sensitivity and spatial resolution, enabling detailed analysis of biomolecule changes within individual bacterial cells [352]. The Synchrotron ATR-FTIR measurements provided comprehensive spectral data on the biomolecular alterations in *P. aeruginosa* and *S. aureus* when exposed to the Bi-BAG coating (Figure. 5.6a & 5.7a PCA highlight the stark contrast between the bacterial cells in conventional BAG and those on Bi-BAG surfaces. Particularly, PC-1 accounts for the majority of variance, reflecting a robust differentiation attributable to the impact of Bi-BAG coating (Figure. 5.6b & 5.6c, Figure 5.7b & 5.7c). The PCA loading spectra identified specific absorption peaks that correspond to the observed biomolecular shifts, substantiating the influence of the Bi-BAG coating on bacterial viability at the molecular level. Specifically, the spectral analyses indicated significant changes in the biomolecular signatures of lipids, proteins, and nucleic acids, all of which are essential to the structural and functional integrity of bacterial cells.

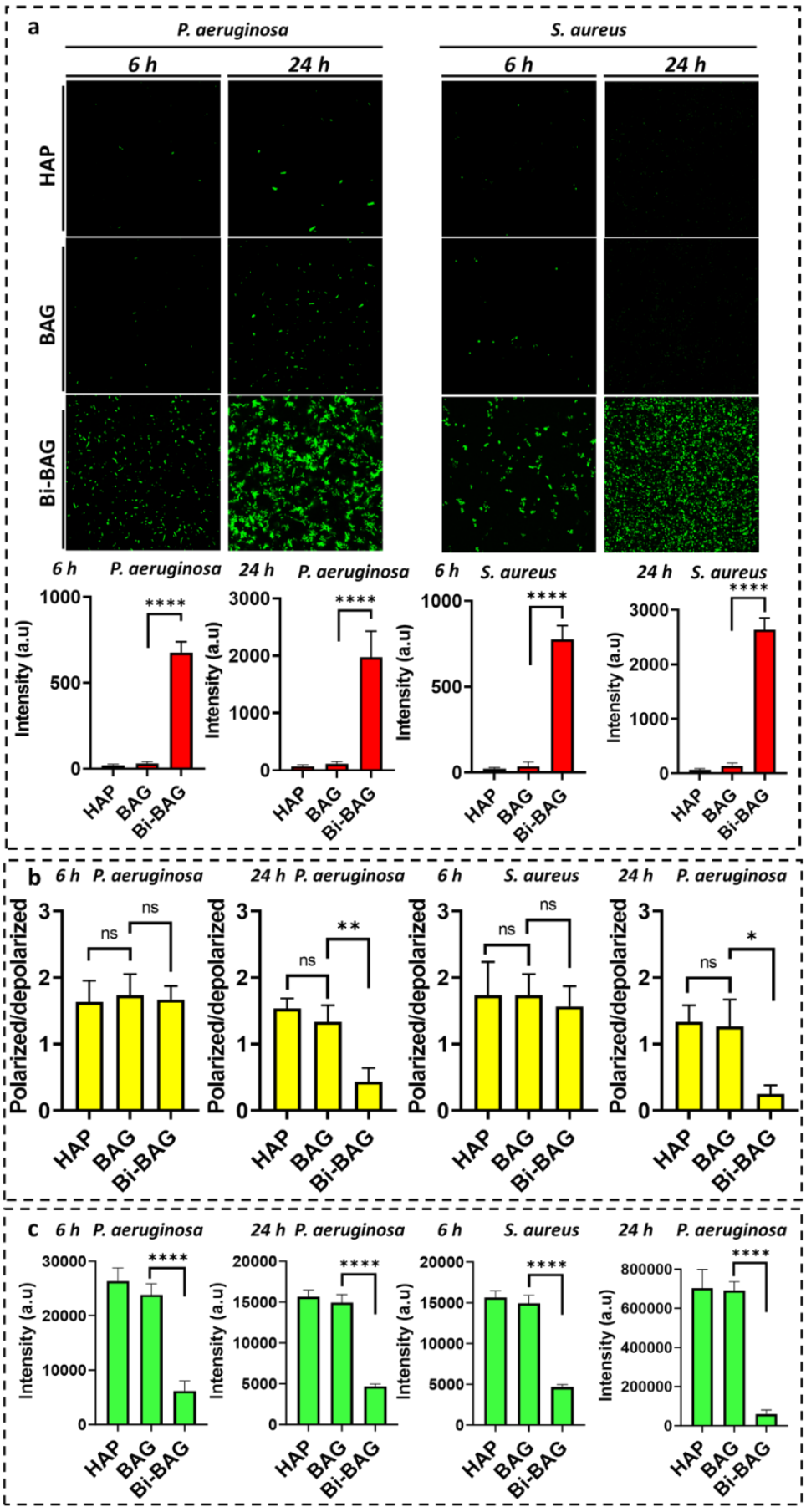
a
P. aeruginosa
S. aureus
6 h
24 h
HAP
BAG
Bi-BAG
6 h P. aeruginosa
24 h P. aeruginosa
6 h S. aureus
24 h S. aureus
Intensity (a.u)
****
b
Polarized/depolarized
ns
**
*
c
Intensity (a.u)

Figure 5.5. Evaluating the antibacterial mechanisms of Bi-BAG coatings on bacterial viability. a) Visualisation of ROS production is shown by the intensity of green fluorescence, where a higher intensity corresponds to elevated ROS levels in bacterial cells. b) The membrane potential disruption. c) The ATP synthesis within the bacterial cells is depicted with a decrease indicating a drop in metabolic activity.

For the spectral intensity within the lipid region (3000-2850 cm^{-1}), there was a marked decrease following exposure to the Bi-BAG coating, suggesting a destabilisation of the bacterial membrane's lipid bilayer (Figure. 5.6d and 5.7d). This observation was further supported by changes in the characteristic peaks of methyl and methylene groups (2925 cm^{-1} and 2852 cm^{-1}), respectively, implying a disruption of membrane integrity which could be attributed to the interaction with released metal ions and the oxidative stress imposed by the coating.

For proteins, a noticeable shift in the amide I and II bands (1700-1450 cm^{-1}) was observed, suggesting a structural alteration likely caused by the oxidative modification of amino acids. Such stress on proteins unfolding or misfolding ultimately hinders bacterial metabolism and leads to cell death. Specifically, the peaks at 1654 cm^{-1} and 1637 cm^{-1}, which correspond to α-helix and β-sheet structures, respectively, showed significant variation, reflecting the impairment of protein synthesis or stability due to the Bi-BAG treatment.

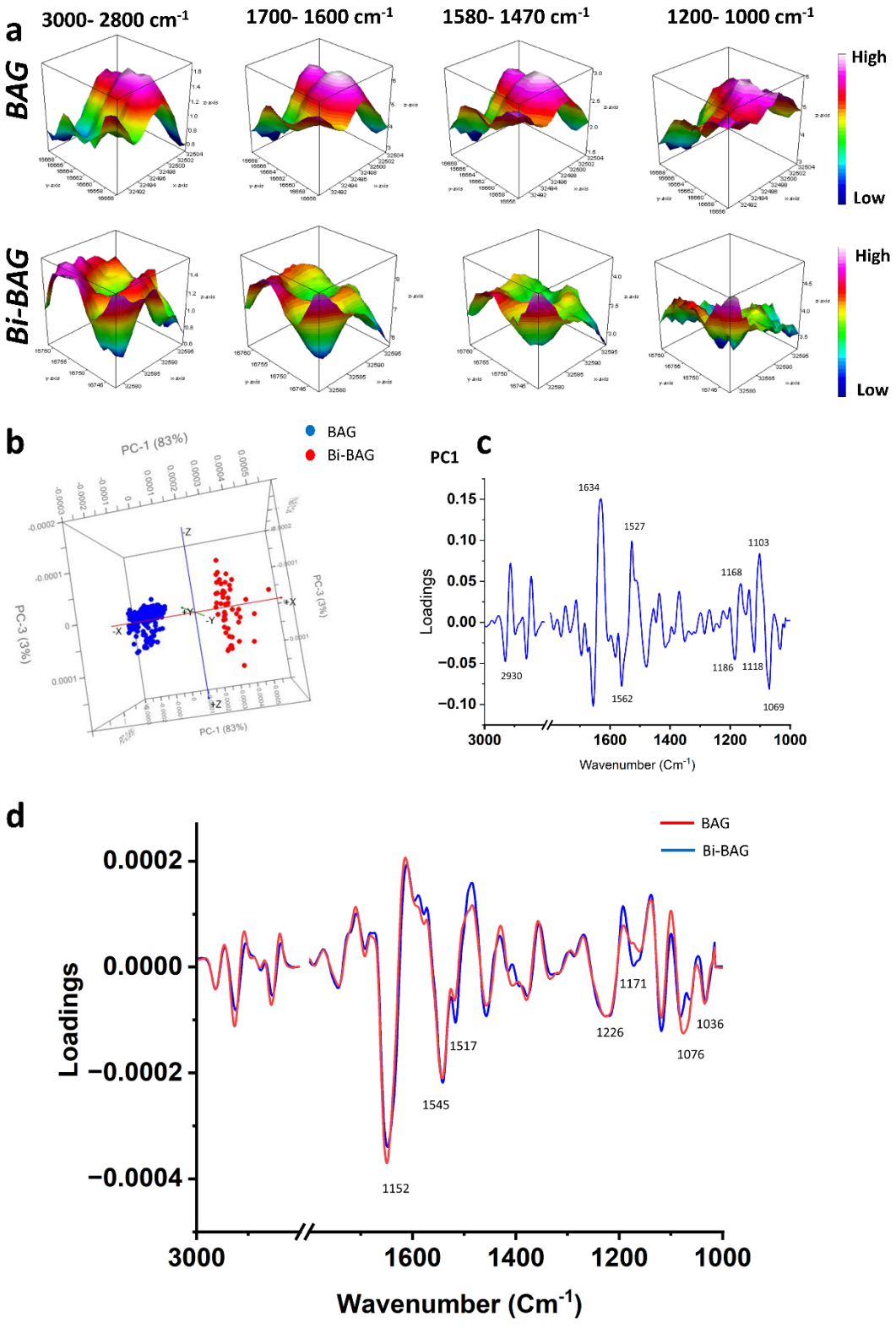

Figure 5.6. Synchrotron-sourced macro-ATR-FTIR microscopy data identified biomolecular changes of *P. aeruginosa* after exposure to Bi-BAG coating. **a)** Synchrotron macro-ATR-FTIR maps, b) PCA score plot, c) PCA loading spectra *P. aeruginosa* BAG.

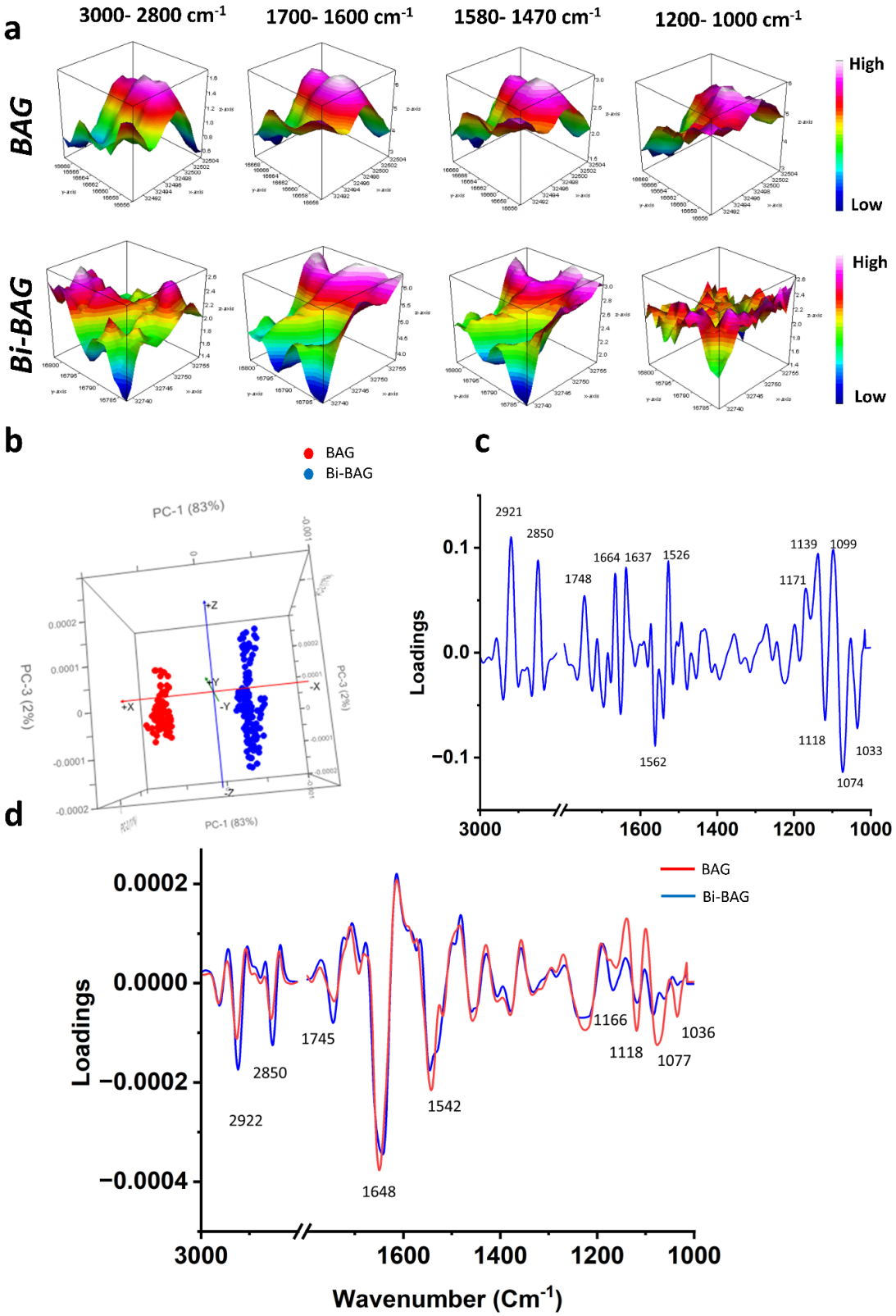

Figure 5.7. Synchrotron-sourced macro-ATR-FTIR microscopy data identified biomolecular changes of *S. aureus* after exposure to Bi-BAG coating. **a)** Synchrotron macro-ATR-FTIR maps, **b)** PCA score plot, **c)** PCA loading spectra *S. aureus* BAG.

In the spectral region associated with nucleic acids (1150-1000 cm^{-1}), both bacterial strains exhibited alterations in the bands corresponding to the phosphate backbone (1236 cm^{-1} and 1080 cm^{-1}). These changes may indicate direct interference with genetic material replication or repair mechanisms. Therefore, the antibacterial action of Bi-BAG not only disrupts bacterial membrane integrity but also affects critical macromolecules, ultimately compromising the overall viability and functionality of bacterial cells

5.2.6 Proteomic analysis of antibacterial mechanisms against *P. aeruginosa* and *S. aureus*

To investigate the antibacterial mechanism of Bi-BAG-coated titanium, we performed a proteomic analysis of *P. aeruginosa* and *S. aureus* [353, 354]. In *P. aeruginosa*, proteomic profiling revealed substantial changes in protein expression after exposure to Bi-BAG. Volcano plot analysis (Figure. 5.8a) identified 155 proteins as significantly upregulated and 211 proteins as downregulated ($p < 0.05$, fold change >2). Hierarchical clustering (Figure. 5.8b) further highlighted the distinct proteomic profiles between the Bi-BAG treated and control groups.

Gene Ontology (GO) enrichment analysis offered functional insights into these alterations. The biological processes (Figure 5.8d) showed significant enrichment in membrane transport and oxidative stress responses, suggesting potential disruptions in nutrient uptake and stress adaptation. The molecular function analysis (Figure. 5.8e) revealed enrichment in ATP binding, transmembrane transporter activity, and oxidoreductase activity, reflecting impaired energy metabolism and transport mechanisms. Finally, cellular component analysis (Figure. 5.8f) highlighted altered proteins localised to the cell membrane, cytoplasm, and extracellular region, emphasising the detrimental impact of the Bi-BAG coating on bacterial integrity

Protein-protein interaction network analysis (Figure. 5.8c) revealed interconnected pathways involving key proteins. Several proteins were downregulated, including the efflux pump membrane transporter (MexA) (responsible for substance efflux and resistance); the type IV

pilus ATPase PilU (which drives pilus assembly); and ATP synthase subunit c (AtpE, critical for ATP production). These decreases suggest compromised efflux, attachment, and energy synthesis. Additional affected proteins include Methionine import ATP-binding protein MetN2 (involved in nutrient acquisition), and Na^+/H^+ antiporter NhaB (crucial for ion homeostasis), indicating impaired bacterial adaptation.

Conversely, certain proteins were upregulated, reflecting stress response mechanisms. Examples include the AAA+ ATPase domain-containing protein ClpX (involved in proteolysis and stress response), and HlyC/CorC family transporter (CorA) (linked to ion transport). In addition, the metal-pseud opaline receptor CntO, associated with mental stress, was elevated, suggesting an attempt by the bacteria to mitigate toxicity caused by the Bi-BAG coating.

Proteomic analysis revealed significant alterations in protein expression profiles in *S. aureus* following exposure to Bi-BAG coatings (Figure. 5.9a). 110 proteins were upregulated, and 90 were downregulated ($p < 0.05$, fold change >2). Hierarchical clustering (Figure. 5.9b) demonstrated distinct expression profiles between treated and untreated samples, providing mechanistic insights into the antibacterial effects of Bi-BAG. Among the key upregulated proteins were Type VII Secretion System Protein EssB, a critical factor for bacterial virulence and stress response, and Efflux RND Transporter Permease Subunit, which facilitates toxin and antibiotic efflux, reflecting bacterial adaptation under Bi-BAG-induced stress.

Diacylglycerol Kinase, an enzyme involved in lipid signalling and membrane repair, and Chaperone Protein DnaJ, an ATP-dependent protein aiding in stress recovery, were also significantly elevated. These responses indicate bacterial efforts to counteract the oxidative damage imposed caused by Bi-BAG coating

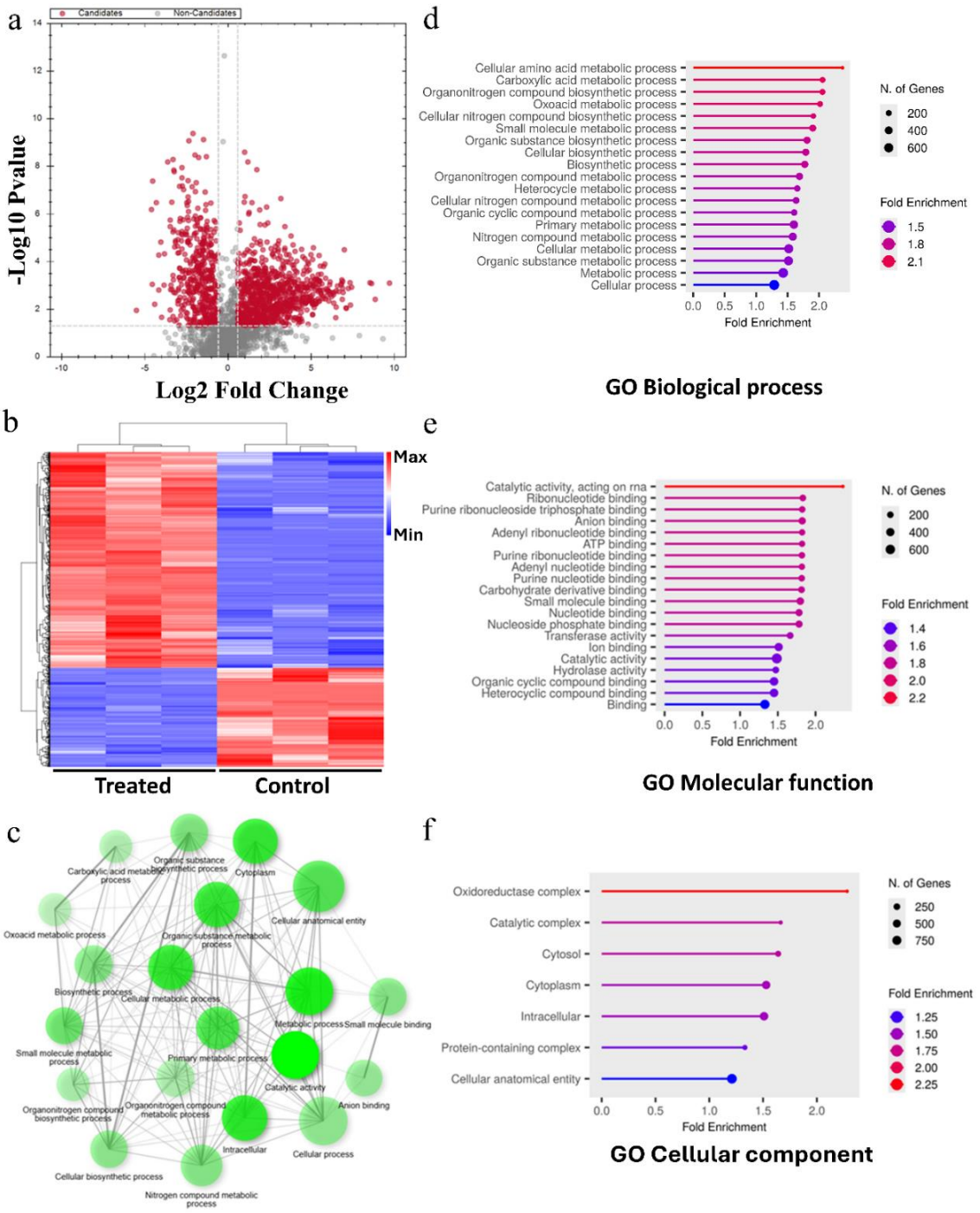

Figure 5.8. The identified proteomic changes of *P. aeruginosa* explain the antibacterial mechanism of Bi-BAG. a) Volcano plot showing the distribution of upregulated and downregulated proteins after Bi-BAG treatment ($p < 0.05$) and fold change (>2-fold). b) Heatmap depicting hierarchical clustering of differentially expressed proteins, categorised into functional groups. c) Protein-protein interaction (PPI) network analysis of differentially expressed proteins. d) Gene ontology (GO) enrichment analysis of biological processes. **e** GO enrichment analysis of molecular functions. **f** GO analysis of cellular components.

Conversely, critical proteins essential for bacterial survival were significantly downregulated. For instance, penicillin-binding protein 2, crucial for peptidoglycan synthesis, was suppressed, compromising cell wall integrity. Similarly, reducing cell division protein FtsA, which plays a key role in bacterial septum formation, impaired cell division. Downregulation of L-lactate Permease, a transporter involved in metabolic processes, and Quinol Oxidase Subunits, components of the electron transport chain, further reaffirm the broad metabolic impact of Bi-BAG on *S. aureus*.

GO enrichment analysis (Figures. 9d–f) revealed that Bi-BAG treatment disrupted critical biological processes such as cell division and peptidoglycan biosynthesis while enhancing pathways related to response to oxidative stress and membrane transport. Molecular functions associated with ATP-dependent processes and membrane-associated proteins were notably affected, highlighting the structural and functional destabilisation.

These proteomic findings are consistent with additional experimental results. Elevated ROS levels (Figure. 5.5a), membrane depolarisation (Figure. 5.5b), and ATP depletion (Figure. 5.5c) aligned with the observed downregulation of energy production pathways. Moreover, SEM imaging (Figure. 5.4a) revealed significant morphological changes, including wrinkled and shrunken bacterial cells, indicative of compromised membranes. CLSM images (Figure. 5.4b) showed reduced fluorescence intensity of membrane dyes, confirming membrane damage. Collectively, these data suggest that Bi-BAG exerts its antibacterial effects through multifaceted mechanisms, including oxidative stress induction, membrane disruption, and metabolic impairment.

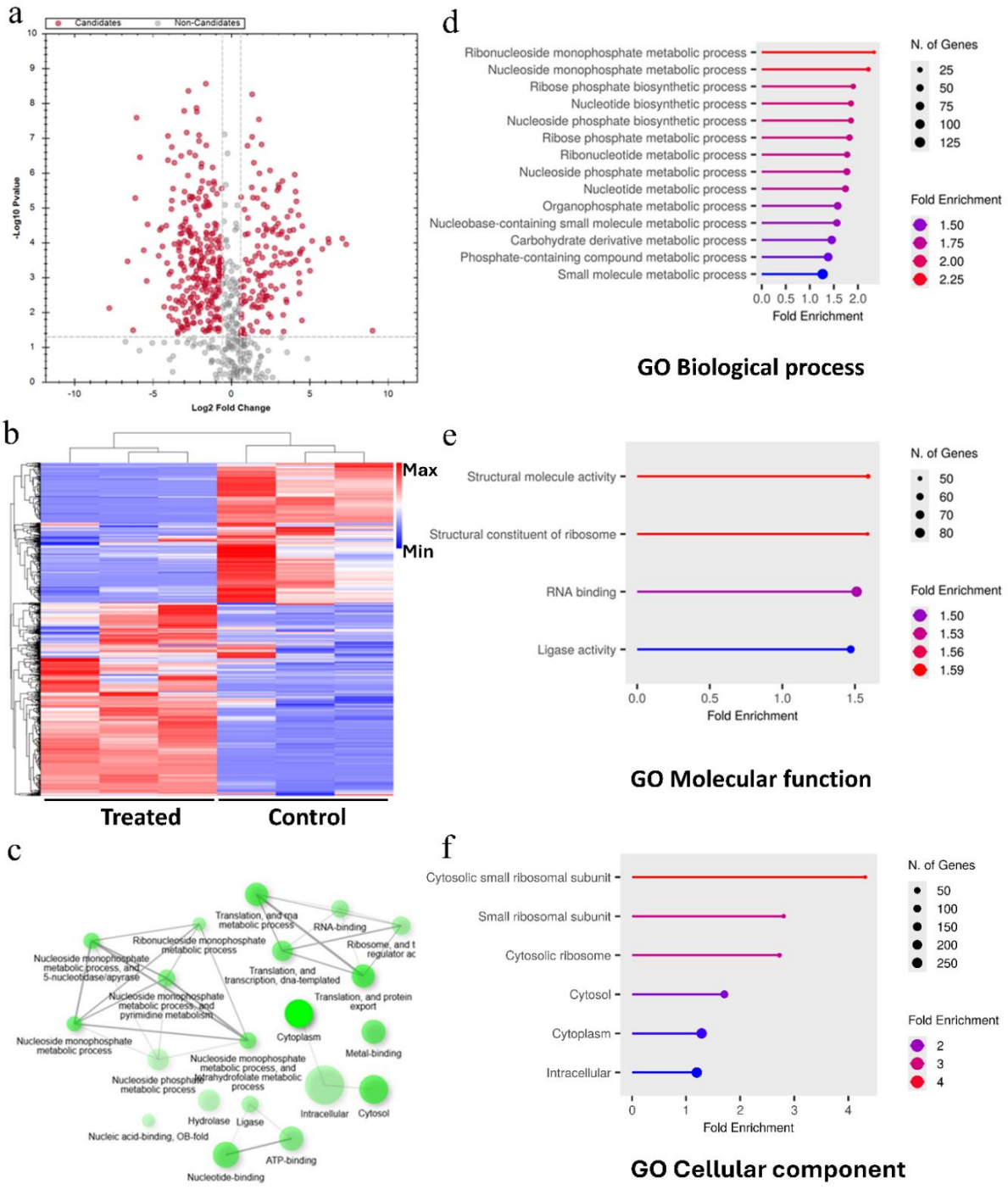

Figure 5.9. The identified proteomic changes of *S. aureus* explain the antibacterial mechanism of Bi-BAG. **a)** Volcano plot showing the distribution of upregulated and downregulated proteins after Bi-BAG treatment ($p < 0.05$) and fold change (>2-fold). b) Heatmap depicting hierarchical clustering of differentially expressed proteins, categorised into functional groups. **c)** Protein-protein interaction network analysis of differentially expressed proteins. **d)** Gene ontology (GO) enrichment analysis of biological processes. **e** GO enrichment analysis of molecular functions. f GO analysis of cellular components.

5.2.7. Bi-BAG coating using flame technology promotes enhanced proliferation and mineralisation of human osteoblast cells

We conducted cell proliferation and mineralisation tests on HAP, BAG, and Bi-BAG coating using human osteoblast cells responsible for forming bone. Osteoblasts achieve this by secreting osteoid proteins, which subsequently mineralize to form bone. Mineralization is a critical step in the bone regeneration process. As shown in Figures 5.10a- 5.10c, human osteoblast cells cultured on Bi-BAG coating showed increased proliferation compared to HAp and BAG at both 1 and 4 days. Furthermore, Bi-BAG had the highest level of mineralisation, followed by BAG and HAp, as indicated by the increased Alizarin Red S staining (Figure. 5.10d & 5.10e). These results suggest that the Bi-BAG coating effectively promotes the deposition of calcium phosphate crystals, which are essential building blocks of bone formation.

5.3. Discussion

Previous studies relied on multi-step processes, including mixing precursor powders, high temperatures calcination, and subsequent pressing and sintering, to produce Bi-BAG bioceramic [23]. Our study introduces a new approach by employing FSP technology for the one-step synthesis and direct deposition of Bi-BAG bioceramic coatings with nano spikes morphology onto titanium substrates (Figure. 5.1 & 5.2). These coatings exhibit strong antibacterial activity, addressing one of the most critical challenges in orthopaedic implants. [22]. The single-step process allows for the rapid and efficient synthesis of Bi-BAG, directly depositing the bioceramics coating onto the substrate, while significantly reducing the number of processing steps. This streamlined approach decreases the time and energy required for fabrication. In addition, FSP enables precise control over the coating's morphology and composition, ensuring uniform particle size, consistent doping, morphology, and reproducibility. This versatility of FSP, combined with the demonstrated antibacterial activity

and biocompatibility of Bi-BAG, positions it as a transformative technology in the field of implant surface modifications.

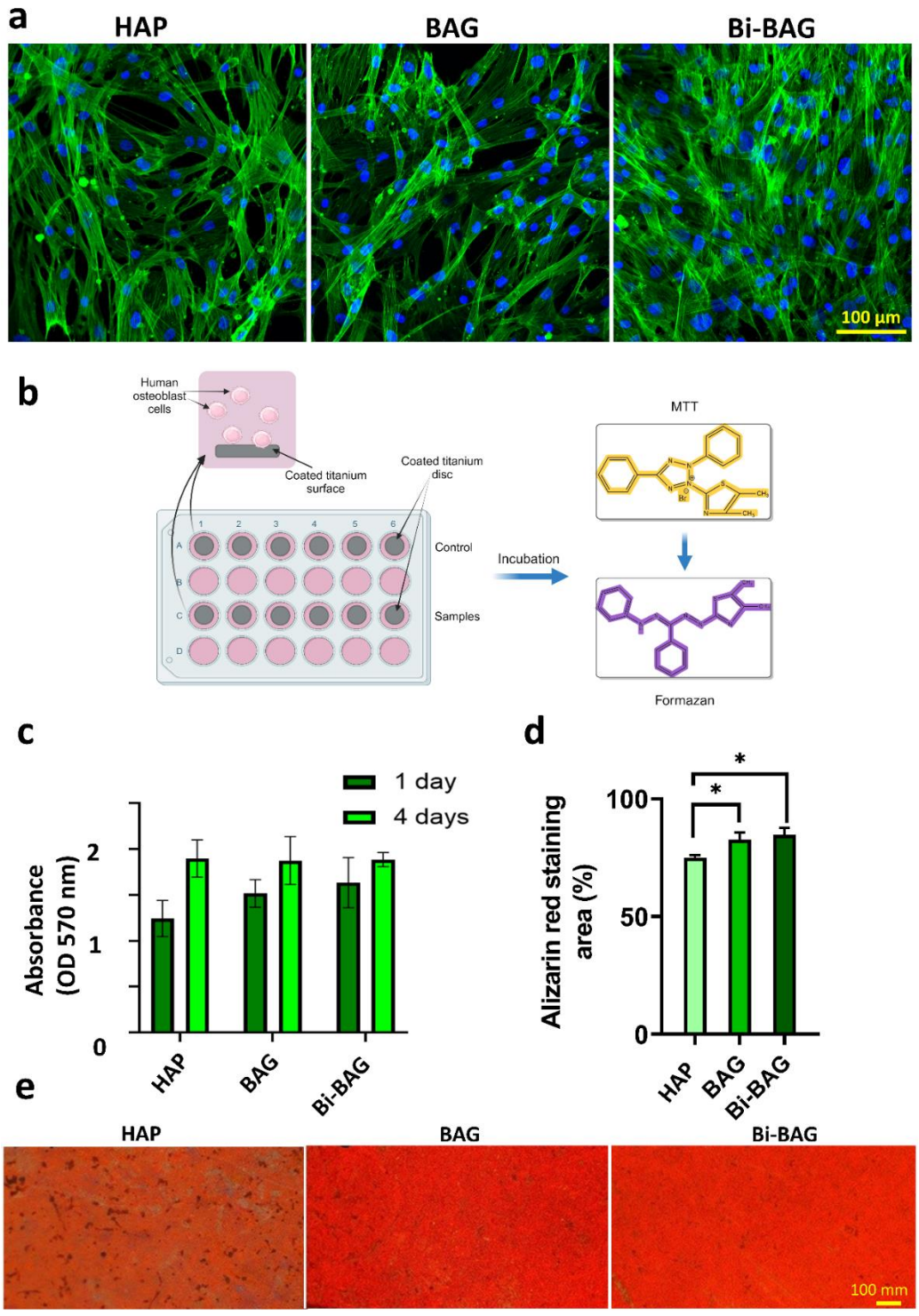

Figure 5.10. Bi-BAG coating using flame technology enhances human HOBs proliferation and mineralisation. a) CLMS images of HOBs cells grown on HAp, BAG, and Bi-BAG coated

titanium discs for 4 days. b) Schematic of the experimental setup for the MTT assay and human osteoblast-like cell culture on coated titanium discs. c) Quantitative MTT assay results at 1 and 4 days show no significant difference in cell viability between the coatings. d) Alizarin Red S staining quantification indicating higher mineralisation for Bi-BAG coated surfaces, marked by an asterisk to denote statistical significance. e) Representative images of Alizarin Red S staining of cells cultured on different surfaces, with Bi-BAG demonstrating enhanced mineral deposition.

We demonstrate that bactericidal surfaces with sharp nanospikes can synergize with Bi^{3+} ions released by BI-BAG. This synergy can effectively prevent surface contamination by pathogens right from the early stages of attachment and remains effective for up to 24 hours. The application of nanospike coatings on titanium for orthopaedic implants has gained significant attention due to their ability to mimic natural structures, such as dragon and cicada wings. These structures not only promote better integration with bone tissue but also prevent bacterial colonisation without antibiotics [342, 355-357]. colonization without relying on antibiotics [339, 363–365]. Although HAp and BAG coatings also feature nano spikes, their antibacterial activity is significantly lower than Bi-BAG (Figure 5.3). This highlights the critical role of bismuth in the observed antibacterial effects. The nano spikes in the Bi-BAG coating enhance antibacterial performance by increasing the surface area for Bi^{3+} release and facilitating closer interaction between the bismuth and bacterial cells. It is important to note that the nanospikes alone, without bismuth, do not exert a strong bactericidal effect. This may be attributed to several factors, such as the specific dimensions and arrangement of the nanospikes, the bacterial species tested, and the overall surface properties of the coating. A plausible explanation is that the Bi-BAG coating acts as a nano-injector, facilitating the penetration of bismuth ions into bacterial cells and enhancing their intracellular antibacterial effects.

The synergistic antibacterial mechanism of Bi^{3+} ions and nano spikes highlights their complementary effects in significantly enhancing bactericidal activity. The physical disruption

caused by the nanospikes, which mimic the mechano-bactericidal structures of natural surfaces like cicada wings, is observed in SEM images (Figure. 5.4a). These images reveal wrinkled and shrunken bacterial cells on Bi-BAG-coated surfaces, in contrast to the intact morphology of bacteria on HAp and BAG surfaces. This physical damage compromises membrane integrity, further supported by FM4-64-stained CLSM images (Figure. 5.4b), which show reduced fluorescence intensity and irregular membrane shapes on Bi-BAG-treated surfaces. In addition, Bi-BAG spike-like nanostructures function similarly to nanoneedles. These nanoneedles mechanically penetrate bacterial membranes and act as conduits for delivering Bi^{3+} directly into bacterial cells. This dual mechanism of sharp nanostructures for mechanical damage and Bi^{3+} release for chemical damage explains why Bi-BAG exhibits significantly stronger bacterial interaction than HAp and BAG (Figure 5.4c).

Bi-BAG disrupts bacterial metabolic processes by generating ROS, impairing proteins, lipids, and nucleic acids. Confocal microscopy images (Figure 5.5a) reveal significantly higher ROS production in Bi-BAG-treated bacterial cells than those treated with HAP and BAG. Proteomic analysis further substantiates these findings, showing the downregulation of ATP synthase subunit c (AtpE), essential for ATP production, and efflux pump transporter MexA, crucial for bacterial survival and resistance (Figure. 8c). These changes indicate that Bi-BAG interferes with energy metabolism and nutrient efflux, critical for bacterial adaptation and growth.

The multifaceted antibacterial mechanisms of Bi-BAG are demonstrated by synchrotron ATR-FTIR spectra, which show significant alterations in the lipid (3000–2850 cm^{-1}), protein (1700–1450 cm^{-1}), and nucleic acid (1150–1000 cm^{-1}) regions for both *P. aeruginosa* and *S. aureus* (Figures. 5.6a & 5.6b, 5.7a & 5.7b). These biochemical disruptions were especially evident in the destabilisation of the lipid bilayer, as evidenced by changes in the methyl and methylene

group peaks at 2925 cm^{-1} and 2852 cm^{-1}, and in protein structural alterations, such as shifts in the amide I and II bands (1654 cm^{-1} and 1637 cm^{-1}).

Proteomic analysis revealed that Bi-BAG-treated *S. aureus* exhibited downregulation of key proteins, including penicillin-binding protein 2, which is essential for peptidoglycan synthesis, and cell division protein FtsA, critical for septum formation during cell division (Figure. 5.9c). This disruption in structural and metabolic proteins aligns with observed membrane depolarisation (Figure. 5.5b) and ATP depletion (Figure. 5.5c), indicating a collapse of bacterial homeostasis. The upregulation of stress response proteins, such as AAA+ ATPase ClpX and Type VII secretion system protein EssB, reflects bacterial attempts to counteract the damage, however, these attempts are insufficient against the multifaceted assault of Bi^{3+} ions and spike-like.

The biocompatibility of Bi-BAG coatings is a critical aspect of their multifunctionality, demonstrating an optimal balance between antibacterial efficacy and the promotion of bone cell activity. This balance is achieved through a carefully engineered design that leverages the distinct biological responses of bacteria and mammalian cells to Bi^{3+} ions and the nanocoating. While the coating effectively disrupts bacterial cells, it simultaneously supports the proliferation and mineralisation of bone cells, as shown in human osteoblast experiments. MTT assay results (Figure. 5.10b) reveal no cytotoxic effects on osteoblasts cultured on Bi-BAG coatings, while Alizarin Red S staining (Figures. 5.10c, 5.10d) indicates significantly enhanced mineralisation compared to HAp and BAG coatings. These findings confirm the dual functionality of Bi-BAG coatings, which effectively combat bacterial infections without compromising bone regeneration.

The selectivity of Bi-BAG coatings in killing bacteria while enhancing HOBs is attributed to the fundamental differences in their cellular structures. Gram-negative bacteria possess an

outer membrane rich in lipopolysaccharide (LPS), a periplasmic space containing a thin peptidoglycan layer [358]. Gram-positive bacteria lack an outer membrane but contain a much thicker peptidoglycan wall interlaced with teichoic acids [359]. The LPS phosphate groups make them highly susceptible to the mechanical and chemical stress induced by nano spikes and Bi^{3+} ions. The sharp nano spikes physically disrupt bacterial membranes, while Bi^{3+} ions generate ROS that damage bacterial proteins, lipids, and nucleic acids. This multifaceted antibacterial mechanism is highly effective against both Gram-negative and Gram-positive bacteria. In contrast, bone cells possess robust cellular machinery, thicker lipid bilayers, and advanced repair mechanisms that allow them to withstand moderate levels of ROS and maintain homeostasis. This structural and functional resilience allows bone cells to thrive on Bi-BAG coatings, supporting their proliferation and activity while targeting bacterial cells.

This is supported by previous research showing that Bi-BAG promotes the differentiation and proliferation of osteoblast cells [23]. Bi-BAG coating has the potential to serve as innovative materials for bone grafts (scaffolds) and coating for tissue engineering applications. The promotion of osteoblast activity by Bi-BAG coatings is further attributed to the bioactivity of Bi^{3+} and BAG, which enhance bone cell attachment and proliferation. Baghdadite's inherent osteoconductive properties facilitate cell anchorage, while the controlled release of Bi^{3+} stimulates osteogenic pathways without inducing cytotoxicity. This dual action is essential for orthopaedic implants, where the surface must prevent bacterial colonisation while fostering integration with host bone tissue. The enhanced mineralisation observed in osteoblasts cultured on Bi-BAG coatings highlights their potential to accelerate bone healing and regeneration, addressing a critical challenge in implant design.

Balancing antibacterial activity with biocompatibility is a pivotal consideration in the engineering of multifunctional coatings. The Bi-BAG coating achieves this balance by fine-

tuning the size, distribution, and concentration of nano spikes and Bi^{3+} ions to ensure selective bacterial targeting while preserving and enhancing bone cell functions. This design strategy minimises potential adverse effects, such as excessive ROS production that could harm mammalian cells. By leveraging the differential susceptibilities of bacteria and bone cells, Bi-BAG coatings provide a novel and effective solution for orthopaedic implants, reducing the risk of implant-associated infections and promoting successful osseointegration. These findings highlight the importance of integrating biological and material science principles in developing next-generation biomaterials for clinical applications.

The successful application of Bi-BAG coatings has significant implications for the future of orthopaedic implant technologies. By providing a robust barrier against bacterial colonisation and promoting tissue integration, Bi-BAG coatings can substantially reduce the rate of surgical revisions due to infections, decrease healthcare costs, and improve patient outcomes. Our research contributes a transformative approach to orthopaedic biomaterials, positioning Bi-BAG coatings as a leading solution for next-generation applications.

5.4. Conclusion

This study highlights the potential of FSP technology to revolutionise the fabrication of bioactive and antibacterial coatings, offering an innovative solution to the enduring challenge of implant-associated infections. The synergy between Bi^{3+} and spike-like nanocoating enhances the antibacterial activity of Bi-BAG coatings by combining physical membrane disruption with chemical metabolic impairment. Morphological, biochemical, and proteomic evidence strongly supports the effectiveness of Bi-BAG coatings as an advanced strategy for preventing implant-associated infections. In addition to addressing bacterial colonisation, this multifunctional coating promotes osteogenesis, offering a dual-action approach to improving orthopaedic implant outcomes. Future research will focus on pre-clinical *in vivo* studies to

validate the safety and efficacy of Bi-BAG coatings for clinical applications, to redefine the standard for orthopaedic implants. This multifunctional coating addresses the critical challenge of bacterial colonisation while simultaneously promoting osteogenesis, providing a dual-action strategy for improving orthopaedic implant outcomes. Future studies will focus on pre-clinical studies *in vivo* to validate the efficacy and safety of Bi-BAG coatings for clinical use and to validate the efficacy and safety of Bi-BAG coatings aiming to revolutionise the standard for orthopaedic implants. Future research will focus on pre-clinical *in vivo* studies, to revolutionise the standard for orthopaedic implants.

5. 5. Materials and methods

Materials. All the chemical reagents and solvents for the material synthesis were used as received without further purification. Ultrapure deionised water (resistivity 18.2 MΩ cm^{-1}) was used in preparing aqueous solutions in all experiments. Titanium substrates were cut into disks with a diameter of 1 cm. The disks were cleaned with deionised (DI) water, then ethanol and DI water sequentially.

HAp, BAG and Bi-BAG fabrication. The materials were prepared using a custom-built flame spray pyrolysis (FSP) system as described in our previous studies[341, 343, 344]. Particularly, calcium naphthenate in mineral spirits (4% Ca), tributyl phosphate (>99%, Sigma-Aldrich), zirconium(IV) isopropoxide solution (70 wt.% in 1-propanol, Sigma-Aldrich), and were dissolved in a 1:1 (vol) mixture of toluene (anhydrous 99.8%, Sigma-Aldrich) and 2-ethylhexanoic acid (99%, Sigma-Aldrich) to obtain concentrations of 0.2 M for metal precursor concentration with nominal stoichiometric ratios to form Ca_5P_3 (HAP), Ca_3ZrSi_2 (BAG), and 15 at.% Bi-doped BAG. The solutions were fed at 5 mL min^{-1} through the FSP system by syringe pumps and atomised with oxygen flow (5 L min^{-1}, BOC grade 2.5) at a constant pressure drop of 4.5 bar. The resulting spray was ignited with a surrounding annular set of

premixed methane/oxygen flame (CH_4-flamelet 1.8 L min^{-1}, O_2-flamelet 2.0 L min^{-1}, COREGAS grade 4.5). The materials were deposited directly on Ti disks in one minute at a high above a burner of 8 cm.

Material Characterization. XRD patterns were measured directly with the samples coated on Ti substrate by a D2 Phaser Bruker system with Cu *Kα* radiation of average wavelength 1.54056 Å at a scan rate of 1.17 min^{-1}. The morphology of the films was investigated using a field-emission scanning electron microscope (FESEM) Zeiss Ultra Plus operating at 3 kV without coating.

XPS analysis was performed using a calibrated ESCALAB250Xi spectrometer (Thermo Scientific, UK) with a monochromated Al Kα source at a power of 120 W (13.8 kV × 8.7 mA). The base pressure in the main vacuum chamber during analysis was typically between 10^{-9} and 10^{-8}mbar. Survey spectra were acquired at a pass energy of 160 eV. To obtain more detailed information about the chemical structure, oxidation states, and so forth, high-resolution spectra were recorded at 20 eV pass energy (yielding a typical peak width for polymers of ≈1 eV). Spectra were collected at normal emission. The data was analysed using CasaXPS software version 2.3.25 PR1.0. Adventitious C 1s (284.8 eV) peak was used to calibrate the spectra.

Preparation and testing of antibacterial coatings. HAp, BAG and Bi-BAG coating were tested for antibacterial activity against two bacterial strains: *Pseudomonas aeruginosa* (ATCC 15692), *Staphylococcus aureus* (ATCC 25923). Bacterial strains were recovered from glycerol stocks stored at -80°C and streaked for purity on tryptone soy agar (TSA). One isolated colony of each species was transferred aseptically from TSA to 5 mL of tryptone soy broth (TSB) and cultured at 37 °C until the late log phase (approximately 6-8 h). Baghdadite and doped baghdadite samples were aseptically placed in sterile 24-well plates and immersed in 0.5mL of the 10^6 CFU/mL bacterial suspensions, then incubated for 6 h or 24 h.

Live/Dead® BacLight™ viability assay. CLSM was used to visualise and quantify the proportions of live and dead cells using the LIVE/DEAD® *Bac*Light™ Bacterial Viability Kit (Molecular Probes, Invitrogen, USA), which contains SYTO9 and propidium iodide fluorescent dyes [356]. SYTO9 enters all cells, binding to nucleic acids and fluorescing green. Propidium iodide (PI) only enters cells with disrupted membranes and has a stronger affinity for nucleic acids than SYTO9. PI fluoresces red and indicates dead or viable cells. SYTO9 and PI were prepared in equal proportions at 1.5 µL/mL in phosphate-buffered saline (PBS), and 1 mL of the solution was used to immerse each sample for 15 minutes in the dark at room temperature. Samples were immediately imaged with a Zeiss_LSM880 (Zeiss, Oberkochen, Germany) CLSM immediately after staining. Using a dual emission filter, the CLSM was set up to image both live cells in green (Syto9, Ex/Em 480/500 nm) and dead cells in red (PI, Ex/Em 490/635 nm).

Colony enumeration. The colony forming unit (CFU) determination and log reduction data were performed. Following incubation, sample discs were vortexed in PBS for 15 seconds, then sonicated for 5 minutes before being vortexed for another 15 seconds and serially (1:10) diluted. In triplicate, serially diluted samples (10 µL) were dropped onto TSA plates and incubated for 18 hours at 37 °C. Viability assays were performed by standard plate counts, and the quantity of CFU per sample was calculated using the number of colonies counted, the aliquot size and the dilution factor.

SEM characterisation of bacterial morphology on the surface. SEM was used to observe the morphological changes according to previous studies [316]. Disc samples were cultured with bacteria (approx. 1 x 10^6 CFU/ml) and incubated in TSB medium at 37oC for 6 h and 24 h. After incubation, all discs were washed twice with PBS (pH 7.4) to remove unattached cells. The bacterial cells were fixed in 4% glutaraldehyde for 1 h at room temperature. The samples

were dehydrated in sequential graded ethanol (30%, 50%, 70%, 90%, 100%). Finally, all samples were coated with 2nm platinum. Samples were then observed in a FEI Inspect F50 (FEI Company, Oregon, USA) at 5kV with a working distance of 5 mm.

FIB-SEM imaging. The bacteria incubated with HAp, BAG, and Bi-BAG are like live and dead assays. Following incubation, the discs were gently rinsed with phosphate-Imaging using a Focused Ion Beam-Scanning Electron Microscope (FIB-SEM, FEI Helios NanoLab, Adelaide Microscope). The system was calibrated for both electron and ion beam operation before starting. The ion beam was used to mill the surface of the disc, exposing cross-sectional views of bacterial cells interacting with the coating. The milling current and dwell time were optimised to prevent thermal damage and ensure precision. High-resolution SEM images of the bacterial cross-sections were captured at 5 kV and 10 µA with a working distance of 5 mm. The interaction between bacterial membranes and the spike-like nanostructures on the disc surface was observed and documented.

The ROS level determination. To investigate the ROS levels in target bacteria, we used an intercellular ROS formation was assessed using a DCFDA/H2DCFDA- Cellular ROS Assay Kit (ab113851, Abcam, USA). Following incubation with HAP, BAG, and Bi-BAG samples, bacteria were incubated with DCFH-DA (50 µM) in the dark for 30 minutes according to the manufacturer's instructions. The samples were then immediately imaged with a Zeiss_LSM880 CLSM using Ex/Em of 485/535 nm. Images were taken at three random locations per sample. The fluorescence intensity of each image was then determined using ImageJ v1.53a (NIH, Maryland, USA). The ROS level was calculated based on the fluorescence intensity of the DCF, which is converted to a highly fluorescent compound by ROS. Higher fluorescence intensity indicates higher ROS levels in the bacterial cells.

Determination of cell membrane potentials. following incubation, the membrane potential of bacterial cells was measured using the *Bac*Light Bacterial Membrane Potential Kit (Invitrogen, ThermoFisher, Massachusetts, USA). The staining procedure was carried out according to the manufacturer's instructions. The samples were then immediately imaged using a Zeiss_LSM880 CLSM, using Ex/Em 482/497 nm. 3 micrographs were taken randomly, and the images were imported into ImageJ v1.53a. Fluorescence intensity was measured in the green and red channels, and a red-to-green ratio was calculated using the acquired intensities.

Synchrotron macro-ATR-FTIR. To study the biochemical changes in bacterial cells exposed to HAp, BAG and Bi-BAG samples, we used synchrotron ATR-FTIR microspectroscopy at the Australian Synchrotron. Bacterial cells were grown and treated according to the previous experimental design for 6 hours with the smooth group of HAp, BAG, and Bi-BAG samples, after which they were collected and deposited onto the ATR crystal of the synchrotron microscope. ATR-FTIR spectra were then collected across the spectral range of 3400-1000 cm-1, allowing for the identification and quantification of various molecular vibrations and functional groups. The resulting spectra were then analysed using various chemometric methods, such as hierarchical clustering analysis (HCA), second derivative spectroscopy, and principal component analysis (PCA), to identify changes in the biochemical composition of the bacteria. HCA was used for quality control and to identify outlier spectra, while second derivative spectroscopy enhanced the resolution of overlapping peaks. PCA was used to explore the clustering patterns and chemical composition differences among the treatment groups.

Proteomic analysis of bacterial interaction with Bi-BAG: P. aeruginosa and *S. aureus* (were incubated with Bi-BAG discs for 24 hours at 37°C in TSB. Post-incubation, the bacterial cells were washed three times with PBS to remove any unbound material. Bacterial cells were

detached from the discs using a bath sonicator for 2 minutes, followed by vortexing for 15 minutes to ensure complete detachment. The cells were then collected by centrifugation at 4,000 g for 10 minutes and prepared for proteomic analysis. The S-Trap™ microspin column digestion protocol was employed for protein alkylation and digestion. The bacterial cell pellets were lysed in sodium dodecyl sulfate lysis buffer (5% SDS, 50 mM Tris, 20 mM dithiothreitol) at 70°C for 60 minutes. To block cysteine residues, 40 mM iodoacetamide (Viodoacetamide:Vsample = 1:25) was added, and the samples were incubated in the dark for 30 minutes at room temperature. Proteins were digested using trypsin at a 1:50 ratio (trypsin:protein) and incubated overnight at 37°C. Digested proteins were eluted using S-Trap microspin columns according to the manufacturer's protocol. Samples were analysed using liquid chromatography-tandem mass spectrometry (LC-MS/MS) in data-dependent acquisition mode for library generation and data-independent acquisition (DIA) mode for quantification. The LC-MS/MS system was calibrated and operated following standard protocols. Label-free quantification was performed using Spectronaut software, which generated MSstats output reports.

Proteomic data were processed using MSstats v3.18.5.71, employing the Turkey median-polish summary approach and run-level quantile normalisation. The analysis utilised the three most important peptide features for each protein, normalised at the run level. A robust linear mixed-effects model was applied to calculate the relative frequencies of the label-free data.

Gene Ontology (GO) enrichment pathway analysis was performed using ShinyGO v0.81 to identify cellular components, molecular functions, and biological processes affected by Bi-BAG and HAp treatment. GO terms were identified based on significantly enriched pathways, with results categorised into functional groups to highlight the biological impact of Bi-BAG and HAp on bacterial cells.

Confocal microscopy for cell morphology: HOBs were seeded onto HAp, BAG, and Bi-BAG-coated titanium discs at a density of 3×10^4 cells per disc and incubated at 37°C with 5% CO_2 for 24 hours. After incubation, the cells were fixed with 4% paraformaldehyde for 20 minutes at room temperature. The samples were then permeabilised with 0.1% Triton X-100 for 10 minutes. The actin cytoskeleton was stained using Alexa Fluor 488-phalloidin (Thermo Scientific) for 90 minutes, followed by counterstaining of the nuclei with DAPI (Thermo Scientific) for 10 minutes. After staining, the samples were washed thoroughly with PBS and mounted for imaging. CLSM was performed using lasers set at 488 nm for Alexa Fluor 488 and 405 nm for DAPI.

MTT assay for cell viability: To evaluate cell viability, HOBs were seeded onto the HAp, BAG, and Bi-BAG-coated titanium discs in a 24-well plate at a density of 1×10^4 cells per disc. The cells were incubated for 1 and 4 days under standard culture conditions (37°C, 5% CO_2). The culture medium was replaced with 200 µL of MTT reagent (0.5 mg/mL in serum-free medium), and the samples were incubated for 4 hours at 37°C. Following incubation, the MTT reagent was carefully removed, and the formazan crystals formed by viable cells were dissolved using 200 µL of DMSO. The optical density (OD) of the solution was measured at 570 nm using a microplate reader. Media without cells served as the negative control. Each group was tested in triplicate, and the results were reported as mean ± SD.

Alizarin red staining for mineralisation: To assess mineralisation, HOBs were cultured on HAp, BAG, and Bi-BAG-coated titanium discs for 14 days in osteogenic medium containing 10 mM β-glycerophosphate, 50 µg/mL ascorbic acid, and 10 nM dexamethasone. At the end of the incubation period, the cells were fixed with 4% paraformaldehyde for 20 minutes and washed with PBS. The fixed samples were stained with 2% Alizarin Red S solution (pH 4.2) for 30 minutes at room temperature to detect calcium deposits. Excess stain was removed by

washing the samples with distilled water, and the stained area was quantified using image analysis software. Representative images of the stained samples were captured under a light microscope, and the percentage of Alizarin Red-stained area was calculated for each group.

Statistical analyses. Statistical significance was evaluated using one-way analysis of variance (ANOVA) with Tukey's multiple comparisons test. p-value < 0.05 was considered statistically significant. All experiments were performed in triplicate and data are presented as mean and standard deviation (SD).

CHAPTER 6:

CONCLUDING REMARK AND FUTURE PERSPECTIVE

Conclusions

This thesis has demonstrated the potential of Mg^{2+} and Bi^{3+} doped BAG bioceramics as next-generation orthopaedic implants, addressing the dual challenges of infection prevention and bone regeneration. Comprehensive analysis revealed that Mg-BAG and Bi-BAG materials exhibit antibacterial activity against clinically significant pathogens such as *P. aeruginosa* and *S. aureus.* This efficacy is linked to ROS generation, membrane depolarisation, and disruption of intracellular biomolecules. Furthermore, osteoblast proliferation and mineralisation studies confirmed that these coatings actively supported bone cell functions, reinforcing their suitability for orthopaedic applications. The study also optimised FSP technology for fabricating uniform nanospike-structured Bi-BAG coatings on titanium implants. These coatings significantly increased surface area and enhanced antibacterial performance without compromising biocompatibility. Studies on osteoblast proliferation and mineralisation confirmed that these coatings actively supported bone cell functions, further solidifying their suitability for orthopaedic applications. By providing a non-antibiotic approach to IAIs while promoting osseointegration, this work represents a significant advancement in developing multifunctional bioceramics for orthopaedic implants. Future efforts will focus on pre-clinical *in vivo* studies to validate the efficacy and safety of these materials, paving the way for their clinical application and transforming the standards for orthopaedic implant design.

In chapter 2, this study reviewed the advancements and challenges of bioceramics for orthopaedic applications, focusing on their antibacterial properties. This chapter provided a foundation for understanding how metal ion doping and surface modifications can enhance antibacterial efficacy and bioactivity, addressing critical gaps in the design of next-generation bioceramics.

In chapter 3, we successfully developed and characterised Mg-BAG. This chapter demonstrated its broad-spectrum antibacterial activity against *P. aeruginosa* and *S. aureus*. The antibacterial mechanisms studies revealed that Mg-BAG induces intracellular ROS generation, membrane depolarisation, and biomolecular disruptions, highlighting its potential as a multifunctional material for preventing implant-associated infections.

In chapter 4, we explored bismuth-doped baghdadite (Bi-BAG), demonstrating its remarkable antibacterial efficacy and unique multi-action mechanisms. Using advanced synchrotron ATR-FTIR and proteomic analyses, we elucidated how Bi-BAG disrupts bacterial membrane integrity, induces oxidative stress, and interferes with biomolecular pathways. These findings established Bi-BAG as a promising candidate for infection-resistant orthopaedic implants. Additionally, Bi-BAG enhanced cellular attachment, proliferation, and metabolic activity, supporting its excellent biocompatibility, critical for bone regeneration and implant integration. Bi-BAG has the capability of antibacterial activity, supporting osteoblast activity while mitigating inflammatory responses, underscores Bi-BAG's potential for preventing implant-associated infections and for enhancing tissue integration and healing. Overall, these findings position Bi-BAG as a highly promising multifunctional biomaterial for orthopaedic implants.

In Chapter 5, we explored the application of Bi-BAG coatings fabricated using flame spray technology, a versatile and scalable method for producing uniform and durable coatings. The findings demonstrated that Bi-BAG coatings exhibit both physical and chemical antibacterial mechanisms, making them highly effective in combating implant-associated infections. The physical antibacterial mechanism was attributed to the spike-like nanostructures formed on the Bi-BAG surface during the flame spray process. These structures act as nanoneedles, physically piercing bacterial membranes, resulting in significant structural deformation and leakage of intracellular contents. Focused ion beam-scanning electron microscopy (FIB-SEM)

revealed extensive bacterial membrane disruption and penetration, underscoring the mechanical effectiveness of the nanostructured surface. The chemical antibacterial mechanism of Bi-BAG coatings was driven by the sustained release of Bi^{3+} ions. These ions induce oxidative stress in bacteria, disrupting critical biomolecular pathways and destabilizing the lipid bilayer of bacterial membranes. Advanced synchrotron ATR-FTIR and proteomic analyses further confirmed alterations in bacterial biochemical profiles, highlighting the disruption of proteins and nucleic acids essential for bacterial survival. Bi-BAG coatings also demonstrated excellent stability under physiological conditions, maintaining their antibacterial efficacy over prolonged periods. Importantly, the flame spray technology allowed for fine control over the coating thickness and surface roughness, optimizing both antibacterial properties and biocompatibility.

Future Perspective

While this thesis has achieved substantial progress, several areas for further exploration remain to optimise the application of Mg-BAG and Bi-BAG materials. Future studies should prioritise long-term *in vivo* investigations to validate the clinical applicability of these materials under complex physiological conditions. Key focus areas include evaluating their interactions with host immune responses, mechanical stresses, and bone healing processes to fully understand their potential in real-world scenarios.

Broadening the spectrum of pathogens studied is another important direction. Investigating the antibacterial performance of these materials against multi-drug-resistant strains and a wider range of clinically relevant bacteria will help confirm their versatility and robustness. Moreover, gaining deeper mechanistic insights into the selective action of Bi-BAG coatings, specifically their ability to target bacteria without harming bone cells, could inform the development of even more targeted and effective therapeutic materials.

Future research should focus on developing personalised smart 3D-printed scaffolds tailored to precisely fit bone defects and capable of releasing antibacterial agents in the presence of bacteria. This targeted approach can ensure effective treatment while minimising side effects and reducing the risk of bacterial resistance. Designing scaffolds with stimulus-responsive mechanisms that adapt to the microenvironment presents another promising avenue. This could include the integration of smart polymers or microfluidic systems that respond to environmental cues such as temperature, pH, or biomarkers, allowing for controlled and localised delivery of therapeutic agents.

Comprehensive preclinical studies in animal models will be crucial to evaluate the long-term safety and efficacy of these scaffolds, particularly for large bone defect repair. This research could pave the cover for human clinical trials, leading to the widespread use of these innovative biomaterials in orthopaedic practice. Such research could pave the way for human clinical trials and ultimately lead to the widespread adoption of these innovative biomaterials in orthopaedic practice.

This research provides a strong foundation for advancing bioceramics as transformative solutions for orthopaedic applications, particularly in an era of rising antibiotic resistance. By addressing critical challenges such as infection control and bone regeneration, these efforts contribute to the development of next-generation biomaterials that hold the promise of significantly improving patient outcomes in orthopaedic medicine.

References

1. Łuczak, J.W., et al., *The Future of Bone Repair: Emerging Technologies and Biomaterials in Bone Regeneration.* International Journal of Molecular Sciences, 2024. **25**(23): p. 12766.
2. Corio, V., *World Congress on Osteoporosis, Osteoarthritis and Musculoskeletal Diseases (WCO-IOF-ESCEO 2023).* Aging Clinical and Experimental Research, 2023. **35**: p. 37-613.
3. Fernandez de Grado, G., et al., *Bone substitutes: a review of their characteristics, clinical use, and perspectives for large bone defects management.* Journal of tissue engineering, 2018. **9**: p. 2041731418776819.
4. Kumawat, V.S., S. Bandyopadhyay-Ghosh, and S.B. Ghosh, *An overview of translational research in bone graft biomaterials.* Journal of Biomaterials Science, Polymer Edition, 2023. **34**(4): p. 497-540.
5. Punj, S., J. Singh, and K. Singh, *Ceramic biomaterials: Properties, state of the art and future prospectives.* Ceramics International, 2021. **47**(20): p. 28059-28074.
6. Ahmed, S.K., et al., *Antimicrobial resistance: impacts, challenges, and future prospects.* Journal of Medicine, Surgery, and Public Health, 2024. **2**: p. 100081.
7. Roohani-Esfahani, S., et al., *Repairing a critical-sized bone defect with highly porous modified and unmodified baghdadite scaffolds.* Acta biomaterialia, 2012. **8**(11): p. 4162-4172.
8. Li, J.J., et al., *Effects of material–tissue interactions on bone regeneration outcomes using baghdadite implants in a large animal model.* Advanced healthcare materials, 2018. **7**(15): p. 1800218.
9. Nasser Atia, G.A., et al., *Baghdadite: A Novel and Promising Calcium Silicate in Regenerative Dentistry and Medicine.* ACS Omega, 2022.
10. Sadeghzade, S., et al., *Recent advances on bioactive baghdadite ceramic for bone tissue engineering applications: 20 years of research and innovation (a review).* Materials Today Bio, 2022: p. 100473.
11. Lu, Z., et al., *Baghdadite ceramics prevent senescence in human osteoblasts and promote bone regeneration in aged rats.* ACS Biomaterials Science & Engineering, 2020. **6**(12): p. 6874-6885.
12. Hobman, J.L. and L.C. Crossman, *Bacterial antimicrobial metal ion resistance.* Journal of medical microbiology, 2015. **64**(5): p. 471-497.
13. Evans, A. and K.A. Kavanagh, *Evaluation of metal-based antimicrobial compounds for the treatment of bacterial pathogens.* Journal of Medical Microbiology, 2021. **70**(5).
14. Jung, W.K., et al., *Antibacterial activity and mechanism of action of the silver ion in Staphylococcus aureus and Escherichia coli.* Applied and environmental microbiology, 2008. **74**(7): p. 2171-2178.
15. Wu, J., et al., *In vitro cytotoxicity of Cu2+, Zn2+, Ag+ and their mixtures on primary human endometrial epithelial cells.* Contraception, 2012. **85**(5): p. 509-518.
16. Woods, E., C. Cochrane, and S. Percival, *Prevalence of silver resistance genes in bacteria isolated from human and horse wounds.* Veterinary microbiology, 2009. **138**(3-4): p. 325-329.
17. Sinulingga, K., et al., *Investigation of antibacterial activity and cell viability of Ag/Mg and Ag/Zn co-doped hydroxyapatite derived from natural limestone.* ACS omega, 2021. **6**(49): p. 34185-34191.

18. Predoi, D., et al., *Synthesis, characterization, and antimicrobial activity of magnesium-doped hydroxyapatite suspensions.* Nanomaterials, 2019. **9**(9): p. 1295.

19. Bi, Q., et al., *Zn-HA/Bi-HA biphasic coatings on Titanium: Fabrication, characterization, antibacterial and biological activity.* Colloids and Surfaces B: Biointerfaces, 2020. **189**: p. 110813.

20. Ciobanu, G. and M. Harja, *Bismuth-doped nanohydroxyapatite coatings on Titanium implants for improved radiopacity and antimicrobial activity.* Nanomaterials, 2019. **9**(12): p. 1696.

21. Li, Y., et al., *Antibacterial properties of magnesium in vitro and in an in vivo model of implant-associated methicillin-resistant Staphylococcus aureus infection.* Antimicrobial agents and chemotherapy, 2014. **58**(12): p. 7586-7591.

22. Mirkhalaf, M., et al., *Highly substituted calcium silicates 3D printed with complex architectures to produce stiff, strong and bioactive scaffolds for bone regeneration.* Applied Materials Today, 2021. **25**: p. 101230.

23. No, Y.J., et al., *Development of a bioactive and radiopaque bismuth doped baghdadite ceramic for bone tissue engineering.* Bone, 2021. **153**: p. 116147.

24. Perera-Costa, D., et al., *Studying the influence of surface topography on bacterial adhesion using spatially organized microtopographic surface patterns.* Langmuir, 2014. **30**(16): p. 4633-4641.

25. Hsu, L.C., et al., *Effect of micro-and nanoscale topography on the adhesion of bacterial cells to solid surfaces.* Applied and environmental microbiology, 2013. **79**(8): p. 2703-2712.

26. Zhao, C., et al., *The role of the micro-pattern and nano-topography of hydroxyapatite bioceramics on stimulating osteogenic differentiation of mesenchymal stem cells.* Acta Biomaterialia, 2018. **73**: p. 509-521.

27. Sorrentino, R., et al., *Reduced bacterial adhesion on ceramics used for arthroplasty applications.* Journal of the European Ceramic Society, 2018. **38**(3): p. 963-970.

28. Kaur, M. and K. Singh, *Review on titanium and titanium based alloys as biomaterials for orthopaedic applications.* Materials Science and Engineering: C, 2019. **102**: p. 844-862.

29. Spriano, S., et al., *A critical review of multifunctional titanium surfaces: New frontiers for improving osseointegration and host response, avoiding bacteria contamination.* Acta biomaterialia, 2018. **79**: p. 1-22.

30. Koons, G.L., M. Diba, and A.G. Mikos, *Materials design for bone-tissue engineering.* Nature Reviews Materials, 2020. **5**(8): p. 584-603.

31. Wu, Q., et al., *Study of Sr–Ca–Si-based scaffolds for bone regeneration in osteoporotic models.* International Journal of Oral Science, 2020. **12**(1): p. 25.

32. Kumar, P., B.S. Dehiya, and A. Sindhu, *Bioceramics for hard tissue engineering applications: A review.* Int. J. Appl. Eng. Res, 2018. **13**(5): p. 2744-2752.

33. Wang, N., et al., *Functions and applications of metallic and metallic oxide nanoparticles in orthopedic implants and scaffolds.* Journal of Biomedical Materials Research Part B: Applied Biomaterials, 2021. **109**(2): p. 160-179.

34. Thippeswamy, P.B., et al., *Updates in postoperative imaging modalities following musculoskeletal surgery.* Journal of Clinical Orthopaedics and Trauma, 2021. **22**: p. 101616.

35. Xie, K., et al., *Additively manufactured biodegradable porous magnesium implants for elimination of implant-related infections: An in vitro and in vivo study.* Bioactive materials, 2022. **8**: p. 140-152.

36. Swain, S., R.N. Padhy, and T.R. Rautray, *Polarized piezoelectric bioceramic composites exhibit antibacterial activity.* Materials Chemistry and Physics, 2020. **239**: p. 122002.

37. Nabiyouni, M., et al., *Magnesium-based bioceramics in orthopedic applications.* Acta biomaterialia, 2018. **66**: p. 23-43.

38. Johnson, C.T. and A.J. García, *Scaffold-based anti-infection strategies in bone repair.* Annals of biomedical engineering, 2015. **43**: p. 515-528.

39. Chen, Z.-Y., et al., *Antibacterial biomaterials in bone tissue engineering.* Journal of Materials Chemistry B, 2021. **9**(11): p. 2594-2612.

40. Beuriat, P.A., et al., *Repair of Cranial Bone Defects in Children Using Synthetic Hydroxyapatite Cranioplasty (CustomBone).* World Neurosurg, 2019. **129**: p. e104-e113.

41. Room, G.N., *Medical Implants Market Size To Worth Around US$ 145.6*. 31 January 2022: https://www.globenewswire.com/news-release/2022/01/31/2375767/0/en/Medical-Implants-Market-Size-to-Worth-Around-US-145-6-Billion-by-2030.html.

42. Tangcharoensathien, V., et al., *Antimicrobial resistance: from global agenda to national strategic plan, Thailand.* Bulletin of the World Health Organization, 2017. **95**(8): p. 599-603.

43. Sumpradit, N., et al., *Thailand's national strategic plan on antimicrobial resistance: progress and challenges.* Bulletin of the World Health Organization, 2021. **99**(9): p. 661-673.

44. Dadgostar, P., *Antimicrobial Resistance: Implications and Costs.* Infect Drug Resist, 2019. **12**: p. 3903-3910.

45. Mahira, S., et al., *Antimicrobial materials—An overview.* 2019.

46. Lum, Z.C., et al., *Mortality during total knee periprosthetic joint infection.* The Journal of arthroplasty, 2018. **33**(12): p. 3783-3788.

47. Izakovicova, P., O. Borens, and A. Trampuz, *Periprosthetic joint infection: current concepts and outlook.* EFORT open reviews, 2019. **4**(7): p. 482-494.

48. Sader, H.S., et al., *Frequency and antimicrobial susceptibility of bacteria causing bloodstream infections in pediatric patients from United States (US) medical centers (2014–2018): Therapeutic options for multidrug-resistant bacteria.* Diagnostic microbiology and infectious disease, 2020. **98**(2): p. 115108.

49. Vertes, A., V. Hitchins, and K.S. Phillips, *Analytical challenges of microbial biofilms on medical devices*. 2012, ACS Publications.

50. Qin, S., et al., *Pseudomonas aeruginosa: pathogenesis, virulence factors, antibiotic resistance, interaction with host, technology advances and emerging therapeutics.* Signal Transduction and Targeted Therapy, 2022. **7**(1): p. 199.

51. Ferraris, S., et al., *Bioactive materials: In vitro investigation of different mechanisms of hydroxyapatite precipitation.* Acta biomaterialia, 2020. **102**: p. 468-480.

52. Hench, L.L. and J.R. Jones, *Bioactive glasses: frontiers and challenges.* Frontiers in bioengineering and biotechnology, 2015. **3**: p. 194.

53. Roohani-Esfahani, S.-I., et al., *A bioceramic with enhanced osteogenic properties to regulate the function of osteoblastic and osteocalastic cells for bone tissue regeneration.* Biomedical Materials, 2016. **11**(3): p. 035018.

54. Zreiqat, H., et al., *The incorporation of strontium and zinc into a calcium–silicon ceramic for bone tissue engineering.* Biomaterials, 2010. **31**(12): p. 3175-3184.

55. Chen, Y.-C., et al., *Long-term in vitro degradation and in vivo evaluation of resorbable bioceramics.* Journal of Materials Science: Materials in Medicine, 2021. **32**: p. 1-11.

56. Tajvar, S., A. Hadjizadeh, and S.S. Samandari, *Scaffold degradation in bone tissue engineering: An overview.* International Biodeterioration & Biodegradation, 2023. **180**: p. 105599.

57. Radunović, A., et al., *Biomimetics in Orthopedic Surgery and Traumatology Diseases traumatology*, in *Bioceramics, Biomimetic and Other Compatible Materials Features for Medical Applications*. 2023, Springer. p. 159-169.

58. Ma, H., et al., *3D-printed bioceramic scaffolds: From bone tissue engineering to tumor therapy.* Acta biomaterialia, 2018. **79**: p. 37-59.

59. Darus, F., et al., *Techniques for fabrication and construction of three-dimensional bioceramic scaffolds: Effect on pores size, porosity and compressive strength.* Ceramics International, 2018. **44**(15): p. 18400-18407.

60. Xu, S., et al., *Copper containing silicocarnotite bioceramic with improved mechanical strength and antibacterial activity.* Materials Science and Engineering: C, 2021. **118**: p. 111493.

61. Pouroutzidou, G.K., et al., *Composite PLGA–Nanobioceramic Coating on Moxifloxacin-Loaded Akermanite 3D Porous Scaffolds for Bone Tissue Regeneration.* Pharmaceutics, 2023. **15**(3): p. 819.

62. Qin, H., et al., *3D printed bioceramic scaffolds: Adjusting pore dimension is beneficial for mandibular bone defects repair.* Journal of Tissue Engineering and Regenerative Medicine, 2022. **16**(4): p. 409-421.

63. Fang, Z., et al., *The development tendency of 3D-printed bioceramic scaffolds for applications ranging from bone tissue regeneration to bone tumor therapy.* Frontiers in Bioengineering and Biotechnology, 2021. **9**: p. 754266.

64. Liu, Z., et al., *Advances in the use of calcium silicate-based materials in bone tissue engineering.* Ceramics International, 2023.

65. Xie, C., et al., *Advanced strategies of biomimetic tissue-engineered grafts for bone regeneration.* Advanced healthcare materials, 2021. **10**(14): p. 2100408.

66. Monfared, M.H., et al., *A deep insight into the preparation of ceramic bone scaffolds utilizing robocasting technique.* Ceramics International, 2022. **48**(5): p. 5939-5954.

67. Tarín-Pelló, A., B. Suay-García, and M.-T. Pérez-Gracia, *Antibiotic resistant bacteria: current situation and treatment options to accelerate the development of a new antimicrobial arsenal.* Expert Review of Anti-infective Therapy, 2022. **20**(8): p. 1095-1108.

68. Chen, X., et al., *Antibacterial coatings on orthopedic implants.* Materials Today Bio, 2023: p. 100586.

69. Mahanty, A. and D. Shikha, *Changes in the morphology, mechanical strength and biocompatibility of polymer and metal/polymer fabricated hydroxyapatite for orthopaedic implants: a review.* Journal of Polymer Engineering, 2022. **42**(4): p. 298-322.

70. Demir-Oğuz, Ö., A.R. Boccaccini, and D. Loca, *Injectable bone cements: What benefits the combination of calcium phosphates and bioactive glasses could bring?* Bioactive Materials, 2023. **19**: p. 217-236.

71. Marin, E., et al., *Explorative study on the antibacterial effects of 3D-printed PMMA/nitrides composites.* Materials & Design, 2021. **206**: p. 109788.

72. Zhao, C., et al., *Bioceramic-based scaffolds with antibacterial function for bone tissue engineering: A review.* Bioactive materials, 2022. **18**: p. 383-398.

73. Farazin, A., et al., *3D bio-printing for use as bone replacement tissues: A review of biomedical application.* Biomedical Engineering Advances, 2023: p. 100075.

74. Zhao, C., et al., *Bioceramic-based scaffolds with antibacterial function for bone tissue engineering: A review.* Bioactive Materials, 2022.

75. Liu, Z., et al., *Surface modification of hydroxyapatite nanoparticles for bone regeneration by controlling their surface hydration and protein adsorption states.* Dalton Transactions, 2022. **51**(25): p. 9572-9583.

76. Song, W., et al., *In vivo biocompatibility and bioactivity of calcium silicate-based bioceramics in endodontics.* Frontiers in Bioengineering and Biotechnology, 2020. **8**: p. 580954.

77. Sampath Kumar, T. and K. Madhumathi, *Antibacterial potential of nanobioceramics used as drug carriers*, in *Handbook of bioceramics and biocomposites*. 2016, Springer. p. 1333-1373.

78. Busscher, H.J., et al., *Biomaterial-associated infection: locating the finish line in the race for the surface.* Science translational medicine, 2012. **4**(153): p. 153rv10-153rv10.

79. Ciofu, O., et al., *Tolerance and resistance of microbial biofilms.* Nature Reviews Microbiology, 2022. **20**(10): p. 621-635.

80. Fathima, A., et al., *Microbial biofilms: A persisting public health challenge*, in *Understanding Microbial Biofilms*. 2023, Elsevier. p. 291-314.

81. Kalelkar, P.P., M. Riddick, and A.J. Garcia, *Biomaterial-based antimicrobial therapies for the treatment of bacterial infections.* Nature Reviews Materials, 2021: p. 1-16.

82. Masters, E.A., et al., *Skeletal infections: microbial pathogenesis, immunity and clinical management.* Nature Reviews Microbiology, 2022. **20**(7): p. 385-400.

83. Musini, A., S.P. Chilumoju, and A. Giri, *Biofilm Formation in Drug-Resistant Pathogen Staphylococcus aureus*, in *Microbial Biofilms*. 2022, CRC Press. p. 23-46.

84. Speziale, P., et al., *Protein-based biofilm matrices in Staphylococci.* Front Cell Infect Microbiol, 2014. **4**: p. 171.

85. Keane, F.M., et al., *Fibrinogen and elastin bind to the same region within the A domain of fibronectin binding protein A, an MSCRAMM of Staphylococcus aureus.* Mol Microbiol, 2007. **63**(3): p. 711-23.

86. Peacock, S.J., et al., *Bacterial fibronectin-binding proteins and endothelial cell surface fibronectin mediate adherence of Staphylococcus aureus to resting human endothelial cells.* Microbiology (Reading), 1999. **145 (Pt 12)**: p. 3477-3486.

87. Tristan, A., et al., *Use of multiplex PCR to identify Staphylococcus aureus adhesins involved in human hematogenous infections.* Journal of clinical microbiology, 2003. **41**(9): p. 4465-4467.

88. Paharik, A.E. and A.R. Horswill, *The staphylococcal biofilm: adhesins, regulation, and host response.* Virulence mechanisms of bacterial pathogens, 2016: p. 529-566.

89. McCourt, J., et al., *Fibronectin-binding proteins are required for biofilm formation by community-associated methicillin-resistant Staphylococcus aureus strain LAC.* FEMS Microbiol Lett, 2014. **353**(2): p. 157-64.

90. Nouri, A., et al., *Smart Materials in Manufacturing.*

91. Adam, B., G.S. Baillie, and L.J. Douglas, *Mixed species biofilms of Candida albicans and Staphylococcus epidermidis.* Journal of medical microbiology, 2002. **51**(4): p. 344-349.

92. Laverty, G., S.P. Gorman, and B.F. Gilmore, *Biofilms and implant-associated infections.* Biomaterial and medical device associated infection, 2015: p. 19-45.

93. Blanco-Cabra, N., et al., *Neutralization of ionic interactions by dextran-based single-chain nanoparticles improves tobramycin diffusion into a mature biofilm.* npj Biofilms and Microbiomes, 2022. **8**(1): p. 52.

94. Francolini, I., et al., *Antifouling and antimicrobial biomaterials: an overview.* Apmis, 2017. **125**(4): p. 392-417.

95. Mas-Moruno, C., B. Su, and M.J. Dalby, *Multifunctional coatings and nanotopographies: toward cell instructive and antibacterial implants.* Advanced healthcare materials, 2019. **8**(1): p. 1801103.

96. Ivanovski, S., P.M. Bartold, and Y.S. Huang, *The role of foreign body response in peri-implantitis: What is the evidence?* Periodontology 2000, 2022. **90**(1): p. 176-185.

97. Kyriakides, T.R., et al., *Foreign body response to synthetic polymer biomaterials and the role of adaptive immunity.* Biomedical Materials, 2022. **17**(2): p. 022007.

98. Franz, S., et al., *Immune responses to implants–a review of the implications for the design of immunomodulatory biomaterials.* Biomaterials, 2011. **32**(28): p. 6692-6709.

99. Croes, M., B.C.H. van der Wal, and H.C. Vogely, *Impact of Bacterial Infections on Osteogenesis: Evidence From In Vivo Studies.* J Orthop Res, 2019. **37**(10): p. 2067-2076.

100. Scherr, T.D., et al., *Hiding in Plain Sight: Interplay between Staphylococcal Biofilms and Host Immunity.* Front Immunol, 2014. **5**: p. 37.

101. Robertson, C.M., et al., *Neutrophil depletion causes a fatal defect in murine pulmonary Staphylococcus aureus clearance.* J Surg Res, 2008. **150**(2): p. 278-85.

102. Brinkmann, V., et al., *Neutrophil extracellular traps kill bacteria.* Science, 2004. **303**(5663): p. 1532-5.

103. Alder, K.D., et al., *Intracellular Staphylococcus aureus in bone and joint infections: a mechanism of disease recurrence, inflammation, and bone and cartilage destruction.* Bone, 2020. **141**: p. 115568.

104. Amin Yavari, S., et al., *Combating implant infections: shifting focus from bacteria to host.* Advanced Materials, 2020. **32**(43): p. 2002962.

105. Kolaczkowska, E. and P. Kubes, *Neutrophil recruitment and function in health and inflammation.* Nat Rev Immunol, 2013. **13**(3): p. 159-75.

106. Vitkov, L., et al., *The initial inflammatory response to bioactive implants is characterized by NETosis.* PLoS One, 2015. **10**(3): p. e0121359.

107. Kaplan, S.S., et al., *Biomaterial-neutrophil interactions: dysregulation of oxidative functions of fresh neutrophils induced by prior neutrophil-biomaterial interaction.* J Biomed Mater Res, 1996. **30**(1): p. 67-75.

108. van Kessel, K.P., J. Bestebroer, and J.A. van Strijp, *Neutrophil-Mediated Phagocytosis of Staphylococcus aureus.* Front Immunol, 2014. **5**: p. 467.

109. Kou, P.M. and J.E. Babensee, *Macrophage and dendritic cell phenotypic diversity in the context of biomaterials.* Journal of biomedical materials research Part A, 2011. **96**(1): p. 239-260.

110. Vallés, G., et al., *Influence of inflammatory conditions provided by macrophages on osteogenic ability of mesenchymal stem cells.* Stem cell research & therapy, 2020. **11**(1): p. 1-15.

111. Hamilton, J.A., *Colony-stimulating factors in inflammation and autoimmunity.* Nat Rev Immunol, 2008. **8**(7): p. 533-44.

112. Spiller, K.L., et al., *The role of macrophage phenotype in vascularization of tissue engineering scaffolds.* Biomaterials, 2014. **35**(15): p. 4477-4488.

113. Gordon, S. and P.R. Taylor, *Monocyte and macrophage heterogeneity.* Nat Rev Immunol, 2005. **5**(12): p. 953-64.

114. Sica, A. and A. Mantovani, *Macrophage plasticity and polarization: in vivo veritas.* J Clin Invest, 2012. **122**(3): p. 787-95.

115. Benoit, M., B. Desnues, and J.-L. Mege, *Macrophage polarization in bacterial infections.* The Journal of Immunology, 2008. **181**(6): p. 3733-3739.

116. Lawrence, T. and G. Natoli, *Transcriptional regulation of macrophage polarization: enabling diversity with identity.* Nat Rev Immunol, 2011. **11**(11): p. 750-61.

117. Chen, Z., et al., *Osteoimmunomodulation for the development of advanced bone biomaterials.* Materials today, 2016. **19**(6): p. 304-321.

118. Guan, Y.-H., et al., *Exploiting autophagy-regulative nanomaterials for activation of dendritic cells enables reinforced cancer immunotherapy.* Biomaterials, 2022. **282**: p. 121434.

119. Wang, S., et al., *The role of dendritic cells in the immunomodulation to implanted biomaterials.* International Journal of Oral Science, 2022. **14**(1): p. 52.

120. Cui, Y., et al., *Dual-functional composite scaffolds for inhibiting infection and promoting bone regeneration.* Materials Today Bio, 2022: p. 100409.

121. Verhoeven, B.M., et al., *The immune cell atlas of human neuroblastoma.* Cell Reports Medicine, 2022. **3**(6): p. 100657.

122. Cui, Y., et al., *Novel insights into nanomaterials for immunomodulatory bone regeneration.* Nanoscale Advances, 2022. **4**(2): p. 334-352.

123. Chung, L., et al., *Key players in the immune response to biomaterial scaffolds for regenerative medicine.* Advanced Drug Delivery Reviews, 2017. **114**: p. 184-192.

124. Yu, F., et al., *Biomimetic hydroxyapatite nanorods promote bone regeneration via accelerating osteogenesis of BMSCs through T cell-derived IL-22.* ACS nano, 2022. **16**(1): p. 755-770.

125. Yu, W.-w., et al., *Engineered extracellular vesicles: Regulating the crosstalk between the skeleton and immune system.* Engineered Regeneration, 2022.

126. Huang, Y., et al., *Regulation of immune response by bioactive ions released from silicate bioceramics for bone regeneration.* Acta biomaterialia, 2018. **66**: p. 81-92.

127. Moriarty, T.F., et al., *Bone infection: a clinical priority for clinicians, scientists and educators.* European Cells & Materials, 2021. **41**: p. 312-333.

128. Barrak, F.N., et al., *Anti-inflammatory properties of S53P4 bioactive glass implant material.* Journal of Dentistry, 2022. **127**: p. 104296.

129. Sadowska, J.M. and M.-P. Ginebra, *Inflammation and biomaterials: role of the immune response in bone regeneration by inorganic scaffolds.* Journal of Materials Chemistry B, 2020. **8**(41): p. 9404-9427.

130. Clézardin, P., et al., *Bone metastasis: Mechanisms, therapies, and biomarkers.* Physiological reviews, 2021. **101**(3): p. 797-855.

131. Soriente, A., et al., *Chitosan/hydroxyapatite nanocomposite scaffolds to modulate osteogenic and inflammatory response.* Journal of Biomedical Materials Research Part A, 2022. **110**(2): p. 266-272.

132. Xiao, L., et al., *Macrophage polarization related to crystal phases of calcium phosphate biomaterials.* International journal of molecular sciences, 2021. **22**(20): p. 11252.

133. Velard, F., et al., *Inflammatory cell response to calcium phosphate biomaterial particles: an overview.* Acta biomaterialia, 2013. **9**(2): p. 4956-4963.

134. Sadowska, J.M., et al., *The effect of biomimetic calcium deficient hydroxyapatite and sintered β-tricalcium phosphate on osteoimmune reaction and osteogenesis.* Acta biomaterialia, 2019. **96**: p. 605-618.

135. Liu, X., et al., *Hydroxyapatite composited PEEK with 3D porous surface enhances osteoblast differentiation through mediating NO by macrophage.* Regenerative Biomaterials, 2022. **9**.

136. Mahon, O.R., et al., *Orthopaedic implant materials drive M1 macrophage polarization in a spleen tyrosine kinase-and mitogen-activated protein kinase-dependent manner.* Acta Biomaterialia, 2018. **65**: p. 426-435.

137. Raja, F.N.S., et al., *The antimicrobial efficacy of zinc doped phosphate-based glass for treating catheter associated urinary tract infections.* Materials Science and Engineering: C, 2019. **103**: p. 109868.

138. Chitra, S., et al., *Impact of copper on in-vitro biomineralization, drug release efficacy and antimicrobial properties of bioactive glasses.* Materials Science and Engineering: C, 2020. **109**: p. 110598.

139. Jaiswal, S., P. McHale, and B. Duffy, *Preparation and rapid analysis of antibacterial silver, copper and zinc doped sol–gel surfaces.* Colloids and Surfaces B: Biointerfaces, 2012. **94**: p. 170-176.

140. Guldiren, D. and S. Aydın, *Antimicrobial property of silver, silver-zinc and silver-copper incorporated soda lime glass prepared by ion exchange.* Materials Science and Engineering: C, 2017. **78**: p. 826-832.

141. Samani, S., et al., *In vitro antibacterial evaluation of sol–gel-derived Zn-, Ag-, and (Zn+ Ag)-doped hydroxyapatite coatings against methicillin-resistant Staphylococcus aureus.* Journal of Biomedical Materials Research Part A, 2013. **101**(1): p. 222-230.

142. Singh, P., et al., *Recent advances in silicate-based crystalline bioceramics for orthopedic applications: a review.* Journal of Materials Science, 2022. **57**(28): p. 13109-13151.

143. Biegański, P., et al., *Brief survey on organometalated antibacterial drugs and metal-based materials with antibacterial activity.* RSC Chemical Biology, 2021. **2**(2): p. 368-386.

144. Fadeeva, I.V., et al., *Antibacterial and cell-friendly copper-substituted tricalcium phosphate ceramics for biomedical implant applications.* Materials Science and Engineering: C, 2021. **129**: p. 112410.

145. Gomes, S., et al., *Cu-doping of calcium phosphate bioceramics: From mechanism to the control of cytotoxicity.* Acta Biomaterialia, 2018. **65**: p. 462-474.

146. Ofudje, E.A., et al., *Synthesis and characterization of Zn-Doped hydroxyapatite: scaffold application, antibacterial and bioactivity studies.* Heliyon, 2019. **5**(5).

147. He, T., et al., *One-step co-doping of ZnO and Zn2+ in osteoinductive calcium phosphate ceramics with synergistic antibacterial activity for regenerative repair of infected bone defect.* Journal of Materials Science & Technology, 2023.

148. Moghanian, A., et al., *The effect of magnesium content on in vitro bioactivity, biological behavior and antibacterial activity of sol–gel derived 58S bioactive glass.* Ceramics international, 2018. **44**(8): p. 9422-9432.

149. Pham, D.Q., et al., *Antibacterial longevity of a novel Gallium liquid metal/hydroxyapatite composite coating fabricated by plasma spray.* ACS Applied Materials & Interfaces, 2022. **14**(16): p. 18974-18988.

150. Mosina, M., et al., *Gallium-Doped Hydroxyapatite Shows Antibacterial Activity against Pseudomonas aeruginosa without Affecting Cell Metabolic Activity.* Journal of Functional Biomaterials, 2023. **14**(2): p. 51.

151. Ibrahim, A.M., et al., *Bioactive and antibacterial metal implant composite coating based on Ce-doped nanobioactive glass and chitosan by electrophoretic deposition method.* Journal of Materials Research, 2021. **36**(9): p. 1899-1913.

152. Guangjian, D., et al., *Synthesis, characterization and antimicrobial activity of zinc and cerium co-doped α-zirconium phosphate.* Journal of Rare Earths, 2012. **30**(8): p. 820-825.

153. Bhattacharjee, A., et al., *Antibacterial and magnetic response of site-specific cobalt incorporated hydroxyapatite.* Ceramics International, 2020. **46**(1): p. 513-522.

154. Chen, F., C. Liu, and Y. Mao, *Bismuth-doped injectable calcium phosphate cement with improved radiopacity and potent antimicrobial activity for root canal filling.* Acta Biomaterialia, 2010. **6**(8): p. 3199-3207.

155. Baheiraei, N., et al., *Effects of strontium ions with potential antibacterial activity on in vivo bone regeneration.* Scientific Reports, 2021. **11**(1): p. 8745.

156. Anastasiou, A., et al., *Antibacterial properties and regenerative potential of Sr2+ and Ce3+ doped fluorapatites; a potential solution for peri-implantitis.* Scientific Reports, 2019. **9**(1): p. 14469.

157. Tseng, C.-F., Y.-C. Fei, and Y.-J. Chou, *Investigation of in vitro bioactivity and antibacterial activity of manganese-doped spray pyrolyzed bioactive glasses.* Journal of Non-Crystalline Solids, 2020. **549**: p. 120336.

158. Panneerselvam, R., et al., *Impact of different transition metal ions in the structural, mechanical, optical, chemico-physical and biological properties of nanohydroxyapatite.* Applied Surface Science, 2020. **506**: p. 144802.

159. Linder, M.C. and M. Hazegh-Azam, *Copper biochemistry and molecular biology.* The American journal of clinical nutrition, 1996. **63**(5): p. 797S-811S.

160. Rigo, A., et al., *Interaction of copper with cysteine: stability of cuprous complexes and catalytic role of cupric ions in anaerobic thiol oxidation.* Journal of inorganic biochemistry, 2004. **98**(9): p. 1495-1501.

161. Festa, R.A. and D.J. Thiele, *Copper: an essential metal in biology.* Current Biology, 2011. **21**(21): p. R877-R883.

162. Scarpa, M., et al., *Activated oxygen species in the oxidation of glutathione A kinetic study.* Biophysical Chemistry, 1996. **60**(1-2): p. 53-61.

163. Silver, S. and L.T. Phung, *A bacterial view of the periodic table: genes and proteins for toxic inorganic ions.* Journal of Industrial Microbiology and Biotechnology, 2005. **32**(11-12): p. 587-605.

164. Franke, S., et al., *Molecular analysis of the copper-transporting efflux system CusCFBA of Escherichia coli.* Journal of bacteriology, 2003. **185**(13): p. 3804-3812.

165. Abicht, H.K., et al., *Non-enzymic copper reduction by menaquinone enhances copper toxicity in Lactococcus lactis IL1403.* Microbiology, 2013. **159**(Pt_6): p. 1190-1197.

166. Calvano, C., et al., *MALDI-TOF mass spectrometry analysis of proteins and lipids in Escherichia coli exposed to copper ions and nanoparticles.* Journal of Mass Spectrometry, 2016. **51**(9): p. 828-840.

167. Liu, J. and R.H. Hurt, *Ion Release Kinetics and Particle Persistence in Aqueous Nano-Silver Colloids.* Environmental Science & Technology, 2010. **44**(6): p. 2169-2175.

168. Zhang, S., et al., *Reduced cytotoxicity of silver ions to mammalian cells at high concentration due to the formation of silver chloride.* Toxicology in Vitro, 2013. **27**(2): p. 739-744.

169. Rai, M., et al., *Metal nanoparticles: The protective nanoshield against virus infection.* Critical Reviews in Microbiology, 2016. **42**(1): p. 46-56.

170. Kędziora, A., et al., *Similarities and Differences between Silver Ions and Silver in Nanoforms as Antibacterial Agents.* International Journal of Molecular Sciences, 2018. **19**(2).

171. Bondarenko, O.M., et al., *Plasma membrane is the target of rapid antibacterial action of silver nanoparticles in Escherichia coli and Pseudomonas aeruginosa.* International Journal of Nanomedicine, 2018. **13**: p. 6779.

172. Shi, C., et al., *Functional hydroxyapatite bioceramics with excellent osteoconductivity and stern-interface induced antibacterial ability.* Biomaterials Science, 2016. **4**(4): p. 699-710.

173. Pham, D., et al., *Strontium-doped hardystonite plasma sprayed coatings with robust antimicrobial activity.* Materials Today Chemistry, 2022. **24**: p. 100822.

174. Ikram, M., et al., *Strontium-doped chromium oxide for RhB reduction and antibacterial activity with evidence of molecular docking analysis.* Frontiers in Chemistry, 2023. **11**: p. 1167701.

175. Marcello, E., et al., *Antibacterial composite materials based on the combination of polyhydroxyalkanoates with selenium and strontium co-substituted hydroxyapatite for bone regeneration.* Frontiers in Bioengineering and Biotechnology, 2021. **9**: p. 647007.

176. Jia, F., et al., *Strontium-calcium doped titanium dioxide nanotubes loaded with GL13K for promotion of antibacterial activity, anti-Inflammation, and vascularized bone regeneration.* Ceramics International, 2023. **49**(22): p. 35703-35721.

177. O'Sullivan, C., et al., *Osteointegration, antimicrobial and antibiofilm activity of orthopaedic titanium surfaces coated with silver and strontium-doped hydroxyapatite using a novel blasting process.* Drug Delivery and Translational Research, 2021. **11**: p. 702-716.

178. Degli Esposti, L., et al., *Antimicrobial activity of remineralizing ion-doped amorphous calcium phosphates for preventive dentistry.* Frontiers in Materials, 2022. **9**: p. 846130.

179. Makvandi, P., et al., *Metal-based nanomaterials in biomedical applications: Antimicrobial activity and cytotoxicity aspects.* Advanced Functional Materials, 2020. **30**(22): p. 1910021.

180. McDevitt, C.A., et al., *A molecular mechanism for bacterial susceptibility to zinc.* PLoS pathogens, 2011. **7**(11): p. e1002357.

181. Siddiqi, K.S., A. ur Rahman, and A. Husen, *Properties of zinc oxide nanoparticles and their activity against microbes.* Nanoscale research letters, 2018. **13**(1): p. 1-13.

182. Xia, P., et al., *Zinc is an important inter-kingdom signal between the host and microbe.* Veterinary Research, 2021. **52**(1): p. 1-14.

183. Belenky, P., et al., *Bactericidal antibiotics induce toxic metabolic perturbations that lead to cellular damage.* Cell reports, 2015. **13**(5): p. 968-980.

184. Godoy-Gallardo, M., et al., *Antibacterial approaches in tissue engineering using metal ions and nanoparticles: From mechanisms to applications.* Bioactive Materials, 2021. **6**(12): p. 4470-4490.

185. Kurtjak, M., et al., *Designing Ga (iii)-containing hydroxyapatite with antibacterial activity.* RSC advances, 2016. **6**(114): p. 112839-112852.

186. Mathews, S., et al., *Contact killing of bacteria on copper is suppressed if bacterial-metal contact is prevented and is induced on iron by copper ions.* Applied and environmental microbiology, 2013. **79**(8): p. 2605-2611.

187. Lemire, J.A., J.J. Harrison, and R.J. Turner, *Antimicrobial activity of metals: mechanisms, molecular targets and applications.* Nature Reviews Microbiology, 2013. **11**(6): p. 371-384.

188. Stohs, S.J. and D. Bagchi, *Oxidative mechanisms in the toxicity of metal ions.* Free radical biology and medicine, 1995. **18**(2): p. 321-336.

189. Macomber, L., C. Rensing, and J.A. Imlay, *Intracellular copper does not catalyze the formation of oxidative DNA damage in Escherichia coli.* Journal of bacteriology, 2007. **189**(5): p. 1616-1626.

190. Anjem, A., S. Varghese, and J.A. Imlay, *Manganese import is a key element of the OxyR response to hydrogen peroxide in Escherichia coli.* Molecular microbiology, 2009. **72**(4): p. 844-858.

191. Xu, F.F. and J.A. Imlay, *Silver (I), mercury (II), cadmium (II), and zinc (II) target exposed enzymic iron-sulfur clusters when they toxify Escherichia coli.* Applied and environmental microbiology, 2012. **78**(10): p. 3614-3621.

192. Xu, H., et al., *Role of reactive oxygen species in the antibacterial mechanism of silver nanoparticles on Escherichia coli O157: H7.* Biometals, 2012. **25**(1): p. 45-53.

193. Valko, M., H. Morris, and M. Cronin, *Metals, toxicity and oxidative stress.* Current medicinal chemistry, 2005. **12**(10): p. 1161-1208.

194. Bhakta, J.N., *Metal toxicity in microorganism*, in *Handbook of research on inventive bioremediation techniques*. 2017, IGI Global. p. 1-23.

195. Lemire, J.A. and R.J. Turner, *Mechanisms underlying the antimicrobial capacity of metals.* Stress and Environmental Regulation of Gene Expression and Adaptation in Bacteria, 2016: p. 215-224.

196. Imlay, J.A., *The mismetallation of enzymes during oxidative stress.* Journal of Biological Chemistry, 2014. **289**(41): p. 28121-28128.

197. Chitambar, C.R., *Gallium and its competing roles with iron in biological systems.* Biochimica et Biophysica Acta (BBA)-Molecular Cell Research, 2016. **1863**(8): p. 2044-2053.

198. Sumner, E.R., et al., *Oxidative protein damage causes chromium toxicity in yeast.* Microbiology, 2005. **151**(6): p. 1939-1948.

199. Amici, A., et al., *Conversion of amino acid residues in proteins and amino acid homopolymers to carbonyl derivatives by metal-catalyzed oxidation reactions.* Journal of Biological Chemistry, 1989. **264**(6): p. 3341-3346.

200. Palza, H., *Antimicrobial polymers with metal nanoparticles.* International journal of molecular sciences, 2015. **16**(1): p. 2099-2116.

201. Warnes, S.L., C.J. Highmore, and C.W. Keevil, *Horizontal transfer of antibiotic resistance genes on abiotic touch surfaces: implications for public health.* MBio, 2012. **3**(6): p. e00489-12.

202. Linley, E., et al., *Use of hydrogen peroxide as a biocide: new consideration of its mechanisms of biocidal action.* Journal of antimicrobial Chemotherapy, 2012. **67**(7): p. 1589-1596.

203. Warnes, S. and C. Keevil, *Mechanism of copper surface toxicity in vancomycin-resistant enterococci following wet or dry surface contact.* Applied and environmental microbiology, 2011. **77**(17): p. 6049-6059.

204. Warnes, S.L. and C.W. Keevil, *Lack of involvement of Fenton chemistry in death of methicillin-resistant and methicillin-sensitive strains of Staphylococcus aureus and destruction of their genomes on wet or dry copper alloy surfaces.* Applied and Environmental Microbiology, 2016. **82**(7): p. 2132-2136.

205. Wang, M. and T. Tang, *Surface treatment strategies to combat implant-related infection from the beginning.* Journal of orthopaedic translation, 2019. **17**: p. 42-54.

206. Campoccia, D., L. Montanaro, and C.R. Arciola, *A review of the biomaterials technologies for infection-resistant surfaces.* Biomaterials, 2013. **34**(34): p. 8533-8554.

207. Raphel, J., et al., *Multifunctional coatings to simultaneously promote osseointegration and prevent infection of orthopaedic implants.* Biomaterials, 2016. **84**: p. 301-314.

208. Hazell, G., et al., *Bioinspired bactericidal surfaces with polymer nanocone arrays.* Journal of colloid and interface science, 2018. **528**: p. 389-399.

209. Tuson, H.H. and D.B. Weibel, *Bacteria–surface interactions.* Soft matter, 2013. **9**(17): p. 4368-4380.

210. Crawford, R.J., et al., *Surface topographical factors influencing bacterial attachment.* Advances in colloid and interface science, 2012. **179**: p. 142-149.

211. Oh, J.K., et al., *The influence of surface chemistry on the kinetics and thermodynamics of bacterial adhesion.* Scientific reports, 2018. **8**(1): p. 1-13.

212. Yuan, Y., et al., *Surface characteristics influencing bacterial adhesion to polymeric substrates.* RSC advances, 2017. **7**(23): p. 14254-14261.

213. Yoda, I., et al., *Effect of surface roughness of biomaterials on Staphylococcus epidermidis adhesion.* BMC microbiology, 2014. **14**(1): p. 1-7.

214. Ammar, Y., et al., *Influence of surface roughness on the initial formation of biofilm.* Surface and Coatings Technology, 2015. **284**: p. 410-416.

215. Wassmann, T., et al., *The influence of surface texture and wettability on initial bacterial adhesion on titanium and zirconium oxide dental implants.* International journal of implant dentistry, 2017. **3**(1): p. 1-11.

216. Dutra, D., et al., *Grinding with diamond burs and hydrothermal aging of a Y-TZP material: effect on the material surface characteristics and bacterial adhesion.* Operative dentistry, 2017. **42**(6): p. 669-678.

217. Kang, D.-H., et al., *Effect of polishing method on surface roughness and bacterial adhesion of zirconia-porcelain veneer.* Ceramics international, 2017. **43**(7): p. 5382-5387.

218. Sarker, A., et al., *Rational design of additively manufactured Ti6Al4V implants to control Staphylococcus aureus biofilm formation.* Materialia, 2019. **5**: p. 100250.

219. Lu, A., et al., *Effects of surface roughness and texture on the bacterial adhesion on the bearing surface of bio-ceramic joint implants: An in vitro study.* Ceramics International, 2020. **46**(5): p. 6550-6559.

220. Edwards, K.J. and A.D. Rutenberg, *Microbial response to surface microtopography: the role of metabolism in localized mineral dissolution.* Chemical Geology, 2001. **180**(1-4): p. 19-32.

221. Liu, J. and R.M. Ford, *Idling time of swimming bacteria near particulate surfaces contributes to apparent adsorption coefficients at the macroscopic scale under static conditions.* Environmental science & technology, 2009. **43**(23): p. 8874-8880.

222. Rieger, K., et al., *Transport of microorganisms into cellulose nanofiber mats.* RSC advances, 2016. **6**(29): p. 24438-24445.

223. Aykent, F., et al., *Effect of different finishing techniques for restorative materials on surface roughness and bacterial adhesion.* The Journal of Prosthetic Dentistry, 2010. **103**(4): p. 221-227.

224. Thio, B.J.R. and J.C. Meredith, *Quantification of E. coli adhesion to polyamides and polystyrene with atomic force microscopy.* Colloids and Surfaces B: Biointerfaces, 2008. **65**(2): p. 308-312.

225. Thomas, W.E., et al., *Bacterial Adhesion to Target Cells Enhanced by Shear Force.* Cell, 2002. **109**(7): p. 913-923.

226. Damiati, L., et al., *Impact of surface topography and coating on osteogenesis and bacterial attachment on titanium implants.* Journal of Tissue Engineering, 2018. **9**: p. 2041731418790694.

227. Tallawi, M., M. Opitz, and O. Lieleg, *Modulation of the mechanical properties of bacterial biofilms in response to environmental challenges.* Biomaterials science, 2017. **5**(5): p. 887-900.

228. Katsikogianni, M., et al., *Adhesion of slime producing Staphylococcus epidermidis strains to PVC and diamond-like carbon/silver/fluorinated coatings.* Journal of Materials Science: Materials in Medicine, 2006. **17**(8): p. 679-689.

229. Rowland, B.M., *Bacterial contamination of dental unit waterlines: what is your dentist spraying into your mouth?* Clinical Microbiology Newsletter, 2003. **25**(10): p. 73-77.

230. Kim, H.-J., et al., *Sanitization efficacy of slightly acidic electrolyzed water against pure cultures of Escherichia coli, Salmonella enterica, Typhimurium, Staphylococcus aureus and Bacillus cereus spores, in comparison with different water hardness.* Scientific reports, 2019. **9**(1): p. 1-14.

231. Ribeiro, M., F.J. Monteiro, and M.P. Ferraz, *Infection of orthopedic implants with emphasis on bacterial adhesion process and techniques used in studying bacterial-material interactions.* Biomatter, 2012. **2**(4): p. 176-194.

232. Kinnari, T.J., et al., *Influence of surface porosity and pH on bacterial adherence to hydroxyapatite and biphasic calcium phosphate bioceramics.* Journal of medical microbiology, 2009. **58**(1): p. 132-137.

233. Pelepenko, L.E., et al., *Physicochemical, antimicrobial, and biological properties of White-MTAFlow.* Clin Oral Investig, 2021. **25**(2): p. 663-672.

234. Huang, Y., et al., *The in vitro antimicrobial activities of four endodontic sealers.* BMC Oral Health, 2019. **19**(1): p. 118.

235. Khoo, X. and M.W. Grinstaff, *Novel infection-resistant surface coatings: A bioengineering approach.* Mrs Bulletin, 2011. **36**(5): p. 357-366.

236. Boda, S.K. and B. Basu, *Engineered biomaterial and biophysical stimulation as combinatorial strategies to address prosthetic infection by pathogenic bacteria.* Journal of Biomedical Materials Research Part B: Applied Biomaterials, 2017. **105**(7): p. 2174-2190.

237. Horváthy, D.B., et al., *Serum albumin as a local therapeutic agent in cell therapy and tissue engineering.* Biofactors, 2017. **43**(3): p. 315-330.

238. Wronska, M.A., et al., *Adding functions to biomaterial surfaces through protein incorporation.* Advanced Materials, 2016. **28**(27): p. 5485-5508.

239. Yang, Z., et al., *Biofunctionalization of zirconia with cell-adhesion peptides via polydopamine crosslinking for soft tissue engineering: effects on the biological behaviors of human gingival fibroblasts and oral bacteria.* RSC Advances, 2020. **10**(11): p. 6200-6212.

240. Eroshenko, D., I. Morozov, and V. Korobov, *The role of plasma, albumin, and fibronectin in Staphylococcus epidermidis adhesion to polystyrene surface.* Current Microbiology, 2015. **70**(6): p. 846-853.

241. Kamarudin, N.H.A., et al., *Unscrambling the effect of C-terminal tail deletion on the stability of a cold-adapted, organic solvent stable lipase from Staphylococcus epidermidis AT2.* Molecular biotechnology, 2014. **56**(8): p. 747-757.

242. Therrien, A., A. Fournier, and M. Lafleur, *Role of the cationic C-terminal segment of melittin on membrane fragmentation.* The Journal of Physical Chemistry B, 2016. **120**(17): p. 3993-4002.

243. Vasconcelos, D.M., et al., *Role of protein environment and bioactive polymer grafting in the S. epidermidis response to titanium alloy for biomedical applications.* Materials Science and Engineering: C, 2014. **45**: p. 176-183.

244. Arciola, C.R., et al., *Presence of fibrinogen-binding adhesin gene in Staphylococcus epidermidis isolates from central venous catheters-associated and orthopaedic implant-associated infections.* Biomaterials, 2004. **25**(19): p. 4825-4829.

245. Charville, G.W., et al., *Reduced bacterial adhesion to fibrinogen-coated substrates via nitric oxide release.* Biomaterials, 2008. **29**(30): p. 4039-4044.

246. Pei, L. and J.-I. Flock, *Functional study of antibodies against a fibrogenin-binding protein in Staphylococcus epidermidis adherence to polyethylene catheters.* The Journal of infectious diseases, 2001. **184**(1): p. 52-55.

247. Vallet-Regí, M., et al., *Biomaterials against bone infection.* Advanced healthcare materials, 2020. **9**(13): p. 2000310.

248. de Lima, G.G., et al., *A novel pH-sensitive ceramic-hydrogel for biomedical applications.* Polymers for Advanced Technologies, 2015. **26**(12): p. 1439-1446.

249. Chakraborty, S., *Novel antibacterial strategies for bioceramic-and polymer-based orthopaedic biomaterials*. 2023, UNSW Sydney.

250. Li, P., et al., *A resilient and flexible chitosan/silk cryogel incorporated Ag/Sr co-doped nanoscale hydroxyapatite for osteoinductivity and antibacterial properties.* Journal of materials chemistry B, 2018. **6**(45): p. 7427-7438.

251. Faruq, O., et al., *A biphasic calcium phosphate ceramic scaffold loaded with oxidized cellulose nanofiber–gelatin hydrogel with immobilized simvastatin drug for osteogenic differentiation.* Journal of Biomedical Materials Research Part B: Applied Biomaterials, 2020. **108**(4): p. 1229-1238.

252. Colilla, M. and M. Vallet-Regí, *Targeted stimuli-responsive mesoporous silica nanoparticles for bacterial infection treatment.* International Journal of Molecular Sciences, 2020. **21**(22): p. 8605.

253. Sadtler, K., et al., *Design, clinical translation and immunological response of biomaterials in regenerative medicine.* Nature Reviews Materials, 2016. **1**(7): p. 1-17.

254. Tofail, S.A., et al., *Additive manufacturing: scientific and technological challenges, market uptake and opportunities.* Materials today, 2018. **21**(1): p. 22-37.

255. Place, E.S., N.D. Evans, and M.M. Stevens, *Complexity in biomaterials for tissue engineering.* Nature materials, 2009. **8**(6): p. 457-470.

256. Ur Rehman, M.A., et al., *Antibacterial and bioactive coatings based on radio frequency co-sputtering of silver nanocluster-silica coatings on PEEK/bioactive glass layers obtained by electrophoretic deposition.* ACS applied materials & interfaces, 2017. **9**(38): p. 32489-32497.

257. Baino, F., et al., *Bioactive glass and glass-ceramic orbital implants.* International Journal of Applied Ceramic Technology, 2019. **16**(5): p. 1850-1863.

258. Johnson, C.T. and A.J. García, *Scaffold-based anti-infection strategies in bone repair.* Ann Biomed Eng, 2015. **43**(3): p. 515-28.

259. Trampuz, A. and A.F. Widmer, *Infections associated with orthopedic implants.* Curr Opin Infect Dis, 2006. **19**(4): p. 349-56.

260. Arciola, C.R., D. Campoccia, and L. Montanaro, *Implant infections: adhesion, biofilm formation and immune evasion.* Nature reviews microbiology, 2018. **16**(7): p. 397-409.

261. Nguyen, A.T. and A.G. Oglesby-Sherrouse, *Interactions between Pseudomonas aeruginosa and Staphylococcus aureus during co-cultivations and polymicrobial infections.* Applied microbiology and biotechnology, 2016. **100**: p. 6141-6148.

262. Hansson, K. and A. Brenthel, *Imagining a post-antibiotic era: a cultural analysis of crisis and antibiotic resistance.* Medical Humanities, 2022. **48**(3): p. 381.

263. Aslam, B., et al., *Antibiotic resistance: retrospect and prospect*, in *Degradation of Antibiotics and Antibiotic-Resistant Bacteria from Various Sources*. 2023, Elsevier. p. 1-37.

264. Li, J.J., et al., *Efficacy of novel synthetic bone substitutes in the reconstruction of large segmental bone defects in sheep tibiae.* Biomedical Materials, 2016. **11**(1): p. 015016.

265. Rodríguez-Sánchez, J., M.Á. Pacha-Olivenza, and M.L. González-Martín, *Bactericidal effect of magnesium ions over planktonic and sessile Staphylococcus epidermidis and Escherichia coli.* Materials Chemistry and Physics, 2019. **221**: p. 342-348.

266. Gittens, R.A., et al., *The effects of combined micron-/submicron-scale surface roughness and nanoscale features on cell proliferation and differentiation.* Biomaterials, 2011. **32**(13): p. 3395-3403.

267. Andrukhov, O., et al., *Proliferation, behavior, and differentiation of osteoblasts on surfaces of different microroughness.* Dental materials, 2016. **32**(11): p. 1374-1384.

268. Yoda, I., et al., *Effect of surface roughness of biomaterials on Staphylococcus epidermidis adhesion.* BMC microbiology, 2014. **14**: p. 1-7.

269. Senevirathne, S., et al., *Bactericidal efficiency of micro-and nanostructured surfaces: a critical perspective.* RSC advances, 2021. **11**(3): p. 1883-1900.

270. Mi, G., et al., *Reducing bacterial infections and biofilm formation using nanoparticles and nanostructured antibacterial surfaces.* Advanced Healthcare Materials, 2018. **7**(13): p. 1800103.

271. Linklater, D.P., et al., *Mechano-bactericidal actions of nanostructured surfaces.* Nature Reviews Microbiology, 2021. **19**(1): p. 8-22.

272. Mendonça, G., et al., *Advancing dental implant surface technology–from micron-to nanotopography.* Biomaterials, 2008. **29**(28): p. 3822-3835.

273. Oopath, S.V., et al., *Nature-Inspired Biomimetic Surfaces for Controlling Bacterial Attachment and Biofilm Development.* Advanced Materials Interfaces, 2023. **10**(4): p. 2201425.

274. Berney, M., et al., *Assessment and Interpretation of Bacterial Viability by Using the LIVE/DEAD BacLight Kit in Combination with Flow Cytometry.* Applied and Environmental Microbiology, 2007. **73**(10): p. 3283-3290.

275. Iqbal, N., et al., *Rapid microwave assisted synthesis and characterization of nanosized silver-doped hydroxyapatite with antibacterial properties.* Materials letters, 2012. **89**: p. 118-122.

276. Balouiri, M., M. Sadiki, and S.K. Ibnsouda, *Methods for in vitro evaluating antimicrobial activity: A review.* Journal of pharmaceutical analysis, 2016. **6**(2): p. 71-79.

277. Chellaiah, E.R., *Cadmium (heavy metals) bioremediation by Pseudomonas aeruginosa: a minireview.* Applied water science, 2018. **8**(6): p. 154.

278. Sullivan, M.J., K.G. Goh, and G.C. Ulett, *Regulatory cross-talk supports resistance to Zn intoxication in Streptococcus.* PLoS Pathogens, 2022. **18**(7): p. e1010607.

279. McNeilly, O., et al., *Emerging concern for silver nanoparticle resistance in Acinetobacter baumannii and other bacteria.* Frontiers in Microbiology, 2021. **12**: p. 652863.

280. Silver, S., et al., *Resistance to Ag (I) cations in bacteria: environments, genes and proteins.* Metal-based drugs, 1999. **6**(4-5): p. 315-320.

281. Terzioğlu, E., et al., *Microbial silver resistance mechanisms: Recent developments.* World Journal of Microbiology and Biotechnology, 2022. **38**(9): p. 158.

282. Dupont, C.L., G. Grass, and C. Rensing, *Copper toxicity and the origin of bacterial resistance—new insights and applications.* Metallomics, 2011. **3**(11): p. 1109-1118.

283. Liu, Y., et al., *Role of implants surface modification in osseointegration: A systematic review.* Journal of Biomedical Materials Research Part A, 2020. **108**(3): p. 470-484.

284. Zheng, S., et al., *Implication of surface properties, bacterial motility, and hydrodynamic conditions on bacterial surface sensing and their initial adhesion.* Frontiers in Bioengineering and Biotechnology, 2021. **9**: p. 643722.

285. Huang, Y., et al., *The construction of hierarchical structure on Ti substrate with superior osteogenic activity and intrinsic antibacterial capability.* Scientific reports, 2014. **4**(1): p. 1-10.

286. Wang, Y., et al., *A trilogy antimicrobial strategy for multiple infections of orthopedic implants throughout their life cycle.* Bioactive materials, 2021. **6**(7): p. 1853-1866.

287. Doyle, R.J., T.H. Matthews, and U. Streips, *Chemical basis for selectivity of metal ions by the Bacillus subtilis cell wall.* Journal of bacteriology, 1980. **143**(1): p. 471-480.

288. Biswas, R., et al., *Overview on the role of heavy metals tolerance on developing antibiotic resistance in both Gram-negative and Gram-positive bacteria.* Archives of microbiology, 2021. **203**: p. 2761-2770.

289. Morth, J.P., et al., *A structural overview of the plasma membrane Na+, K+-ATPase and H+-ATPase ion pumps.* Nature reviews Molecular cell biology, 2011. **12**(1): p. 60-70.

290. Khater, M.S., et al., *Study to elucidate effect of titanium dioxide nanoparticles on bacterial membrane potential and membrane permeability.* Materials Research Express, 2020. **7**(3): p. 035005.

291. Messner, K.R. and J.A. Imlay, *The identification of primary sites of superoxide and hydrogen peroxide formation in the aerobic respiratory chain and sulfite reductase complex of Escherichia coli.* Journal of Biological Chemistry, 1999. **274**(15): p. 10119-10128.

292. Korshunov, S. and J.A. Imlay, *Two sources of endogenous hydrogen peroxide in Escherichia coli.* Molecular microbiology, 2010. **75**(6): p. 1389-1401.

293. Mammari, N., et al. *Current Knowledge on the Oxidative-Stress-Mediated Antimicrobial Properties of Metal-Based Nanoparticles*. Microorganisms, 2022. **10**, DOI: 10.3390/microorganisms10020437.

294. Imlay, J.A., *The molecular mechanisms and physiological consequences of oxidative stress: lessons from a model bacterium.* Nature Reviews Microbiology, 2013. **11**(7): p. 443-454.

295. Vitale, A.A., et al., *New insights of the Fenton reaction using glycerol as the experimental model. Effect of O2, inhibition by Mg2+, and oxidation state of Fe.* The Journal of Physical Chemistry A, 2016. **120**(28): p. 5435-5445.

296. Luque-Agudo, V., et al., *The role of magnesium in biomaterials related infections.* Colloids and surfaces B: Biointerfaces, 2020. **191**: p. 110996.

297. Truskewycz, A., et al., *Fluorescent magnesium hydroxide nanosheet bandages with tailored properties for biocompatible antimicrobial wound dressings and pH monitoring.* ACS Applied Materials & Interfaces, 2021. **13**(24): p. 27904-27919.

298. Ioannou, C.J., G.W. Hanlon, and S.P. Denyer, *Action of disinfectant quaternary ammonium compounds against Staphylococcus aureus.* Antimicrob Agents Chemother, 2007. **51**(1): p. 296-306.

299. Anastassopoulou, J. and T. Theophanides, *The Role of Metal Ions in Biological Systems and Medicine*, in *Bioinorganic Chemistry: An Inorganic Perspective of Life*, D.P. Kessissoglou, Editor. 1995, Springer Netherlands: Dordrecht. p. 209-218.

300. Li, L., et al., *ROS-catalytic transition-metal-based enzymatic nanoagents for tumor and bacterial eradication.* Advanced Functional Materials, 2022. **32**(1): p. 2107530.

301. Shaw, Z., et al., *Illuminating the biochemical interaction of antimicrobial few-layer black phosphorus with microbial cells using synchrotron macro-ATR-FTIR.* Journal of Materials Chemistry B, 2022. **10**(37): p. 7527-7539.

302. Hu, X.-J., et al., *Synchrotron FTIR spectroscopy reveals molecular changes in Escherichia coli upon Cu 2+ exposure.* Nuclear Science and Techniques, 2016. **27**: p. 1-8.

303. Cheeseman, S., et al., *Applications of synchrotron-source IR spectroscopy for the investigation of insect wings*, in *Synchrotron Radiation-Useful and Interesting Applications*. 2019, Intechopen.

304. Kumar, S., et al., *The bacterial cell wall: from lipid II flipping to polymerization.* Chemical Reviews, 2022. **122**(9): p. 8884-8910.

305. Kulkarni, R., E.A. Wiemer, and W. Chang, *Role of lipid rafts in pathogen-host interaction-a mini review.* Frontiers in Immunology, 2022. **12**: p. 815020.

306. Pettersen, J.M., Y. Yang, and A.S. Robinson, *Advances in nanodisc platforms for membrane protein purification.* Trends in Biotechnology, 2023.

307. Díaz-Visurraga, J., et al., *Metal nanostructures as antibacterial agents.* Science against microbial pathogens: communicating current research and technological advances, 2011. **1**: p. 210-218.

308. Vongsvivut, J., et al., *FTIR microspectroscopy for rapid screening and monitoring of polyunsaturated fatty acid production in commercially valuable marine yeasts and protists.* Analyst, 2013. **138**(20): p. 6016-6031.

309. Ojeda, J., et al., *In situ monitoring of the biofilm formation of Pseudomonas putida on hematite using flow-cell ATR-FTIR spectroscopy to investigate the formation of inner-sphere bonds between the bacteria and the mineral.* Mineralogical Magazine, 2008. **72**(1): p. 101-106.

310. Bocker, U., et al., *592 Egelandsdal, B.; Kohler, A. Revealing covariance structures in Fourier transform infrared and 593 Raman microspectroscopy spectra: A study on pork muscle fiber tissue subjected to different 594 processing parameters.* Appl. Spectrosc, 2007. **61**(10): p. 1032-1039.

311. Parikh, S.J. and J. Chorover, *ATR-FTIR spectroscopy reveals bond formation during bacterial adhesion to iron oxide.* Langmuir, 2006. **22**(20): p. 8492-8500.

312. Movasaghi, Z., S. Rehman, and D.I. ur Rehman, *Fourier Transform Infrared (FTIR) Spectroscopy of Biological Tissues.* Applied Spectroscopy Reviews, 2008. **43**(2): p. 134-179.

313. Wood, B.R., *The importance of hydration and DNA conformation in interpreting infrared spectra of cells and tissues.* Chemical Society Reviews, 2016. **45**(7): p. 1980-1998.

314. Tomas, R.C., et al., *Detection of breast cancer by ATR-FTIR spectroscopy using artificial neural networks.* PLoS One, 2022. **17**(1): p. e0262489.

315. Ivanova, E.P., et al., *Bactericidal activity of black silicon.* Nature communications, 2013. **4**(1): p. 2838.

316. Pham, D.Q., et al., *Antibacterial Longevity of a Novel Gallium Liquid Metal/Hydroxyapatite Composite Coating Fabricated by Plasma Spray.* ACS Applied Materials & Interfaces, 2022. **14**(16): p. 18974-18988.

317. Smith, B.D. and D.A. Grande, *The current state of scaffolds for musculoskeletal regenerative applications.* Nature Reviews Rheumatology, 2015. **11**(4): p. 213-222.

318. Sadeghzade, S., et al., *Recent advances on bioactive baghdadite ceramic for bone tissue engineering applications: 20 years of research and innovation (a review).* Materials Today Bio, 2022. **17**: p. 100473.

319. Roope, L.S., et al., *The challenge of antimicrobial resistance: what economics can contribute.* Science, 2019. **364**(6435): p. eaau4679.

320. Naghavi, M., et al., *Global burden of bacterial antimicrobial resistance 1990–2021: a systematic analysis with forecasts to 2050.* The Lancet, 2024. **404**(10459): p. 1199-1226.

321. Lambert, J. and P. Midolo, *The actions of bismuth in the treatment of Helicobacter pylori infection.* Alimentary pharmacology & therapeutics, 1997. **11**(S1): p. 27-33.

322. Deng, T., et al., *Bismuth drugs reverse tet (X)-conferred tigecycline resistance in gram-negative bacteria.* Microbiology Spectrum, 2022. **10**(1): p. e01578-21.

323. Bacakova, L., et al., *Modulation of cell adhesion, proliferation and differentiation on materials designed for body implants.* Biotechnology advances, 2011. **29**(6): p. 739-767.

324. Rosa, A.L., et al., *Osseointegration and osseoconductivity of hydroxyapatite of different microporosities.* Journal of materials science: Materials in medicine, 2002. **13**: p. 1071-1075.

325. Ishak, D.H.A., et al., *A bismuth diethyldithiocarbamate compound promotes apoptosis in HepG2 carcinoma, cell cycle arrest and inhibits cell invasion through modulation of the NF-κB activation pathway.* Journal of Inorganic Biochemistry, 2014. **130**: p. 38-51.

326. Cheng, T., et al., *Bismuth drugs tackle Porphyromonas gingivalis and attune cytokine response in human cells†.* Metallomics, 2019. **11**(7): p. 1207-1218.

327. Li, C., et al., *Design of biodegradable, implantable devices towards clinical translation.* Nature Reviews Materials, 2020. **5**(1): p. 61-81.

328. Mont, M.A., et al., *Nontraumatic osteonecrosis of the femoral head: where do we stand today?: a 5-year update.* The Journal of Bone and Joint Surgery. American Volume, 2020. **102**(12): p. 1084.

329. Caldara, M., et al., *Environmental, microbiological, and immunological features of bacterial biofilms associated with implanted medical devices.* Clinical Microbiology Reviews, 2022. **35**(2): p. e00221-20.

330. Yu, X., et al., *Biomaterials for bone regenerative engineering.* Advanced healthcare materials, 2015. **4**(9): p. 1268-1285.

331. Li, B. and T.J. Webster, *Bacteria antibiotic resistance: New challenges and opportunities for implant-associated orthopedic infections.* Journal of Orthopaedic Research®, 2018. **36**(1): p. 22-32.

332. Zimmerli, W., *Clinical presentation and treatment of orthopaedic implant-associated infection.* Journal of internal medicine, 2014. **276**(2): p. 111-119.

333. Bohara, S. and J. Suthakorn, *Surface coating of orthopedic implant to enhance the osseointegration and reduction of bacterial colonization: A review.* Biomaterials Research, 2022. **26**(1): p. 26.

334. Lam, S.J., et al., *Combating multidrug-resistant Gram-negative bacteria with structurally nanoengineered antimicrobial peptide polymers.* Nature microbiology, 2016. **1**(11): p. 1-11.

335. Greulich, C., et al., *The toxic effect of silver ions and silver nanoparticles towards bacteria and human cells occurs in the same concentration range.* RSC advances, 2012. **2**(17): p. 6981-6987.

336. Li, Y., J. Ho, and C.P. Ooi, *Antibacterial efficacy and cytotoxicity studies of copper (II) and titanium (IV) substituted hydroxyapatite nanoparticles.* Materials Science and Engineering: C, 2010. **30**(8): p. 1137-1144.

337. Wang, R., et al., *Bismuth antimicrobial drugs serve as broad-spectrum metallo-β-lactamase inhibitors.* Nature communications, 2018. **9**(1): p. 439.

338. Griffith, D.M., et al., *Medicinal chemistry and biomedical applications of bismuth-based compounds and nanoparticles.* Chemical Society Reviews, 2021. **50**(21): p. 12037-12069.

339. Li, H., R. Wang, and H. Sun, *Systems approaches for unveiling the mechanism of action of bismuth drugs: new medicinal applications beyond Helicobacter pylori infection.* Accounts of chemical research, 2018. **52**(1): p. 216-227.

340. Tran-Phu, T., et al., *Understanding the activity and stability of flame-made Co3O4 spinels: A route towards the scalable production of highly performing OER electrocatalysts.* Chemical Engineering Journal, 2022. **429**: p. 132180.

341. Tran-Phu, T., et al., *Nanostructured β-Bi2O3 fractals on carbon fibers for highly selective CO2 electroreduction to formate.* Advanced Functional Materials, 2020. **30**(3): p. 1906478.

342. Jenkins, J., et al., *Antibacterial effects of nanopillar surfaces are mediated by cell impedance, penetration and induction of oxidative stress.* Nature communications, 2020. **11**(1): p. 1626.

343. Tran-Phu, T., et al., *From Stochastic Self-Assembly of Nanoparticles to Nanostructured (Photo) Electrocatalysts for Renewable Power-to-X Applications via Scalable Flame Synthesis.* Advanced Functional Materials, 2022. **32**(13): p. 2110020.

344. Tran-Phu, T., et al., *Understanding the Role of (W, Mo, Sb) Dopants in the Catalyst Evolution and Activity Enhancement of Co3O4 during Water Electrolysis via In Situ Spectroelectrochemical Techniques.* Small, 2023: p. 2208074.

345. Nguyen, N.H., et al., *Engineering antibacterial bioceramics: Design principles and mechanisms of action.* Materials Today Bio, 2024. **26**: p. 101069.

346. Nguyen, H.N., et al., *Antibacterial Activity and Mechanisms of Magnesium-Doped Baghdadite Bioceramics for Orthopedic Implants.* Advanced NanoBiomed Research, 2024: p. 2400119.

347. Wang, J., et al., *Biomimetic Bacterium-like Particles Loaded with Aggregation-Induced Emission Photosensitizers as Plasma Coatings for Implant-Associated Infections.* ACS Applied Materials & Interfaces, 2024. **16**(15): p. 18449-18458.

348. Wong, F., et al., *Cytoplasmic condensation induced by membrane damage is associated with antibiotic lethality.* Nature communications, 2021. **12**(1): p. 2321.

349. Gray, D.A., et al., *Membrane depolarization kills dormant Bacillus subtilis cells by generating a lethal dose of ROS.* Nature Communications, 2024. **15**(1): p. 6877.

350. Mu, X., T.D. Evans, and F. Zhang, *ATP biosensor reveals microbial energetic dynamics and facilitates bioproduction.* Nature Communications, 2024. **15**(1): p. 5299.

351. Fasnacht, M. and N. Polacek, *Oxidative stress in bacteria and the central dogma of molecular biology.* Frontiers in Molecular Biosciences, 2021. **8**: p. 671037.

352. Nguyen, T.T., et al., *Synchrotron macro ATR-FTIR micro-spectroscopy to unlock silver ion-induced biochemical alterations in bacteria.* Materials Advances, 2023. **4**(23): p. 6342-6352.

353. Le, P.H., et al., *Apoptosis of Multi-Drug Resistant Candida Species on Microstructured Titanium Surfaces.* Advanced Materials Interfaces, 2023. **10**(34): p. 2300314.

354. Lok, C.-N., et al., *Proteomic analysis of the mode of antibacterial action of silver nanoparticles.* Journal of proteome research, 2006. **5**(4): p. 916-924.

355. Bhadra, C.M., et al., *Antibacterial titanium nano-patterned arrays inspired by dragonfly wings.* Scientific reports, 2015. **5**(1): p. 16817.

356. Hayles, A., et al., *Vancomycin tolerance of adherent Staphylococcus aureus is impeded by nanospike-induced physiological changes.* npj Biofilms and Microbiomes, 2023. **9**(1): p. 90.

357. Ivanova, E.P., et al., *Natural bactericidal surfaces: mechanical rupture of Pseudomonas aeruginosa cells by cicada wings.* Small, 2012. **8**(16): p. 2489.

358. Okuda, S., et al., *Lipopolysaccharide transport and assembly at the outer membrane: the PEZ model.* Nature Reviews Microbiology, 2016. **14**(6): p. 337-345.

359. Weidenmaier, C. and A. Peschel, *Teichoic acids and related cell-wall glycopolymers in Gram-positive physiology and host interactions.* Nature Reviews Microbiology, 2008. **6**(4): p. 276-287.